Copyright

by

Rudra Narayan Chatterjee

2016

The Dissertation Committee for Rudra Narayan Chatterjee Certifies that this is the approved version of the following dissertation:

Os isotopic compositions of mantle peridotites and steels: Implications for Pt-Re-Os evolution of the Earth's upper mantle and continental crust

Committee:

John Lassiter, Supervisor

James Gardner

Jaime Barnes

Luc Lavier

Staci Loewy

Jonathan Snow

Os isotopic compositions of mantle peridotites and steels: Implications for Pt-Re-Os evolution of the Earth's upper mantle and continental crust

by

Rudra Narayan Chatterjee, B.S, M.S

Dissertation

Presented to the Faculty of the Graduate School of

The University of Texas at Austin

in Partial Fulfillment

of the Requirements

for the Degree of

Doctor of Philosophy

The University of Texas at Austin

August 2016

Dedication

This dissertation is dedicated to my parents, Swati and Biswajit, my sister, Rudrani and my wife, Proma. It is also dedicated to the memory of my late grandfather, Dr. R.N. Chatterjee.

Acknowledgements

This dissertation would not be complete without the help and guidance of many people. First and foremost is my doctoral advisor, John Lassiter, whose support and mentorship guided me throughout this project. John encouraged me to think critically, taught me to express my ideas in a clear and concise fashion and helped shape me into becoming a full-fledged geochemist. I am confident that the many lessons I learnt from John over these years will leave an indelible impact on the way I do science in the future.

I greatly benefitted through the numerous discussions and constructive reviews I received from all my committee members. Jim Gardner gave me valuable lessons in volcanology and petrology. Jaime's (Jaime Barnes) door was always open for any questions I had. John Snow gave me useful pointers about mantle geochemistry, particularly during our meetings at AGU. I learnt a number of useful concepts on geodynamics through my discussions with Luc Lavier. Staci Loewy provided valuable assistance in the Radiogenic TIMS lab but also gave me useful advice on my writing and mass-spectrometry skills.

I spent the vast majority of my time in the various analytical labs throughout the department. Staci Loewy and Shuangquan Zhang provided me with countless assistance and useful tips during the hours I spent in the Radiogenic TIMS lab. I am also grateful for all the help I received from Allison Koleszar, Toti Larsen, Nate Miller, and Donggao Zhao in running other spectrometric facilities in the department.

My friends and fellow graduate students helped me stay motivated and focused and I am indebted to the innumerable assistances and insight I have received from them. From listening to my practice talks, proofing over my AGU abstract, to sharing the wet-chemistry lab work and the countless discussions on topics involving geochemistry and beyond, I am deeply indebted to my fellow research group members- Benjamin Byerly, Ruohan Gao, Ed Marshall and Leslie Bruce. A special shout to all my friends here at Austin and at Houston, particularly to Chinmoy, Sundaram, Harish, Subhendu, Garima, Avhishek, Tania, Prasenjit, Damayanti, and Arnab who have helped maintain my sanity on countless evenings and often provided much required distractions outside the TIMS lab.

I greatly acknowledge the generous financial support received from the Jackson School of Geosciences in the form of teaching and research assistantships, and the National Science foundation for financial assistance in the form of grants EAR-1321937 and EAR-0911253.

I cannot express my indebtedness to my parents and my sister, Rudrani for their untold confidence in me. Finally, I could not have done this without you, Proma Bhattacharyya, my wife, who stood by me and provided me with unconditional love and support.

Os isotopic compositions of mantle peridotites and steels: Implications for Pt-Re-Os evolution of the Earth's upper mantle and continental crust

Rudra Narayan Chatterjee, PhD

The University of Texas at Austin, 2016

Supervisor: John Lassiter

The ^{190}Pt-^{186}Os system can be useful to examine a number of different geologic processes including core-mantle interaction, examining the role of pyroxenites or sulfides in mantle melting and dating of Platinum Group Element (PGE) based ores. Limited natural variation of ^{186}Os/^{188}Os in the mantle requires extremely high precision to detect natural variations. I identified Johnson noise on baseline integrations to be the largest source of analytical error for the quantities of Os and ^{186}Os beam intensities utilized in previous ^{186}Os/^{188}Os studies. Increasing the duration of baseline measurement significantly reduces the Johnson noise error, allowing to achieve maximum external precision for a given sample size.

^{186}Os/^{188}Os variations in mantle peridotites provide constraints on the long-term Pt/Os evolution of the depleted mantle and the Pt/Os ratio of the primitive upper mantle (PUM). Fertility-^{186}Os/^{188}Os correlations in mantle peridotites were used to infer PUM ^{186}Os/^{188}Os and Pt/Os ratios. I found that PUM Pt/Os ratio is broadly chondritic, consistent with a late veneer addition of chondritic materials and similar to most fertile peridotites. I proposed

that the departures in PUM Pd/Ir and Ru/Ir ratios from chondritic values could be explained by minor metal or sulfide segregation to the Earth's core occurring concurrently with late veneer addition. Combined $^{186}Os/^{188}Os$-$^{187}Os/^{188}Os$ isotopic and Pt/Os and Re/Os variability in peridotites suggest an average mantle homogenization timescale of ~1.2 Ga, consistent with timescales predicted for whole mantle convection.

Steels offer a unique opportunity to determine ^{186}Os-^{187}Os compositions of crustal- and mantle-reservoirs sampled by iron ore, coal and chromitites used in its manufacture. My results indicate that mixing between unradiogenic, upper mantle-like Os derived from chromitites and radiogenic, crustal like Os from iron ore and coal can explain the observed Os concentration and isotope variations in steels. Extrapolation of $^{187}Os/^{188}Os$ - $^{187}Os/^{188}Os$ trend in steels allows inference of its mantle and crustal- end member components. Extrapolation of $^{187}Os/^{188}Os$-$^{186}Os/^{188}Os$ trends to the estimated $^{187}Os/^{188}Os$ of chromitites yields a $^{186}Os/^{188}Os$ value consistent with derivation of chromitites from mantle sources during Archean to Proterozoic and subsequent evolution with sub-chondritic Pt/Os ratios. Extrapolation of steel $^{187}Os/^{188}Os$-$^{186}Os/^{188}Os$ trends to $^{187}Os/^{188}Os$ values typical for banded iron formations and coal yields a $^{186}Os/^{188}Os$ value indistinguishable from present-day upper mantle and within uncertainty of the PUM at the time of BIF and/or coal formation, but systematically lower than bulk upper continental crust (UCC). Previous studies (McDaniel et al., 2004) also report similar unradiogenic (in comparison to upper continental crust) $^{186}Os/^{188}Os$ values for seawater derived marine Mn-nodules and black shales. Preferential weathering of crustal sulfides with low Pt/Os ratios and lower $^{186}Os/^{188}Os$ values than bulk UCC can explain the

systematically lower $^{186}Os/^{188}Os$ values in crustal weathering products relative to bulk UCC.

Table of Contents

List of Tables

List of Figures

Introduction

The Re-Os and Pt-Os systems have several unique geochemical characteristics that make them incredibly powerful tools in geochemical studies examining mantle evolution. Os is highly compatible during mantle melting whereas both Re and Pt are generally moderately incompatible during partial melting. Therefore, Re-Os and Pt-Os isotope systems could both be potentially used to study mantle melt depletion. A greater compatibility of rhenium in sulfide melt relative to Pt (Fleet et al., 1996; Sattari et al., 2002; Day et al., 2013) could allow utilization of Pt/Os and Re/Os ratios to potentially distinguish fractionation from silicate melting and sulfide melt migration. The highly siderophile nature of Pt, Re and Os also make the Pt-Os and Re-Os systems particularly well suited for studying chemical interaction between the core and the mantle (cf. Brandon et al., 1998) or for testing the late veneer hypothesis (cf. Brandon et al., 2006).

Despite the potential for studying a range of geologic processes, the Pt-Os isotope system suffers from a major caveat in comparison to the Re-Os system. A very low abundance of the parent isotope ^{190}Pt (0.0129 % of total Pt) and long half-life (~468 Ga) (Begemann et al., 2001) for the ^{190}Pt-^{186}Os system results in limited ^{186}Os/^{188}Os variations in the mantle (~150 ppm; cf. Brandon et al., 1998). This requires a very high level of analytical precision (better than 30 ppm) in Pt-Os studies. The significant analytical challenge of generating sufficiently high precision ^{186}Os/^{188}Os measurements has largely limited the widespread use of the Pt-Os system.

In this dissertation, I examine different geochemical problems related to the chemical evolution of the upper mantle and the continental crust utilizing the ^{190}Pt-^{186}Os isotope system. The first study (presented in Chapter 1) examines the sources of error in high precision ^{186}Os/^{188}Os measurements and proposes refined analytical procedures that allow for maximization of analytical precision for a given sample size. The second study (presented in Chapter 2) utilizes fertility index vs ^{186}Os/^{188}Os correlations in variably melt-depleted mantle peridotites (^{187}Os/^{188}Os) to constrain the ^{186}Os/^{188}Os and Pt/Os ratio of the Primitive Upper Mantle (PUM). Estimated PUM Pt/Os ratio is combined with other estimated HSE ratios to explore how a combination of late veneer addition and core segregation processes can explain observed HSE abundances and ratios in the upper mantle. Finally, isotopic and parent/daughter ratio variability in Re-Os and Pt-Os isotope systems in peridotites are used to constrain the homogenization timescales for mixing of mantle heterogeneities. The third study (presented in Chapter 3) examines Os and Pb isotope compositions in industrial steels to constrain the sources of Os and Pb in steel. Trends between ^{186}Os/^{188}Os-^{187}Os/^{188}Os in steels are utilized to infer the ^{186}Os/^{188}Os of the crustal sources of Os in steel, namely iron ores and coal. Comparison with constraints from black shales, marine Mn nodules, loess and freshwater water Mn nodules allow evaluation of the Pt-Re-Os evolution of different crustal reservoirs.

QUANTIFYING THE VARIOUS SOURCES OF ERROR IN ^{186}OS/^{188}OS MEASUREMENTS USING N-TIMS

Over the last decade, the ^{190}Pt-^{186}Os isotope system has generated considerable attention owing to its potential to track core-mantle signatures within plume-derived

lavas. Additionally, it may be a useful proxy for melt depletion, examining the role of pyroxenite/sulfides in mantle melting and for dating PGE based ores. However, as the total natural variation of $^{186}Os/^{188}Os$ is limited (~150 ppm in the mantle), the requirements for analytical precision and accuracy are very high so as to discern any natural variations. Although previous studies have achieved the necessary external precisions for $^{186}Os/^{188}Os$ measurements, their analytical protocol have required processing of several hundreds of grams of material for obtaining tens of ng's of Os and thus is far from optimal.

In this study, I have quantified the various sources of systematic biases and random errors associated with high precision $^{186}Os/^{188}Os$ measurements and compared theoretical predictions with empirical results. Based on my findings, I recommend refined analytical procedures to minimize the various sources of errors associated with $^{186}Os/^{188}Os$ measurements and achieve maximum external precisions for a given sample size. My key findings indicate that Johnson noise on intra-block baseline measurements is the largest source of error for $^{186}Os/^{188}Os$ measurements for the quantities of Os and beam intensities utilized in previous studies and can be reduced by increasing the duration of baseline measurements. Determination of the oxygen isotope composition required for offline oxide correction of the Os isotopes through pre- and post- Os run measurement is sufficient, therefore allowing greater time to be spent on measuring the primary Os isotopes. Although use of $^{189}Os/^{188}Os$ as the normalizing ratio for correcting mass fractionation introduces lower uncertainty derived from oxide correction of the Os isotopes, this effect is overwhelmed by the greater propagated error from mass

fractionation correction. Thus it is preferable to use $^{192}Os/^{188}Os$ as the normalizing ratio as it generates the least propagated error from mass fractionation. Monitoring and stripping of PtO_2^- interferences is necessary as more critical interferences such as WO_3^- and organic material may be masked behind the PtO_2^- peaks.

USING $^{186}OS/^{188}OS$-FERTILITY TRENDS IN MANTLE PERIDOTITES TO CONSTRAIN PT/OS RATIO OF THE PRIMITIVE UPPER MANTLE AND IMPLICATIONS FOR LATE VENEER ACCRETION AND MANTLE-MIXING TIMESCALES

Mantle peridotites are extremely useful to examine the interior of the Earth as they provide a direct snapshot of the otherwise inaccessible upper mantle. In chapter 2, I report new $^{186}Os/^{188}Os$ data in a suite of peridotites from continental (Rio Grande Rift/Colorado Plateau) and oceanic (Lena Trough/Hawaii) settings. Broad correlations between several indices of melt depletion (e.g., spinel Cr#, clinopyroxene Cr#, clinopyroxene Yb, and bulk rock Al_2O_3) and $^{186}Os/^{188}Os$ suggest that $^{186}Os/^{188}Os$ variations and long-term Pt/Os variations in the upper mantle are largely controlled by melt depletion. I utilize these fertility trends to constrain the primitive upper mantle $^{186}Os/^{188}Os$ and Pt/Os ratio, providing new constrains on the processes controlling Highly Siderophile Element (HSE) abundances in the mantle. My results show that the Primitive Upper Mantle (PUM) has roughly chondritic $^{186}Os/^{188}Os$. This suggests that the Silicate Earth has evolved with chondritic bulk Pt/Os, lending support to the late veneer hypothesis. Although some other HSE element pairs appear to be non-chondritic in the upper mantle (e.g., Ru/Ir, Pd/Ir) (Becker et al., 2006), I discuss the possibility of how several processes including metal or sulfide segregation during late veneer addition can potentially explain these minor departures from chondritic HSE relative abundances in the mantle, without invalidating

the late veneer hypothesis or requiring accretion of exotic components not sampled in current meteorite collections. The degree of Os-isotope and Re/Os and Pt/Os variation in mantle peridotites provides constraints on the mixing and homogenization timescale for the mantle. The homogenization timescale suggested by Os-isotope heterogeneity is ~1.2 Gyrs, which is consistent with mixing timescales suggested by geodynamic models for whole-mantle convection. The origin of elevated $^{186}Os/^{188}Os$ in plume-derived lavas from Hawaii and Gorgona is also widely debated (cf. Brandon et al., 2005). I show that melting of fertile mantle components with variable additions of recycled oceanic crust cannot explain these elevated $^{186}Os/^{188}Os$ values.

EXAMINING THE OS ISOTOPIC COMPOSITION OF INDUSTRIAL STEELS TO CONSTRAIN THE SOURCES OF OS IN STEEL AND UTILIZE $^{187}Os/^{188}Os$-$^{186}Os/^{188}Os$ TRENDS IN STEEL TO INFER THE OS ISOTOPE COMPOSITION OF CRUSTAL SOURCES OF STEEL

PPGE (Platinum-Platinum group elements; Pt, Pd) and Re are moderately compatible to moderately incompatible during mantle melting relative to IPGE (Iridium-PGE; Ir, Os, Ru), which are highly compatible (cf. Day et al., 2013). Therefore, extraction of the continental crust from the upper mantle should result in elevated PPGE/IPGE patterns in the continental crust. The majority of the measured PGE data for direct samples of the continental crust show highly elevated Pt/Os and/or Pd/Ir ratios (Puecker-Ehrenbrink and Jahn, 2001). Indirect estimates of the Pt/Os of the Upper Continental Crust (UCC) based on Os isotopic measurements of loess and freshwater Mn nodules also indicate high Pt/Os ratios in bulk crust (McDaniel et al., 2004). In contrast, measurements of black shales and seawater inferred from marine Mn nodules both show unradiogenic to slighty radiogenic $^{186}Os/^{188}Os$ values, consistent with a modest Pt/Os ratio in their crustal source

(McDaniel et al., 2004). This presents the question, that if shales and seawater derived Os from the upper continental crust as indicated from their highly radiogenic $^{187}Os/^{188}Os$ values at the time of formation, why are the $^{186}Os/^{188}Os$ values and by inference, Pt/Os ratios in these weathered products of the continental crust systematically lower compared to bulk UCC?

Industrial steels offer a unique opportunity to indirectly determine the Os isotope compositions of distinct crustal reservoirs sampled by iron ores and coal used in its manufacture. I examined Os concentrations and isotopic compositions in industrial steels spanning a range of compositions (Fe~ 64-98 wt.%; Cr ~0-22 wt.%). Steels show a wide range in Os concentrations from 0.03 to 22 ppb and highly, radiogenic $^{187}Os/^{188}Os$ (~0.1435-4.118). The primary components used in steel manufacture are iron ore, coal, and chromitite. Chromitites have high average Os concentrations and mantle-like $^{187}Os/^{188}Os$ ratios. In contrast, both iron ores and coal are derived from crustal sources with highly radiogenic $^{187}Os/^{188}Os$. Correlations between Os and Cr content suggest that chromite-derived Os dominates the Os budget in high-Cr steels. Correlations between Os concentrations and $^{187}Os/^{188}Os$ in steels are consistent with two-component mixing of Os derived from unradiogenic, upper-mantle-like chromitites and highly radiogenic, continental-crust-like Os from crustal iron ores and coke. Because the radiogenic crustal end member in steels are inherited from a roughly 50:50 Os contribution from coke and iron ore, extrapolation of the $^{187}Os/^{188}Os$-$^{186}Os/^{188}Os$ trend in steels can constrain the $^{186}Os/^{188}Os$ of these crustal sources. My results surprisingly indicate that the crustal sources for both iron ore and coke have unradiogenic $^{186}Os/^{188}Os$ values indistinguishable

from the average upper mantle, despite having high $^{187}Os/^{188}Os$ at their sources in the time of deposition. My results are in agreement with the systematically lower $^{186}Os/^{188}Os$ values also obtained for shales and seawater inferred from marine Mn nodules, all of which are ultimately derived from weathering of the upper continental crust. Crustal sulfides with high Os concentrations and low Pt/Os ratios could develop over time unradiogenic $^{186}Os/^{188}Os$ values relative to bulk UCC. Preferential removal of such low Pt/Os phases during oxidative crustal weathering can supply unradiogenic $^{186}Os/^{188}Os$ to the weathering products of the UCC and explain this discrepancy between weathering products and direct samples of the bulk UCC.

Chapter 1: High precision Os isotopic measurement using N-TIMS: Quantification of various sources of error in $^{186}Os/^{188}Os$ measurements

ABSTRACT

The ^{190}Pt-^{186}Os system could be useful to study a number of different geologic processes. Over the last decade, this system has received considerable attention owing to its potential to detect core-mantle signatures in plume-derived lavas. Additionally, this system may also be useful as a proxy for melt depletion, examining the role of pyroxenites/sulfides in mantle melting and for dating of Platinum Group Element (PGE) based ores. The total natural variation of $^{186}Os/^{188}Os$ is limited (~150 ppm in the mantle), which thus requires extremely high levels of accuracy and precision to discern natural variations. $^{186}Os/^{188}Os$ ratios were measured in laboratory standards and natural samples to examine and quantify the sources of error affecting high precision $^{186}Os/^{188}Os$ measurements and a set of refined analytical procedures to minimize and reduce these various sources of error were recommended.[1] [2]

Inter and intra-run variations in oxygen isotopic composition used in oxide correction of OsO_3^- peaks can produce systematic shifts in $^{186}Os/^{188}Os$. Useful analysis time is wasted in measuring O isotopic composition line-by-line and it is sufficient to utilize pre- and post-run determination of O isotopic composition for performing oxide correction.

---

[1] The contents of this chapter has been published as: Chatterjee, R., Lassiter, J.C., 2015. High precision Os isotopic measurement using N-TIMS: Quantification of various sources of error in $^{186}Os/^{188}Os$ measurements, *Chemical Geology 396, 112-123*.

[2] The material presented in this chapter is my original work completed under the supervision of Dr. Lassiter.

Although the use of $^{189}Os/^{188}Os$ as a normalizing ratio for mass fractionation results in lower uncertainty in Os isotopes from oxide correction, this benefit is overwhelmed by the increased error propagation from mass fractionation. Instead, usage of the $^{192}Os/^{188}Os$ normalization generates the least propagated error due to mass fractionation and is recommended. Earlier studies have variably used different O isotopic compositions for oxide correction and different normalizations for mass fractionation correction, which can generate systematic shifts in the reduced data. Use of mutually consistent normalizing values for mass fractionation largely reduces the offsets between reduced data using different normalizing schemes, thus improving data comparison across laboratories.

For the quantities of Os and beam intensities of ^{186}Os utilized in previous $^{186}Os/^{188}Os$ studies (several 10's of ng Os, 80-250 mV of ^{186}Os with a 10^{11} Ω resistor), the largest source of analytical error is derived from Johnson noise on baseline integrations. Increasing the duration of baseline measurement significantly reduces the Johnson noise error, allowing to achieve maximum external precision for a given sample size. Several $^{186}Os/^{188}Os$ analyses reported in the literature seem to have been compromised by an interference, which may be WO_3^-, organics or some other unidentified species that affects both the $^{186}Os/^{188}Os$ and the $^{184}Os/^{188}Os$ ratios. This makes it extremely critical to monitor and correct PtO_2^- interferences, which could mask other potential interferences that directly affect $^{186}Os/^{188}Os$ measurements.

1. INTRODUCTION

The Re-Os and Pt-Os systems are geochemically unique compared to other long-lived radiogenic trace element systems such as Rb-Sr, Sm-Nd and U-Th-Pb. Because Os is highly compatible during mantle melting whereas Re is moderately incompatible, the Re-Os system has been widely used to study mantle melt depletion (c.f., Snow et al., 1995), recycled components in OIB sources (c.f., Lassiter et al., 1998) and evolution of the Sub-Continental Lithospheric Mantle (SCLM) (c.f., Reisberg et al., 1995). Platinum is less compatible than Os during mantle melting but more compatible than Re (Becker et al., 2006). This allows the Pt-Os and Re-Os systems to be used in conjunction to provide stronger constraints on the extent and timing of melt depletion and refertilization. Rhenium is also more compatible in sulfide melt than Pt [$D_{Pt}^{\textbf{sulfide/silicate}} \approx 6\text{-}14 \times 10^3$; $D_{Re}^{\textbf{sulfide/silicate}} \approx 3.3\text{-}5.2 \times 10^4$ (Fleet et al., 1996; Sattari et al., 2002; Day et al., 2013)], so that comparison of Pt/Os and Re/Os ratios can potentially distinguish fractionation from silicate melting and sulfide melt migration. The siderophile nature of Pt, Re and Os also make the Pt-Os and Re-Os systems useful for study of core-mantle interaction (c.f., Brandon et al., 1998) or for testing of the late veneer hypothesis (c.f., Brandon et al., 2006).

Several geologic processes strongly fractionate Re from Os, leading to orders of magnitude variations in Re/Os ratios between mantle residues and basaltic lavas. Combined with the high abundance of the parent isotope ^{187}Re (~63% of total Re), rapid ingrowth of ^{187}Os in high Re/Os materials creates a wide natural range in ^{187}Os/^{188}Os observed in diverse geological samples [e.g., ^{187}Os/^{188}Os ranges from ~0.113 to 0.129 in

abyssal peridotites (c.f., Snow et al., 1995, Harvey et al., 2006, Lassiter et al., 2014), ~0.12 to 1 in basalts (c.f., Carlson., 2005), ~1 to 10 in black shales (c.f., Carlson., 2005) and is nearly ~1.1 in the continental crust (Puecker-Ehrenbrink et al., 2001)]. Because of this large $^{187}Os/^{188}Os$ variability, per-mil precision measurements are sufficient for most studies, which are achievable with very small sample sizes (tens of picograms of Os or less) via ion counting techniques. In contrast, the reduced natural variation of Pt/Os compared to Re/Os in most geologic materials, extremely low abundance of the parent isotope ^{190}Pt (0.0129 % of total Pt) and long half-life (~468 Ga) (Begemann et al., 2001) results in much more limited $^{186}Os/^{188}Os$ variations in the mantle (~150 ppm; c.f., Brandon et al., 1998). This requires a much higher level of analytical precision (better than 30 ppm) in Pt-Os studies. Although the Pt-Os system has potential for studying a range of geologic processes including core-mantle interaction (Walker et al., 1997; Brandon et al., 1998, 2003; Puchtel et al., 2005), melting of pyroxenites or pyroxenite-derived sulfides (c.f., Luguet et al., 2008a) or for dating the formation of platinum-group-minerals (Walker et al., 1997; Coggon et al., 2012) and ancient mantle melting (Coggon et al., 2013), the analytical challenge of generating sufficiently high precision $^{186}Os/^{188}Os$ measurements has limited the widespread use of the Pt-Os system.

Although modern TIMS instruments can easily achieve precisions better than 30 ppm, achieving this analytical precision is particularly challenging in $^{186}Os/^{188}Os$ studies for several reasons. Several tens of nanograms of Os are required to generate the large signal intensities necessary for high precision measurements. Because Os abundances in natural samples are low (≤few ppb), large quantities of material (up to several hundred grams)

are often processed to obtain enough Os for a single analysis (c.f., Ireland et al., 2011). Most analyses utilize ^{186}Os beam intensities of a few hundred mV at most, due to the low abundance of ^{186}Os (~1.5% of total Os; 100 mV ^{186}Os $\approx$ 2.5 V ^{192}Os). N-TIMS measurement of Os as OsO_3^- also generates a number of isobaric Os oxide interferences. Therefore, precise knowledge of the O isotope composition of the generated OsO_3^- species is required to account for these interferences. Additionally, potential interferences such as PtO_2^-, ReO_3^-, WO_3^- and organics can interfere with various Os isotopes. Additional sources of error inherent to any isotopic measurement include errors from mass fractionation (MF) correction, Johnson noise on baseline and signal integrations, and counting statistics. Because different laboratories have utilized various data processing strategies and methods to quantify and correct for these sources of error, there is the potential for systematic offsets in the corrected data from different laboratories.

In this chapter, the primary sources of systematic bias and random error associated with high precision ^{186}Os/^{188}Os measurements are examined in detail and empirical results are compared with theoretical predictions. These results suggest methods to optimize analytical procedures to maximize precision for a given sample size. The magnitudes of error from a variety of sources are evaluated and Johnson noise on baseline measurements is shown to be the leading source of random error in typical ^{186}Os/^{188}Os measurements. Increasing the duration of baseline measurements significantly reduces Johnson noise and improves external precision of ^{186}Os/^{188}Os measurements. Oxygen isotopic composition measured before and after an analysis is sufficient for oxide

correction and within-run measurement is not necessary. The effects of using different approaches to correct for oxide interferences and mass fractionation are evaluated. This allows direct comparison of datasets generated in laboratories using different data processing techniques.

2. METHODS

Os standards were loaded following procedures outlined in previous studies (c.f., Byerly et al., 2012, Luguet et al., 2008b). Johnson Mathey Os standard (UMD standard) and the Durham Romil Os standard (DROsS) were used. For each analysis, 36-40 nanograms of Os were loaded on Pt filaments. Micropipette tips were used to load the Os solution onto a small portion of the filament. Next, 0.3-0.4 μL of an activator solution (0.56 g $Ba(OH)_2$ mixed with 30 ml of 0.1 M NaOH) was loaded to aid ionization. Samples were usually run between temperatures of 780 and 820 °C but occasionally as high as 860°C. Oxygen was bled into the source chamber from a tank of compressed oxygen and the chamber pressure was maintained at ~3 $X10^{-7}$ mbar. A liquid N_2 cold finger was used to reduce organic interferences.

Os was measured using a Triton Thermal Ionization Mass Spectrometer in negative ion mode (N-TIMS) using a static multi-collector routine for 10 blocks, each comprising 20 cycles, for a total of 200 ratios. Integration time for each cycle was 16.77 s. Most analyses were measured using ~100 mV $^{186}OsO_3$ beam. However, beam intensity was varied from 50-150 mV $^{186}OsO_3$ to evaluate the effect of beam size on external precision. Baselines were measured at the beginning of each block by deflecting the beam. Baseline

measurement durations were varied from 30 s to 5 min to evaluate the effect of baseline Johnson noise on measurement precision. Interferences (masses 228-233) were measured via Secondary Electron Multiplier (SEM) using 4.2 s integration time for 1 block of 10 cycles, before and after the Os routine. Oxygen isotopic composition was determined by measuring peaks 241 and 242 with 2 s integrations either within run via a peak hopping routine or separately before and after the Os routine. Cup configurations for these routines are listed in Table A.1.

Data corrections were performed in the following order on the raw data: MF correction before O stripping, removal of 2 σ outliers, correction for PtO_2^- interferences, oxide correction and residual MF correction. Initial oxide correction used the measured tank O-isotope composition but was iteratively adjusted using the measured in-run O isotopic composition until the O-isotope composition and calculated β factor converged to stable values (usually after 2 iterations). The initial MF correction and the 2σ exclusion were performed online. All other data processing was performed off-line. Correction steps are outlined in more detail in the online supplemental material.

3. Sources of error in $^{186}Os/^{188}Os$ measurements

Several independent factors contribute to total measurement error. Two of the most important errors in any measurement are counting statistics and amplifier noise, which affects both baseline determinations and individual signal integrations. As discussed in section 6, total amplifier noise closely approximates Johnson noise (Nyquist, 1928).

Considering the major components of random measurement error, the net theoretical error of an isotopic ratio A/B is represented by

$$\sigma_{TTE} \approx \sqrt{\left(\sigma_{CS,A}\right)^2 + \left(\sigma_{CS,B}\right)^2 + \left(\sigma_{JNB,A}\right)^2 + \left(\sigma_{JNB,B}\right)^2 + \left(\sigma_{JNS,A}\right)^2 + \left(\sigma_{JNS,B}\right)^2} \quad (1)$$

where σ_{TTE} is total theoretical error, $\sigma_{CS,A}$ and $\sigma_{CS,B}$ are errors from counting statistics for isotopes A and B, $\sigma_{JNB,A}$ and $\sigma_{JNB,B}$ are Johnson noise errors on baseline integrations for isotopes A and B and $\sigma_{JNS,A}$ and $\sigma_{JNS,B}$ are Johnson noise errors on signal integrations for isotopes A and B. The net theoretical error is approximately given by

$$\sigma_{TTE} \approx \sqrt{\left(\sigma_{CS,A}\right)^2 + \left(\sigma_{JNB,A}\right)^2 + \left(\sigma_{JNS,A}\right)^2} \quad (2)$$

if the isotopic abundance of A << B.

Error from counting statistics and Johnson noise during baseline and signal integrations can be estimated by

$$\sigma_{CS} \approx \frac{1}{\sqrt{N_A}} \quad (3)$$

where $N_A = I \times t_S \times N_R \times cn$ ($cn = \Omega_R/C$ where Ω_R = amplifier resistance in ohms, and C ≈ 6.242×10^{18} electron charges)

$$\sigma_{JN_B} \approx \frac{JN_B}{I \times \sqrt{N_B}} \quad (4)$$

$$\sigma_{JN_S} \approx \frac{JN_S}{I \times \sqrt{N_R}} \quad (5)$$

where $N_R = N_B \times N_C$, σ_{CS} is standard error from counting statistics, σ_{JN_B} is standard error due to Johnson noise on baselines (c.f., Section 6), σ_{JN_S} is standard error due to Johnson noise on signal integrations (c.f., Section 6), N_A is total number of measured

atoms of the smallest peak utilized in a ratio, I is signal intensity in V, t_S is the signal integration time in s, N_R is number of ratios of measurement, cn is the number of atoms in a 1 V beam size, JN_B is Johnson noise on baseline integrations in V, N_B is number of blocks of measurement, JN_S is Johnson noise on signal integrations in V and N_C is number of cycles/block.

Errors from oxide corrections and from mass fractionation correction also contribute to the total error, but their effects require more detailed evaluation and are discussed separately in Sections 4 and 5. Figure 1.1 shows the theoretical magnitude of different sources of measurement error as a function of beam intensity. For measurements using standard 30 s baseline determinations, Johnson noise from baseline integrations is the leading source of error for signal intensities <~1.2 V. As shown in figure 1.2, actual measured external reproducibility closely matches predicted theoretical errors (2 SE) for different Os isotopes and variable signal intensities. In the following sections, magnitudes of the various sources of error are quantified and their effects on $^{186}Os/^{188}Os$ precisions are examined.

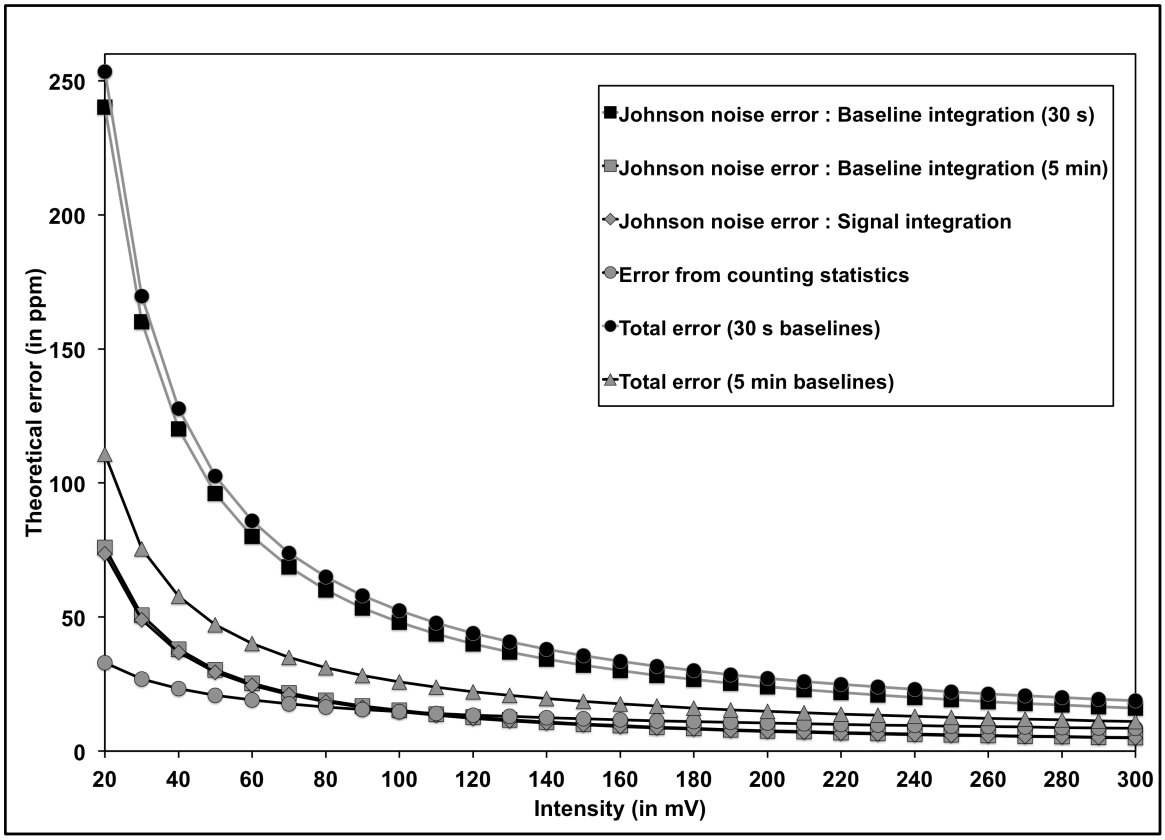

Figure 1.1 Contributions of various sources of error for beam intensities ranging from 20 to 300 mV.

Johnson noise error due to baseline integrations is determined utilizing 30 s and 300 s integrations for 10 blocks of measurements. Johnson noise error due to signal integrations is computed for 16 s integrations on 200 ratios. Error associated with counting statistics is based on 200 measured ratios.

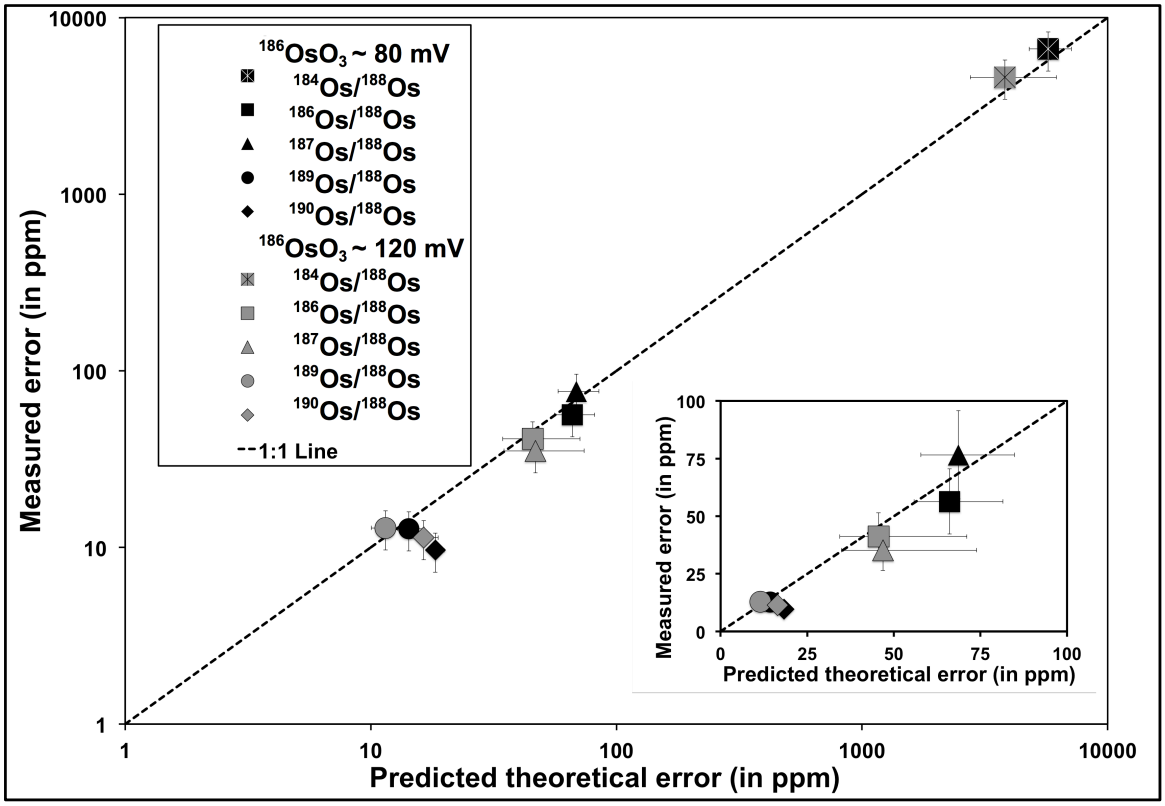

Figure 1.2 Log-log plot of measured analytical error (2 SD) versus predicted theoretical error (2 SE) for Os isotopic ratios ($^{184}Os/^{188}Os$, $^{186}Os/^{188}Os$, $^{187}Os/^{188}Os$, $^{189}Os/^{188}Os$ and $^{190}Os/^{188}Os$) at $^{186}OsO_3$ intensities of 80 mV and 120 mV.

Uncertainties for measured error are 2 SE of the measured error (n = 16 for both 80 mV and 120 mV populations). 2 SD of the signal intensities for populations with mean ~80 mV and 120 mV $^{186}OsO_3$ intensity (n = 16 for both populations) are utilized to compute uncertainties in the estimates for theoretical error.

4. ERROR FROM O ISOTOPE UNCERTAINTY

4.1 Uncertainty due to oxide correction

Because Os is measured as a tri-oxide, knowledge of the oxygen isotopic composition is required to correct for isobaric interferences involving ^{17}O and ^{18}O. Earlier studies have employed different approaches for oxide correction. One method (c.f., Brandon et al., 1998) assumes the Nier O value (Nier, 1950) as the O isotopic composition. Later studies (e.g., Brandon et al., 2005) determined the isotopic composition of O bled into the source from measured ReO_4^- on standards. Ireland et al., (2011) used the average O isotopic composition measured from several Os analyses to correct other Os analyses. Luguet et al., (2008b) measured the O isotopic composition during each analysis and corrected Os isotopic ratios on a line-by-line basis. Below I examine the intra- and inter-run variation of O isotopic composition during N-TIMS analyses and evaluate the sensitivity of Os isotopes to variations in O isotopic composition.

Oxide correction affects both the "target" isotopic ratios (e.g., $^{186}Os/^{188}Os$) as well as the isotopic ratio used for MF correction (e.g., $^{192}Os/^{188}Os$). Therefore, the choice of the normalizing isotope pair affects the sensitivity of Os isotopes to oxide correction. Whereas $^{192}Os/^{188}Os$ is more sensitive to variations in ^{18}O abundance (due to the large oxide interference from $^{190}Os^{16}O_2{}^{18}O$), $^{189}Os/^{188}Os$ is more susceptible to variations in ^{17}O (due to interference from $^{188}Os^{16}O_2{}^{17}O$). Assuming O-isotopes vary along a MF line, departures in assumed O isotopic composition from the "true" value result in -0.25 to 2.2 ppm/‰ and -0.55 to 2.43 ppm/‰ shifts in Os isotopic ratios using $^{189}Os/^{188}Os$ and $^{192}Os/^{188}Os$ normalizations respectively (Figure 1.3). Smaller shifts are observed in

$^{186}Os/^{188}Os$ and $^{187}Os/^{188}Os$ (~-0.25 vs 0.87 ppm/‰ and ~0.05 vs 0.6 ppm/‰, respectively) using the $^{189}Os/^{188}Os$ normalization relative to $^{192}Os/^{188}Os$. In the absence of other sources of errors, use of $^{189}Os/^{188}Os$ for MF correction minimizes error due to O-isotope uncertainty.

During this study, $\delta^{18}O$ varied between runs by up to ~31 ‰ (~13 ‰ 2 SD) and was on average ~13 ‰ lower than the measured tank O value (Figure 1.4a), similar to variations reported in other studies (Luguet et al., 2008b; Liu et al., 1998). The maximum departure in measured $\delta^{18}O$ composition from the tank value translates to a ~27 ppm shift in calculated $^{186}Os/^{188}Os$ using the $^{192}Os/^{188}Os$ normalization. Individual samples corrected using an assumed O isotopic composition may be significantly shifted from values corrected with measured in-run O isotopic composition, thus producing occasional "anomalous" $^{186}Os/^{188}Os$ values. However, $^{186}Os/^{188}Os$ data oxide-corrected using within-run O isotopic composition shows minimal improvement in precision overall because other, larger sources of random error overwhelm this effect. Using a fixed tank O-isotope composition for data reduction, there is also a residual positive correlation between calculated $^{190}Os/^{188}Os$ and the difference between measured and assumed O isotopic compositions. Figure 1.5 shows that the theoretical trend agrees well with the observed trends. The maximum observed departure in measured $\delta^{18}O$ composition from the tank value creates a shift of ~34 ppm in the calculated $^{190}Os/^{188}Os$. Use of measured within-run O isotopic compositions eliminates this residual correlation and improves $^{190}Os/^{188}Os$ reproducibility from ~17 ppm to ~10 ppm (Table 1.1, 30 s baseline measurements). Therefore, use of run-specific O isotopic composition is recommended for data reduction.

Oxygen isotopes can be measured either during an Os isotope analysis via peak hopping (c.f., Luguet et al., 2008b) or at the beginning and end of an analysis via a separate routine. The maximum $\delta^{18}O$ variation observed between the beginning and end of an individual analysis is ~8 ‰. However, the average within-run variability is only ~2 ‰ (2 SD), comparable to average and maximum within-run $\delta^{18}O$ variation observed in Luguet et al., (2008b) (2.3 ‰ and 5 ‰, respectively). Luguet et al., (2008b) utilized a peak-hopping routine to measure O isotope composition at masses at 239-243 for 4s and Os peaks for 8 s with 4 s of settling time after each peak hop, leading to a >50 % loss of measurement time for the primary Os peaks. Because within-run O isotope variation is small, I recommend measuring O isotopic composition before and after a run using the mean value as an approximation of the within-run O isotopic composition. Our O-isotope measurement sequence (1 block of 10 cycles with 2 s on the 241-242 peaks and 5 s idle per cycle) requires a total measurement time of ~2 minutes (combining pre and post run determinations) compared to ~36 minutes required by Luguet et al., (2008b) using within-run peak hopping. Measurement precisions close to 2 ‰ are achieved by pre and post-run O isotopic measurements, which is sufficient for accurate oxide corrections to the Os isotopes. Therefore, a cursory analysis before and after the primary Os isotope measurement is sufficient.

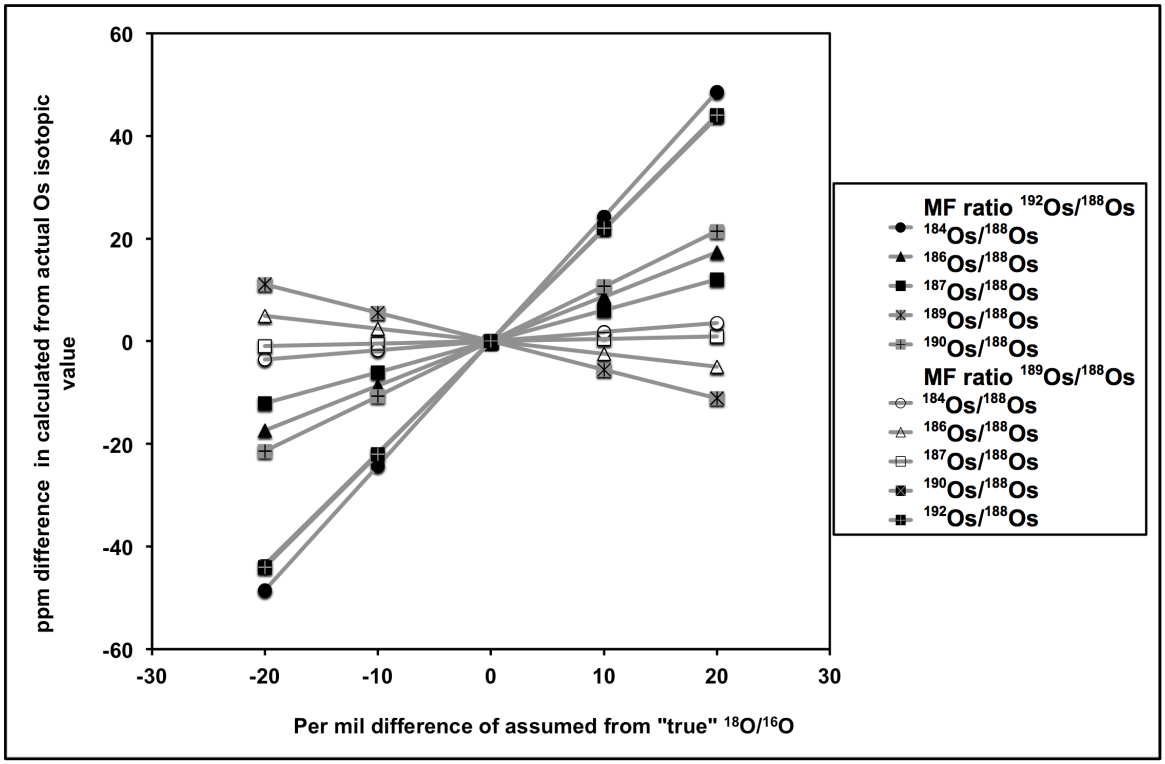

Figure 1.3 Shift in ppm (theory) in calculated Os isotopic ratios from actual Os isotopic values versus ‰ difference of assumed from "true" $^{18}O/^{16}O$.

Use of both $^{192}Os/^{188}Os$ and $^{189}Os/^{188}Os$ as the normalizing ratio for mass fractionation is shown as they have different sensitivities to uncertainty in O isotopic compositions. $^{186}Os/^{188}Os$ shows a smaller effect due to uncertainty in O isotopic composition when $^{189}Os/^{188}Os$ is used as the normalizing ratio (open triangle) relative to $^{192}Os/^{188}Os$ (solid triangle).

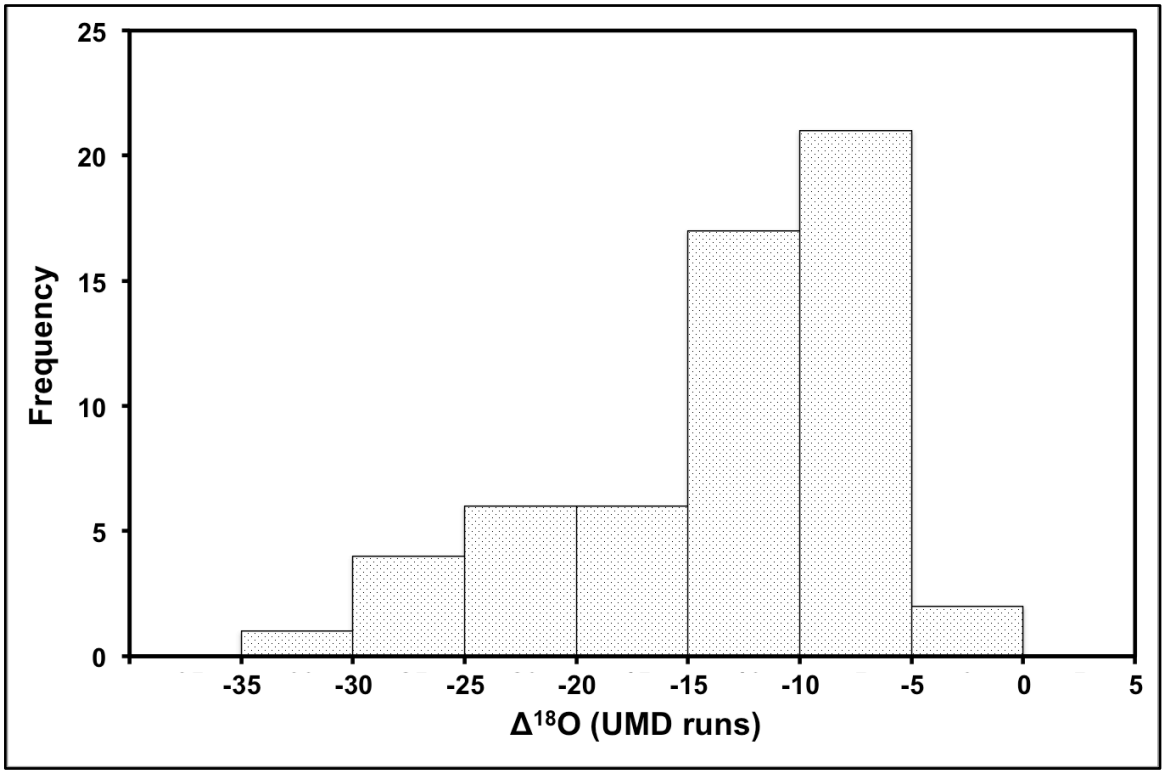

Figure 1.4a Histogram showing shifts in within-run O isotopic composition from the tank value for different runs of the UMD standard.

Although the total variation in O isotopic composition spans >30 ‰ from the tank value, majority of the UMD runs show 5-15 ‰ shifts from our measured tank O isotopic composition.

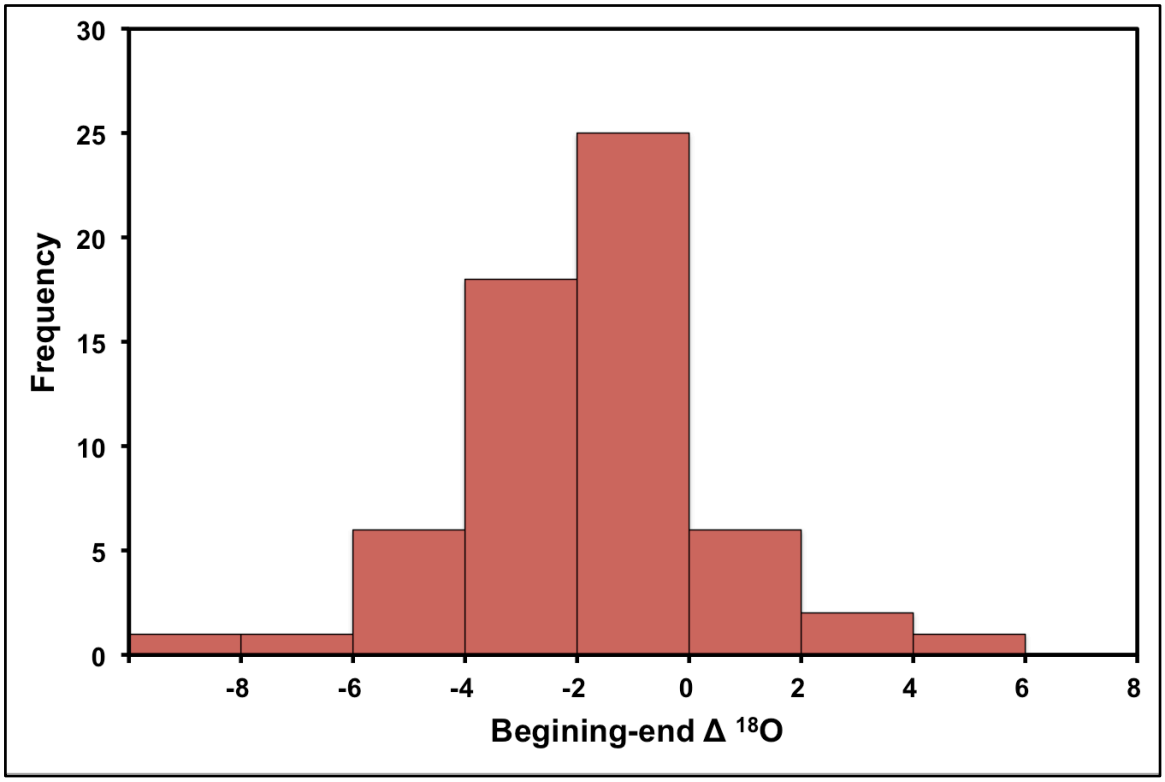

Figure 1.4b Histogram showing difference in $\Delta^{18}O$ between the beginning and the end of UMD standard runs.

Although the variability between the beginning and end of runs spans up to 8 ‰, most runs show shifts of ~2 ‰ from the beginning to the end of a run.

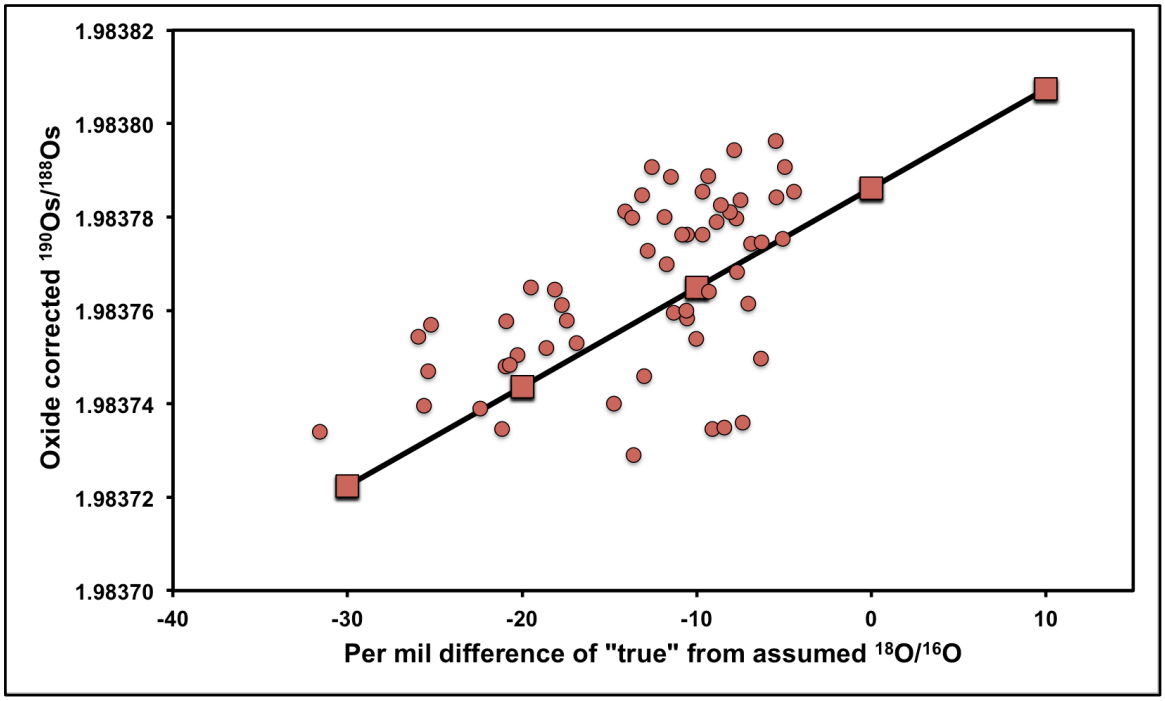

Figure 1.5 Oxide corrected $^{190}Os/^{188}Os$ using an assumed O isotopic composition versus ‰ difference in $^{18}O/^{16}O$ of "true" from assumed value, when MF is corrected using the $^{192}Os/^{188}Os$ normalization.

The theoretical trend (solid squares) fit well with the UMD data (solid circles) corrected using the tank O isotopic composition.

UMD Standard	$^{184}Os/^{188}Os$	$^{186}Os/^{188}Os$	$^{187}Os/^{188}Os$	$^{189}Os/^{188}Os$	$^{190}Os/^{188}Os$
Using tank O isotopic composition					
MEAN (this study, 30 s Baselines; n=34)	0.001304	0.1198450	0.113792	1.219744	1.983769
2 SD	0.000007	0.0000060	0.000007	0.000018	0.000034
ppm	5470.57	50.22	57.52	14.40	17.20
MEAN (this study, 5 min Baselines; n=23)	0.001305	0.1198461	0.113791	1.219740	1.983759
2 SD	0.000005	0.0000034	0.000005	0.000016	0.000038
ppm	3538.30	28.38	43.82	13.17	19.38
Using within-run O isotopic composition					
MEAN (this study, 30 s Baselines; n=34)	0.001304	0.1198466	0.113793	1.219729	1.983794
2 SD	0.000007	0.0000057	0.000007	0.000016	0.000020
ppm	5,462.88	47.61	58.38	13.16	10.07
MEAN (this study, 5 min Baselines; n=23)	0.001305	0.1198474	0.113791	1.219727	1.983775
2 SD	0.000005	0.0000036	0.000005	0.000017	0.000035
ppm	3,520.66	30.06	45.32	13.86	17.69

Table 1.1 Os isotopic compositions using assumed tank O and measured, within-run O isotopic composition for oxide correction

4.2 Offset due to use of assumed O composition & $^{189}Os/^{188}Os$ normalization for mass fractionation correction

O isotope determinations reported in most previous studies lie close to the same MF line (Figure 1.6). However Nier O and Ireland O isotopic compositions (Nier, 1950; Ireland et al., 2011) have much lower $^{17}O/^{16}O$ for a given $^{18}O/^{16}O$ compared to most other studies (e.g., $^{17}O/^{16}O_{Nier} = {}^{17}O/^{16}O_{Ireland} = 0.000375$ vs $^{17}O/^{16}O_{tank} = 0.000385$ in this study). Using $^{192}Os/^{188}Os$ normalization, $^{186}Os/^{188}Os$ data reduced using the Nier O or Ireland O isotopic composition is shifted by ~3 and ~9 ppm relative to data reduced using our measured tank O isotopic composition (Table 1.2). In contrast, using $^{189}Os/^{188}Os$ normalization, $^{186}Os/^{188}Os$ data corrected using the Nier O or Ireland O isotopic composition is shifted by ~32 and 25 ppm towards higher values relative to our measured tank O isotopic composition (Table 1.2). Oxide correction using Nier O or Ireland O isotopic composition creates large shifts in $^{186}Os/^{188}Os$ values due to the large difference in $^{17}O/^{16}O$ ratio between Nier O/Ireland O compositions from our tank O isotopic composition. This is particularly problematic because earlier ^{186}Os studies (c.f., Brandon et al., 1998) used Nier O isotopic composition and $^{189}Os/^{188}Os$ normalization for data reduction. However, repeated standard measurements from these studies do not show this expected shift in $^{186}Os/^{188}Os$ (Brandon et al., 1998, 1999) relative to later studies (Luguet et al., 2008b, this study) using measured O-isotope composition and $^{192}Os/^{188}Os$ normalization (Table 1.3). As discussed in section 5, this likely is due to the fact that the canonical $^{189}Os/^{188}Os$ and $^{192}Os/^{188}Os$ values commonly used for MF correction (c.f., Brandon et al., 1998, 2005) are mutually inconsistent. Use of $^{189}Os/^{188}Os$ normalization

rather than $^{192}Os/^{188}Os$ results in a systematic offset in corrected $^{186}Os/^{188}Os$ data in the opposite direction as the use of Nier O/ Ireland O isotopic composition for oxide correction. This leads to a partial cancellation of error when both Nier O/ Ireland O isotopic composition and $^{189}Os/^{188}Os$ normalization are utilized for data reduction.

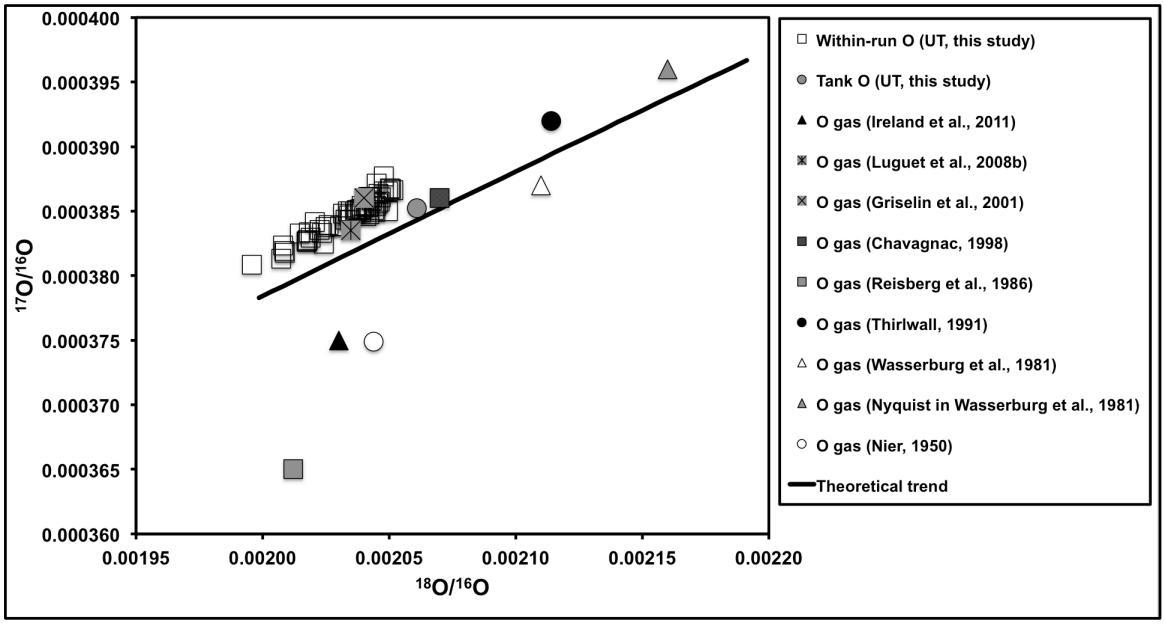

Figure 1.6 $^{17}O/^{16}O$ vs $^{18}O/^{16}O$ for within-run (open squares), tank (solid circle) and published O isotopic compositions for different studies

The UT within-run O isotopic compositions are either mean of measured O isotopic compositions determined before and after an Os analysis or the mean O isotopic composition determined line by line during an Os analysis. The solid line represents the theoretical mass fractionation trend computed with the tank O isotopic composition using exponential law. UT within-run O isotopic compositions lie close to the theoretical mass fractionation trend as does most other published values. Nier and Ireland O isotopic compositions (utilizing the $^{17}O/^{16}O$ of Nier O) (Nier., 1950; Ireland et al., 2011) as well as the O isotopic composition determined in the Reisberg et al., (1986) study fall off this theoretical trend due to systematic differences in $^{17}O/^{16}O$ from the rest of the studies.

Data Type	Mass Fractionantion Correction	Tank O	Nier O	Ireland O	Measured O
AVERAGE (30 sec baseline; n=34)	$^{192}Os/^{188}Os = 3.083$	0.1198448	0.1198451	0.1198459	0.1198466
2*STDEV		0.0000058	0.0000058	0.0000058	0.0000057
average ppm shift from tank O			2.62	9.22	15.38
AVERAGE (5 min baseline; n=24)		0.1198461	0.1198464	0.1198472	0.1198474
2*STDEV		0.0000034	0.0000034	0.0000034	0.0000036
average ppm shift from tank O			2.63	9.23	10.99
AVERAGE (30 sec baseline; n=34)	$^{189}Os/^{188}Os = 1.21978$	0.1198375	0.1198414	0.1198406	0.1198363
2*STDEV		0.0000073	0.0000073	0.0000073	0.0000073
average ppm shift from tank O			32.34	25.17	(10.48)
average ppm shift from 192Os/188Os normalization		(60.26)	(30.55)	(44.31)	(86.12)
AVERAGE (5 min baseline; n=24)		0.1198389	0.1198428	0.1198419	0.1198377
2*STDEV		0.0000054	0.0000054	0.0000054	0.0000055
average ppm shift from tank O			(32.34)	(25.17)	10.68
average ppm shift from 192Os/188Os normalization		(59.53)	(29.82)	(43.58)	(81.19)
Offsets in corrected 186Os/188Os using different O isotopic values and mass fractionation normalizations (mutually consistent normalizing values)					
AVERAGE (30 sec baseline; n=34)	$^{189}Os/^{188}Os = 1.21973$	0.1198458	0.1198497	0.1198488	0.1198456
2*STDEV		0.0000073	0.0000073	0.0000073	0.0000074
average ppm shift from tank O			32.43	25.27	(1.95)
average ppm shift from 192Os/188Os normalization		8.51	38.31	24.55	(8.82)
AVERAGE (5 min baseline; n=24)		0.1198472	0.1198511	0.1198502	0.1198471
2*STDEV		0.0000054	0.0000054	0.0000054	0.0000054
average ppm shift from tank O			32.43	25.27	(0.90)
average ppm shift from 192Os/188Os normalization		9.24	39.04	25.28	(2.65)

Table 1.2 Offsets in corrected $^{186}Os/^{188}Os$ using different O isotopic values and mass fractionation normalizations (mutually inconsistent normalizing values)

	$^{184}Os/^{188}Os$	$^{186}Os/^{188}Os$	$^{187}Os/^{188}Os$	$^{189}Os/^{188}Os$	$^{190}Os/^{188}Os$
UMD Standard					
MEAN (Walker et al., 1997; n=12)		0.1198480	0.113791		
2 SD		0.0000062	0.000009		
ppm		52.03	82.20		
MEAN (Brandon et al., 1998; n=38)		0.1198473	0.113783		
2 SD		0.0000040	0.000005		
ppm		33.38	43.94		
MEAN (Brandon et al., 1999, 2000; n=28)	0.001314	0.1198464	0.113807		
2 SD	0.000011	0.0000063	0.000011		
ppm	8,054.04	52.98	97.64		
MEAN (Brandon et al., 2003; n=42; at UMD)		0.1198471	0.113799		
2 SD		0.0000058	0.000027		
ppm		48.67	233.49		
MEAN (Brandon et al., 2003; n=5; at JSC)		0.1198466	0.113807		
2 SD		0.0000056	0.000007		
ppm		46.64	62.87		
MEAN (Puchtel et al., 2004, 2005; n=26)	0.001309	0.1198462	0.113789		
2 SD	0.000001	0.0000021	0.000005		
ppm	840.21	17.52	39.55		
MEAN (Walker et al.,2005; at UMD; Campaign 1)		0.1198520			
2 SD		0.0000022			
ppm		18.36			
MEAN (Walker et al.,2005; at UMD; Campaign 2)		0.1198485			
2 SD		0.0000015			
ppm		12.52			
MEAN (Brandon et al., 2005, 2006; n=38; at JSC)	0.001309	0.1198470	0.113791	1.219692	1.983793
2 SD	0.000006	0.0000016	0.000004	0.000015	0.000019
ppm	4430.86	13.35	31.64	11.89	9.68
MEAN (Brandon et al., 2007; n=6)	0.001314	0.1198518	0.113800		
2 SD	0.000004	0.0000023	0.000006		
ppm	2892.81	19.19	56.24		
MEAN (Luguet et al., 2008b; n=35)	0.001304	0.1198427	0.113787	1.219710	1.983801
2 SD	0.000013	0.0000067	0.000008	0.000017	0.000026
ppm	9969.33	55.91	70.31	13.94	13.11
MEAN (Ireland et al., 2011; n=31; at UMD)	0.001306	0.1198443	0.113785	1.219731	1.983819
2 SD	0.000005	0.0000035	0.000016	0.000011	0.000025
ppm	3,829.36	29.20	140.62	8.94	12.75
MEAN (Ireland et al., 2011; n=10; at JSC)		0.1198467	0.113791		
2 SD		0.0000020	0.000003		
ppm		16.69	21.97		
MEAN (this study, 30 s Baselines; n=34)	0.001304	0.1198466	0.113793	1.219729	1.983794
2 SD	0.000007	0.0000057	0.000007	0.000016	0.000020
ppm	5,462.88	47.61	58.38	13.16	10.07
MEAN (this study, 5 min Baselines; n=23)	0.001305	0.1198474	0.113791	1.219727	1.983775
2 SD	0.000005	0.0000036	0.000005	0.000017	0.000035
ppm	3,520.66	30.06	45.32	13.86	17.69
DROsS Standard					
MEAN (this study; 5 min Baselines; n=8)	0.001305	0.1199304	0.160922	1.219725	1.983779
2 SD	0.000002	0.0000029	0.000003	0.000022	0.000038
ppm	1,207.13	23.95	15.98	18.42	19.04
MEAN (Luguet et al., 2008b; n=8)	0.001305	0.1199293	0.160924	1.219705	1.983803
2 SD	0.000005	0.0000058	0.000004	0.000015	0.000015
ppm	3831.42	48.36	24.86	12.30	7.56

Table 1.3 Os isotopic compositions of UMd standard and DROsS standard by different studies

5. MASS FRACTIONATION

5.1 Error due to mass fractionation correction

Previous studies have used either $^{189}Os/^{188}Os$ or $^{192}Os/^{188}Os$ (c.f., Brandon et al., 1998, 2005) to correct for MF. Error on the measured normalization ratio results in error propagation to the corrected isotopic ratios. A 4x larger mass spread between ^{192}Os and ^{188}Os compared to ^{189}Os and ^{188}Os leads to a 4x smaller uncertainty in beta for a fixed uncertainty in $^{192}Os/^{188}Os$ relative to $^{189}Os/^{188}Os$, resulting in smaller propagated errors on MF-corrected ratios. In detail, an offset to the numerator peak alone has the same effect as an offset on the normalizing ratio considered as a whole, whereas an offset to the denominator peak results in an additional offset for ratios involving lower masses, but partial cancellation of errors for high-mass ratios. For example, a 10 ppm overestimation of ^{189}Os results in 40, 20 and 10 ppm overestimations of $^{184}Os/^{188}Os$, $^{186}Os/^{188}Os$ and $^{187}Os/^{188}Os$ but 20 and 40 ppm underestimations of $^{190}Os/^{188}Os$ and $^{192}Os/^{188}Os$ when $^{189}Os/^{188}Os$ is used for MF correction. In contrast, a 10 ppm overestimation of ^{188}Os results in a net overestimation of $^{184}Os/^{188}Os$, $^{186}Os/^{188}Os$ and $^{187}Os/^{188}Os$ by 50 (4 x 10 ppm shift from $^{189}Os/^{188}Os$ and 10 ppm shift from ^{188}Os), 30 and 20 ppm but underestimation of $^{190}Os/^{188}Os$ and $^{192}Os/^{188}Os$ by only 10 and 30 ppm. In essence, errors on the normalizing ratios and on the non-MF corrected ratios are not truly independent, because both errors incorporate error to the ^{188}Os measurement. Errors to the normalizing ratio and to the non-MF-corrected ratios resulting from error in the ^{188}Os measurement are additive for low-mass ratios (e.g., $^{186}Os/^{188}Os$) but partially offsetting for high-mass ratios (e.g., $^{190}Os/^{188}Os$). In practice, however, the difference between independent

treatment of numerator and denominator errors and simple consideration of the cumulative error to the normalizing ratio is small.

Error propagation in beta produces residual correlations in corrected Os isotopes. For example, a positive correlation between $^{190}Os/^{188}Os$ and $^{192}Os/^{188}Os$ corrected using $^{189}Os/^{188}Os$ normalization was observed (Figure 1.7) that closely matches the theoretical trend. However, such correlations are not observed between $^{192}Os/^{188}Os$ and other ratios involving lower abundance isotopes such as $^{186}Os/^{188}Os$ or $^{187}Os/^{188}Os$ because the MF-induced error is swamped by other, larger sources of error. Using the $^{192}Os/^{188}Os$ normalization, propagated errors due to MF are much smaller and are overshadowed by other sources of error.

Although use of $^{189}Os/^{188}Os$ normalization improves error associated with oxide corrections (c.f., Section 4.1), larger MF-induced errors overwhelm this benefit. For example, theoretical errors on $^{192}Os/^{188}Os$ and $^{189}Os/^{188}Os$ are ~8.4 and 10.1 ppm respectively for a 100mV $^{186}OsO_3^-$ beam using 30 s baseline determinations (c.f., Section 3). Error on $^{186}Os/^{188}Os$ resulting from MF correction increases from ~4.2 to ~20.2 ppm when one uses $^{189}Os/^{188}Os$ for normalization instead of $^{192}Os/^{188}Os$. The same shift in normalization reduces errors associated with O isotopic uncertainty from ~11.4 to ~3.2 ppm (c.f., Section 4.1) for the mean measured in-run $\delta^{18}O$ offset of 13 ‰ from measured tank O-isotope composition. Because the error derived from uncertainty in beta is larger than the error associated with oxide correction, use of $^{189}Os/^{188}Os$ normalization results in a small net increase in total measurement error. Therefore, $^{192}Os/^{188}Os$ normalization is recommended for MF correction.

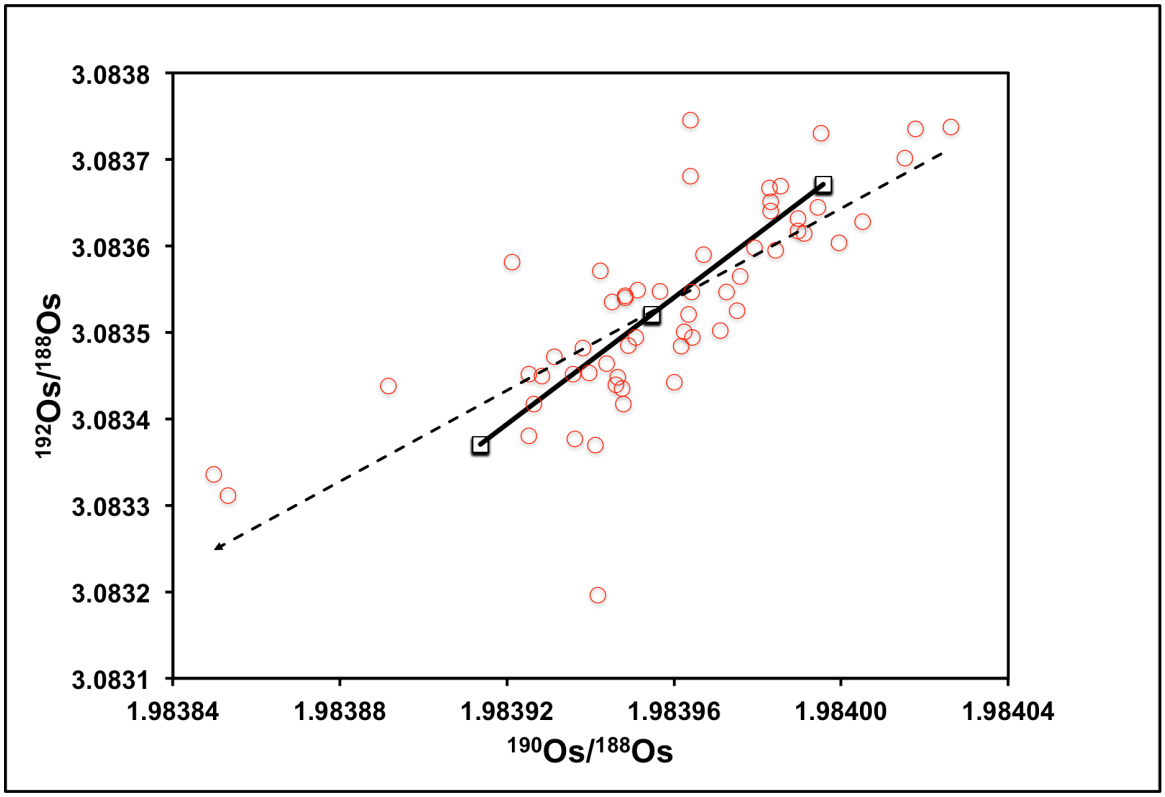

Figure 1.7 Mass fractionation corrected $^{192}Os/^{188}Os$ vs $^{190}Os/^{188}Os$ using the $^{189}Os/^{188}Os$ normalization ($^{189}Os/^{188}Os$ =1.21978) for UMD standard runs (open circles).

Theoretical trends treating the uncertainties in the numerator and denominator separately (solid line) match with the regression (dotted line) through actual UMD data.

5.2 Offsets due to mutually inconsistent normalizing values

Canonical values for $^{189}Os/^{188}Os$ (1.21978) and $^{192}Os/^{188}Os$ (3.083) used for normalization in most Os-isotope studies (c.f., Brandon et al., 1999, 2006; Walker et al., 1989; Luck et al., 1983) are mutually inconsistent. Figure 1.8 shows a plot of ln ($^{189}Os/^{188}Os$) versus ln ($^{192}Os/^{188}Os$) where the $^{189}Os/^{188}Os$ value = 1.21978 (c.f., Brandon et al., 1998) plots off the observed fractionation trend suggesting that these values are mutually inconsistent. Instead, the $^{189}Os/^{188}Os$ value equivalent to $^{192}Os/^{188}Os$ = 3.083 is ~1.21973, consistent with measured $^{189}Os/^{188}Os$ values (1.21970-1.21973) reported in multiple studies (Brandon et al., 2005; Luguet et al., 2008b; Ireland et al., 2011, this study) that use $^{192}Os/^{188}Os$ = 3.083 for normalization.

Use of mutually inconsistent canonical values for different isotope ratios used for MF correction produces systematic shifts in Os data corrected using different normalizing ratios. Table 1.2 outlines average UMD $^{186}Os/^{188}Os$ values for data corrected using different O isotopic compositions and different normalizations for MF. Standards corrected using tank O isotopic composition for oxide correction and $^{189}Os/^{188}Os$=1.21978 for MF correction have $^{186}Os/^{188}Os$ values ~60 ppm lower than when the same data are processed using $^{192}Os/^{188}Os$ = 3.083 as the normalizing ratio. Luguet et al., (2008b) reported an even greater offset of ~115 ppm in $^{186}Os/^{188}Os$ for standards corrected for MF using $^{189}Os/^{188}Os$ relative to standards corrected using $^{192}Os/^{188}Os$. A somewhat smaller offset of ~30 and ~44 ppm is observed between $^{189}Os/^{188}Os$-normalized and $^{192}Os/^{188}Os$-normalized data when oxide corrections are performed using Nier O and Ireland O isotopic compositions (Nier, 1950, Ireland et al., 2011) respectively.

Studies simultaneously using $^{189}Os/^{188}Os$ normalization and Nier O-isotope composition (Brandon et al., 1998) do not show such offsets in $^{186}Os/^{188}Os$ compared to studies using $^{192}Os/^{188}Os$ normalization and measured within-run or tank O-isotope composition (Luguet et al., 2008b; this study) (Table 1.3). Because the $^{189}Os/^{188}Os$ normalization lowers the $^{186}Os/^{188}Os$ value and the Nier O-isotope composition increases the $^{186}Os/^{188}Os$ value by ~60 and ~32 ppm respectively relative to $^{192}Os/^{188}Os$ normalization and use of our measured, tank O isotopic composition (Table 1.2), there is only a ~28 ppm net shift towards lower values within uncertainties reported in the Brandon et al., (1998) study. Thus, systematic differences between these correction schemes are obscured due to these offsetting effects.

Use of $^{189}Os/^{188}Os$ = 1.21973 for MF correction consistent with $^{192}Os/^{188}Os$ = 3.083, reduces the difference in corrected $^{186}Os/^{188}Os$ between the two normalization schemes to just ~9 and ~3 ppm using tank O and measured O isotopic compositions respectively. Use of mutually consistent normalizing values allows meaningful comparison of datasets between laboratories that use different isotopic ratios for normalization.

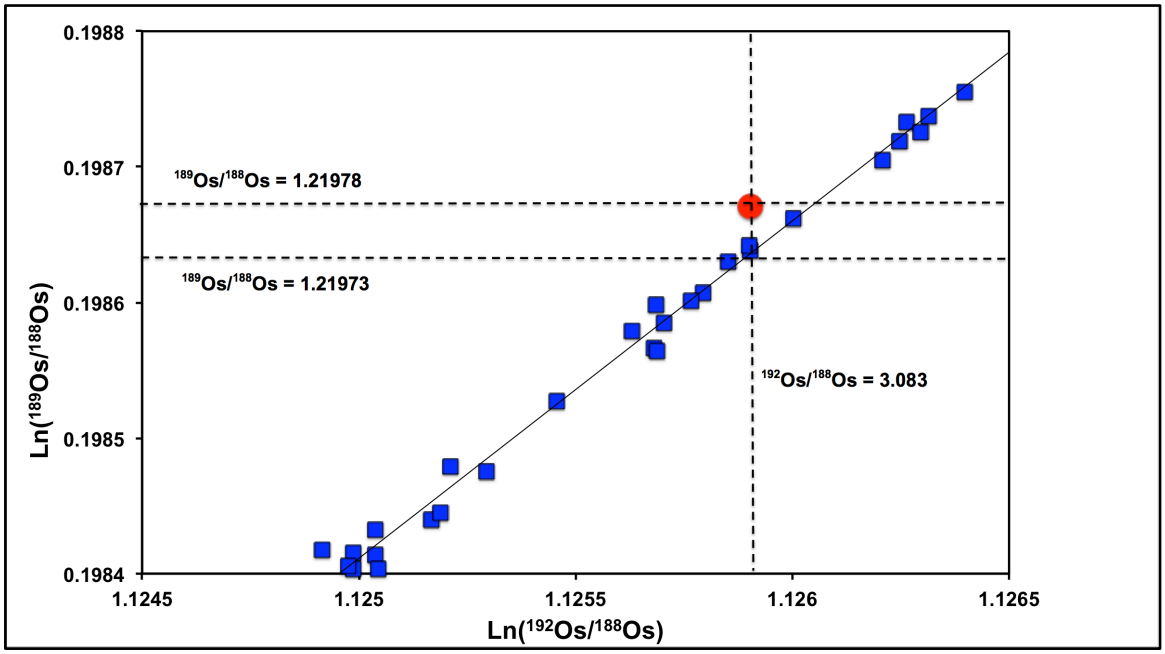

Figure 1.8 Ln-Ln plots of raw $^{192}Os/^{188}Os$ vs $^{189}Os/^{188}Os$ (squares) that have been oxide stripped using the tank O isotopic composition for UMD standard runs.

Canonical values used in the literature for $^{189}Os/^{188}Os$ (1.21973) and $^{192}Os/^{188}Os$ (3.083) normalizations are plotted (circle). These normalizing values are not consistent with each other and plot off the $^{192}Os/^{188}Os$ vs $^{189}Os/^{188}Os$ trend. The $^{189}Os/^{188}Os$ value consistent with $^{192}Os/^{188}Os = 3.083$ is 1.21973.

6. ERROR DUE TO JOHNSON NOISE

Johnson noise is the electronic noise caused by the thermal agitation of electrons inside an electrical resistor (Nyquist, 1928). It varies directly with the resistance, temperature of the conductor and the frequency over which the noise is measured. The mean square root of Johnson noise expressed in V is given by the following equation

$$Johnson\ Noise = \sqrt{4 \times K_B \times T \times \Delta f \times R} \qquad (6) \qquad \text{(Nyquist, 1928)}$$

where K_B = Boltzmann constant (~ 1.38 x 10^{-23} J/K) , T = temperature of the conductor (in K), Δf = frequency window in Hz = (1/Time period in s) and R = resistance of the conductor in ohms. During analytical measurement, errors associated with Johnson noise arise during both baseline measurement and signal integrations. Johnson noise during baseline integration (JN_B) and signal integration (JN_S) expressed in V can be calculated from the above formula

$$JN_B = \sqrt{4 \times K_B \times T \times \frac{1}{t_B} \times R} \qquad (7)$$

$$JN_S = \sqrt{4 \times K_B \times T \times \frac{1}{t_S} \times R} \qquad (8)$$

where t_B is the duration of baseline integration (in s) and t_S is the duration of signal integration (in s). For example, from equation (7) the Johnson noise for a 30s baseline measurement on a 10^{11} Ω resistor at 36ºC is calculated to be ~15.1 μV (2 RMSD). Increasing baseline measurement to 5 min reduces Johnson noise to ~4.8 μV (2 RMSD). Observed variations in amplifier baselines measured over a 2 day period closely match

theoretical Johnson noise predictions (Figure 1.9), indicating that Johnson noise is the primary source of amplifier noise for modern amplifiers.

A large part of the analytical error involving minor peaks (e.g., $^{184}OsO_3$ or $^{186}OsO_3$) derives directly from baseline error and can be reduced without increasing sample size simply by increasing the baseline measurement duration in proportion to the signal measurement time. For example, for a 100 mV $^{186}OsO_3$ signal measured for 10 blocks (20 cycles/block) using 30 s baselines, Johnson noise error on baseline integrations can be calculated from equations 4 and 7 to contribute ~48 ppm measurement error (Figure 1.1). In contrast, Johnson noise error using 16 s signal integrations and error from counting statistics for 200 ratios are only ~15 ppm each. Increasing the baseline duration to 5 minutes reduces σ_{JNB} from ~48 ppm to ~15 ppm (comparable in magnitude to σ_{JNS} and σ_{CS}) and the net theoretical $^{186}Os/^{188}Os$ error from ~54 to ~28 ppm. Although longer baseline integration time requires sacrificing a larger number of Os ions during the baseline measurements, it nonetheless significantly improves the analytical precision as long as the baseline error is larger than other sources of error (Ludwig, 1997). For example, external reproducibility of measured $^{186}Os/^{188}Os$ for UMd standard improved from ~48 ppm to ~30 ppm using 5 minute baseline measurements instead of 30 s measurements, closely in line with theoretical predictions (Figure 1.10; Table 1.3). External reproducibility for the DROsS standard using 5 min baseline integrations is ~24 ppm (Table 1.3), also in agreement with theoretical estimates (Figure 1.1). Significant improvement of $^{184}Os/^{188}Os$ reproducibility is also observed (reduction from ~5460 to

~3520 ppm) using longer baseline measurements, again consistent with theoretical predictions.

Although several recent studies report comparable or better $^{186}Os/^{188}Os$ external precisions (13 to 30 ppm) relative to this study (c.f., Table 1.3), these high external precisions are often achieved using large quantities of material (100-500 g) to load 100-200 nanograms of Os per analysis (Brandon et al., 1999, 2007; Ireland et al., 2011). This allows analyses at high $^{186}OsO_3$ intensities (~100-250 mV) for a large number of ratios and often involves re-running the same filament up to 6 times (up to 1200 signal integrations). However, most previous studies utilized 30 s baseline measurements (Luguet et al., 2008b; *R.J. Walker, Pers. Comm.*). Although extended or repeated measurement can eventually "beat down" all random measurement errors, including Johnson noise, it is not the most time- or sample-efficient method for doing so. Because Johnson noise is the single largest source of random error in typical $^{186}Os/^{188}Os$ measurements, longer baseline measurements allow maximum external precision for a given sample size.

Reducing baseline Johnson noise by increasing baseline measurement duration may aid the measurement of other low-abundance isotopes besides ^{184}Os and ^{186}Os. For example, p-process isotopes typically have low abundances relative to r- and s-process isotopes, making high precision measurement of these isotopes particularly challenging in sample-limited meteoritic studies. However, improved measurement of p-process isotopes could provide insights into the carrier phases for p-process anomalies and

improve our understanding of nucleosynthetic p-processes occurring in stellar environments (c.f., Yokoyama et al., 2007).

To demonstrate the broad applicability of addressing Johnson noise during isotopic measurements, I analyzed Sr-isotopes for sets of NBS 987 standards (N=19 in both cases) using two analytical routines at a fixed beam intensity of ~4V ^{88}Sr (~ 26 mV ^{84}Sr). At this intensity, the dominant source of measurement error on the minor ^{84}Sr peak using standard 30 s baseline measurements is baseline Johnson noise. The first routine analyzed Sr for 9 blocks (180 ratios), with 30 s baseline determinations for each block. The second routine only measured 5 blocks (100 ratios) but measured baselines for 5 min before each block. The total measurement time for both routines was roughly equal. Although the standard routine spent nearly 2x as much analysis time on peak compared to the second routine, the routine with longer baselines had ~30% improvement in external precision (from ~ 150 ppm 2 SD to ~108 ppm 2 SD). As counterintuitive as it may seem, sometimes it is best to throw away ions for the sake of measuring nothing. Evaluation of the theoretical sources of error allows optimization of analytical routines regardless of the target isotopes.

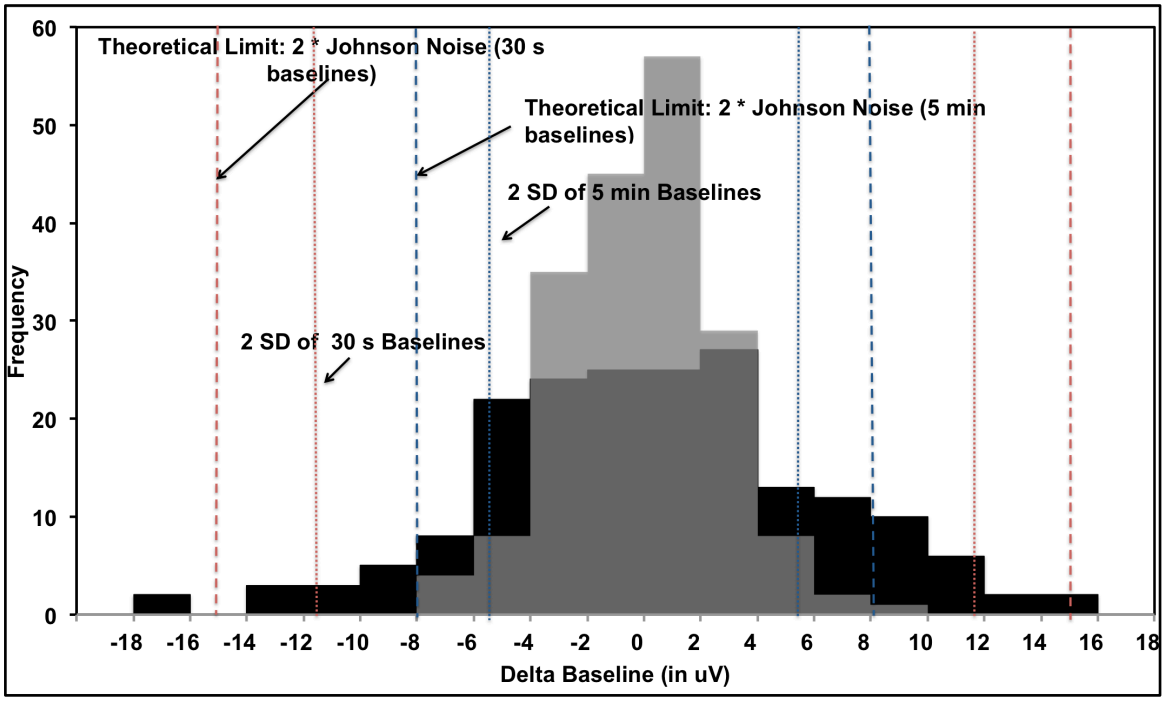

Figure 1.9 Histogram of baseline variations from 3-hour moving averages for 30 s (shaded black) and 5 min (shaded grey) baseline durations measured over a 2-day period.

Baseline deviations were calculated relative to a 3-hour moving average, to simulate the duration of a high precision $^{186}Os/^{188}Os$ analysis and to eliminate additional sources of long-term baseline drift such as minor temperature fluctuations. 2 SD of 30 s and 5 minute baselines lie within and close to the theoretical limit of Johnson noise (2 RMSD).

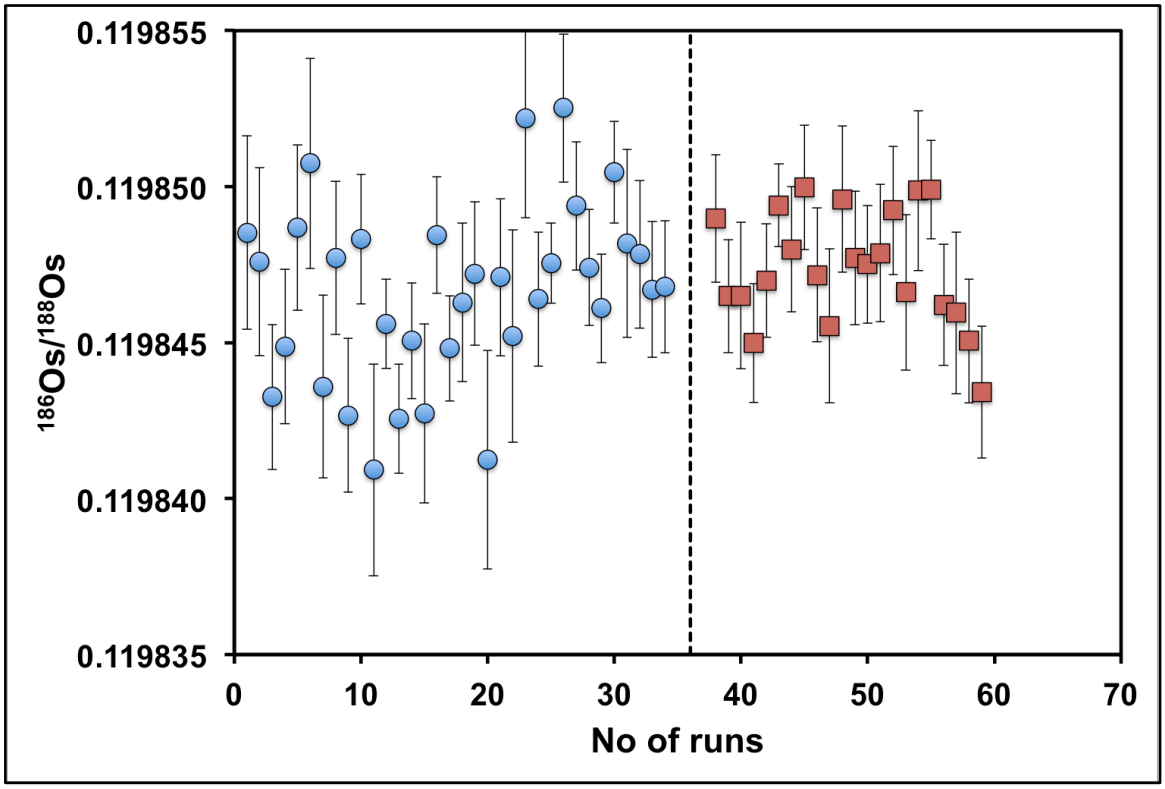

Figure 1.10 $^{186}Os/^{188}Os$ measurements for UMD standard runs using 30 s (solid circles) and 5 minute (solid squares) baseline determinations.

External reproducibility improves from 48 ppm to 30 ppm changing from 30 s to 5 min baseline integrations.

7. INTERFERENCES

Molecular interferences including oxides of Pt, Re and W are a potentially serious source of non-random error in $^{186}Os/^{188}Os$ measurements. $^{186}WO_3^-$ directly interferes on the $^{186}OsO_3^-$ peak making it particularly problematic. Early studies (c.f., Brandon et al., 1999) examined $^{184}Os/^{188}Os$ variations to monitor WO_3^- interferences but included analyses of both standards and samples with $^{184}Os/^{188}Os$ values far outside the normal range. For example, $^{184}Os/^{188}Os$ values in early manuscripts (Brandon et al., 1999, 2003) ranged up to 0.001325 for the UMD standard and up to 0.00146 in sample analyses. Later studies (Brandon et al., 2005, Luguet et al., 2008, Ireland et al., 2011, this study) reported much lower and more consistent $^{184}Os/^{188}Os$ values (0.001304-0.001309) (Table 1.3). Monitoring WO_3^- interferences using variations in $^{184}Os/^{188}Os$ is also problematic due to poor measurement precision of the $^{184}Os/^{188}Os$ ratio. Because the $^{184}OsO_3$ beam is very small, $^{184}Os/^{188}Os$ measurement precision in most studies is low (~4000 to ~10,000 ppm 2 SD; c.f., Table 1.3). This inherent measurement uncertainty in the 232/236 ratio can mask a 4-10 μV $^{184}W^{16}O_3$ signal on a ~1 mV $^{184}OsO_3^-$ beam (~100 mV of $^{186}OsO_3^-$). However, a $^{184}WO_3$ beam of this size corresponds to up to a ~50 ppm $^{186}WO_3$ interference on the $^{186}OsO_3$ peak.

Furthermore, because PtO_2^- directly interferes on mass 232, subtraction of Pt peaks is also necessary for accurate measurement of $^{184}Os/^{188}Os$. However, most previous studies utilizing 232/236 to monitor WO_3^- interferences have not subtracted PtO_2^- interferences (c.f., Brandon et al., 1999). Luguet et al., (2008b) recommended measurement of 228 and 230-233 peaks to measure PtO_2^- interferences and monitor Pt-stripped 230 and 231 peaks

for WO_3^- ($^{182}W^{16}O_3^-$ and $^{183}W^{16}O_3^-$ peaks respectively) interferences. Although some studies (Walker et al., 2005, Meibom et al., 2004) have monitored masses 230 and 231, only a few studies (Luguet et al., 2008b, Ireland et al., 2011) have employed PtO_2^- correction before monitoring for WO_3^- interferences. Below we discuss our protocol for monitoring various interferences.

Masses 228-233 were measured for PtO_2^- interferences via peak hopping using the ion counter for 10 cycles pre and post-Os measurements. The mean PtO_2^- signal of the pre- and post-run routines was considered a reasonable estimate for the analysis as the within-run variation was small and never exceeded a factor of ~2. Peaks at 228 and 230 ranged from ~33,000 to ~930,000 cps (median ~185,000 cps) and from ~9500 to 270,000 (median ~54,000 cps) comparable to previous studies (c.f., Luguet et al., 2008b, Ireland et al., 2011)). These intensities correspond to Pt peaks of 0.6-18 μV (median ~3.5 μV) on $^{184}OsO_3^-$ and 0.6-18 nV (median ~3.5 nV) on $^{186}OsO_3^-$. Pt interferences thus significantly affect measured $^{184}Os/^{188}Os$ but are negligible for $^{186}Os/^{188}Os$. Accordingly, stripping the PtO_2 peaks at 232 lowers the average measured $^{184}Os/^{188}Os$ (from 0.001310 to 0.001305) and significantly improves measurement precision (e.g., from ~7900 to ~5460 ppm for 30 s baseline determinations and from ~5410 to ~3520 ppm using 5 minute baseline determinations).

Because Pt peaks can mask other, more critical interferences such as WO_3^-, or organics, peaks at 229-231 were stripped of PtO_2 interferences. Details of the Pt stripping procedure are discussed in the online supplement S1. Median residual counts on 231 are 42 cps, consistent with other studies (Ireland et al., 2011). Residual counts on 231 are not

correlated with $^{184}Os/^{188}Os$ or $^{186}Os/^{188}Os$, suggesting the absence of WO_3^- interferences in most runs. However, occasional standard and sample analyses have much higher residual 229 and 231 counts as well as elevated $^{184}Os/^{188}Os$. Figure 1.11a shows $^{184}Os/^{188}Os$ and $^{186}Os/^{188}Os$ values measured in a UMD standard run three times from the same filament. Each successive run had higher $^{184}Os/^{188}Os$ and $^{186}Os/^{188}Os$ values than the previous run, although other Os-isotope ratios (e.g., $^{189}Os/^{188}Os$) remained normal. The same UMD standard also displays correlations between $^{186}Os/^{188}Os$ and residual $231/^{188}OsO_3$, closely following the ^{183}W-^{186}W trend (Figure 1.11b). The slope of the $^{184}Os/^{188}Os$-$^{186}Os/^{188}Os$ and $231/^{188}OsO_3$-$^{186}Os/^{188}Os$ correlations are consistent with the presence of a W-oxide interference, although organic interferences could also generate the observed correlations.

Occasional analyses reported in earlier studies may have been compromised by unrecognized isobaric interferences. For example, Brandon et al., 1998 report an elevated $^{186}Os/^{188}Os$ value for Hawaiian sample KOO-17A (0.1198526$\pm$34), well outside the upper mantle range (c.f., Brandon et al., 1998, 2006). The reported analysis for this sample also had anomalously high $^{184}Os/^{188}Os$ (0.001346$\pm$8). Subsequent reanalysis of this sample produced both lower $^{184}Os/^{188}Os$ (0.001313$\pm$2) and $^{186}Os/^{188}Os$ (0.1198343$\pm$22) (Brandon et al., 1999). Similarly, Ireland et al. reported $^{186}Os/^{188}Os$ and $^{184}Os/^{188}Os$ values for Hawaiian sample H-11 that are lower than the original values reported by Brandon et al. (1999). In our experience, when a standard or sample fails to run well (e.g., lower than normal total ion yield, potentially indicative of filament poisoning), the resultant measured $^{186}Os/^{188}Os$ value is almost always anomalously high.

Luguet et al., (2008b) reported residual correlations between interference- and MF-corrected $^{184}Os/^{188}Os$ and $^{186}Os/^{188}Os$ ratios and between $^{189}Os/^{188}Os$ and $^{190}Os/^{188}Os$. Although WO_3^- interferences could explain correlations observed between $^{184}Os/^{188}Os$ and $^{186}Os/^{188}Os$, W interferences cannot account for correlations between $^{189}Os/^{188}Os$ and $^{190}Os/^{188}Os$. Furthermore, Luguet et al., (2008b) report that Pt filaments doped with W and run at analytical conditions used in Os isotopic studies, failed to produce discernible WO_3^- peaks, suggesting that WO_3^- does not typically ionize under normal Os analytical conditions. It is possible that some matrix contaminant can on occasion act to catalyze WO_3^- ionization during Os TIMS analyses. However, it appears equally likely that some other, as yet unidentified compound(s) such as organic molecules generate the occasionally observed correlated increases in Pt-corrected mass 231, $^{184}Os/^{188}Os$ and $^{186}Os/^{188}Os$. Note that most analyses appear devoid of these effects. I also did not observe any residual correlation between $^{189}Os/^{188}Os$ and $^{190}Os/^{188}Os$ as observed by Luguet et al. (2008b). However, given that occasional analyses do appear to be compromised by unidentified interferences, it is critical that all runs are closely inspected for evidence of residual interferences, and that clear protocols are consistently used to exclude all questionable analyses.

Mass 233 ($^{185}Re^{16}O_3^-$) was measured via ion counter before and after main Os-isotope analysis routine to monitor $^{187}Re^{16}O_3^-$ that directly interferes with $^{187}Os^{16}O_3^-$. Median counts on Pt and Os-oxide-stripped mass 233 were <5 cps (maximum ~180 cps). Applying the maximum observed Re correction to mass 235 lowers the $^{187}Os/^{188}Os$ ratio

by 24 ppm, well within analytical uncertainty (~45 ppm 2 SD). Thus, no ReO_3^- corrections are typically necessary.

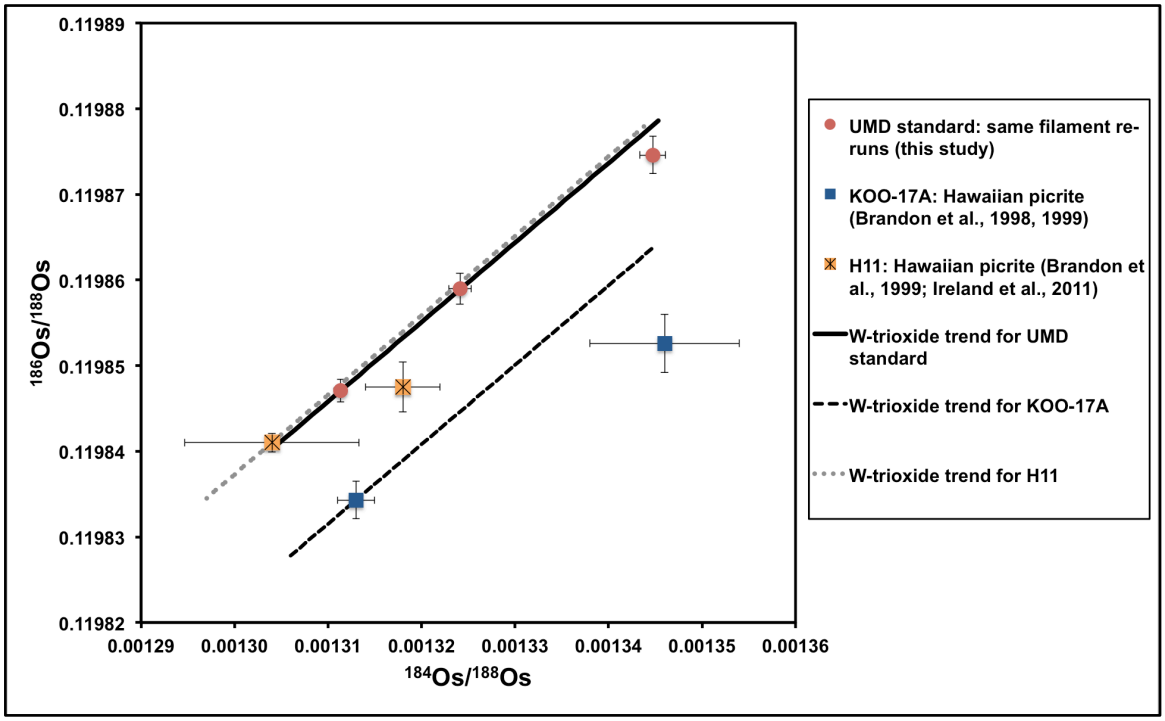

Figure 1.11a $^{184}Os/^{188}Os$-$^{186}Os/^{188}Os$ plots showing a positive correlation for i) successive re-runs of the same filament for a UMD standard analyzed in this study and ii) duplicate digestions of two Hawaiian lavas (Brandon et al., 1998, 1999; Ireland et al., 2011).

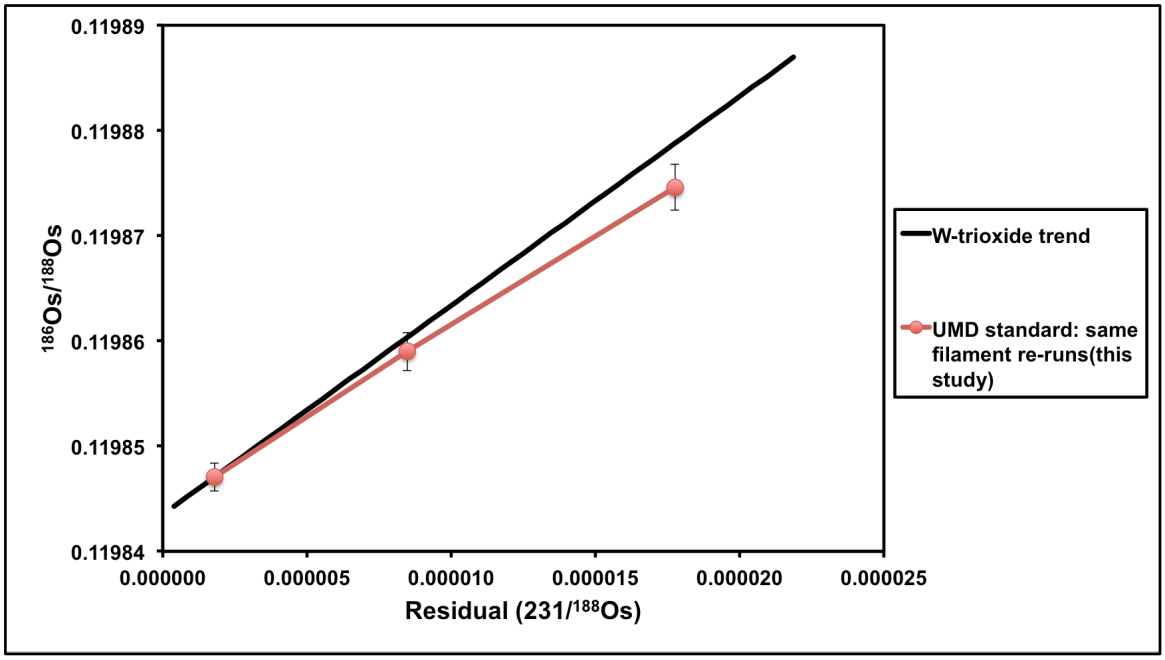

Figure 1.11b Plot of $^{186}Os/^{188}Os$ – Residual $231/^{188}Os$ after platinum stripping for successive re-runs of the same filament for the same UMD standard shown in figure 1.11a.

There is a correlated increase in residual $231/^{188}Os$ and $^{186}Os/^{188}Os$ that matches the expected trend for WO_3^- interference.

8. CONCLUSIONS

$^{186}Os/^{188}Os$ measurements require high analytical precision due to limited $^{186}Os/^{188}Os$ variability in the mantle (~150 ppm; c.f., Brandon et al., 1998). This can be best achieved by quantifying the primary sources of analytical error and refining current analytical procedures to maximize precision for a given sample size. Although determining in-run O isotopic composition is important for oxide correction, O isotopic measurement before and after Os measurement routine is more efficient and conserves analytical time relative to line-by-line O isotopic measurement. Although usage of $^{189}Os/^{188}Os$ normalization introduces lower uncertainty from oxide correction of the Os isotopes, greater MF-propagated error in the corrected ratios overwhelms this benefit. Instead, use of $^{192}Os/^{188}Os$ normalization generates lower uncertainties in the corrected ratios and is preferable. Usage of mutually consistent normalizing values is necessary to compare datasets corrected using two different normalizations for MF correction. As occasional runs of both standards and samples are compromised by interferences such as WO_3^-, it is important to evaluate each analysis after stripping PtO_2^- interferences for other interferences that directly affect the $^{186}OsO_3^-$ peak, which may be obscured behind PtO_2^- peaks. Johnson noise error in baseline determinations is the largest analytical error at typical $^{186}OsO_3^-$ beam intensities. This can be reduced by increasing baseline measurement duration even when the total number of measured Os ions are lowered.

Acknowledgements

This work was supported by NSF grant EAR-1321937 and by the Jackson School of Geosciences, University of Texas at Austin. This manuscript benefitted from editor comments from Klaus Mezger and reviewer comments from Ambre Luguet and an anonymous reviewer and are greatly appreciated.

Chapter 2: $^{186}Os/^{188}Os$ variations in upper mantle peridotites: Constraints on the Pt/Os ratio of primitive upper mantle, and implications for late veneer accretion and mantle mixing timescales

ABSTRACT

$^{186}Os/^{188}Os$ variations in mantle peridotites provide constraints on the long-term Pt/Os evolution of the depleted mantle and the Pt/Os ratio of the primitive upper mantle (PUM). I report new $^{186}Os/^{188}Os$ data for mantle peridotites from continental (Rio Grande Rift and Colorado Plateau) and oceanic (Lena Trough and Hawaiian Islands) settings that span a wide range in fertility (Al_2O_3 ≈0.67-4.42 wt.%) and $^{187}Os/^{188}Os$ ratios (0.1138-0.1305). Although peridotite $^{186}Os/^{188}Os$ values span only a narrow range (from 0.1198345 to 0.1198384), $^{186}Os/^{188}Os$ broadly correlates with indices of melt depletion, including bulk rock Al_2O_3, spinel Cr#, and clinopyroxene Cr#, consistent with Pt depletion in residual peridotites.[3 4]

PUM $^{186}Os/^{188}Os$ is estimated to be 0.1198378±23 (2 SD) based on extrapolation of $^{186}Os/^{188}Os$-fertility trends, which is lower than H-chondrites [≈0.1198398±16 (2 SD); Brandon et al., 2006]. This value is consistent with a PUM Pt/Os of 1.7±0.2, similar to average Pt/Os ratios of fertile continental peridotites. The inferred PUM Pt/Os is ~10% lower than but within error of Pt/Os values measured in several classes of chondrites [Carbonaceous ≈1.8±0.2, Ordinary ≈1.9±0.1 and Enstatite ≈1.9±0.1 (Brandon et al.,

---

[3] The contents of this chapter has been published as: Chatterjee, R., Lassiter, J.C., 2016. $^{186}Os/^{188}Os$ variations in upper mantle peridotites: Constraints on the Pt/Os ratio of primitive upper mantle, and implications for late veneer accretion and mantle mixing timescales, *Chemical Geology 442, 11-22*

[4] The material presented in this chapter is my original work completed under the supervision of Dr. Lassiter.

2006)] indicating that PUM Pt/Os is chondritic. In contrast, estimates for PUM Ru/Ir and Pd/Ir (cf. Becker et al., 2006) extrapolated from measured ratios in peridotites are suprachondritic. The addition of a chondritic late veneer alone cannot create a combination of chondritic and suprachondritic HSE ratios for the PUM. Instead, minor core segregation occurring concurrently with the addition of a late veneer may explain the observed mantle HSE abundances and ratios.

Combined $^{186}Os/^{188}Os$-$^{187}Os/^{188}Os$ isotopic and Pt/Os and Re/Os variability in peridotites suggest an average mantle homogenization timescale of ~1.2 Gyrs. In contrast, combined Hf-Nd isotopic and Lu/Hf and Sm/Nd variability in peridotites indicate much shorter homogenization timescales (<0.4 Gyrs), potentially reflecting their greater susceptibility to homogenization by melt-rock interaction to which the Pt-Os and Re-Os systems are relatively immune. The mechanical mixing timescale inferred from Os isotopes is consistent with timescales predicted for whole mantle convection.

1. Introduction

Core formation resulted in almost complete sequestration of the Highly Siderophile Elements (HSE) from the Earth's mantle (cf. Newsom et al., 1990). However, abundances of HSE in the Earth's mantle are substantially higher than expected from metal-silicate partition coefficients experimentally determined at low pressures (Capobianco et al., 1993; Newsom et al., 1990). Furthermore, most of the HSE in the Earth's mantle occur in broadly chondritic relative proportions, although there is significant variation in measured HSE ratios of mantle peridotites (cf. Meisel et al., 2001;

Becker et al., 2006; Brandon et al., 2006). These observations have been taken as evidence for the addition of a 'late veneer' of chondritic material to Earth's mantle after core formation (cf. Morgan, 1986), which would have elevated mantle HSE abundances and re-established their chondritic relative proportions. Although core segregation under high pressure and/or high temperature (high P-T) conditions may explain the mantle abundances of many slightly and moderately siderophile elements and possibly some HSE such as Pd (cf. Righter et al., 2008; Righter, 2011), it is uncertain whether a lowered metal-silicate K_D during high P-T core segregation relative to low pressure conditions can account for the near- chondritic relative abundances of a wide range of HSE in the mantle.

Elemental ratios are susceptible to modification by processes such as melt-infiltration, metasomatism, and/or weathering and alteration. This makes reliable estimation of Primitive Upper Mantle (PUM) compositions using measured elemental ratios subject to large uncertainties reflecting inherent scatter in the data resulting from the complicated, multi-stage history of many peridotites. For example, Becker et al. (2006) estimated $Re/Os_{PUM} \approx 0.096 \pm 0.029$ (1 SE) by extrapolating Re/Os ratios in variably depleted peridotites to primitive mantle compositions (Al_2O_3 ~4.45 weight %; McDonough and Sun, 1995), but the sizable error in this estimated ratio reflects the large inherent scatter in mantle peridotite Re/Os ratios. Long-lived radiogenic isotope ratios (e.g. $^{187}Os/^{188}Os$) can potentially provide more precise constraints on some primitive mantle elemental ratios as they reflect time-integrated parent/daughter ratios and are largely immune to recent modification. Extrapolation of PUM parent/daughter ratios from isotopic

compositions in peridotites also provides an independent check on estimates based on elemental abundances. Because ^{187}Re decays to form ^{187}Os [$t_{1/2}$ ~42 Gyrs (Selby et al., 2007)], ^{187}Os/^{188}Os ratios in peridotites can constrain long-term Re/Os ratios in the mantle. Previous studies (cf. Meisel et al., 2001) have inferred that the ^{187}Os/^{188}Os of the PUM is ≈0.1296±9. From this estimate, Re/Os_{PUM} is calculated to be ≈0.090±0.001 (1 SE), which is consistent with, but significantly more precise than estimates utilizing measured elemental ratios (cf. Becker et al., 2006). This estimate is statistically indistinguishable from the estimated Re/Os of ordinary and enstatite chondrites (cf. Horan et al., 2003; Brandon et al., 2006). Thus, the Re/Os of the silicate Earth appears to be chondritic, consistent with the late veneer model (cf. Becker et al., 2006).

Values of ^{186}Os/^{188}Os can be similarly used to infer the Pt/Os ratio of the PUM, because ^{190}Pt decays to form ^{186}Os [$t_{1/2}$ ~468 Ga; Begemann et al. (2001)]. Previous studies have examined ^{186}Os/^{188}Os in a variety of upper mantle materials. This dataset includes Os-Ir alloys (Walker et al., 2005) and chromitites (cf. Brandon et al., 1998; Walker et al., 2005). Most of these samples have sub-chondritic ^{187}Os/^{188}Os values. Other analyzed upper mantle materials include a small set of abyssal peridotites (AP) from a single section of the Kane Fracture Zone (KFZ). These peridotites span a narrow range in isotopic composition (^{187}Os/^{188}Os ≈0.1226-0.1276) and extent of melt depletion (whole rock Al_2O_3 ≈ 1.2-1.8 %) (Brandon et al., 2000), which makes it difficult to evaluate correlations between ^{186}Os/^{188}Os and peridotite composition or melt-depletion history.

In this chapter, I report ^{186}Os/^{188}Os in peridotites from continental (Rio Grande Rift and Colorado Plateau) and oceanic (Lena Trough and Hawaiian Islands) settings that

span a wide range in fertility and $^{187}Os/^{188}Os$. Correlations between fertility and $^{186}Os/^{188}Os$ are utilized to investigate the extent to which long-term Pt/Os fractionation in the upper mantle is controlled by melt depletion and to constrain the Pt/Os ratio of the PUM. Pt/Os_{PUM} inferred from $^{186}Os/^{188}Os$ of fertile peridotites is combined with PUM estimates for other HSE ratios to evaluate the late veneer hypothesis. I found that the addition of a late veneer cannot fully explain a combination of chondritic (e.g., Pt/Os) and suprachondritic (e.g., Pd/Ir) mantle HSE ratios and thus examined alternate models involving minor metal or sulfide segregation concurrent with late veneer addition. Finally, the degree of isotopic ($^{186}Os/^{188}Os$ and $^{187}Os/^{188}Os$) and parent/daughter (Pt/Os and Re/Os) variability observed in upper mantle peridotites is utilized to constrain the timescale of mantle mixing and homogenization.

2. SAMPLES

Mantle peridotites were selected from both continental (Rio Grande Rift and Colorado Plateau) and oceanic (Hawaiian Island and Lena Trough) settings that span a wide range in fertility and $^{187}Os/^{188}Os$. Details of each of the sampling locations are given below.

a) Lena Trough:

Abyssal peridotites (AP) from the Lena Trough were recovered from deep-sea dredges during the *Polarstern* ARK-XV-2 (1999) and *Polarstern* ARK-XX-2 (2004) cruises. Samples have undergone variable degrees of seafloor weathering and

serpentinization (LOI ~11-17%) (Snow & Petrology Group, 2007). Serpentinization processes generally do not mobilize PGE in peridotites and are likely to have a minor effect on primary PGE abundances (cf. Marchesi et al., 2013). The studied samples have coarse porphyroclastic textures and are optically devoid of plagioclase and crosscutting magmatic veins. High degree of serpentinization in most samples does not allow a clear distinction of former clinopyroxene and/or orthopyroxene (Snow and Petrology Group, 2007). Selected samples have moderately to highly refractory compositions with bulk rock Al_2O_3 contents ranging between ~1.2 and 2.8 wt%. $^{187}Os/^{188}Os$ span a wide range (~0.1191-0.1281). REE patterns show variable LREE depletion and flat MREE-HREE trends, consistent with variable melt depletion (Lassiter et al., 2014). Earlier studies suggested that these peridotites may be remnants of Sub Continental Lithospheric Mantle (SCLM) exposed during continental rifting (cf. Snow et al., 2011). However, more recent studies interpret these samples to derive from the convecting upper mantle, based on the LREE-depleted, flat MREE-HREE patterns and Os isotope compositions, similar to abyssal peridotites (APs) worldwide (Lassiter et al., 2014). More detailed geographic and petrologic information are provided in Snow & Petrology Group (2007) and Lassiter et al. (2014).

b) Salt Lake Crater, Oahu, Hawaii:

Xenoliths from Salt Lake Crater (SLC), Oahu, are spinel lherzolites from the Jackson collection from the National Museum of Natural History (NMNH), Smithsonian Institution. These xenoliths occur within Honolulu Volcanic Series lavas, which mark the

post-erosional stage of volcanism of Koolau volcano (cf. Bizimis et al., 2007 and references therein). All of the studied samples are fresh and show no visible signs of metasomatism or melt infiltration. However, the xenoliths are variably LREE enriched and have characteristic hump-like REE patterns, thought to reflect metasomatic overprinting (Bizimis et al., 2007). Studied samples are typically allotriomorphic-granular and coarse-grained porphyroclastic with large olivines and orthopyroxenes (> 2mm). Clinopyroxene and spinels are much smaller in size and have a low modal abundance (clinopyroxene- <5% to <15%; Spinel- <5%). Selected samples have Os isotopic ratios ranging from very unradiogenic to PUM-like values ($^{187}Os/^{188}Os$ ~0.1138-0.1301). Bulk rock Al_2O_3 content ranges from highly refractory to moderately depleted (~0.8-3.3 wt.%).

I attempted to analyze the same xenoliths from SLC that were previously analyzed by Bizimis et al. (2007). However, although the xenolith aliquots provided by NMNH have the same curation number as the previously reported xenoliths, I discovered on analysis that these xenoliths actually derive from different xenoliths from the same Jackson field sample and/or NMNH storage drawer (labeled as "miscellaneous SLC xenoliths" in the Jackson Collection). In several instances, the new samples have very different mineral major-element compositions and $^{187}Os/^{188}Os$ values from the xenoliths reported by Bizimis et al. (2007). Except for sample NMNH 115048-26, for which I was able to utilize the same powder aliquot as that prepared for the Bizimis et al. (2007) study, all of the SLC xenoliths utilized in this study are distinct from the previously analyzed samples

with the same NMNH number. To avoid future confusion, I have added a suffix (a) to the NMNH sample numbers to denote the new xenolith utilized in the current study.

Xenoliths from Salt Lake Crater were previously interpreted to be ancient (>2 Ga) recycled lithospheric mantle related to the Hawaiian plume, based on extremely depleted Os and Hf isotopic signatures observed in these xenoliths (Bizimis et al., 2007). However, recent studies (cf. Stracke et al., 2011; Byerly and Lassiter, 2014) have shown that ultra-depleted domains are more widely distributed in the DMM than previously thought. Lassiter et al. (2014) showed that the mean and the distribution of Os isotopes in APs and ocean island xenoliths worldwide is statistically indistinguishable, and concluded that most ocean island xenoliths, including the SLC xenoliths, derive from the same heterogenous DMM reservoir as abyssal peridotites.

c) Rio Grande Rift/Colorado Plateau:

Spinel peridotite xenoliths were collected from two different localities in Central New Mexico: Elephant Butte (Central Rio Grande Rift) and Cerro Chato (eastern margin of the Colorado Plateau). The xenoliths primarily comprise olivine-rich peridotites containing Cr-rich clinopyroxenes and spinels that have equigranular to coarse protogranular textures (Byerly and Lassiter, 2012). The studied xenoliths typically have large clinopyroxene modal abundances (~10-17%) except one sample (BELB 9-15). Sample BELB 9-15 has a low clinopyroxene modal abundance (~3 %) with coarse-grained olivine and orthopyroxenes (~4-7 mm). Selected samples for this study span a wide range in peridotite fertility (e.g., bulk rock Al_2O_3 ~0.67-4.42 wt.%) and Os isotopic

composition ($^{187}Os/^{188}Os$ ~0.1172-0.1305). They include i) samples with fertile major-element compositions, depleted LREE patterns, and isotopic compositions similar to APs that are interpreted to derive from recently-emplaced asthenospheric mantle; and ii) samples with refractory major element compositions, enriched LREE signatures, enriched Sr-Nd-Pb and unradiogenic Os isotopic compositions that are interpreted to derive from remnant Proterozoic Sub-Continental-Lithospheric-Mantle (SCLM) (cf. Byerly and Lassiter, 2012). More detailed geologic and petrologic information is provided elsewhere (Byerly and Lassiter, 2012).

3. ANALYTICAL METHODS

Detailed description of all analytical methods including standard values can be found in the supplementary materials. Most of the samples selected for this study have been previously analyzed for whole rock and mineral major and trace element compositions and detailed procedures are reported elsewhere (cf. Bizimis et al., 2007; Byerly and Lassiter, 2012; Lassiter et al., 2014). For this study, whole rock major and trace element compositions were analyzed via XRF and ICP-MS at the Geo-Analytical laboratory, Washington State University. All other analyses were performed at UT Austin. Mineral major element and clinopyroxene trace element compositions were determined using EMPA and LA-ICP-MS respectively. Bulk-rock measurements were reproducible to within ~5% for most major elements and within ~10% for most trace elements (Table B.5). Mineral major element compositions are reproducible within 5% (2 SD). Average analyses of LA-ICP-MS standard BCR-2g, were accurate within ~10% for all elements

(Table B.7). Duplicate analyses of the BCR-2g standard were reproducible to within 10% (2 SD) (Byerly and Lassiter, 2012; Lassiter et al., 2014).

For Re and Os analyses, bulk rock powder was digested in inverse aqua regia using an *Anton Paar* HPAS for 12 hours at 300 ºC. Osmium was extracted by solvent extraction (CCl_4) using procedures outlined in Lassiter et al. (2014). Osmium was back extracted from CCl_4 using HBr. Osmium was then further purified by micro-distillation (Birck et al., 1997). Re was separated from the same aliquot as Os following column chromatographic procedures outlined in Lassiter et al. (2003). Re and Os concentrations were determined by isotope dilution with a mixed ^{185}Re-^{190}Os spike using the department's *Isoprobe* MC-ICP-MS and *Triton* N-TIMS respectively. Re and Os concentrations were determined using a small (1-2 g) portion of the same vial of powder as that prepared for major and trace element analyses and subsequent unspiked ^{186}Os/^{188}Os measurements. For high precision ^{186}Os/^{188}Os measurements, 15-40 g of unspiked whole rock powder was processed. This was necessary to extract at least ~60 nanograms of Os for each analysis, which was sufficient to generate ≥100 mV of $^{186}OsO_3^-$ during N-TIMS analyses. Five quartz tubes, each containing ~3g of whole rock powder, were processed in a single HPAS digestion. Therefore, 2-3 HPAS digestions were typically necessary to process a single sample. All of the HBr back-extracted from CCl_4 from the multiple digestions was pooled together and dried before performing micro-distillation of the pooled Os cut. Os was loaded using procedures described in Chatterjee and Lassiter (2015). Samples were typically run between 780 and 820 °C but occasionally as high as 860°C. Oxygen was bled into the source chamber from a tank of

compressed oxygen and the chamber pressure was maintained at ~$3x10^{-7}$ mbar. A liquid N_2 cold finger was used to reduce organic interferences. Os blanks ranged from 107 to 360 fg per gram of processed powder during the course of the study.

Full details of Os measurement and data reduction procedures are given in Chatterjee and Lassiter (2015). In brief, Os was measured using a Triton Thermal Ionization Mass Spectrometer in negative ion mode (N-TIMS) using a static multi-collector routine for 10 blocks of 20 cycles (16.77 s integration time). $^{186}OsO_3$ beam intensity ranged from ~100-170 mV. Baselines were measured for 5 minutes at the beginning of each block to reduce Johnson noise during baseline integrations, the largest source of analytical error in $^{186}Os/^{188}Os$ measurements (Chatterjee and Lassiter, 2015). Interferences (masses 228-233) were measured via Secondary Electron Multiplier (SEM) before and after the Os routine. Within-run O isotopic composition of the OsO_3^- species was also determined by measuring peaks 240, 241 and 242 before and after the Os routine. Raw Os data were corrected for instrumental mass fractionation relative to $^{192}OsO_3/^{188}OsO_3$ =3.092585 using the exponential fractionation law. Subsequent stages of data correction use the within-run O isotopic composition and correct any residual mass fractionation. Pt peaks were calculated and stripped using measured IC (Ion counter) analyses of 228/236 measured before and after the Os isotope routine. Stripping the PtO_2 peaks at 232 lowers the average measured $^{184}Os/^{188}Os$ of the peridotites from 0.001308 to 0.001306 and improves the external reproducibility (2 SD) of $^{184}Os/^{188}Os$ from ~2700 to ~2200 ppm. Finally, after oxide correction using measured O-isotope composition, an instrumental mass fractionation correction was applied to all the ratios (232/236-238/236, 240/236) with

$^{192}Os/^{188}Os$=3.083 using the exponential law. Many filaments had sufficient Os to be analyzed multiple times. In these cases, the line measurements from the multiple runs of the same filament were pooled for data processing and these results are reported as a single analysis in Table 2.1.

$^{186}Os/^{188}Os$ analyses are occasionally affected by interferences of unknown origin, possibly WO_3^- interferences or organic material (Chatterjee and Lassiter, 2015). The presence of potential interferences was assessed by examining the $^{184}Os/^{188}Os$ ratio and the residual peak at 231 after correcting for PtO_2^- interferences. Samples with high residual 231 (>10 cps) and/or anomalous $^{184}Os/^{188}Os$ values (outside 2 SD of the normal value) are considered suspect and should be excluded from further consideration. Four of the Lena Trough samples (PS 66-253-6-6, PS 66-251-57, PS 66-255-7 and PS 66-253-36-1) analyzed in this study show anomalously high residual 231 (40-360 cps), well outside the normal range for other standards and samples, and three of the four samples also have anomalous $^{184}Os/^{188}Os$ outside the normal range (Figure B.1). Therefore, these analyses are less robust than the remaining analyses and are excluded from all fertility-$^{186}Os/^{188}Os$ regressions (Section 5.1), although they are within the same $^{186}Os/^{188}Os$ range as the other peridotites. These $^{186}Os/^{188}Os$ analyses are reported in Table 2.1 but should be used for comparative purposes only.

During the course of this study, the UT Triton was serviced twice to correct Faraday and/or amplifier drift problems. Most peridotites were measured in a single period following these two service visits. The average $^{186}Os/^{188}Os$ of the Johnson Mathey Os standard (UMD) analyzed during this period was 0.1198449$\pm$10 (2 SE, n=18). The four

Lena Trough peridotites with anomalous $^{184}Os/^{188}Os$ and/or residual 231 (as discussed above) were analyzed in earlier campaigns before and after the first Triton servicing. For these two periods, the average $^{186}Os/^{188}Os$ of the Johnson Mathey Os standard (UMD) were 0.1198478±8 (2 SE, n=12) and 0.1198467±15 (2 SE, n=8) respectively. For direct data comparison with other laboratories, all samples were corrected to the long term UMD $^{186}Os/^{188}Os$ mean of 0.1198470 reported in Brandon et al. (2006) using the mean UMD value for the respective analytical period.

Within-run precisions (2 SE) are reported in Table 2.1, and range from ~8-35 ppm. Internal error is inversely correlated with average signal size and with total number of signal integrations. During the period over which most samples were analyzed, the external $^{186}Os/^{188}Os$ reproducibility of 18 Os standards was ~35 ppm (2 SD). However, most standards were analyzed over shorter durations (200 ratios) and lower beam intensities than most samples. During the same time period, 8 standards were analyzed twice from the same filament load and the results from each filament pooled in the fashion described above. For these standards, the external reproducibility is ~30 ppm (2 SD). Three duplicate sample measurements (separate Os digestions), including two duplicates measured for this study, suggest external reproducibility of ~12 ppm. Finally, the standard deviation of all samples reported in Table 2.1 is ~18 ppm (2 SD), which places an upper bound on the sample external reproducibility (which would require zero natural variation in the measured $^{186}Os/^{188}Os$, which is unlikely based on the fertility-$^{186}Os/^{188}Os$ trends discussed in Section 5.1). Therefore, it appears that the external reproducibility of the Os standards overestimates the sample measurement error.

Nevertheless, in the following discussion, we use the standard reproducibility of 30 ppm as a conservative estimate of sample reproducibility.

Sample #	Location	Re (ppb)	Os (ppb)	No of ratios	$^{184}Os/^{188}Os$	Residual 231 (in cps)	Measured $^{186}Os/^{188}Os$	Corrected $^{186}Os/^{188}Os$ (Brandon et al., 2006)	$^{187}Os/^{188}Os$	WR Al_2O_3 wt. %	Spinel Cr#	Cpx Cr#	Cpx Yb (ppm)
PS66-253-6-6	LT	0.03	2.00	200	0.001296(4)	113	0.1198362(41)	0.1198354(41)	0.126005(4)	1.32			
PS66-251-57	LT	0.21	1.92	200	0.001300(2)	358	0.1198384(26)	0.1198377(26)	0.119131(3)	*1.69*		*15.0*	
PS66-255-7	LT	1.76	2.57	200	0.001306(1)	40	0.1198394(16)	0.1198397(16)	0.128155(2)	*2.81*			
PS66-251-47	LT		3.02	400	0.001306(1)	6	0.1198344(12)	0.1198364(12)	0.125251(1)	*2.29*	23.8	*11.8*	*1.38*
PS66-253-36-1	LT	0.03	3.40	200	0.001310(1)	201	0.1198395(16)	0.1198398(16)	0.123700(2)	1.22			
PS66-262-106	LT	*0.16*	*2.30*	400	0.001305(1)	3	0.1198336(18)	0.1198357(18)	0.123429(2)	*1.18*	*26.5*	*17.3*	*1.04*
NMNH 115048-5a	SLC	0.59	1.82	600	0.001306(1)	2	0.1198343(12)	0.1198363(12)	0.121881(1)	3.30		12.0	1.28
NMNH 115048-26a	SLC	3.29	1.60	800	0.001306(1)	5	0.1198332(13)	0.1198352(13)	0.122004(2)	2.18	50.7	25.3	0.82
NMNH 115048-2a	SLC	0.01	2.07	800	0.001306(1)	4	0.1198357(10)	0.1198377(10)	0.120489(1)	2.40		16.6	0.88
NMNH 115048-4a	SLC	0.40	1.00	200	0.001305(1)	2	0.1198330(27)	0.1198350(27)	0.130137(9)	2.39		17.1	1.43
NMNH 115048-3a	SLC	0.10	2.00	800	0.001305(1)	2	0.1198349(10)	0.1198370(10)	0.121886(2)	1.83	34.9		
NMNH 115048-3a_DUPLICATE	SLC			800	0.001305(1)	3	0.1198353(9)	0.1198374(9)	0.122034(1)				
NMNH 115048-25a	SLC	0.03	1.68	800	0.001306(1)	3	0.1198336(11)	0.1198356(11)	0.124637(2)	3.17	33.9	18.1	0.82
NMNH 115048-26	SLC		2.20	400	0.001306(1)	6	0.1198344(14)	0.1198364(14)	0.113859(1)	*0.82*	*30.4*	*16.5*	*0.87*
BELB 9-15	EB, RGR	*0.02*	*2.74*	400	0.001306(1)	3	0.1198325(14)	0.1198345(14)	0.117253(1)	*0.67*	*50.0*	*22.6*	*0.14*
07EB 4.01	EB, RGR	*0.30*	*2.21*	600	0.001306(1)	4	0.1198352(10)	0.1198373(10)	0.130502(1)	*4.42*	*8.2*	*5.6*	*2.10*
07EB 4.21	EB, RGR	*0.17*	*2.39*	600	0.001304(1)	5	0.1198364(12)	0.1198384(12)	0.125141(1)	*3.60*	*11.1*	*7.9*	*1.61*
CC07-2-01	CC, CP	*0.01*	*2.35*	400	0.001307(1)	2	0.1198354(12)	0.1198374(12)	0.121444(1)	*2.73*	*20.8*	*12.6*	*1.07*
CC07-2-01_DUPLICATE	CC, CP			400	0.001305(1)	3	0.1198347(13)	0.1198367(13)	0.12219(1)				

$^{186}Os/^{188}Os$ and $^{187}Os/^{188}Os$ errors listed in parantheses are 2 SE (combined internal precision) determined by combining repeat runs from the same filament; Cr # = (molar Cr/(Cr+Al)) x 100;
Location abbreviation: LT=Lena Trough, SLC = Salt Lake Crater, Hawaii, EB = Elephant Butte,CC=Cerro Chato, RGR= Rio Grande Rift, CP= Colorado Plateau;Data marked in italics previously reported (LT- Lassiter et al., 2014; SLC-Bizimis et al., 2007; RGR,CP- Byerly and Lassiter, 2012)

Table 2.1 Re-Os concentrations and Os isotopic compositions of peridotites

4. RESULTS

Bulk rock major and trace element concentrations are reported in table B.1. Mineral major element compositions are reported in tables B.2-B.3 and clinopyroxene trace element concentrations are reported in table B.4. Measured peridotites span a wide range of compositions. Bulk rock Al_2O_3 content ranges from 0.67 to 4.42 wt.%. Spinel Cr# [molar Cr/(Cr+Al)] ranges from 8.2 to 50. Clinopyroxene Cr# varies from 5 to 25. Whole rock Al_2O_3, spinel Cr#, clinopyroxene Cr# and clinopyroxene Yb contents are all well correlated and overlap with compositional trends observed in peridotites globally (Figures B.2-B.4). Observed correlations between whole-rock Al_2O_3, spinel Cr#, clinopyroxene Cr# and clinopyroxene Yb content in peridotites most likely reflect varying degrees of prior melt extraction (cf. Hellebrand et al., 2001).

Os isotope compositions are reported in table 2.1. $^{187}Os/^{188}Os$ values also span a wide range from sub-chondritic (0.1138) to slightly super-chondritic values (0.1305). Peridotite $^{187}Os/^{188}Os$ values correlate with bulk rock Al_2O_3 and overlap with global peridotite trends (Figure B.5). $^{186}Os/^{188}Os$ values range from 0.1198345 to 0.1198384. The average value of the measured peridotites is 0.1198364±6 (2 SE, n=13), which is nearly identical to values previously reported for abyssal peridotites from the Kane Fracture Zone [≈0.1198359±7 (2 SE); Brandon et al., 2000], Os-Ir alloys from the Josephine ophiolite [≈0.1198376±8 (2 SE); Walker et al., 2005; Brandon et al., 2006], and ophiolite-derived chromitites [≈0.1198341±22 (2 SE); Brandon et al., 1998, 2006]. Average $^{186}Os/^{188}Os$ values for the 3 studied locations are statistically indistinguishable [Lena Trough ≈0.1198360±7 (2 SE, n=2), Hawaii ≈0.1198362±7 (2 SE, n =7) and Rio

Grande Rift/Colorado Plateau ≈0.1198369±17 (2 SE, n=4)]. However, despite the limited range in $^{186}Os/^{188}Os$, $^{186}Os/^{188}Os$ correlates with several indices of melt depletion- bulk-rock Al_2O_3, spinel Cr#, clinopyroxene Cr # and clinopyroxene Yb contents (Figure 2.1).

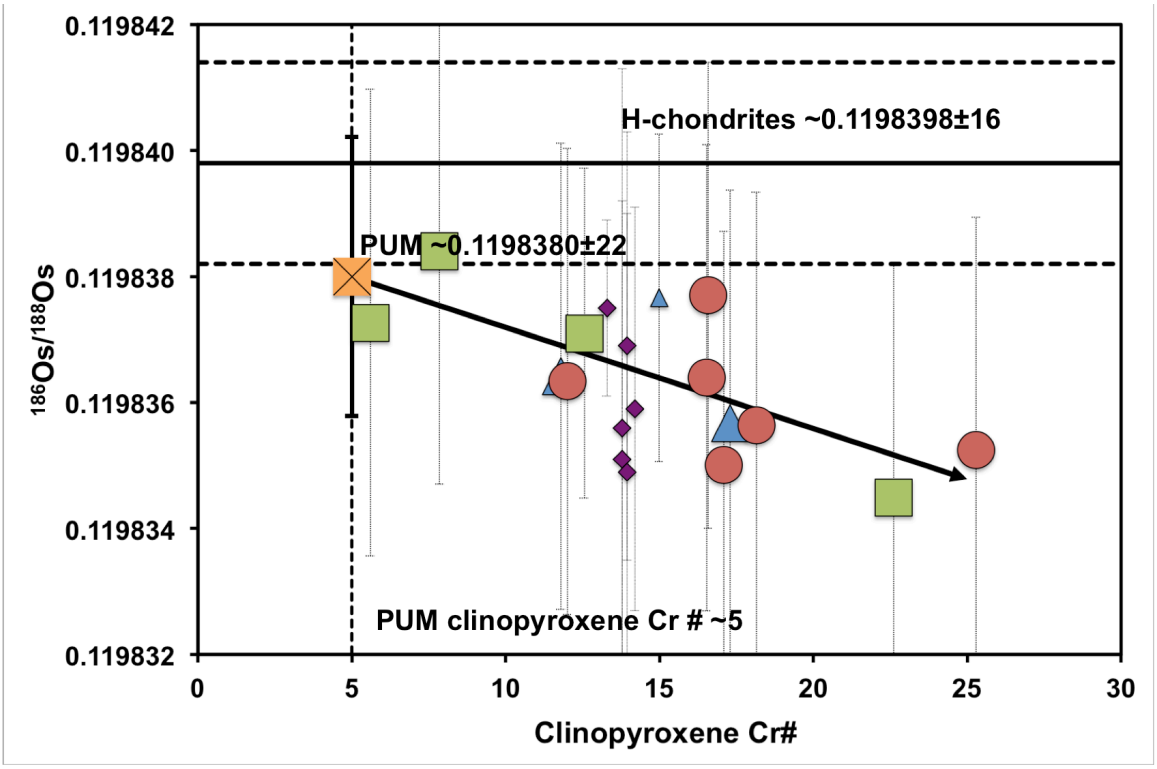

Figure 2.1a $^{186}Os/^{188}Os$ vs clinopyroxene Cr# in mantle peridotites using error-weighted-regression.

Data for abyssal peridotites previously measured from Kane Fracture Zone (Brandon et al., 2000) shown for comparison but not used in regression. More refractory samples (low Al_2O_3, high Cr# and low clinopyroxene Yb content) have lower average $^{186}Os/^{188}Os$ than fertile samples. Symbols: Lena Trough- blue triangles, Rio Grande Rift/Colorado Plateau- green squares, Hawaii- red circles, Kane Fracture zone- violet diamonds, PUM estimate- orange square with cross (this study). (H-chondrite range from Brandon et al., 2006; Kane fracture zone Cr# data from Snow, *pers. comm*). Clinopyroxene Cr# errors are smaller than the symbol size. Four Lena Trough samples not utilized in the fertility-

$^{186}Os/^{188}Os$ regressions are shown by smaller symbols (see section 3 for details). R-value and the statistical significance of these regressions in figure 2.1 are discussed in the text.

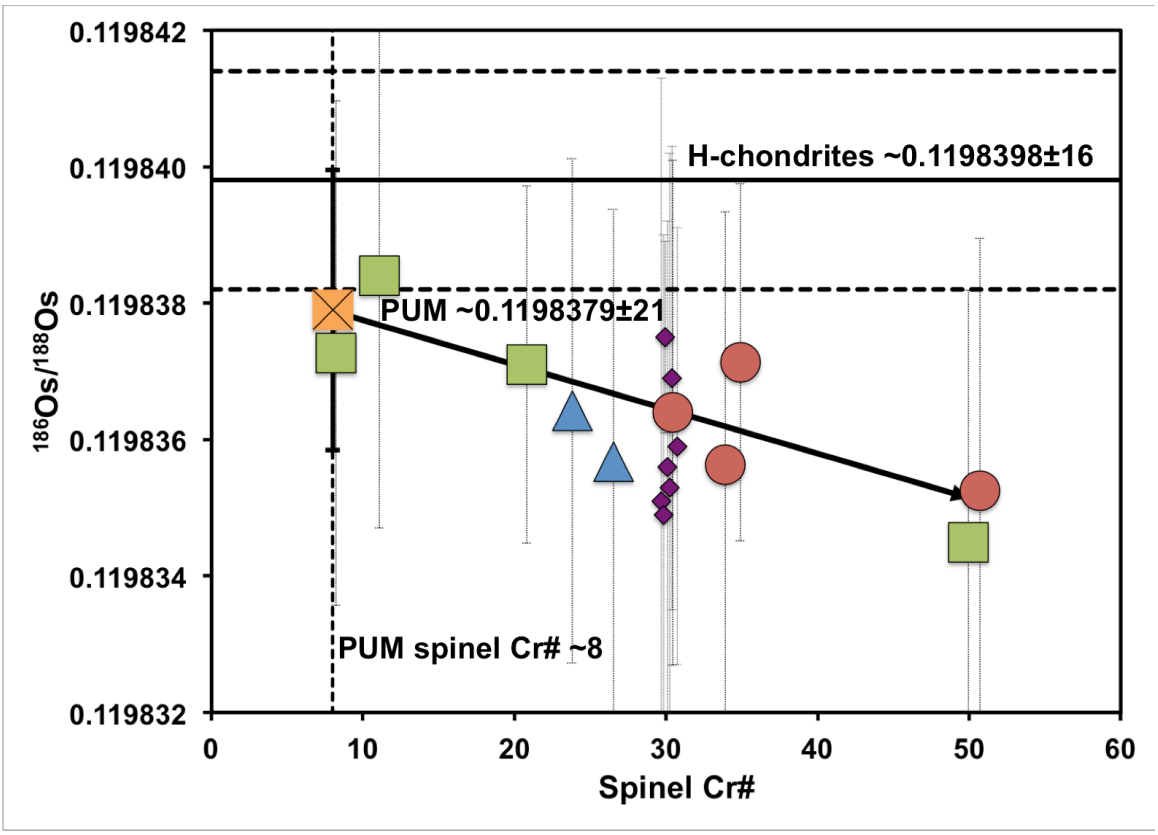

Figure 2.1b $^{186}Os/^{188}Os$ vs spinel Cr# in mantle peridotites using error-weighted-regression.

Data and symbols same as figure 2.1a. Spinel Cr# errors are smaller than the symbol size.

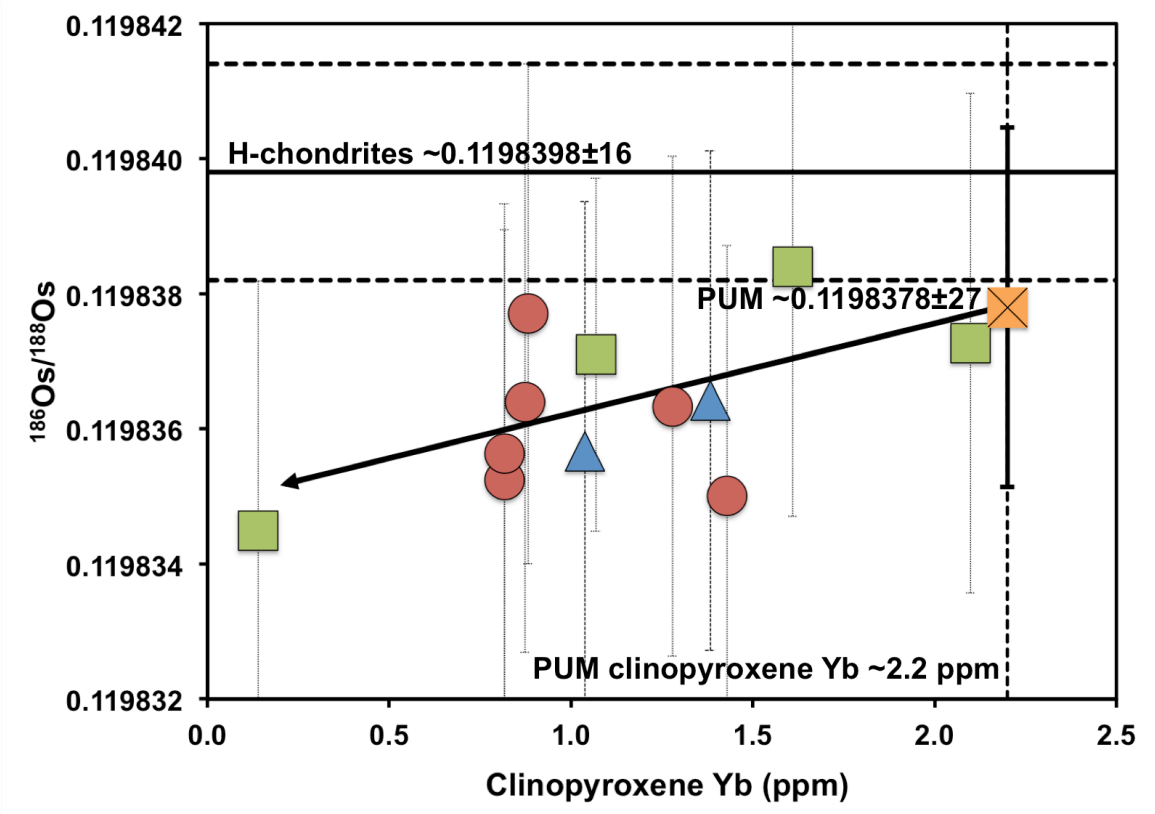

Figure 2.1c $^{186}Os/^{188}Os$ vs clinopyroxene Yb in mantle peridotites using error-weighted-regression.

Data and symbols same as figure 2.1a. Clinopyroxene Yb errors are smaller than the symbol size.

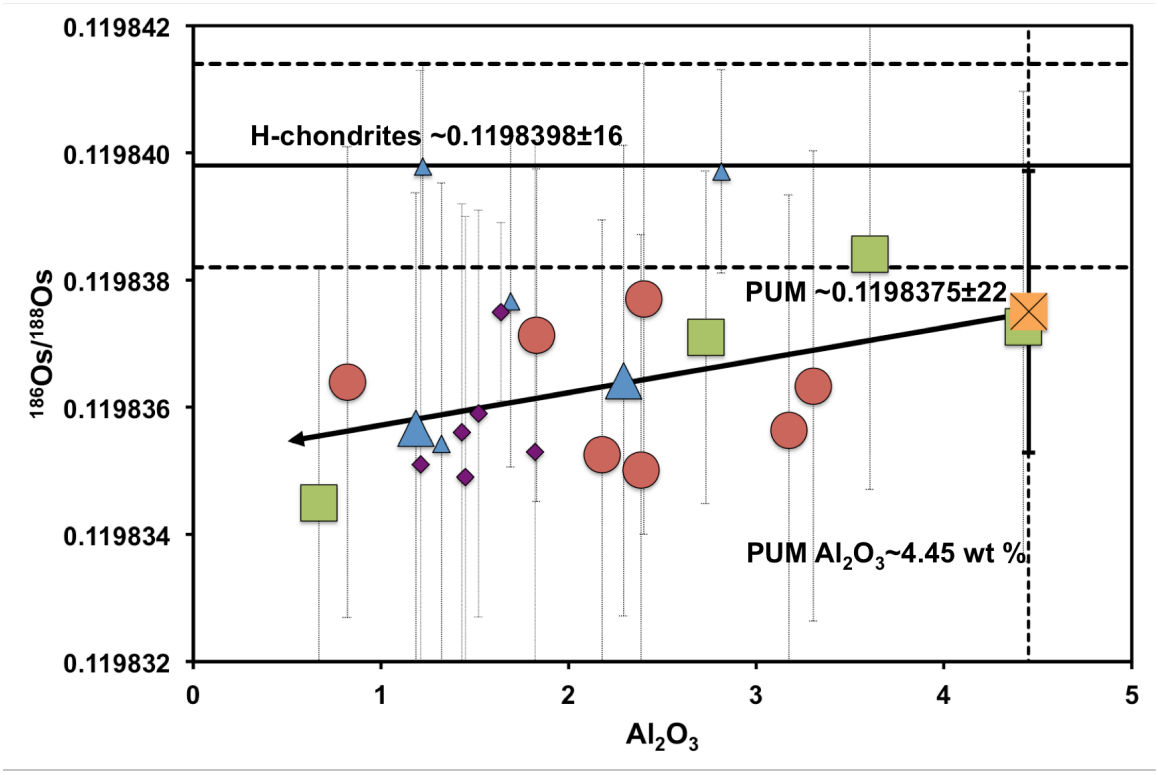

Figure 2.1d $^{186}Os/^{188}Os$ vs bulk rock Al_2O_3 wt.% in mantle peridotites using error-weighted-regression.

Data and symbols same as figure 2.1a. Bulk-rock Al_2O_3 wt.% errors are smaller than the symbol size.

5. DISCUSSION

5.1 Effect of melt depletion on mantle ^{190}Pt-^{186}Os evolution and constraints on the Pt/Os ratio of the PUM

Extrapolation of ^{186}Os/^{188}Os-fertility trends can be used to constrain PUM ^{186}Os/^{188}Os and Pt/Os in the same way previous studies (cf. Meisel et al., 2001) have utilized ^{187}Os/^{188}Os–fertility trends in peridotites to constrain PUM ^{187}Os/^{188}Os and Re/Os. In addition, if Pt/Os in peridotites is controlled by melt depletion, fertile peridotites may extend to higher Pt/Os and therefore higher ^{186}Os/^{188}Os values than the refractory peridotites analyzed to date (Brandon et al., 2000). Previous studies have reported ^{186}Os/^{188}Os in plume-derived lavas from Hawaii and Gorgona that extend to higher values than observed in refractory abyssal peridotites (cf. Brandon et al., 1999, 2000). The origin of these elevated ^{186}Os/^{188}Os values is the subject of considerable debate (cf. Brandon et al., 1998; Lassiter, 2006) and mechanisms including core-mantle interaction (cf. Brandon et al., 1998) and melting of pyroxenites/metasomatic sulfides (cf. Luguet et al., 2008) have been proposed. However, all mantle peridotites previously analyzed that form the baseline for the estimate of upper mantle ^{186}Os-isotope composition have refractory major-element compositions ($Al_2O_3 \approx$ 1.2-1.8 wt%) and sub-chondritic ^{187}Os/^{188}Os. Therefore, depending on the slope of any potential fertility-^{186}Os/^{188}Os trend, it is possible that elevated ^{186}Os/^{188}Os in plume-derived lavas reflect derivation from more fertile mantle components than the refractory peridotites previously analyzed.

Numerous studies show that Os behaves compatibly during mantle melting and fractional crystallization (cf. Lassiter and Luhr, 2001; Becker et al., 2006). In contrast, Pt

can behave either compatibly or moderately incompatibly, depending strongly on the presence or absence of sulfide phases (cf. Luguet et al., 2003). For example, Pt compatibility significantly increases during fractionation of lavas from Kohala, Hawaii at <8 wt% MgO, which likely reflects the onset of sulfide saturation (Jamais et al., 2008). Pt/Os ratios in mantle peridotites are broadly correlated with index of melt depletion (bulk-rock Al_2O_3)(Figure 2.2). Pt/Os ratios show considerable scatter, but no clear correlation with fertility for samples with ≥2 wt% Al_2O_3. However, Pt/Os ratios decrease sharply in refractory samples (≤1.5-2 wt% Al_2O_3) suggesting extraction of Pt during high degrees of partial melting. The break in slope at ~1.5 to 2 wt% Al_2O_3 may reflect exhaustion of residual sulfides in refractory peridotites, consistent with sulfide exhaustion at high degrees of partial melting (cf. Luguet et al., 2003). The considerable scatter in the Pt/Os-fertility trends can be attributed to several processes, including migration of sulfide melts (cf. Luguet et al., 2003) and melt-rock reaction/metasomatism (cf. Rehkampher et al., 1999). This makes it difficult to utilize these trends to tightly constrain the PUM Pt/Os ratio.

Peridotites from this study span most of the compositional range defined by peridotites globally (Figure B.2-B.4). The trends defined by correlations between bulk Al_2O_3 and spinel Cr#, clinopyroxene Cr#, and clinopyroxene [Yb] are controlled primarily by melt depletion, which lowers Al_2O_3 content and incompatible element abundances, and increases the Cr# in residual peridotite minerals (cf. Hellebrand et al., 2001). Fractional melting within the spinel peridotite stability field is modeled as a function of spinel Cr# and clinopyroxene Yb content after Hellebrand et al. (2001) and

Johnson et al. (1990) (Figure B.6). The model trend generally follows the depletion trend observed in our samples and for peridotites globally and indicates that the peridotites from this study have undergone extents of melt extraction that ranges from ~0 to ~20%. Estimates of primitive mantle composition vary. Most studies suggest primitive mantle $Al_2O_3 \approx$ 4-4.5 wt.% (e.g. Jagoutz et al., 1979; McDonough and Sun, 1995; Meisel et al., 2001). For this study, I have used the estimate of McDonough and Sun (1995) of 4.45 wt% Al_2O_3 in primitive mantle. Using this value, I estimate spinel Cr# of ~8, clinopyroxene Cr# of ~5, and clinopyroxene [Yb] of ~2.2 ppm for fertile spinel peridotites with a bulk composition similar to PUM. In the following discussion, these estimated PUM values are utilized to extrapolate $^{186}Os/^{188}Os$-fertility trends to PUM composition.

Although there is only limited $^{186}Os/^{188}Os$ variability in the peridotites analyzed for this study, apparent correlations between $^{186}Os/^{188}Os$ and several indices of melt depletion, including bulk rock Al_2O_3, spinel and clinopyroxene Cr#, and clinopyroxene Yb content were observed (Figure 2.1). Error-weighted linear regressions of these fertility-$^{186}Os/^{188}Os$ trends are shown in figure 2.1. The statistical robustness of the correlations was evaluated by computing r^2, statistical siginificance and mean square weighted deviation (MSWD). The slopes and PUM intercepts of the error-weighted regressions with respective uncertainties and the statistical robustness of these trends were calculated using Isoplot 4.1, a statistical tool developed by the Berkeley Geochronology Center (Ludwig, 2009). The statistical significance was determined using the 2-tailed t-test that measures the probability of the null hypothesis that a given

correlation coefficient between two quantities for a given sample size could result from chance (Pearson, 1895). The calculated slope, PUM intercept with respective uncertainties, coefficient of determination (r^2), statistical significance and MSWDs of the fertility-$^{186}Os/^{188}Os$ trends are reported in Table 2.2.

$^{186}Os/^{188}Os$ is negatively correlated with spinel Cr# ($r \approx 0.83$, MSWD = 0.18, n=10) and clinopyroxene Cr# ($r \approx 0.76$, MSWD =0.18, n=12), and positively correlated with bulk rock Al_2O_3 ($r \approx 0.52$, MSWD =0.33, n=13), with ~99.7 %, ~99.6 % and ~93.2 % statistical significance, respectively (Figure 2.1). Clinopyroxene Yb content, a trace element indicators of partial melting (Hellebrand et al., 2001) also correlate with $^{186}Os/^{188}Os$ ($r \approx 0.57$, MSWD =0.32, n=12) with statistical significance of ~94.8 % (Figure 2.1). In all cases, the more melt-depleted samples have lower average $^{186}Os/^{188}Os$ than more fertile samples, which suggests that $^{186}Os/^{188}Os$ variations are linked to long-term Pt/Os fractionation produced by mantle melting. For small data sets, apparent correlations that lack any physical significance can result from inclusion of one or two outlier data points. However, the observed correlations reported above appear robust in that the slopes of the observed correlations are little affected by arbitrary exclusion of either the most or least radiogenic sample from each regression. Although most individual $^{186}Os/^{188}Os$ analyses are within analytical error of each other, there is real and systematic isotopic variability that is related to sample fertility. Note that the MSWDs calculated above are all <1. Typically, MSWDs <1 indicate either 1) a population has been overfitted, or 2) measurement errors have been overestimated. Given that for these linear regressions, the # samples » # fit parameters, it appears more likely that the estimated

error is too large (see Section 3). Use of internal SE instead of standard external SD would increase the above MSWDs to 1.8 (spinel Cr#), 1.6 (clinopyroxene Cr#), 2.9 (bulk rock Al_2O_3), and 2.4 (clinopyroxene Yb content).

Although Pt/Os ratios in mantle peridotites display considerable scatter independent of peridotite fertility, refractory samples with < ~2 wt.% Al_2O_3 extend to lower Pt/Os on average than more fertile samples (Figure 2.2). Overall, refractory continental xenoliths extend to lower Pt/Os ratios relative to oceanic peridotites. I therefore would expect a change in slope in the Al_2O_3-$^{186}Os/^{188}Os$ correlation at ~2 wt.% Al_2O_3. However, this is not observed in the data presented here. This could reflect the fact that most of the peridotites I analyzed are from the convecting upper mantle, not SCLM. Pt/Os variations due to recent melting or metasomatism would also not be reflected in Al_2O_3-$^{186}Os/^{188}Os$ correlations.

Previous studies have suggested that correlations between index of fertility (Al_2O_3) and $^{187}Os/^{188}Os$, could potentially reflect melt refertilization rather than melt depletion (cf. Becker et al., 2006). However, recent melt refertilization should result in strongly curved mixing trends between index of fertility and $^{186}Os/^{188}Os$ or $^{187}Os/^{188}Os$ (cf. Luguet and Reisberg, 2016; Reisberg and Lorand, 1995). Generation of linear mixing trends between Al_2O_3, and either $^{186}Os/^{188}Os$ or $^{187}Os/^{188}Os$ through late refertilization is highly unlikely. This requires extremely high Os concenetrations and isotopic compositions in the infiltrating melts (see figure 14a in Luguet and Reisberg, 2016) and yet, such melt compositions with the required high Os concentrations are almost never observed. Furthermore, refertilization should create a positive correlation between indices of

fertility and lithophile trace element ratios sensitive to melt percolation such as La/Sm and La/Yb. Instead, La/Sm (and La/Yb) is negatively correlated with indices of fertility, indicating that it is the most refractory samples that have experienced the greatest metasomatic overprinting, as is commonly observed in peridotites worldwide. Although metasomatic processes can create incompatible trace element enrichments in refractory peridotites without affecting their major element compositions, refertilization is unlikely to affect the major element compositions of peridotites without also producing incompatible trace element enrichments.

Other studies (cf. Luguet et al., 2003, 2008) suggest that addition of metasomatic Base Metal Sulphides (BMS) could introduce radiogenic $^{186}Os/^{188}Os$ or $^{187}Os/^{188}Os$ to depleted peridotites. Metasomatic BMS addition could occur either directly from percolating sulfide melts (Luguet et al., 2003) or by the co-precipitation of BMS and metasomatic clinopyroxene or spinel from sulfur-saturated silicate melts (cf. Luguet and Reisberg, 2016; Rudnick and Walker, 2009). In principle, sulphide melt metasomatism could be decoupled from silicate melt metasomatism, although sulfide-melt migration through silicates is largely impeded in the absence of silicate melts due to the large dihedral (wetting) angle (>60°) of sulphide melts (cf. Mungall and Su, 2005). Furthermore, global correlations between Al_2O_3 and $^{187}Os/^{188}Os$ in peridotites would be absent if sulphide metasomatism routinely decoupled HSE and silicate/oxide phases (cf. Rudnick and Walker, 2009). Luguet and Reisberg (2016) argue against creation of $^{187}Os/^{188}Os$ vs. Al_2O_3 correlations by addition of radiogenic sulfides because this process would also produce positive correlations between Os concentration and Al_2O_3, which are

rarely observed. In accordance with this observation, the peridotite suites considered in our study do not show any relationship between Os concentration and Al_2O_3. Given the correlation between indices of silicate melt depletion and $^{186}Os/^{188}Os$ observed in this study and the lack of evidence for widespread sulfide or modal metasomatism in any of the examined peridotite suites, it appears most likely that this correlation primarily reflects the effects of melt depletion on peridotite Pt/Os ratios rather than processes such as silicate melt or sulfide melt metasomatism.

Extrapolating the clinopyroxene Cr#-$^{186}Os/^{188}Os$ trend to PUM clinopyroxene Cr# composition of ~5 yields $^{186}Os/^{188}Os_{PUM}$ ≈0.1198380±22 (2 SD) (Figure 2.1). Similarly, extrapolation of $^{186}Os/^{188}Os$-fertility trends to i) PUM spinel Cr#, ii) PUM clinopyroxene Yb, and iii) PUM bulk rock Al_2O_3 yield indistinguishable $^{186}Os/^{188}Os$ estimates for the PUM of 0.1198379±21, 0.1198380±27 and 0.1198375±22 (2 SD) respectively (Figure 2.1). Taking a weighted average of the PUM $^{186}Os/^{188}Os$ estimated from correlation with whole rock Al_2O_3 and mineral major and trace elements, I inferred PUM $^{186}Os/^{188}Os$ to be 0.1198378±23 (2 SD). This estimate is slightly lower than H-chondrites (≈0.1198398±16; 2 SD), which is currently the best constraint on chondrite $^{186}Os/^{188}Os$ compositions (Brandon et al., 2006). Due to the shallow slope of the fertility-$^{186}Os/^{188}Os$ regressions, the uncertainties noted above in PUM major element composition have very little effect on the estimated $^{186}Os/^{188}Os$ of the PUM.

Meisel et al. (2001) utilized a similar approach to infer the $^{187}Os/^{188}Os$ of PUM using fertility-$^{187}Os/^{188}Os$ correlations in several suites of peridotites. Peridotite suites with different melt depletion ages define individual trends with distinct slopes, which

converge at the approximate PUM composition. The peridotites from this study appear to define a single broad trend between peridotite fertility and $^{186}Os/^{188}Os$. This likely reflects the fact that most of the peridotites I analyzed derive directly or indirectly from the convecting upper mantle. Only two samples (BELB 9-15 and CC-07-2-01) appear to derive from the Proterozoic SCLM beneath the RGR (Byerly and Lassiter, 2012). Future studies of Archean and Proterozoic SCLM xenolith suites may further refine the PUM $^{186}Os/^{188}Os$ and Pt/Os estimates presented here.

Using a $^{186}Os/^{188}Os_{solar\ system\ initial}$ of ~0.1198269±14 (2 SD) (Brandon et al., 2006), our estimated PUM $^{186}Os/^{188}Os$ ratio and the age of Earth (~4.567 Ga), I estimated the Pt/Os ratio of the PUM to be 1.7±0.2 (1 SD). The inferred Pt/Os_{PUM} is nearly identical with but slightly lower than several different chondrite classes [Figure 2.3; Carbonaceous ≈1.8±0.2; Ordinary ≈1.9±0.1; Enstatite ≈1.9±0.1 (1 SE); Horan et al., 2003; Brandon et al., 2006]. Inferred Pt/Os_{PUM} is also nearly identical to average Pt/Os ratios in relatively fertile (≥2 wt% Al_2O_3) continental peridotites but slightly lower than average Pt/Os ratios in fertile oceanic peridotites [Figures 2.2-2.3; Continental =1.83±0.1 (1 SE); Oceanic = 2.04 ±0.1(1 SE)]. In addition, the average measured $^{186}Os/^{188}Os$ in mantle peridotites [~0.1198364±6 (2 SD)] suggests a long-term average Pt/Os of the depleted upper mantle of ~1.5±0.1 (1 SE) (for an age of ~4.567 Ga). This value is significantly lower than those of most chondrites or fertile (> 2 wt% Al_2O_3) peridotites (Figure 2.3), but is consistent with measured Pt/Os ratios in many refractory peridotites [average ≈ 1.54±0.1 (1 SE); Data sources: Same as figure 2.2]

Both Pt/Os and Re/Os may be lowered in residual peridotites by melt extraction, although Re is more susceptible at low melt fractions due to the lower compatibility of Re in sulfides than Pt (cf. Fleet et al., 1996; Brenan, 2008). Therefore correlations between $^{187}Os/^{188}Os$ and $^{186}Os/^{188}Os$ are expected in residual peridotites, particularly in highly refractory samples that may have experienced sulfide exhaustion during melting. Peridotite $^{186}Os/^{188}Os$-$^{187}Os/^{188}Os$ ratios define a very weak, statistically insignificant correlation ($R \approx 0.07$). However, if all upper mantle materials for which ^{186}Os- and ^{187}Os-isotope data exist are included in the regression (e.g. chromitites, osmiridium alloys), the global $^{186}Os/^{188}Os$-$^{187}Os/^{188}Os$ correlation improves significantly ($R \approx 0.37$, statistical significance~99.6%) (Figure 2.4), although considerable scatter is still apparent. Radiogenic $^{187}Os/^{188}Os$ in plume-derived lavas from Hawaii have been suggested to reflect variable contributions of recycled oceanic lithosphere + sediments (cf. Lassiter and Hauri, 1998). Addition of recycled crustal materials should shift the $^{186}Os/^{188}Os$-$^{187}Os/^{188}Os$ trend in the direction opposite of the melt extraction trend to supra-chondritic $^{186}Os/^{188}Os$ and $^{187}Os/^{188}Os$ values. However, the slope of the mantle $^{186}Os/^{188}Os$-$^{187}Os/^{188}Os$ correlation is very shallow (solid black line in Figure 2.4), reflecting the relative insensitivity of Pt/Os ratios to modest degrees of melt extraction/addition. This trend does not pass through most Hawaiian and Gorgona lavas with elevated $^{186}Os/^{188}Os$ (cf. Brandon et al., 1999; Brandon et al., 2003; Ireland et al., 2011). This suggests the addition of recycled bulk crust to plume sources cannot explain the elevated $^{186}Os/^{188}Os$ values in some plume-derived lavas.

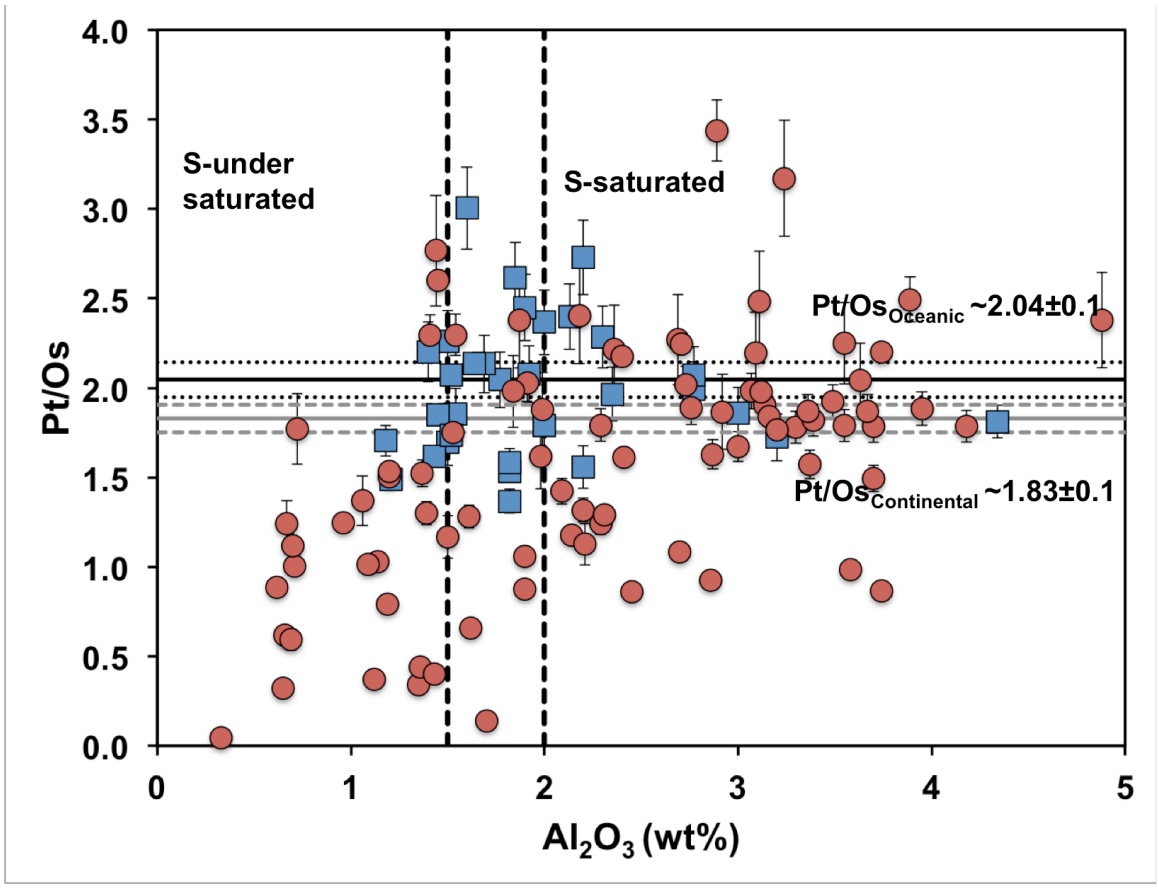

Figure 2.2: Global Pt/Os ratios and bulk rock Al_2O_3 in global compilation of peridotites.

Samples with >2 wt% Al_2O_3 show a flat trend with no clear correlation. However, samples with <1.5-2 wt% Al_2O_3 show a trend of decreasing Pt/Os with decreasing bulk rock Al_2O_3. The break in slope at ~1.5-2 wt.% may reflect a decrease in Pt compatibility following exhaustion of residual sulfides at high degrees of melt depletion. Average Pt/Os ratios of fertile (≥2 wt% Al_2O_3) peridotites are plotted for reference (Grey solid

line: average of continental peridotites; Grey dashed line: ±1 SE of average of continental peridotites; Black solid line: average of oceanic peridotites; Black dotted lines: ±1 SE of average of oceanic peridotites). Pt/Os uncertainties are reported as ±1 SE. Symbols: Continental xenoliths- red circles and oceanic peridotites- blue squares (see supplementary material for data sources).

Regression Statistics	$^{186}Os/^{188}Os$-Al_2O_3	$^{186}Os/^{188}Os$- spinel Cr#	$^{186}Os/^{188}Os$- clinopyroxene Cr#	$^{186}Os/^{188}Os$- clinopyroxene Yb
Slope	0.00000051(96)	-0.00000007(8)	-0.00000016(20)	0.0000013(23)
PUM Intercept	0.1198375(22)	0.1198379(21)	0.1198380(22)	0.1198378(27)
No of samples (n)	13	10	12	12
R	0.52	0.83	0.76	0.57
Statistical significance	93.2%	99.7%	99.6%	94.8%
MSWD	0.33	0.18	0.18	0.32

Table 2.2 Regression statistics using weighted errors of $^{186}Os/^{188}Os$-fertility correlations

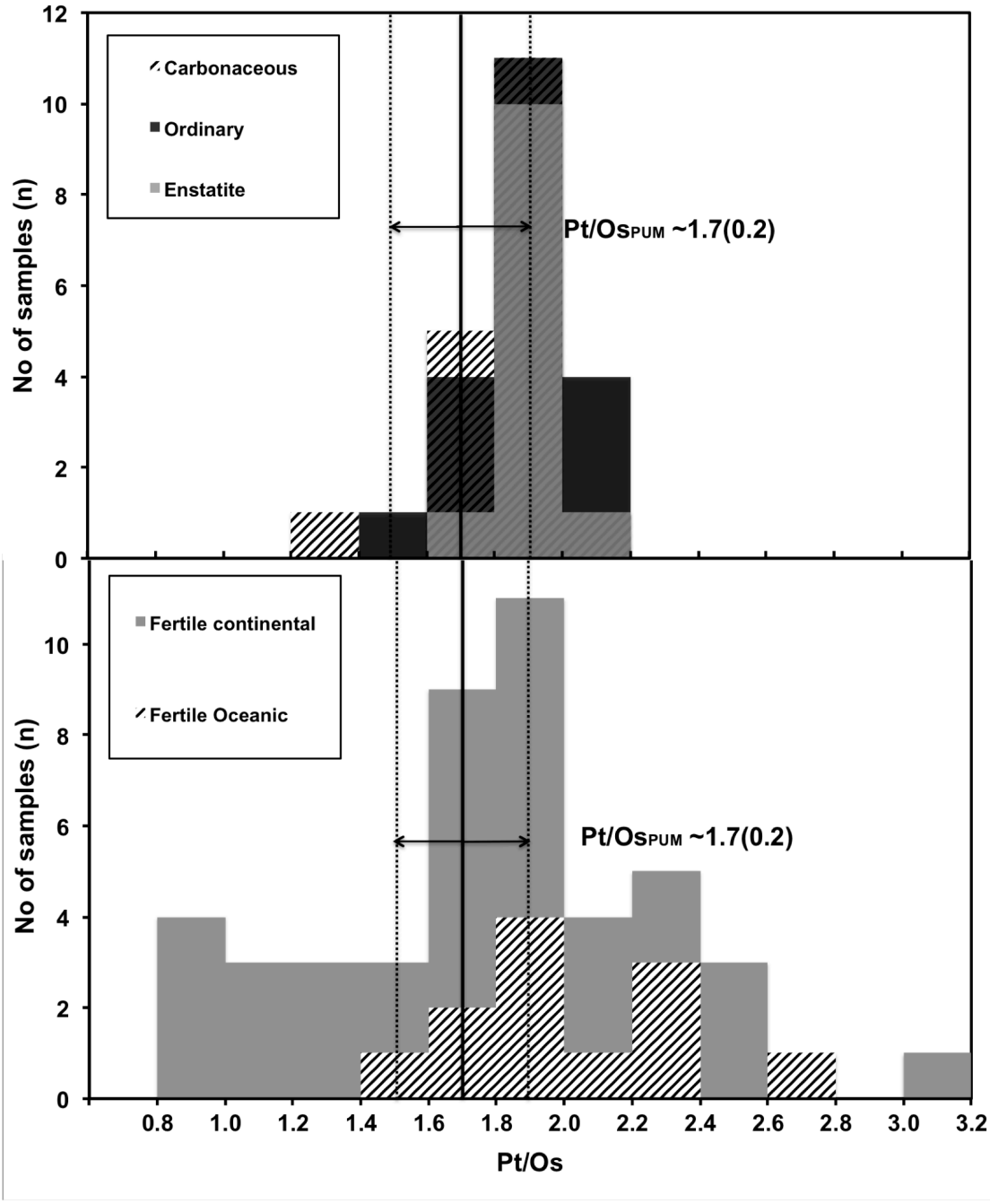

Figure 2.3 Comparison of Pt/Os reported for chondrite meteorites, fertile mantle peridotites (≥2 wt% Al_2O_3) and PUM estimate.

Chondrite data are from Horan et al. (2003) and Brandon et al. (2005). Data sources for peridotites are as in figure 2.2.

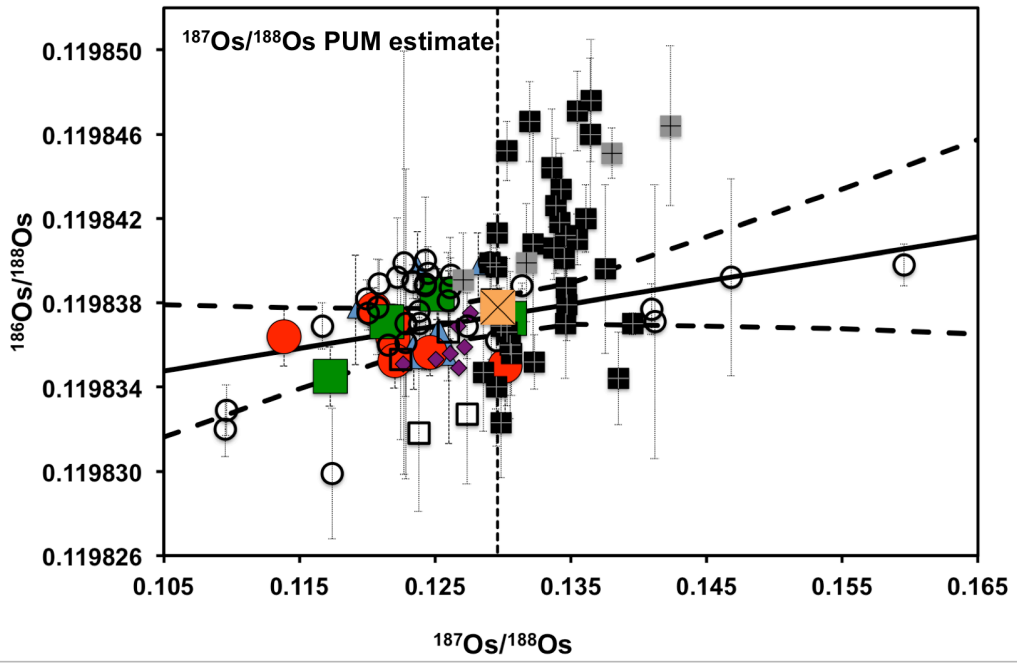

Figure 2.4 $^{186}Os/^{188}Os$ vs $^{187}Os/^{188}Os$ in upper mantle peridotites, Os-Ir alloys and chromitites.

Solid dashed line represents the linear regression through the $^{186}Os/^{188}Os$-$^{187}Os/^{188}Os$ data for upper mantle samples and dashed black curve is the 2 SD uncertainty in the regression. Dashed vertical line is the $^{187}Os/^{188}Os$ PUM estimate (Meisel et al., 2001). (Symbols: Peridotites- same as in figure 2.1; Os-Ir alloys- open circles; chromitites- open squares; Hawaiian picrites- black squares with gray crosses; Gorgona komatiites- grey squares with black crosses). Data: Kane fracture zone APs (Brandon et al., 2000), Os-Ir alloys (Walker et al., 2005; Brandon et al., 2006), chromitites (Brandon et al., 1998, 2006; Walker et al., 2005), Hawaiian lavas (Brandon et al., 1999; Ireland et al., 2011) and Gorgona komatiites (Brandon et al., 2003).

5.2 Are estimated primitive mantle PGE ratios consistent with the late veneer hypothesis?

Mantle HSE abundances are significantly higher than predicted from metal-silicate partition coefficients determined at low pressures and moderate temperatures (cf. Capobianco et al., 1993; Newsom et al., 1990) and mantle HSE ratios occur in broadly chondritic relative proportions. This has been generally taken as evidence for addition of a 'late veneer' of chondritic material following core formation (cf. Morgan, 1986). The late veneer hypothesis predicts that HSE ratios in the primitive mantle should be chondritic. Some estimated primitive mantle HSE ratios do appear to be chondritic based on both isotopic constraints on parent/daughter ratios [cf. Re/Os_{PUM} (Meisel et al., 2001); Pt/Os_{PUM} (this study; Brandon et al., 2006)] and extrapolation of elemental ratios in variably depleted peridotites to fertile compositions (cf. Becker et al., 2006). However, previous studies suggest that several other PUM HSE ratios depart significantly from chondritic values (PUM Ru/Ir_N ≈1.34 and PUM Pd/Ir_N ≈1.39, both normalized to Enstatite chondrites) (cf. Becker et al., 2006). The combination of chondritic and non-chondritic HSE ratios inferred for the PUM poses a challenge for the late veneer hypothesis.

One potential explanation is that estimates of PUM HSE ratios are in error due to pervasive metasomatic alteration of HSE abundances and ratios in mantle peridotites, which obscures mantle melting trends (e.g., Rehkampher et al., 1999, Lorand et al., 2009, 2010). Non-chondritic mantle HSE ratios (e.g. suprachondritic Pd/Ir and Ru/Ir) could reflect widespread melt-rock reaction and/or refertilization via addition of metasomatic

sulfides in peridotites (e.g., Rehkampher et al., 1999, Luguet et al., 2003; LeRoux et al., 2007; Ackerman et al., 2009; Lorand et al., 2009, 2010; vanAcken et al., 2010). However, although suprachondritic Pd/Ir in fertile peridotites could be generated via refertilization, it is more difficult to reconcile suprachondritic Ru/Ir by similar processes, because Ru/Ir ratios show relatively constant suprachondritic values over a wide range of bulk rock Al_2O_3 in the majority of peridotites (cf. Fischer-Godde et al., 2011; Becker et al., 2006).

Alternatively, some studies (cf. Fischer-Godde et al., 2011; Becker et al., 2006) propose that the elevated Pd/Ir and Ru/Ir in the PUM reflects admixture of a unique, largely unsampled meteoritic component during late veneer accretion. However, Ru/Ir and Pt/Ir ratios in different chondrite classes define a positive correlation that does not intersect with the PUM ratios (Figure 2.5). Any meteorite component that could produce the inferred PUM Pt/Ir and Ru/Ir ratios would therefore fall off the trend defined by most chondrites, which seems unlikely. Therefore, in the discussion below I evaluate whether processes such as minor metal or sulfide segregation concurrent with chondritic late veneer addition could explain mantle HSE abundances and ratios without requiring appeal to additional exotic components.

The 'late veneer' component was likely delivered by multiple impactors of variable sizes and composition that included both differentiated and undifferentiated bodies (cf. Rubie et al., 2011). For larger differentiated bodies, part of the impactor cores could have remained intact and scavenged HSE from Earth's mantle during segregation to the core. This could potentially result in modest fractionation of HSE ratios while still producing

an overall elevation of HSE abundance during late veneer addition. HSE segregation concurrent with the late veneer could also have occurred by the removal of sulphides to the Earth's core. Some studies have proposed late stage separation of sulphides following metal core segregation to explain the Pb and Tl isotopic composition of the BSE (cf. Wood et al., 2008). An increase in oxygen fugacity during late stage accretion would have helped stabilize sulphides in the Earth's mantle (cf. Wade and Wood, 2005). Cooling and crystallization of magma bodies after regional or global melting events caused by large impacts could have resulted in segregation of immiscible sulfide melts, producing minor PGE fractionation due to the strongly chalcophile behavior of these elements.

The effects of minor metal or sulfide segregation concurrent with late veneer addition is mathematically analogous to the effects of coupled assimilation and fractional crystallization in evolving magma bodies (DePaolo, 1981). In order to examine the potential for these processes to simultaneously generate elevated PGE abundances with non-chondritic PGE ratios, I modeled core segregation coupled with late veneer addition for a range of impactor addition/core segregation ratios, using the mathematical formulation of DePaolo (1981). For illustrative purposes, I utilized average metal-silicate K_D values measured at ~2578 K and ~18 GPa from Mann et al. (2012). Because K_D values vary significantly as a function of temperature, pressure, and oxygen fugacity, there is considerable uncertainty regarding the K_D values that would correspond to the processes modeled here.

Representative model results are shown in figure 2.6. Mantle HSE abundances and ratios were calculated for varying ratios of metal or sulfide segregation to late veneer addition. In the absence of accompanying core segregation, late veneer addition quickly generates chondritic HSE ratios, inconsistent with the observed elevated Pd/Ir and Ru/Ir ratios in the mantle (Figure 2.6). However, concurrent core segregation results in fractionated HSE ratios, with the degree of fractionation increasing as the ratio of core segregation to late veneer addition increases. For example, if the metal-silicate partition coefficients for Ru and Pd are lower than for Ir, metal segregation will increase mantle Ru/Ir and Pd/Ir ratios. Several experimental studies (cf. Mann et al., 2012 and references therein) have shown that metal-silicate K_D values for Ru and Pd are consistently lower than for Ir over wide ranges of temperature, pressure, and oxygen fugacity. Therefore, metal segregation coupled to late veneer addition is expected to result in an increase in Pd/Ir and Ru/Ir ratios in the mantle relative to chondritic values. Using the metal-silicate K_D values from Mann et al. (2012), mantle HSE abundances and ratios can be simultaneously satisfied by addition of ~0.6 to ~1% late veneer with concurrent metal segregation for a metal/late veneer ratio of ~1.9×10^{-6} (Figure 2.6a).

Sulphide segregation can also fractionate mantle HSE ratios relative to chondritic abundances. As with metal-silicate K_Ds, sulphide-silicate K_D values vary as functions of temperature, pressure, and oxygen fugacity. However, few studies have examined the high-pressure partitioning of HSE in sulfides. I utilized the average sulphide-silicate K_D values of Fleet et al. (1996) because these experiments were conducted at relatively oxidizing conditions (ΔQFM~-1). However, these experiments were measured at

pressures lower than are likely relevant for late-stage sulfide segregation. Future experiments are required to examine the effects of pressure on sulphide-silcate K_D. Using the sulphide-silicate K_D values of Fleet et al. (1996), mantle HSE abundances and ratios can be simultaneously satisfied by addition of ~0.9 to ~1.2% late veneer with concurrent sulphide segregation for a sulphide/late veneer ratio of ~1.7 x 10^{-3} (Figure 2.6b).

The models presented above likely oversimplify the processes involved in late veneer accretion. For example, if late-stage metal segregation occurred due to the partial preservation of sinking impactor cores, then the assumption that these cores would equilibrate with the entire mantle is unlikely. In addition, large uncertainties exist regarding the temperature, pressure, or oxygen fugacity appropriate for modeling late-stage metal or sulfide segregation. This results in significant uncertainty in metal-silicate and sulfide-silicate K_D and in the resultant HSE fractionation patterns. Nonetheless, any late-stage metal or sulfide segregation during or following late veneer addition is expected to fractionate HSE ratios. Therefore, the existence of modestly non-chondritic HSE ratios (e.g., Pd/Ir and Ru/Ir) in the mantle does not require accretion of non-chondritic meteoritic components as suggested by earlier studies (cf. Becker et al., 2006).

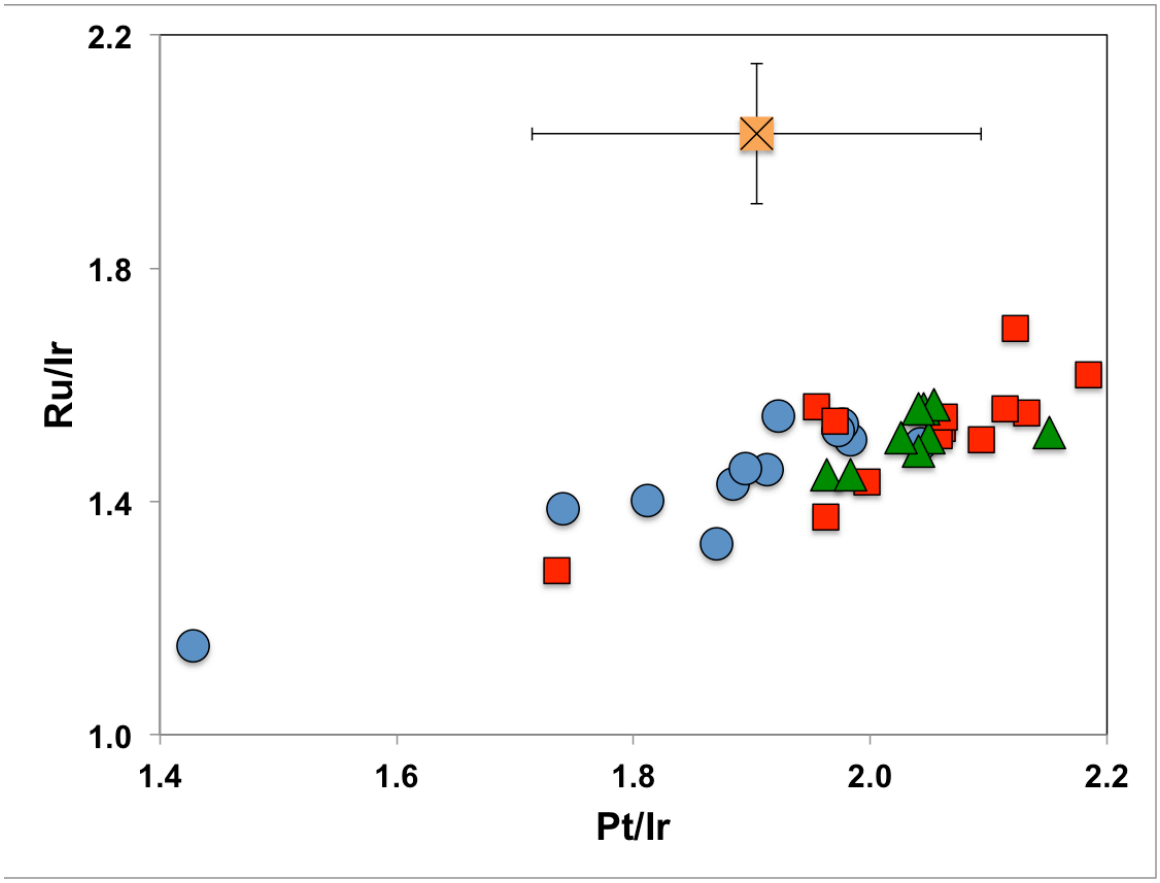

Figure 2.5 Comparison of Ru/Ir versus Pt/Ir reported for chondrite meteorites and PUM estimate

Symbols are carbonaceous chondrites-blue circle, Ordinary chondrites- red squares, Enstatite chondrite- green triangles, PUM- orange square with cross [Pt/Os-this study, Ru/Ir- Becker et al. (2006)]. Data source for chondrites are same as in figure 2.3.

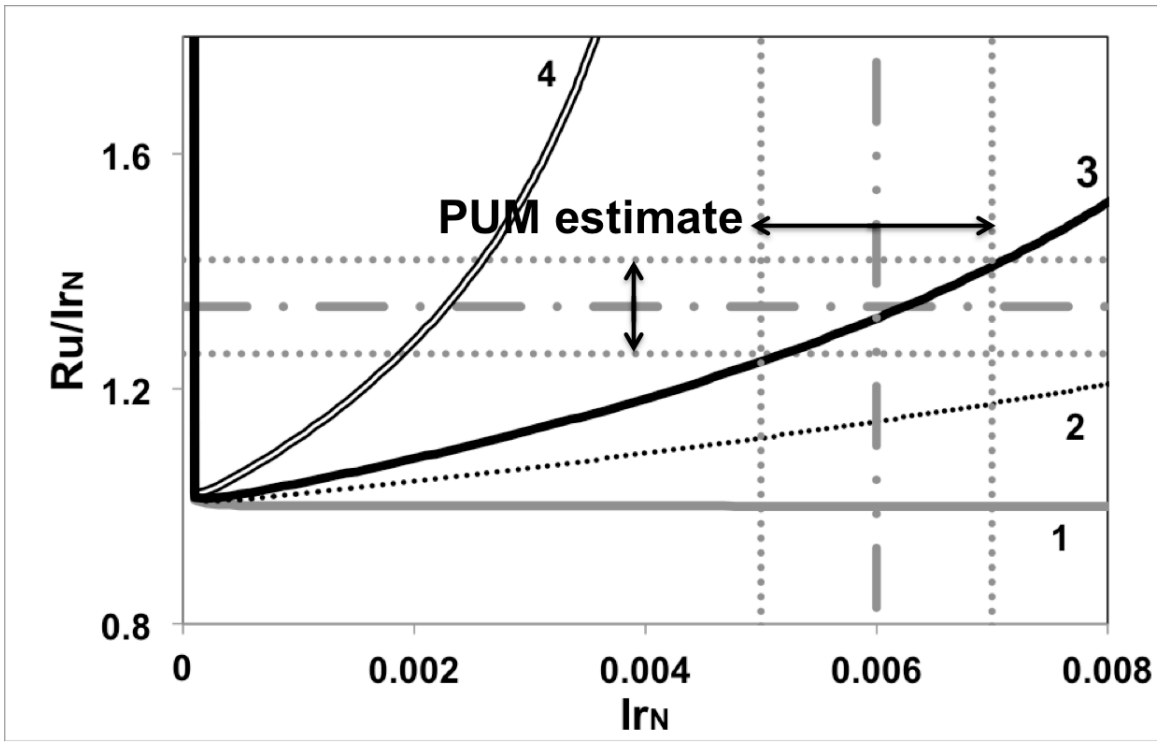

Figure 2.6a Model effects of late veneer addition on mantle Ir concentration and Ru/Ir ratios (normalized to Enstatite chondrites) assuming concurrent metal segregation.

Model 1 (solid grey) shows the effect of addition of a late veneer without concurrent core segregation. Model 2 (dotted black), 3 (solid black) and 4 (black band) shows the effect of increasing metal core segregation accompanying late veneer addition where metal/late veneer ratios are ~1 x 10-6, ~1.9 x 10-6 and ~5 x 10-6, respectively. Model 3 shows that both mantle Ir abundance and the Ru/Ir ratio could be satisfied by metal core segregation concurrent with the addition of ~0.6 to ~1% late veneer addition. Average metal-silicate KD values measured at ~2578 K and ~18 GPa were utilized and were: Ru= 2.7 x 106 and Ir= 4.3 x 107. (Data: PUM estimates from Becker et al. (2006); Enstatite chondrite- Horan et al. (2003); Metal-silicate KD values- Mann et al. (2012)]

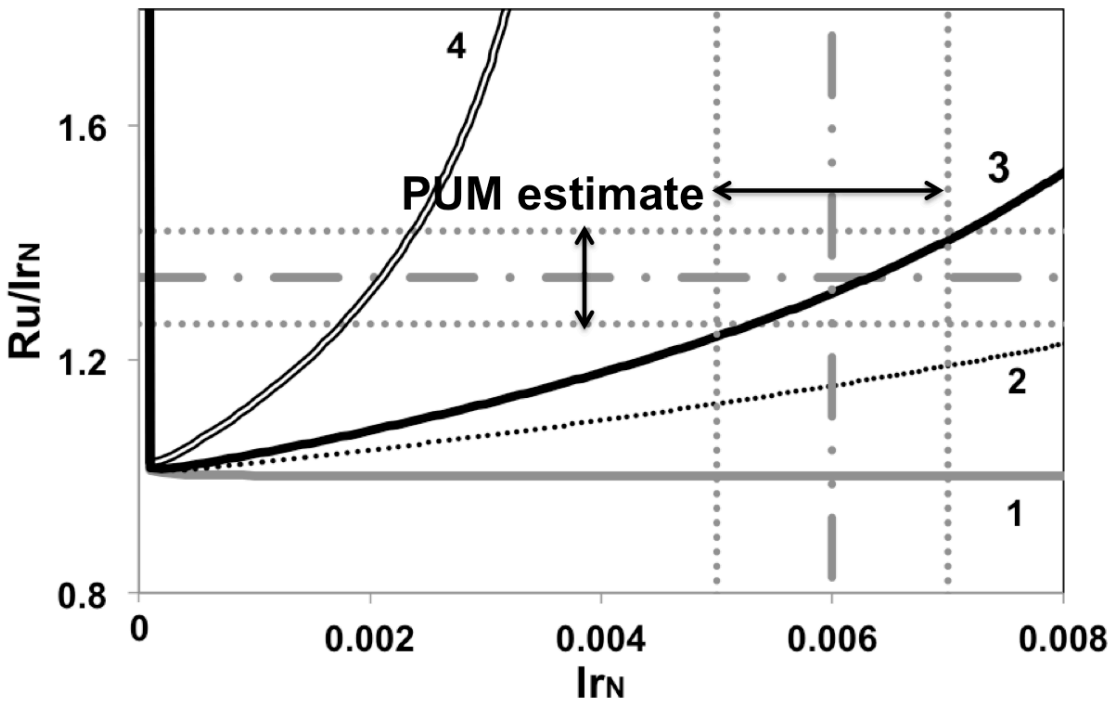

Figure 2.6b Model effects of late veneer addition on mantle Ir concentration and Ru/Ir ratios (normalized to Enstatite chondrites) assuming concurrent sulfide segregation.

Model 1 (solid grey) shows the effect of addition of a late veneer without any concurrent core segregation. Model 2 (dotted black), 3 (solid black) and 4 (black band) shows the effect of increasing sulfide core segregation accompanying late veneer addition where sulfide/late veneer ratios are ~1 x 10^{-3}, ~1.7 x 10^{-3} and ~5 x 10^{-3}, respectively. Model 3 shows that both mantle Ir abundance and the Ru/Ir ratio could be satisfied by sulfide core segregation concurrent with the addition of ~0.8 to ~1.2% late veneer addition. Average sulfide-silicate K_D values measured at ~1500 K, 1 bar pressure and at a oxygen fugacity of ~QFM-1 were utilized and were: Ru= 1.1 x 10^4 and Ir= 5.2 x 10^4. (Data: PUM estimates from Becker et al. (2006); Enstatite chondrite- Horan et al. (2003); Sulfide-silicate K_D values- Fleet et al. (1996)]

5.3 Constraints on homogenization timescales for mantle heterogeneities in the convective upper mantle

The Earth's convecting upper mantle is chemically and isotopically heterogeneous over a range of length scales (e.g. Hart, 1984). This is reflected in highly variable major element, trace element and isotopic compositions of oceanic peridotites (APs and ocean island xenoliths) and MORB, which are believed to sample the convecting upper mantle. Several geologic processes such as partial melting (e.g. Frey and Green, 1974), subduction of sediments and oceanic lithosphere (e.g. Hofmann and White, 1982), and delamination of continental lithosphere (e.g. Bird, 1979) generate chemical heterogeneity in the Earth's convecting mantle (Hofmann, 1997). Other geologic processes including melt-infiltration (e.g. Schiano and Bourdon, 1999), metasomatism (e.g. Harte, 1983), and re-fertilization (e.g. van-Acken et al., 2010) can both create chemical heterogeneity and dampen existing isotopic heterogeneities through isotopic homogenization and resetting. In addition, convective mixing eventually reduces heterogeneity length scales sufficiently for solid-state diffusion to re-homogenize heterogeneities (cf. Kellogg and Turcotte, 1987, 1990). The degree of isotopic heterogeneity in the mantle provides constraints on the timescales over which variations in parent/daughter ratios are preserved in distinct pockets of mantle, which in turn is related to convective vigor and the extent of melt and fluid percolation through the mantle. Different isotopic systems may indicate different homogenization timescales due to their different sensitivities to mechanical mixing relative to melt-infiltration/percolation.

The range of radiogenic isotope variation in mantle peridotites is a function of the degree of variability in parent/daughter ratios and the timescales over which these heterogeneities are destroyed. This is illustrated by the following equation:

$$\Delta I = \Delta R \times (e^{\lambda t} - 1) \quad (1)$$

where t = homogenization timescale, ΔR represents the degree of parent/daughter heterogeneity and ΔI represents the radiogenic isotope variability. Different isotopic systems such as $^{143}Nd/^{144}Nd$, $^{176}Hf/^{177}Hf$, $^{187}Os/^{188}Os$ and $^{186}Os/^{188}Os$ can be utilized to estimate homogenization timescales. Because the parent and daughter elements of the Nd and Hf isotopic systems are incompatible during partial melting, these systems are likely to be sensitive to melt/fluid percolation within the convecting mantle. In contrast, because Os is compatible during partial melting and Re and Pt are only moderately incompatible, Os isotopic systems are less sensitive to the effects of melt percolation and metasomatism relative to other long lived radiogenic systems and can therefore better constrain timescales of mechanical mixing. In the following discussion, I evaluate chemical and isotopic heterogeneity in oceanic peridotites to estimate timescales of mechanical mixing and homogenization in the convecting upper mantle.

I utilized $^{186}Os/^{188}Os$ data measured in this study and previously published $^{187}Os/^{188}Os$, Re/Os and Pt/Os data for oceanic peridotites for constraining homogenization timescales (see data sources in supplementary materials for references). Previous studies have suggested that samples with unusually low Os concentrations are likely affected by high degrees of melt-rock reaction and/or weathering and alteration (cf. Handler et al., 1999). Therefore, I restricted our analysis to samples with >1ppb Os (cf. Lassiter et al., 2014).

For the $^{187}Os/^{188}Os$ and Re/Os database, a few samples have unusually high Re/Os and/or $^{187}Os/^{188}Os$ ratios (e.g. $^{187}Os/^{188}Os$> 0.135; Re/Os>0.2). Because these analyses are unlikely to represent typical convecting upper mantle and enhance the population variability beyond what is generally observed in oceanic peridotites, I removed all samples that were $\geq 2\sigma$ outliers from the mean of the Re/Os and $^{187}Os/^{188}Os$ populations. Upper mantle peridotites display very limited $^{186}Os/^{188}Os$ variations (~19 ppm 2 SD). However, Pt/Os ratios span a wide range, from ~0.1 to 4.6 with an average value of ~1.4 and 2 SD of $\pm$1.6, which translates to $^{190}Pt/^{188}Os$ variability of $\pm$0.0015 (2 SD). Utilizing equation 1 above, I calculate the homogenization timescale for Pt/Os and ^{186}Os isotopic heterogeneities in the convecting upper mantle to be ~1 Gyr (Figure 2.7). Upper mantle peridotite $^{187}Os/^{188}Os$ and Re/Os ratios show 2 SD variability of ~$\pm$0.006 and $\pm$0.06 respectively (~$\pm$0.3 for $^{187}Re/^{188}Os$). This constrains the homogenization timescale for Re/Os and $^{187}Os/^{188}Os$ heterogeneities to be ~1.3 Gyr (Figure 2.7). Thus, Os isotopic compositions in peridotites suggest an average homogenization timescale of ~1.2 Gyr for the convecting upper mantle. Because Os isotopic systems are relatively insusceptible to the effects of melt percolation and metasomatism, this timescale likely reflects the time required for convective mixing to reduce heterogeneity length scales sufficiently for solid-state diffusion to homogenize them. Note that, although Os-isotopes in mantle peridotites are relatively insensitive to metasomatism or melt/mantle interaction, the poor correlation between Re/Os and melt depletion indices in many peridotites may reflect recent modification of Re/Os ratios by these processes. Recent generation of parent/daughter heterogeneity through these processes would result in underestimation of

mantle mixing timescales. Therefore, the mixing timescales estimated from $^{187}Os/^{188}Os$ and $^{186}Os/^{188}Os$ heterogeneity in oceanic mantle peridotites likely represent a lower bound on the mixing timescale.

Other radiogenic isotopic systems such as $^{143}Nd/^{144}Nd$ and $^{176}Hf/^{177}Hf$ are more easily disturbed by melt infiltration and/or metasomatism during melt generation at MOR or subduction zones. Although these processes can generate parent/daughter heterogeneity, they can also reduce heterogeneity by re-fertilizing previously melt-depleted domains in the convecting upper mantle. I utilized existing $^{143}Nd/^{144}Nd$ and $^{176}Hf/^{177}Hf$, and Sm/Nd and Lu/Hf data from a global compilation of oceanic peridotites (see data sources in supplementary materials for references). Isotopic variations in $^{143}Nd/^{144}Nd$ and $^{176}Hf/^{177}Hf$ in these peridotites are $\pm$0.0003 and $\pm$0.0013 (2 SD), respectively. Variations in Sm/Nd and Lu/Hf ratios from the same dataset are $\pm$1.3 and $\pm$1.1 (2 SD), respectively, which translate to $^{147}Sm/^{144}Nd$ and $^{176}Lu/^{177}Hf$ variations of $\pm$0.76 and $\pm$0.16 (2 SD). This results in calculated homogenization timescales of ~0.1 and ~0.4 Gyr for Nd and Hf isotopic heterogeneities in the mantle. Previous studies (cf. Stracke et al., 2011) have reported decoupling of Hf and Nd isotopes in residual peridotites. This decoupling has been attributed to the greater susceptibility of Nd isotopes to melt-rock reaction, which is consistent with the lower inferred homogenization timescale of Nd isotopes relative to Hf isotopes reported here. Both of these estimates are significantly younger than the homogenization timescale suggested by Os isotopes, which is likely due to the greater susceptibility of Nd and Hf to resetting by melt-rock interaction. Therefore,

homogenization timescales constrained by Os isotopes are likely to more accurately represent timescales for mechanical mixing by convective stirring in the upper mantle.

An outstanding debate on the nature of mantle convection is whether it occurs as a single layer involving the whole mantle or whether it is divided into two layers at the 660 km discontinuity (cf. Davies and Richards, 1992). Geodynamic studies (cf. Kellogg and Turcotte, 1987, 1990) have examined how large scale folding and stretching within the convecting mantle can deform and thin several-km-sized heterogeneities (comparable to the length-scale of subducted oceanic crust) to centimeter length scales required for solid-state diffusion to homogenize them. Numerical models show that heterogeneities with an initial size of 6 km are homogenized over timescales of ~240 Myr for layered mantle convection, but this timescale increases to the order of ~1 Gyr for whole mantle convection (Kellogg and Turcotte, 1990). Our estimates for the timescales of convective mixing are therefore consistent with predicted homogenization timescales required for whole-mantle convection.

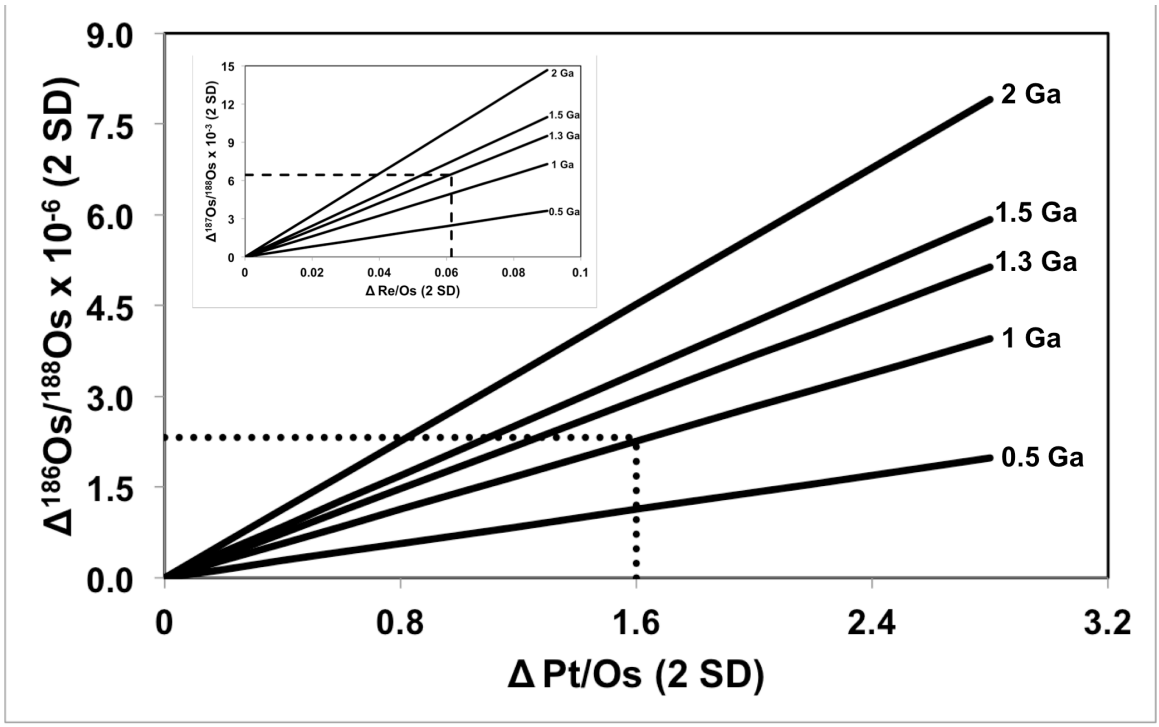

Figure 2.7 $^{186}Os/^{188}Os$ isotopic variability versus variability in Pt/Os ratios.

Solid lines represent timescales required to generate $\Delta^{186}Os/^{188}Os$ ($\Delta^{187}Os/^{188}Os$ in insert panel) variability for a given ΔPt/Os (ΔRe/Os in insert panel) variability. Horizontal dotted line shows the observed $^{186}Os/^{188}Os$ isotopic variation in global peridotites (2 SD) and the vertical dotted line shows the observed Pt/Os variability (2 SD). Observed isotopic and parent/daughter variability indicate a homogenization timescale of ~1 Gyr. Insert panel shows $^{187}Os/^{188}Os$ isotopic variability versus variability in Re/Os ratios. Observed isotopic and parent/daughter variability for the ^{187}Re-^{187}Os system indicate a homogenization timescale of ~1.3 Gyr.

6. CONCLUSIONS

$^{186}Os/^{188}Os$ ratios in variably melt-depleted peridotites from continental (Rio Grande Rift and Colorado Plateau) and oceanic (Lena Trough and Hawaiian Islands) settings correlate with various indices of peridotite fertility. This suggests that melt depletion largely controls $^{186}Os/^{188}Os$ variations in the upper mantle. Extrapolation of $^{186}Os/^{188}Os$-fertility trends to PUM compositions suggests a mean PUM $^{186}Os/^{188}Os$ of 0.1198378±23 (2 SD), which is slightly lower than H-chondrites [≈0.1198398±16 (2 SD); Brandon et al. (2006)]. This estimate is considerably lower than $^{186}Os/^{188}Os$ observed in some plume-derived lavas from Hawaii and Gorgona [up to 0.1198481; cf. Brandon et al. (1999, 2003); Ireland et al. (2011)] suggesting that partial melting of fertile mantle cannot explain high $^{186}Os/^{188}Os$ values in these lavas. Our estimated PUM Pt/Os ratio of ~1.7±0.2 is consistent with average Pt/Os ratios of fertile peridotites, and overlaps with Pt/Os ratios of various chondrite classes.

Mantle HSE ratios for some HSE pairs (e.g., Re/Os, Pt/Os) are chondritic. In contrast, other HSE ratios (e.g., Pd/Ir, Ru/Ir) are significantly suprachondritic. Addition of a late veneer alone cannot explain both chondritic and suprachondritic HSE ratios. Instead, addition of a late veneer occurring concurrently with either minor metal or sulfide segregation can modestly fractionate HSE ratios without severely depleting HSE abundances in the mantle.

Variability in Os isotopic ($^{186}Os/^{188}Os$, $^{187}Os/^{188}Os$) and respective parent/daughter ratios (Pt/Os, Re/Os) in peridotites constrain the timescale required for homogenization

of chemical heterogeneities by convective stirring in the Earth's mantle to be of the order of ~1.2 Gyr. In contrast, combined Nd-Hf isotopic and Sm/Nd and Lu/Hf ratios in peridotites indicate significantly shorter mixing timescales (<0.4 Gyr) and likely reflecting resetting by melt-rock reaction/metasomatism. Because Os isotopes have a much lower susceptibility to melt-rock reaction relative to Nd-Hf isotopes, homogenization timescales inferred from Os isotopes likely more accurately reflect timescales of mechanical mixing in the convecting mantle. These timescales are consistent with homogenization timescales predicted for whole mantle convection.

Acknowledgements

This work was supported by NSF Grant EAR-1321937 and by the Jackson School of Geosciences, University of Texas at Austin. This manuscript benefitted from constructive comments by Laurie Reisberg, an anonymous reviewer and editor Catherine Chauvel as well as comments by Graham Pearson on an earlier draft.

Chapter 3: $^{187}Os/^{188}Os$-$^{186}Os/^{188}Os$ isotopic variations in steels: Constraints on the Os-isotope compositions and Pt-Re-Os evolution of the iron ore, coal, and chromitite deposits used in steel manufacture

ABSTRACT

The isotopic compositions of steels should reflect the primary components used in steel manufacture, namely iron ore, chromitite, and coal. Chromium used in steels is derived from chromitites, which have high average Os concentrations and upper-mantle-like $^{187}Os/^{188}Os$ ratios. Most iron ores are derived from Precambrian Banded Iron Formations (BIF) or their weathered residues. Both iron ores and coal have low Os concentrations and radiogenic present-day and initial $^{187}Os/^{188}Os$ values consistent with Os derivation from crustal weathering processes. Osmium concentrations in steel span a wide range, from 0.03 to 22 ppb. $^{187}Os/^{188}Os$ ranges from upper mantle-like values to highly radiogenic values (~0.1435 to 4.118). Os concentrations in steel are positively correlated with Cr content and negatively correlated with $^{187}Os/^{188}Os$. These correlations are consistent with mixing of unradiogenic Os derived from chromitites and radiogenic Os derived from iron ores and coal. Model mixing trends between chromitites, iron ores, and coal can reproduce the observed concentration and isotopic variations in steels, consistent with Os conservation during smelting processes.

$^{187}Os/^{188}Os$-$^{186}Os/^{188}Os$ variations in steel can provide constraints on the $^{186}Os/^{188}Os$ compositions of the different end members used in steel manufacture. High Re/Os and Pt/Os ratios in bulk UCC should result in radiogenic $^{187}Os/^{188}Os$ and $^{186}Os/^{188}Os$ in most crust-derived materials. Although steels have $^{187}Os/^{188}Os$ values that span a wide range

and extend to highly radiogenic, crust-like values, $^{186}Os/^{188}Os$ is not correlated with $^{187}Os/^{188}Os$. $^{186}Os/^{188}Os$ values range from 0.1198304 to 0.1198391 and are indistinguishable from the average present-day upper mantle (Chatterjee and Lassiter, 2016). Extrapolation of $^{187}Os/^{188}Os$-$^{186}Os/^{188}Os$ trends to the estimated $^{187}Os/^{188}Os$ of chromitites yields a $^{186}Os/^{188}Os$ value of 0.1198339±15, consistent with values previously reported for chromitites (Walker et al., 2005; Brandon et al., 1998) but slightly lower than present-day average upper mantle (Chatterjee and Lassiter, 2016). This is consistent with derivation of chromitites from mantle sources during Archean to Proterozoic and subsequent evolution with sub-chondritic Pt/Os ratios. Extrapolation of steel $^{187}Os/^{188}Os$-$^{186}Os/^{188}Os$ trends to $^{187}Os/^{188}Os$ values typical for banded iron formations and coal yields a $^{186}Os/^{188}Os$ value of 0.1198352±20, which is also indistinguishable from present-day upper mantle and within uncertainty of the PUM at the time of BIF and/or coal formation. However, the $^{186}Os/^{188}Os$ values inferred for these components are systematically lower than bulk upper continental crust (UCC). Previous studies (McDaniel et al., 2004) also report similar unradiogenic (in comparison to upper continental crust) $^{186}Os/^{188}Os$ values for seawater derived marine Mn-nodules and black shales. Preferential weathering of crustal sulfides with low Pt/Os ratios and lower $^{186}Os/^{188}Os$ values than bulk UCC can explain the systematically lower $^{186}Os/^{188}Os$ values in crustal weathering products relative to bulk UCC.

1. INTRODUCTION

The origin of continental crust is a matter of considerable debate. Different models of crust formation include island arc accretion (e.g. Card, 1990; de Wit et al., 1992; Moyen et al., 2006; Percival, 2007) and accretion of oceanic plateaus generated by mantle plumes (e.g., Van Kranendonk et al., 2007). Average continental crust has higher silica content than most mantle-derived melts. This may reflect direct melting of oceanic crust during subduction (e.g. Drummond and Defant, 1990; Martin, 1994), intra-crustal differentiation and delamination of lower, mafic crust (cf. Rudnick et al., 1995), or chemical weathering and preferential recycling of Fe and Mg rich sediments into the mantle (e.g. Lee et al., 2008; Albarade, 1998). The composition of continental crust provides important clues regarding the relative importance of these processes. For example, trace element patterns in the continental crust resemble island arc lavas, suggesting an important role for subduction zone processes in its generation (cf. Kelemen, 1995). Similarly, high $\delta^{18}O$ values in most continental crustal rocks highlight the importance of chemical weathering and recycling of weathered sediments in crust generation (e.g. Muehlenbachs, 1998).

Because the surface of the Earth has a much higher oxygen fugacity than Earth's interior, one way of evaluating the relative importance of magmatic versus weathering processes in the generation of continental crust is through examination of elements sensitive to redox processes, such as the transition metals and the Platinum Group Elements (PGE). Most continental crustal rocks are characterized by high PPGE and Re to IPGE ratios (PPGE: Platinum-PGE; Pt, Pd, Rh; IPGE: Iridum-PGE; Ir, Os, Ru) (cf.

Wedepohl et al., 1995, Puecker Ehrenbrink et al., 2001; Park et al., 2012). This is consistent with the greater incompatibility of the PPGE relative to IPGE during partial melting (cf. Day et al., 2013). High Re/Os and Pt/Os in many crustal rocks (Re/Os up to ~400; Pt/Os up to ~100; cf. Puecker-Ehrenbrink and Jahn, 2001; Baioumy et al., 2011; McDaniel et al., 2004; Gao et al., 1998; Ravizza and Pyle, 1997; Wedepohl; 1995) result in the evolution of radiogenic $^{187}Os/^{188}Os$ and $^{186}Os/^{188}Os$ over time through the decay of ^{187}Re and ^{190}Pt. These radiogenic compositions are observed in many crustal rocks (Puecker Ehrenbrink et al., 2001; Hattori et al., 2003; McDaniel et al., 2004).

Many studies have used sediments and sedimentary rocks derived from chemical and physical weathering such as shales and loess to estimate the average composition of upper continental crust (e.g., Taylor and McLennan, 1985; Gao et al., 1998; Gallet et al., 1998; Jahn et al., 2001; Hu and Gao, 2008). The average upper crust compositions estimated from shales and from loess are very similar in most respects (e.g. Rudnick and Gao, 2003). The composition of seawater is also strongly influenced by the input of soluble components derived from continental weathering, as reflected in the radiogenic $^{87}Sr/^{86}Sr$ and $^{187}Os/^{188}Os$ of seawater (e.g. Veizer, 1989; Ravizza, 1993; Puecker-Ehrenbrink et al., 1995). In contrast, $^{186}Os/^{188}Os$ inferred for seawater from measurement of marine Mn nodules is not significantly elevated above mantle values, as would be predicted from the elevated Pt/Os and $^{186}Os/^{188}Os$ of average continental crust (McDaniel et al., 2004). Black shales also have unradiogenic to slightly radiogenic $^{186}Os/^{188}Os$ despite having highly elevated continental-crust-like $^{187}Os/^{188}Os$ (McDaniel et al., 2004). This suggests that continental weathering processes preferentially mobilize Os derived

from low Pt/Os components (cf. Puecker–Ehrenbrink and Jahn, 2001; McDaniel et al., 2004). However, the present dataset for $^{186}Os/^{188}Os$ in weathered crustal materials is extremely limited (cf. McDaniel et al., 2004) and it is unclear whether the low Pt/Os signature for weathered continental sediments inferred from black shales is representative. Examination of $^{186}Os/^{188}Os$ and $^{187}Os/^{188}Os$ in additional crustal materials derived from continental weathering would place constraints on the long-term Pt/Os and Re/Os ratios in their crustal sources and provide additional constraints on how PGE are fractionated during weathering, erosion and transport.

Industrial steels provide an indirect way of examining crustal materials derived from weathering of continental crust. The primary components utilized in steel manufacturing include iron ore and coal (in the form of coke). Iron ores worldwide are primarily derived from Banded Iron Formations (BIFs) (Povermo, 1999), which are believed to have originated from the oxidation and precipitation of Fe^{3+} from reduced seawater (e.g. Frei et al., 2007; Poulton e al., 2010). Because Os in seawater is largely derived from the weathering of continental crust in addition to a smaller input from hydrothermal alteration of oceanic crust and from cosmic sources (e.g. Esser and Turekian, 1988, 1993; Puecker-Ehrenbrink et al., 1995), iron ores obtained from BIFs can provide constraints on the $^{187}Os/^{188}Os$ and $^{186}Os/^{188}Os$ of the weathering products of the continental crust and therefore the time-integrated Re/Os and Pt/Os of their crustal sources. Similarly, coals are formed by the burial and degradation of biotic material in terrigenous environments and can similarly provide constraints on the Pt/Os and Re/Os ratios of crustal weathering products.

In this chapter, I examine Os and Pb concentrations and isotope variations in common industrial steels spanning a wide range in composition. Os concentrations and Os and Pb isotope compositions in steels are used to examine whether the observed isotope variations can be explained by mixing between the primary components used in steel manufacture. $^{187}Os/^{188}Os$-$^{186}Os/^{188}Os$ trends place constraints on the $^{186}Os/^{188}Os$ composition of the crustal (iron ore+coke) and mantle (chromitite) end members in steel. The inferred $^{186}Os/^{188}Os$ of iron ores and coke are compared with existing data from black shales, seawater, freshwater Mn nodules and loess (cf. McDaniel et al., 2004; Puecker-Ehrenbrink and Jahn, 2001). Possible mechanisms to account for the systematically different Pt-Os evolutionary histories of shales and seawater relative to most crustal materials are explored.

2. SAMPLES AND ANALYTICAL METHODS:

Common industrial steels were selected that span a wide range of composition (e.g. Fe ranges from 64-98 wt.%; Cr ranges from 0-22 wt.%). Samples were ordered from McMaster Carr and Speedy metals (specific lot # available upon request). The majority of the steels were manufactured outside the United States, although the country of origin for some samples could not be determined (*Personal Comm,* McMaster Carr and Speedy metals; Table 3.1).

Steel rods were cut into mm-sized shavings for chemical analyses. Major and trace element compositions were analyzed via solution mode ICP-MS at UT Austin using an *Agilent* 7500ce quadrupole. Steel shavings were dissolved in a $HCl:HNO_3$ solution and

were diluted in 2% HNO_3 before analysis. NIST SRM-1643e was used as a secondary standard. Average analyses of the NIST-SRM 1643e for Fe, Cr, Mn, Ni, and Mo were accurate to better than ~5% of the accepted values (Butler et al., 2009; Table C.1). Duplicate analyses were reproducible to within 3% (2 SD) (Table C.1). C and S concentrations could not be determined using solution mode ICP-MS and were estimated by subtracting the cumulative weight % of all major elements from 100.

Pb isotopic compositions were determined by digesting ~1 g of steel shavings in HF: HNO_3 solution. Prior to digestion, steel shavings were cleaned of surficial oil contamination by thorough rinsing and ultrasonification in acetone followed by ultrapure water. Pb was extracted and purified following procedures similar to Lassiter et al. (2003) using AG1-X8 resin. Purified Pb was loaded with a phosphoric acid-silica gel solution and run on single Re filaments using the Triton TIMS at the University of Texas at Austin. Mass fractionation was corrected via double-spike method for most samples (Todt et al., 1993). Double-spike corrected values for NBS 981 Pb standard during the period of analyses were $^{206}Pb/^{204}Pb$ of 16.932 ± 0.001 (2 SD), $^{207}Pb/^{204}Pb$ of 15.486 ± 0.001 (2 SD), and $^{208}Pb/^{204}Pb$ of 36.682 ± 0.005 (2 SD) and are in agreement with previously published values (Todt et al., 1996). Two samples were run using an ion counter with a peak-hopping routine. These samples were corrected for 1.3‰ per AMU mass fractionation based on measured values for NBS 981. Pb blanks ranged from 6 to 70 pg during the course of the study. Blank corrections up to a maximum of ~2% were applied to the Pb isotopic ratios.

For Os-isotope analyses, high-pressure asher (HPAS) digestion was not utilized due to the generation of hydrogen gas during reaction of metal and acid. Instead, ~1 g of steel shavings were digested in concentrated HCl (~2-3 mls) for 24 hours in loosely sealed vessels (to allow escape of hydrogen gas) and dried down. Next, 1 ml CCl_4 was added to the digestion vial (~2 ml) and digestions were continued in inverse aqua regia (10 ml of HCl and 15 ml of HNO_3) within tightly sealed Teflon vials at ~200°C. Os was extracted by solvent extraction (CCl_4) after 24 hours. CCl_4 was added again to the digestion vial and the vial was heated again at ~200°C. This process was repeated 4 more times for a total of six extractions. CCl_4 from the different extractions was pooled together and Os was back extracted from CCl_4 using HBr. Osmium was then further purified by micro-distillation (Birck et al., 1997).

Although HPAS digestion is commonly used for digestion of silicate samples in Os-isotope studies, this is not required for easily digested metal or sulfide phases. To evaluate Os yields using our modified digestion technique, Os concentration in one steel sample was determined by isotope dilution with a mixed ^{185}Re-^{190}Os spike added at the beginning of digestion. Next, a separate sample split was digested and the pooled CCl_4 extractions were spiked to determine the cumulative Os content extracted. The Os yield determined from this procedure was ~80 % (Figure C.1), comparable to Os yields from silicate whole rock powders using HPAS digestion (Chatterjee and Lassiter, unpublished data).

Os concentrations and ^{187}Os/^{188}Os were determined from a small (~1 g) portion of steel shavings by isotope dilution using a mixed ^{185}Re-^{190}Os spike. For high precision

$^{186}Os/^{188}Os$ measurements, ~5-20 g of unspiked steel shavings were then processed in order to extract at least ~80-100 nanograms of Os for each analysis, which was generally sufficient to generate ≥100 mV of $^{186}OsO_3^-$ during N-TIMS analyses, although a few analyses were performed at lower intensities. Digestion in ~5-20 vials, each containing ~1g of steel shavings, was typically necessary to process a single sample. All of the HBr back-extracted from CCl_4 from the multiple digestions was then pooled and dried before micro-distillation of the pooled Os cut. Os blanks ranged from 107 to 360 fg per g of processed rock powder during the course of the study. Osmium was loaded onto Pt filaments and analyzed using procedures outlined in Chatterjee and Lassiter (2015).

High precision $^{186}Os/^{188}Os$ measurements were performed via N-TIMS for 80-200 ratios using a $^{186}OsO_3$ beam intensity of ~30-140 mV. PtO_2 interferences were monitored by measuring masses 228-233 via SEM before and after the Os routine. Other potential interferences (e.g. WO_3^-, organics) were monitored by examining the $^{184}Os/^{188}Os$ ratio and residual 231 counts after stripping for PtO_2^- peaks. Two samples (H13 and MF) have high residual 231 counts (~69 to 343 cps), outside the normal range for other standards and samples (< 40 cps). In addition, two samples (MF and 304) also had high $^{184}Os/^{188}Os$ (0.001311-0.001313), outside the normal range observed for other standards and samples (0.001304-0.001308) (Chatterjee and Lassiter, 2016). Although these analyses are considered less robust, they are included in Table 3.2 because the measured $^{186}Os/^{188}Os$ values are in the same range as the other steels and our past experience is that interferences almost always result in anomalously elevated $^{186}Os/^{188}Os$ values rather than anomalously low values. The reported values therefore can be considered upper limits for

these samples. Detailed discussion of the $^{186}Os/^{188}Os$ measurements and data correction procedures are provided in Chatterjee and Lassiter (2015).

During the course of this study, the UT Triton was serviced once to correct Faraday and amplifier drift problems. To avoid systematic offsets in $^{186}Os/^{188}Os$ values following the service, I have divided our analytical campaign into two periods. For these periods, the average $^{186}Os/^{188}Os$ of the Johnson Mathey Os standard (UMD) standard were 0.1198467±15 (2 SE, n=8) and 0.1198449±10 (2 SE, n=18) respectively. Samples 410, A6 and H13 were analyzed following the Triton servicing. For direct data comparison with other laboratories, all samples were corrected to the long term UMD $^{186}Os/^{188}Os$ mean of 0.1198470 reported in Brandon et al. (2006) using the mean UMD value for the respective analytical period.

Within-run precisions (2 SE) are reported in Table 3.2. The external reproducibility of the UMD standard during both analytical periods is ~37 ppm. Errors reported in figure 3.7 and used in the $^{187}Os/^{188}Os$-$^{186}Os/^{188}Os$ regressions are the greater of the analysis within-run internal precision (2 SE) or the standard external reproducibility (2 SD). The external reproducibility of one duplicate analysis (separate unspiked digestions) was ±14 ppm for $^{186}Os/^{188}Os$ and ±9 ppm for $^{187}Os/^{188}Os$, consistent with the measured internal standard error of the individual analyses. Spiked and unspiked $^{187}Os/^{188}Os$ measurements are reproducible to better than 3 ‰ (Table 3.2).

Sample ID	Country of origin	Fe	Cr	C + S (+ others)	Mn	Ni	Mo
303		72.3	16.3	1.5	1.6	8.0	0.3
304		72.0	16.8	1.1	1.8	8.3	
309	Outside US	64.5	21.7	-	1.8	11.7	0.2
410	Outside US	87.9	10.9	-	0.6	0.4	0.1
416		86.7	11.6	-	1.3	0.2	0.2
1018	USA	98.2	0.1	0.9	0.7	0.1	0.0
A6	Russia	94.3	1.0	1.9	1.9	0.1	0.8
Cast Iron	Brazil	94.4	0.1	4.7	0.7		
H13	Russia	93.5	4.3	0.7	0.3	0.2	1.0
MF		78.2	20.1	1.7			
O1		97.6	0.4	0.8	1.0	0.1	0.1
1117	USA	97.0	0.0	2.0	1.0	0.0	

Table 3.1 Major element compositions (weight %) of industrial steels

Table 3.2 [Os] and Os and Pb isotope compositions of industrial steels

Sample ID	Os (ppb)	No of ratios in unspiked analyses	$^{184}Os/^{188}Os$	Residual 231 (in cps)	Measured $^{186}Os/^{188}Os$	Corrected $^{186}Os/^{188}Os$ (Brandon et al., 2006)	$^{187}Os/^{188}Os$	$^{187}Os/^{188}Os$ Spiked	Pb (ppm)	$^{206}Pb/^{204}Pb$	$^{207}Pb/^{204}Pb$	$^{208}Pb/^{204}Pb$
303	22.2	200	0.001306(1)	35	0.1198339(19)	0.1198342(19)	0.195188(2)	0.19512(2)	0.15	18.62	15.64	38.31
303 Duplicate		100	0.001307(4)	4	0.1198323(41)	0.1198326(41)	0.195190(5)					
304	10.9	160	0.001313(3)	8	0.1198324(36)	0.1198327(36)	0.143763(3)	0.14352(8)	0.19	18.78	15.65	38.47
309	7.8							0.18099(4)	0.03	*19.58*	*15.74*	*38.76*
410	16.5	140	0.001308(2)	19	0.1198333(29)	0.1198354(29)	0.142579(3)	0.14255(2)	0.01	*18.67*	*15.64*	*38.38*
416	14.3	80	0.001304(3)	14	0.1198301(49)	0.1198304(49)	0.156657(5)	0.1566(3)	0.71	18.40	15.59	38.30
1018	0.3							0.5511(9)	0.52	18.07	15.61	38.05
A6	2.8	160	0.001306(5)	2	0.1198368(69)	0.1198388(69)	4.118828(59)	4.122(2)	0.20	18.25	15.64	38.33
A6 Duplicate									0.22	18.25	15.63	38.31
Cast Iron	0.0							0.666(2)	0.02	18.60	15.64	38.80
H13	5.6	120	0.001308(2)	343	0.1198318(37)	0.1198338(37)	0.450837(7)	0.4509(1)	0.09	18.01	15.59	38.00
MF	16.0	140	0.001311(2)	69	0.1198368(28)	0.1198372(28)	0.171150(3)	*0.1709(11)*	0.19	*19.17*	*15.70*	38.69
O1	1.5							0.2788(1)	0.02	18.12	15.60	37.93
1117	0.1							0.5253(8)				

$^{184}Os/^{188}Os$, $^{186}Os/^{188}Os$, and $^{187}Os/^{188}Os$ errors listed in parantheses are 2 SE (internal precision). Pb isotopic data are either double spiked corrected or corrected using standard-sample bracketing (italicized). Errors for $^{187}Os/^{188}Os$ spiked analyses are either 2 SE (internal precision) or 2 SD external reproducibility (italicized)

3. RESULTS:

Major element compositions are presented in Table 3.1. Measured major element compositions are consistent with previously reported concentrations (Figure C.2-C.3; cf. McMaster-Carr, 2010a-b). Iron ranges from 64 to 98 wt.%. Chromium ranges from 0 to 21.7 wt. %. C+S ranges from 0 to 4.7 wt.%. Steels with >15 wt.% Cr usually also have elevated Ni, ranging from 8 to 12 wt.%. Other steels have ≤0.5 wt.% Ni.

Os concentration and isotopic data are presented in Table 3.2. Os concentrations span several orders of magnitude, from 30 ppt to 22.2 ppb. Os concentration is positively correlated with Cr content (Figure 3.1). Most samples follow a linear trend. Three samples (marked by open squares) are offset towards lower Os concentrations for a given Cr content relative to the other samples (marked by open squares). $^{187}Os/^{188}Os$ also span a very wide range, from 0.1425-4.12. $^{187}Os/^{188}Os$ is negatively correlated with Os concentration and Cr content (Figure 3.2). High-[Os] samples (7-22 ppb) and high-Cr samples (> 10 wt.%) have less radiogenic and less variable $^{187}Os/^{188}Os$ (0.144 to 0.195). In contrast, low-[Os] samples (30 ppt- 2 ppb) and low-Cr samples (< 10 wt.%) have highly radiogenic $^{187}Os/^{188}Os$ ranging from 0.27 to 4.12. $^{186}Os/^{188}Os$ values range from 0.1198304 to 0.1198372. $^{186}Os/^{188}Os$ and $^{187}Os/^{188}Os$ are not correlated with each other.

Lead concentration and isotopic data are also presented in Table 2. Lead concentrations range from 14 to 707 ppb. $^{206}Pb/^{204}Pb$ ranges from 18.0 to 19.6, $^{207}Pb/^{204}Pb$ ranges from 15.6 to 15.7, and $^{208}Pb/^{204}Pb$ ranges from 37.9 to 38.8. All samples plot above the North Hemispheric Reference Line (NHRL) (Hart, 1984), with systematically higher $^{207}Pb/^{204}Pb$ and $^{208}Pb/^{204}Pb$ for a given $^{206}Pb/^{204}Pb$, similar to the majority of rocks derived

from continental crust (Figure 3.3; cf. Hofmann, 1997). Steels show a negative correlation between $^{206}Pb/^{204}Pb$ and Fe wt.% (Figure 3.4). Samples that are offset from the main Cr-Os trend to lower Os concentrations also possess the most radiogenic Pb isotopic compositions.

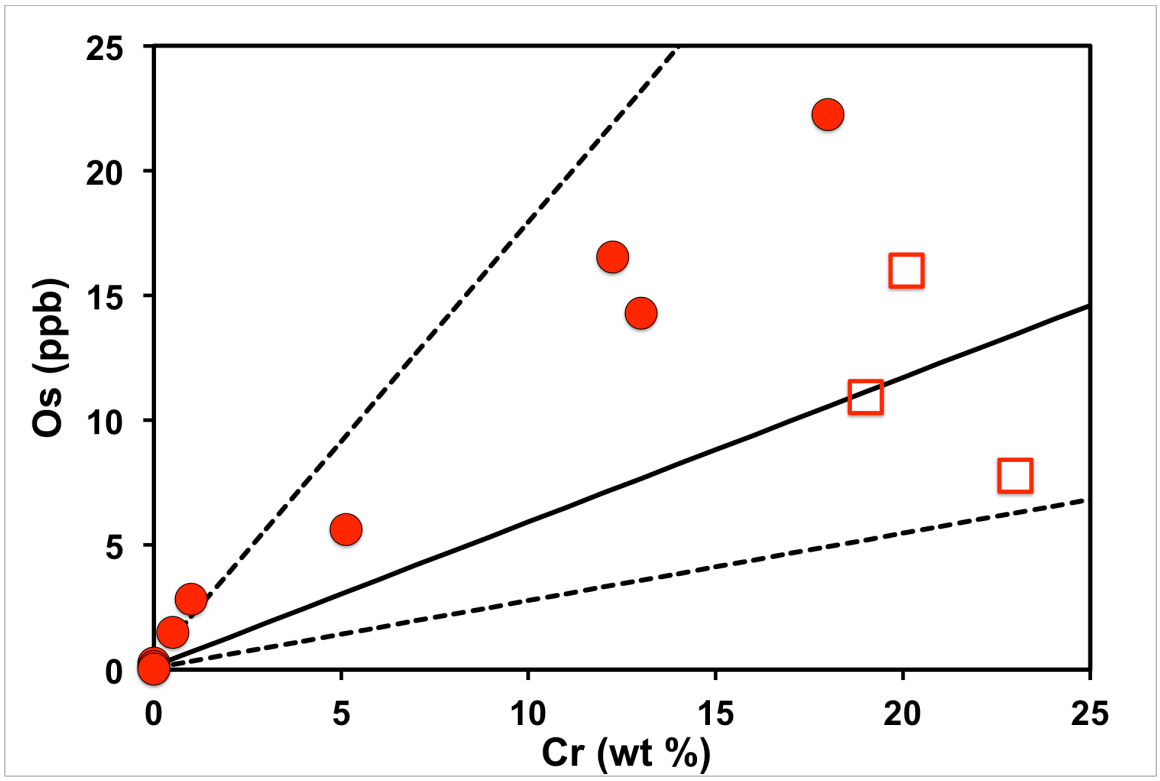

Figure 3.1 Os vs Cr concentrations in steels.

Solid black line represents mixing between end member chromitite (+coke) and iron ore (+coke) using median Os concentrations for chromitites, coke and iron ore (see text for details). Median values rather than mean values are used due to the non-Gaussian distribution of Os concentrations in the different components. Dashed lines reflect uncertainties in Os concentrations for the end member components and are calculated from the 20th percentile and 80th percentile Os concentrations in a cumulative frequency distribution. Most samples define a linear Os-Cr correlation (filled red circles). Three samples fall off the linear trend towards lower Os concentrations for a given Cr content (open red squares).

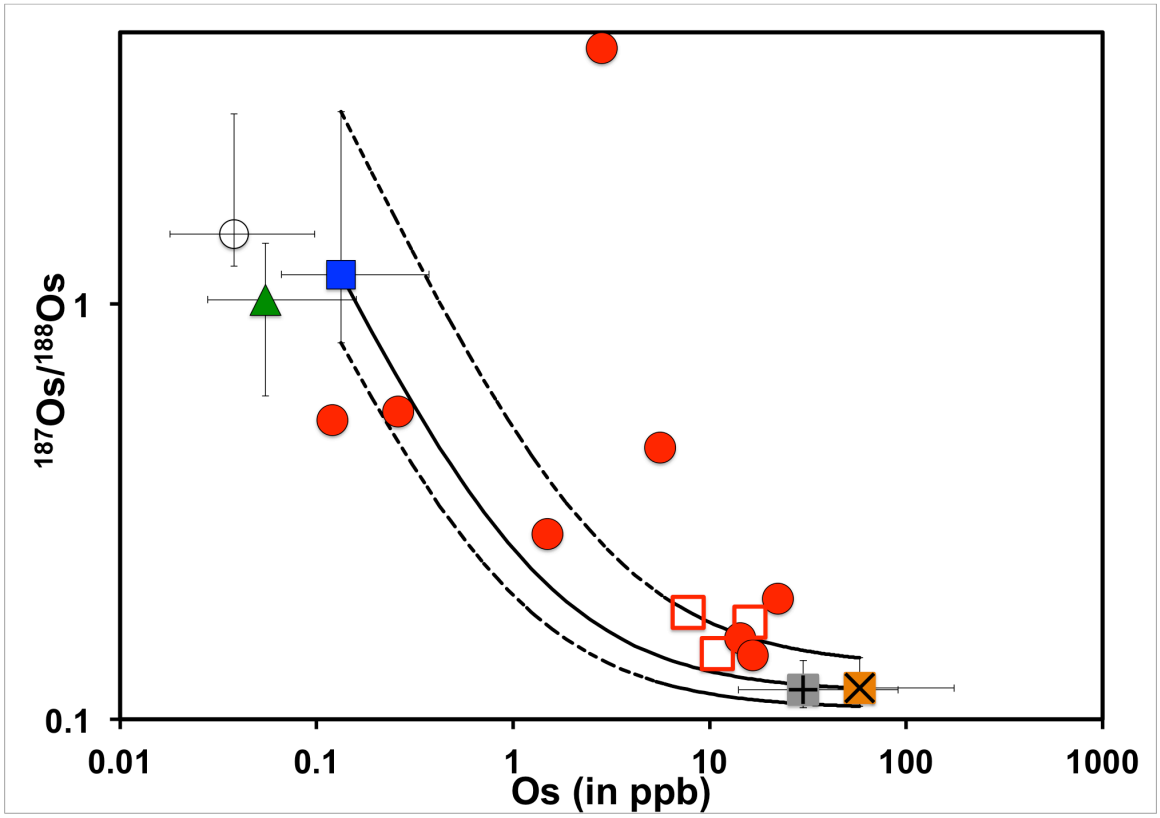

Figure 3.2 $^{187}Os/^{188}Os$ vs Os concentration in steels.

Median values of BIF (filled green triangle), coal (open circle), and chromitites (grey filled square with black plus sign) are also shown. Also shown are the calculated Os concentration and isotopic composition of Cr metal (filled orange square with black cross) and Fe metal (filled blue square) obtained from the reduction of chromitite and iron ore assuming Os is conserved during the smelting process (see text for details). Mixing uncertainties are calculated as in Figure 3.1. Steel symbols are same as in figure 3.1.

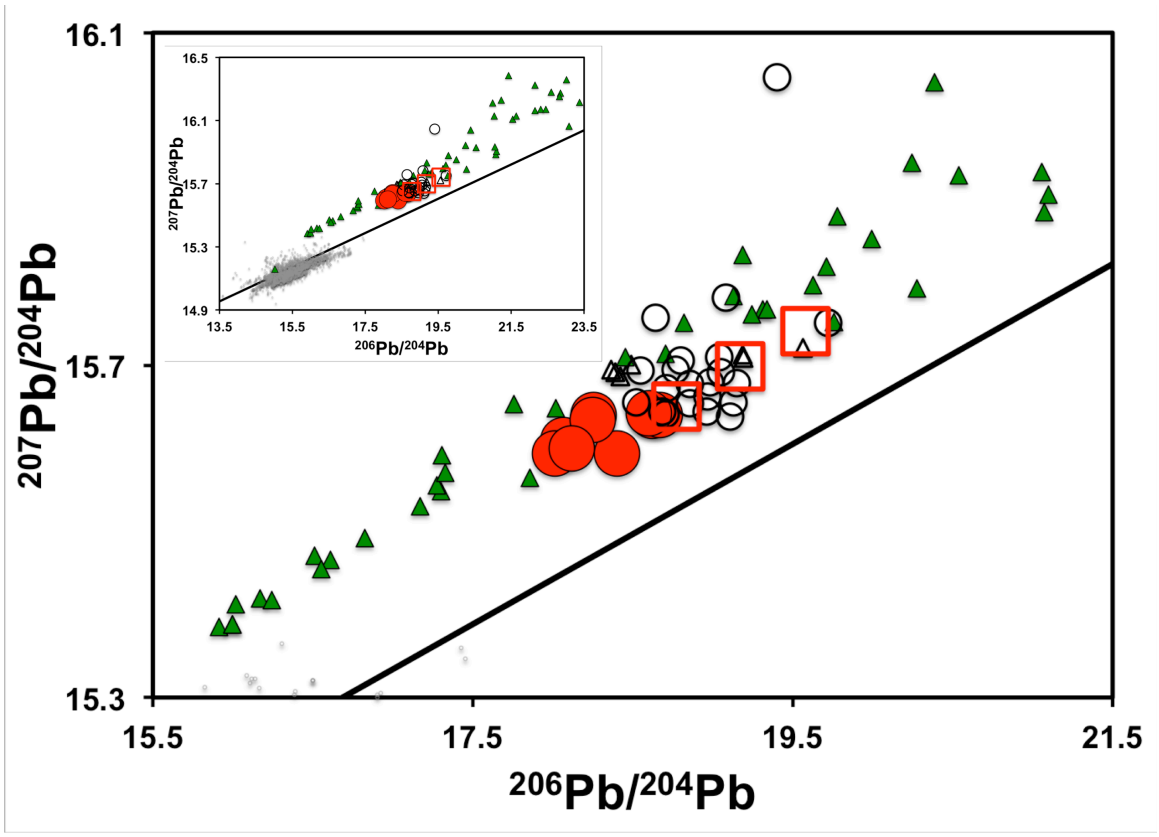

Figure 3.3 $^{206}Pb/^{204}Pb$ vs $^{207}Pb/^{204}Pb$ in steels.

Also shown are MORB (grey circles; age corrected to ~2 Ga mantle source, see text for explanation), BIF (green filled triangles), coals (US-open circles, European-open triangles, Asian-filled diamonds). Steels plot above the NHRL similar to BIFs and coals, consistent with Pb derivation from crustal materials. Solid line is the Northern Hemisphere Reference Line after Hart, 1984. Steel symbols are same as in figure 3.1.

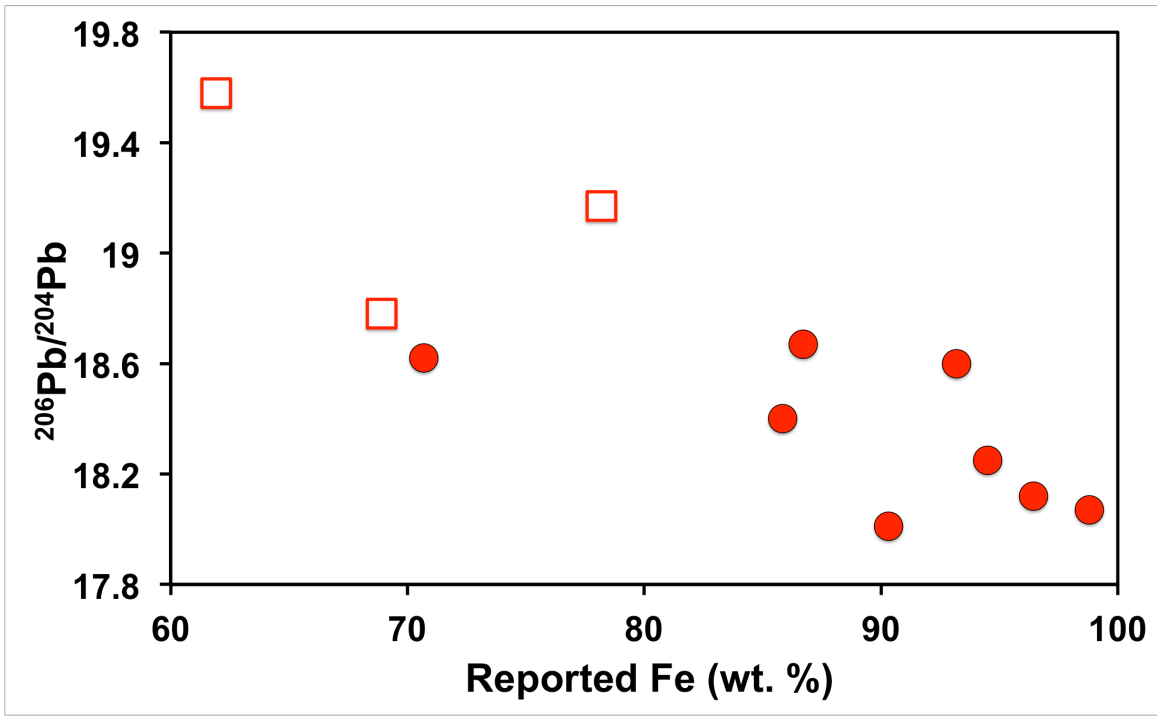

Figure 3.4 $^{206}Pb/^{204}Pb$ vs Fe wt. % in steels.

$^{206}Pb/^{204}Pb$ Steel symbols are same as in figure 3.1.

4. DISCUSSION

4.1 Crustal and mantle sources of Os and Pb in steel:

Previous studies (cf. Brauns et al., 2013) have shown that Os and Sr isotope variations in steels can be used to trace the compositions of the components used in steel manufacture. For example, the Os and Sr isotope compositions of archaeological steels are similar to the compositions of local iron ores utilized to manufacture these steels (Brauns et al., 2013). Furthermore, the Os isotope compositions in steels manufactured experimentally from iron ores and charcoal of known composition reflect binary mixing of these components, suggesting that Os is conserved during smelting processes (Brauns et al., 2013). Similarly, Pb isotope compositions in archaeological steels represent a mixture of the raw materials used in their manufacture (cf. Degryse et al., 2007). Therefore, isotope variations in steels should reflect the primary components used in steel manufacture, namely iron ore, chromitite, and coke.

Steel is manufactured by smelting processes in which iron ores are chemically reduced inside a blast furnace. Chromium (chromite) is added to prevent oxidative corrosion. Coke, which is derived from low-ash, low-sulfur metallurgic coals, is added during smelting to reduce the Fe and Cr ores to metals. Inside the blast furnace, reaction of coke with hot air generates carbon monoxide, which then reduces the metal ores (cf. Geerdes et al., 2015). The chief reactions during smelting are

$$Fe_3O_4 + 2C \rightarrow 3Fe + 2CO_2 \quad (1)$$

$$2Fe_2O_3 + 3C \rightarrow 4Fe + 3CO_2 \quad (2)$$

$$2Cr_2O_3 + 3C \rightarrow 4Cr + 3CO_2 \quad (3)$$

Both steel and the components used in its manufacture are global commodities (World Steel Association, 2014a). For example, China is the largest producer of steels

(~45 % of global production), but ~65 % of the iron ore used for steel manufacture in China is imported (Barry et al., 2013). The leading producers of iron ore include China, Australia, Brazil, and India, which account for ~84 % of global iron ore production (Barry et al., 2013). Chromium used in steels is derived from chromitites, which are predominantly mined from Precambrian stratiform chromite deposits from South Africa, India, Zimbabwe, Finland and Brazil (Schulte et al., 2010). The leading producers of coal include China, United States, Australia and India, which account for ~70 % of global coal production. Similar to iron ores, coal used in steel manufacture is globally traded depending on supply and demand (International Energy Agency, 2015). For example, China imports ~15 % of global coals despite being the leading producer of coal (Barry et al., 2013). Therefore, it is generally impossible to uniquely assess a particular source for the components used to manufacture a particular sample of steel, even when the country of origin is known. Below, we examine published data on the Os and Pb concentrations and isotope compositions of chromitites, coal and iron ore to obtain a representative estimate for these components.

Most iron ore (~85%) is derived from Precambrian Banded Iron Formations (BIF) or weathered residues of BIF (Povermo, 1999). Major producers of iron ore include Hamersley province (Australia), Carajas mine (Brazil), Sishen province (South Africa) and Bihar-Orissa region (India), all of which have BIF-type iron ore deposits. Previous studies (cf. Ripley et al., 2008) show that BIFs have Os concentrations ranging from ~10 to 238 ppt (median ~55 ppt) and highly radiogenic present-day (0.81-1.42; median ~1.02) and initial $^{187}Os/^{188}Os$ (~0.3 to ~0.5) values (Table 3.3). Many models of BIF formation (Frei et al., 2007; Poulton et al., 2010) hypothesize oxidation and precipitation of iron as Fe^{3+} from reduced seawater. Based on the radiogenic initial $^{187}Os/^{188}Os$ signature in BIFs (Suzuki and Kato, 2003; Ripley et al., 2008), a significant fraction of the Os in ancient

seawater appears to have derived from continental crust, similar to Os in the oceans today (cf. Cohen et al., 1999, 2004, McDaniel et al., 2004). BIFs have highly heterogeneous Pb concentrations (0.6 to 12 ppm; median ~2.2 ppm) and isotope compositions (e.g. $^{206}Pb/^{204}Pb$ ranges from 12.59 to 43.34) (Frei et al., 2007, 2008, 2009). Radiogenic Pb isotopes in some BIFs are due to radiogenic ingrowth and high U/Pb ratios. However, most BIFs have more modest $^{206}Pb/^{204}Pb$ (median ~19.24) and form a distinct trend above the North Hemispheric Reference Line (NHRL) (Hart, 1984), with systematically higher $^{207}Pb/^{204}Pb$ and $^{208}Pb/^{204}Pb$ for a given $^{206}Pb/^{204}Pb$ (cf. Frei et al., 2008, 2009), similar to most crustal rocks (e.g. Hofmann, 1997).

Coals are formed by the deposition and compaction of biotic materials in anoxic terrigenous environments. Most coals have Os concentrations ranging from 5 to 302 ppt, although some have up to ~1.7 ppb (median ~38 ppt) (Qi et al., 2008; Baioumy et al., 2011). $^{187}Os/^{188}Os$ in coals is highly radiogenic (1.06 to 3.73; median ~1.47), in part due to high Re/Os ratios (~5 to ~138) and post-depositional radiogenic ingrowth. However, initial $^{187}Os/^{188}Os$ are also radiogenic (0.99 to 1.9), suggesting Os derivation from crustal sources (Baioumy et al., 2011; Table 3.3). Coals have highly variable Pb concentrations (~3 to ~170 ppm; Chow and Earl, 1972; Diaz-Somoano et al., 2007). Pb isotopic compositions span a wide range (e.g. $^{206}Pb/^{204}Pb$ ranges from 18.37 to 19.72) (Chow and Earl, 1972; Diaz-Somoano et al., 2007) and form a distinct trend above the North Hemispheric Reference Line (NHRL) (Hart, 1984). Therefore, Pb isotope compositions in coals are consistent with derivation from crustal materials (cf. Hofmann, 1997).

Chromium is mined from chromitites (Papp and Lipin, 2001). Chromitites typically form either by crystallization from mantle melts in dunite lenses or by melt-rock and melt-melt interactions (Ballhaus, 1998; Zhou et al., 1998). Almost 75% of the world's chromite is mined from Precambrian stratiform-type chromite deposits: namely the

Bushveld Complex (South Africa), Nausahi and Sukinda deposits (India), Great Dyke (Zimbabwe), Kemi intrusion (Finland) and Ipueira-Medrado Sill (Brazil), all of which formed prior to ~2 Ga (Schulte et al., 2010). Os concentrations are highly heterogeneous (~2 to ~815 ppb), with a median concentration of ~30 ppb. $^{187}Os/^{188}Os$ in chromitites range from ~0.1037 to ~0.1489, though the majority are subchondritic (median ~0.1177) (e.g., Walker et al., 2002). There is no available Pb isotope data on chromitites. Existing constraints on spinel-melt partition coefficients (cf. Elkins et al., 2008) indicate that a very small fraction of Pb is likely inherited from the melt during crystallization of chromite due to very low K_D for spinel (~0.0005). Whitehouse and Neumann (1995) show that cumulate xenoliths such as dunites often closely associated with chromitite have MORB-like Pb isotopic compositions and low [Pb] (<0.6 ppm). I assumed average [Pb] of MORB as an upper bound for chromitites. Because most chromitites are >2 Gyrs in age, they likely inherit the Pb isotopic composition of melts derived from the Archean mantle. Therefore, I corrected present- day MORB for radiogenic ingrowth for 2 Gyrs using U/Pb and Th/Pb values for estimated MORB source mantle to infer average chromitite Pb isotope compositions (cf. Stracke et al., 2003; MORB Data source: GeoRef and PetDB). Inferred Pb isotope compositions for chromitites span a wide range (e.g. $^{206}Pb/^{204}Pb$ ranges from 13.59 to 17.45) and are less radiogenic than most BIFs and coals (Table 3.3).

The above constraints suggest that chromitites have high [Os], low [Pb] and unradiogenic Os and Pb isotopes reflecting their derivation from upper mantle-derived melts. In contrast, iron ores and coal have lower [Os] and highly radiogenic Os isotopes, suggesting ultimate Os derivation from continental crust components. Iron ores and coal also have variable Pb isotope compositions that plot above the NHRL, consistent with Pb derivation from continental sources. Below I show the correlations between major

elements and [Os], and Os and Pb isotopes in steel can be explained by the mixing of these primary components.

Os concentration is positively correlated with Cr content in steel (Figure 3.1). This is consistent with the much higher [Os] in chromitites relative to iron ore and coke. The scatter in the Cr-Os trend is likely related to the highly heterogeneous [Os] in chromitites (~2 ppb to ~815 ppb; Table 3.3). I model the Cr-Os trend by mixing a high Cr, high Os component (chromitites+coke) with a low Cr, low Os component (iron ore+coke). During smelting, Fe and Cr metal are obtained by reducing Fe-ore (BIF) and Cr-ore (chromitite) with coke using a typical ore:coke ratio of ~1.33 and ~1.55 respectively (World Steel Association, 2014b). I assume that all of the Os in the primary components is conserved during the smelting process. Using median values for [Os] and $^{187}Os/^{188}Os$ in iron ore (BIF), Cr ore and coke (cf. Table 3.3), mass balance calculations indicate [Os] and $^{187}Os/^{188}Os$ in the reduced Fe metal to be ~133 ppt and ~1.17 respectively and in the reduced Cr metal to be ~58 ppb and ~0.1188 respectively (Figure 3.2). Despite considerable uncertainty, mixing between chromitites and iron ore is consistent with the observed Cr-Os trend (Figure 3.1). The broad fit between the modeled mixing trend and the measured steels suggests that Os is primarily conserved during the smelting process. The negative correlation between $^{187}Os/^{188}Os$ and Os concentration is also consistent with mixing between an unradiogenic Os component (chromitites+coke) and a radiogenic Os component (iron ore+coke) as shown by our mixing model (Figure 3.2).

In contrast to Os isotopes, Pb isotopes in steel should primarily reflect a mixture of Pb from BIFs and coals due to the much lower Pb concentrations in chromitites (Table 3.3). Pb concentration variations in steels do not provide direct constraints on the primary sources of Pb due to volatile Pb loss during smelting processes (>90-95%; Paycna, 1984). However, Pb isotopes are not significantly fractionated during smelting and can be

utilized to examine the sources of Pb in steel. Both BIFs and coals plot above the NHRL (Figure 3.3). Previous studies (e.g. Hofmann, 1997) have shown that a majority of continental samples from different environments plot above the NHRL, reflecting the ancient age of continental materials. In contrast, inferred Pb isotope compositions of chromitites have values consistent with derivation from the Archean mantle and plot near the NHRL. $^{206}Pb/^{204}Pb$, $^{207}Pb/^{204}Pb$, and $^{208}Pb/^{204}Pb$ are positively correlated in steels and define a distinct trend above the NHRL similar to that defined by BIFs and coals (Figure 3.3). This is consistent with Pb derivation primarily from BIFs and coals and confirms that chromitites have limited influence on the Pb isotope variations in steels.

Pb isotopes are negatively correlated with Fe content in steels and positively correlated with Cr (Figure 3.4). Coke has a significantly higher Pb concentration (~37 ppm) relative to BIF (~2.2 ppm) and chromitite (~0.08 ppm) (Table 3.3). Because chromitites have a much lower median Pb concentration relative to BIFs, the Cr-end member component in steels should primarily reflect the Pb isotope composition of the coke used to reduce Cr-ore to Cr, whereas Pb in the Fe-end member should reflect a mixture of Pb from coke and BIFs. BIFs have highly heterogeneous Pb isotope compositions that extend to less radiogenic values than observed in steels and coal. The observed negative correlation between Fe content and Pb isotopes suggests BIFs with systematically lower isotope compositions than most coals are used in the steelmaking process.

In summary, Os concentration variations and Os and Pb isotope variations in steels reflect mixing between the primary components used in steel manufacture. Os in steels represents a mixture of chromitites with unradiogenic, mantle-like $^{187}Os/^{188}Os$ and iron ores and coal with highly radiogenic $^{187}Os/^{188}Os$, which is derived from the weathering of the continental crust. In the following section, I examine $^{187}Os/^{188}Os$-$^{186}Os/^{188}Os$ variations

in steels to constrain the $^{186}Os/^{188}Os$ compositions and the long-term Pt/Os evolution of these weathered components.

Table 3.3 [Os], [Pb], and isotopic compositions of different components in industrial steels

Component	[Os] ng/g	Median	$^{187}Os/^{188}Os$	Median	[Pb] ug/g	Median	$^{206}Pb/^{204}Pb$	Median
Chromitite*	2-815	30	0.104-0.149	0.1177	0.015-0.021	0.018	13.59-17.45	15.39
BIF	0.010-0.24	0.055	0.56-1.42	1.02	0.4-17	2.25	12.59-43.34	19.25
Coal	0.005-1.7	0.038	1.06-3.73	1.47	3-170	37	18.37-19.72	18.86

Os and Pb isotopic and concentration data are based on literature

4.2 $^{186}Os/^{188}Os$ variations in steels: Constraints on the $^{186}Os/^{188}Os$ and Pt/Os evolution of chromitites, iron ores and coal

Measured PGE patterns in a variety of crustal materials including loess, marine, and non-marine shales typically show elevated PPGE+Re/IPGE ratios relative to the Earth's mantle (e.g., Baioumy et al., 2011, Puecker-Ehrenbrink and Jahn, 2001; Figure 3.5). Estimates for the bulk UCC inferred from loess, riverine sediments, and impact melts have supra-chondritic PPGE+Re/IPGE patterns (cf. Wedepohl, 1995; Schidmt et al., 1997; Puecker-Ehrenbrink and Jahn, 2001). For example, estimated Pt/Os ratios in bulk UCC are enriched by a factor of 10 relative to the PUM (Figure 3.6). Previous studies (e.g., Day et al., 2013) indicate that PPGE and Re have lower partition coefficients than the IPGE during partial melting, resulting in elevated PPGE/IPGE ratios in mantle-derived melts. Therefore, the PPGE/IPGE enrichment of the continental crust is consistent with its generation from magmatic processes.

High Pt/Os in the UCC should result in radiogenic $^{186}Os/^{188}Os$ due to the decay of ^{190}Pt to ^{186}Os over time. $^{186}Os/^{188}Os$ data on crustal materials is very limited, and direct measurements are difficult due to the low [Os] typical of most crustal materials. However, McDaniel et al. (2004) reported elevated $^{186}Os/^{188}Os$ (0.119848±10 to 0.119865±16) for loess and freshwater Mn-nodules relative to the upper mantle [~0.1198364±13; Chatterjee and Lassiter, 2016] (Figure 3.7). $^{186}Os/^{188}Os$ measurements in crustal materials can be used to infer the long-term Pt/Os ratio of UCC in the same way previous studies have used $^{187}Os/^{188}Os$ to constrain the long-term Re/Os of the UCC (Puecker-Ehrenbrink and Jahn, 2001; Hattori et al., 2003). Using an average age of

continental crustal rocks of ~2 Ga (e.g. Miller et al., 1986), the offset in $^{186}Os/^{188}Os$ between loess and freshwater Mn nodules and average upper mantle suggests an average Pt/Os ratio for crustal rocks of ~8.1. This estimate is similar to previous estimates for bulk UCC (~10-16) (cf. Puecker-Ehrenbrink and Jahn, 2001) (Figure 5).

Seawater is characterized by highly radiogenic $^{187}Os/^{188}Os$ relative to the upper mantle, indicating that a significant fraction (~70-80%) of its Os is derived from crustal weathering (e.g. Esser and Turekian, 1993; Sharma et al., 1997, 1999). Similarly, highly radiogenic $^{187}Os/^{188}Os$ in black shales is consistent with derivation from continental crust (e.g. Xu et al., 2009; Singh et al., 1999). Therefore, both shales and seawater should inherit the radiogenic $^{186}Os/^{188}Os$ signature observed in average continental crust. However, previous analyses show $^{186}Os/^{188}Os$ values for marine Mn nodules and black shales (~0.119814±20 to ~0.119847±10; Figure 3.7) that are generally less radiogenic than reported for the UCC (McDaniel et al., 2004). McDaniel et al. (2004) suggested that the unradiogenic $^{186}Os/^{188}Os$ inferred for seawater might reflect preferential sampling of Os from black shales due to their higher Os concentrations and greater susceptibility to chemical weathering relative to bulk UCC. However, this does not explain how black shales themselves inherit their unradiogenic $^{186}Os/^{188}Os$ values. In principle, high Re/Os and modest Pt/Os ratios in black shales could result in significant radiogenic ingrowth of ^{187}Os decoupled from ^{186}Os ingrowth. However, the Cambrian black shales investigated by McDaniel et al. (2004) have highly radiogenic initial $^{187}Os/^{188}Os$ values (~0.5 to ~2.2) but initial $^{186}Os/^{188}Os$ values that are indistinguishable from the upper mantle. Given that Os in black shales and seawater is ultimately derived from weathering of continental

crust, the unradiogenic $^{186}Os/^{188}Os$ in products of crustal weathering is surprising and requires further examination.

Os in steels represents a mixture of Os from unradiogenic chromitites and radiogenic coals and iron ores. Radiogenic $^{187}Os/^{188}Os$ in iron ores and coals is consistent with Os derivation from crustal weathering processes (e.g. Baioumy et al., 2011; Ripley et al., 2008). Therefore, $^{187}Os/^{188}Os$-$^{186}Os/^{188}Os$ variations in steels can be used to infer the $^{186}Os/^{188}Os$ of its crustal- (iron ores and coals) and mantle-derived components (chromitite) and provide additional constraints on the $^{186}Os/^{188}Os$ compositions of crustal weathering products. Although $^{187}Os/^{188}Os$ extends to highly radiogenic values in steel (up to ~4.2), the correlation between $^{187}Os/^{188}Os$ and $^{186}Os/^{188}Os$ is extremely weak and not statistically significant (Figure 3.7). $^{186}Os/^{188}Os$ in steels ranges from 0.1198304 to 0.1198388. Given the inherent uncertainties in $^{186}Os/^{188}Os$ measurements, individual steel analyses are not analytically resolvable from each other. The average $^{186}Os/^{188}Os$ value of all samples (~0.1198345±21) is indistinguishable from values reported for upper mantle peridotites (e.g. Chatterjee and Lassiter, 2016; Brandon et al., 2000) (Figure 3.7).

High-Cr (>10 wt.%) steel samples have slightly lower $^{186}Os/^{188}Os$ values (0.1198304-0.1198372) on average than the upper mantle (~0.1198345-0.1198384; Chatterjee and Lassiter, 2016). Extrapolation of the $^{187}Os/^{188}Os$-$^{186}Os/^{188}Os$ trend in steels to the median $^{187}Os/^{188}Os$ value reported for chromitites from major economic Cr-deposits (~0.1177; cf. Section 4.1; Table 3.3) yields an estimated $^{186}Os/^{188}Os$ value of 0.1198339±15 for average chromitites used in steel manufacture (Figure 3.7). The $^{186}Os/^{188}Os$ value for chromitites inferred from the $^{187}Os/^{188}Os$-$^{186}Os/^{188}Os$ trend is unresolvable from the

$^{186}Os/^{188}Os$ value (~0.1198338±28) calculated by simply averaging the values observed in high Cr-steels (>10 wt.%). This estimate is consistent with $^{186}Os/^{188}Os$ previously measured in chromitites [0.1198350±45 (2 SD); Walker et al., 2005; Brandon et al., 1998], but is slightly lower than the present-day average upper mantle [~0.1198364±13; Chatterjee and Lassiter, 2016]. Most major economic chromite deposits are Proterozoic to Archean in age [e.g. Nausahi and Sukinda deposits (India) (~3.2 Ga); Stillwater complex (U.S) (~2.7 Ga); Great Dyke (Zimbabwe) and Kemi intrusion (Finland) (~2.5 Ga); Bushveld Complex (South Africa) and Ipueira-Medrado Sill (Brazil) (~2Ga); Schulte et al., 2010]. Chromitites on average have sub-chondritic Re/Os (~0.0001-0.1; median ~0.015) and Pt/Os ratios (~0.1-1.5; median~0.3) (e.g. Kocks et al., 2007; Distler et al., 2008; Uysal et al., 2009). Sub-chondritic $^{187}Os/^{188}Os$ values previously reported for many chromitites (e.g. Walker et al., 2002) and low $^{186}Os/^{188}Os$ values reported by Brandon et al. (1998) and inferred from this study are consistent with long-term evolution with sub-chondritic Re/Os and Pt/Os ratios. Assuming an average age of ~2.5 Ga for chromitite deposits used in steel manufacture (e.g. Schulte et al., 2010), I calculate an initial $^{186}Os/^{188}Os$ value of ~0.1198330±15, similar to the inferred average primitive upper mantle (PUM) at ~2.5 Ga (~0.1198319±7), which I calculate using an upper mantle Pt/Os of ~1.7 and modern day PUM $^{186}Os/^{188}Os$ of ~0.1198379±7 (Chatterjee and Lassiter, 2016).

Extrapolating the $^{187}Os/^{188}Os$-$^{186}Os/^{188}Os$ trend to the estimated $^{187}Os/^{188}Os$ of the crustal components used in steel manufacture (BIF+coal $^{187}Os/^{188}Os$ ≈1.2, see Table 3.3) yields a $^{186}Os/^{188}Os$ value of ~0.1198352±20 (2 SE), indistinguishable from modern

upper mantle (Figure 3.7). Again, this estimate is indistinguishable from the $^{186}Os/^{188}Os$ estimate of ~0.1198363±50 calculated by averaging the analyses of low-Cr steels (<10 wt.% Cr; $^{187}Os/^{188}Os$ ~0.45-4.2). This estimate is similar to unradiogenic $^{186}Os/^{188}Os$ values reported for black shales and seawater-derived marine Mn nodules but systematically lower than estimates for bulk UCC (McDaniel et al., 2004). The high-$^{187}Os/^{188}Os$ end member in steels derives from roughly equal Os contributions from iron ore and coke. Because it is difficult to uniquely deconvolve the $^{186}Os/^{188}Os$ of BIFs and coals and given the limited $^{186}Os/^{188}Os$ heterogeneity observed in steels, I assume that BIFs and coals both have similar present-day $^{186}Os/^{188}Os$ values.

A majority of BIFs formed during the Late Archean to Early Proterozoic with an average age of ~2.2 Gyrs (Klein et al., 2005). Similarly, coals primarily formed during the Carboniferous-Permian age (average age ~0.2 Ga; Nelson et al., 2016). Although BIFs and coals have mantle-like present-day $^{186}Os/^{188}Os$ values, it is more appropriate to compare their initial $^{186}Os/^{188}Os$ values with the crust and mantle at their time of formation. Very little data on the PGE patterns of BIFs and coals are available. It is possible that BIFs and coals with supra-chondritic Pt/Os ratios fortuitously evolved from sub-mantle $^{186}Os/^{188}Os$ values to upper-mantle-like present-day $^{186}Os/^{188}Os$ values. This seems unlikely given that both BIFs and coals have radiogenic initial $^{187}Os/^{188}Os$ values consistent with derivation of Os from crustal weathering (cf. Suzuki and Kato, 2003; Ripley et al., 2008; Baioumy et al., 2011). An upper bound for the initial $^{186}Os/^{188}Os$ value in BIFs and coals is the present-day value, which would require evolution with a Pt/Os ratio of 0. Even here, the initial $^{186}Os/^{188}Os$ value for BIFs would only be slightly

higher than the PUM at ~2.2 Ga (~0.1198326±7; calculated using the present-day PUM Pt/Os and $^{186}Os/^{188}Os$ estimated by Chatterjee and Lassiter, 2016). Similarly, the initial $^{186}Os/^{188}Os$ value of coals in this case would be within uncertainty of the PUM at ~0.2 Ga (~0.1198374±7). In contrast, average continental crust has high Pt/Os (~10.6; Puecker-Ehrenbrink and Jahn, 2001) and therefore should have $^{186}Os/^{188}Os$ significantly higher than the upper mantle (McDaniel et al., 2004). Our results are consistent with previous results for seawater-derived marine Mn nodules and black shales (McDaniel et al., 2004) and suggest that the $^{186}Os/^{188}Os$ of materials that primarily contain Os derived from crustal weathering is systematically lower than in bulk UCC, despite the fact that these components are characterized by highly radiogenic $^{187}Os/^{188}Os$.

The apparent decoupling between $^{186}Os/^{188}Os$ and $^{187}Os/^{188}Os$ in crustal weathering products is surprising given that the majority of crustal and mantle derived rocks define a broad positive correlation between Pt/Os and Re/Os (Figure 3.5). This decoupling may reflect the heterogeneous distribution of PGE in crustal rocks and preferential weathering of low Pt/Os phases. Previous studies (e.g. Burton et al., 1999; Harvey et al., 2011) show that over 90% of the Os in many mantle peridotites is hosted in Fe-Ni-Cu BMS (base metal sulfides), consistent with the high sulfide-silicate K_D for Os (~>10^5) (e.g. Brenan et al., 2016). In contrast, Re has a lower sulfide-silicate K_D relative to Os, which results in silicate phases hosting a larger fraction of Re (Burton et al., 1999). Os has higher sulfide-silicate K_D values relative to Pt (e.g. Fleet et al., 1996), consistent with lower Pt/Os ratios observed in many peridotite sulfides relative to bulk peridotite (e.g. Lorand et al., 2010). Direct studies that examine the distribution of PGE in continental crustal rocks are

lacking. However, based on the partitioning behavior described above, the PGE in crustal rocks are likely to be hosted in a number of different phases with variable Pt/Os and Re/Os, and in particular, crustal sulfides are likely to host a significant fraction of crustal Os and to have lower Pt/Os ratios relative to bulk upper continental crust. Consequently, crustal sulfides are expected to develop lower $^{186}Os/^{188}Os$ values relative to bulk continental crust over time.

Previous studies indicate that Re and Os may be preferentially mobilized relative to Pt during weathering (e.g. Jaffe et al., 2002; Puecker-Ehrenbrink and Hannigan, 2000). In particular, crustal sulfides, which are likely a significant Os reservoir in crustal rocks, are highly susceptible to oxidative weathering (e.g. Anbar et al., 2007). The lower median Pt/Os ratio in black shales (~3.8) relative to bulk UCC (~10) (e.g. McDaniel et al., 2004; Puecker-Ehrenbrink and Jahn, 2001; Baioumy et al., 2011) is consistent with preferential mobilization of Os relative to Pt during weathering. Oxidation of Os and Re to OsO_4 and ReO_4 makes these PGE highly soluble and more labile than Pt, resulting in their preferential removal during oxidative weathering processes (e.g. Kendall et al., 2014; Anbar et al., 2007). Preferential weathering of sulfides may result in the preferential mobilization of Os with unradiogenic $^{186}Os/^{188}Os$ relative to average upper continental crust. This can explain the apparent discrepancy in $^{186}Os/^{188}Os$ values between products of crustal weathering and bulk UCC. Os susceptibility to weathering likely increased following the Great Oxidation Event (GOE) (~2.2 to ~2.4 Ga; Sessions et al., 2009). Higher median Pt/Os ratios (~6; e.g. Siebert et al., 2005) in pre-GOE Archean shales relative to Phanerozoic shales (~3.8; Jaffe et al., 2002) are consistent with greater Os

mobilization during crustal weathering after the GOE. Examination of Pt/Os and/or $^{186}Os/^{188}Os$ variations in Archean sediments in future studies may provide additional constraints on the redox conditions associated with continental weathering in the ancient past.

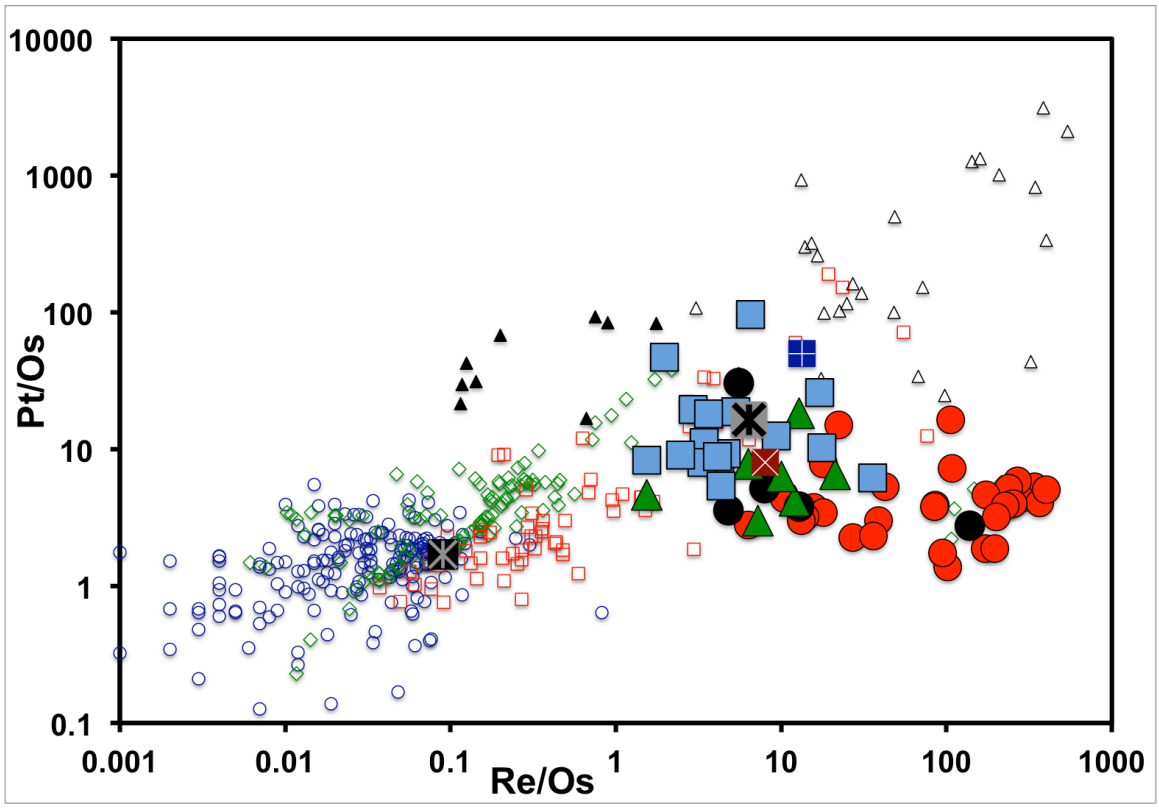

Figure 3.5 Pt/Os vs Re/Os in different mantle- and crustal-derived materials.

Re/Os and Pt/Os define a broad positive correlation in most materials. Data for black shales (filled red circles), non-marine shales (filled green triangles), coals (filled black circles), and loess (filled blue squares) are from McDaniel et al. (2004), Baioumy et al. (2011), Puecker-Ehrenbrink and Jahn (2001), and Horan et al. (1994). UCC Pt/Os and Re/Os estimates are from Wedepohl (1995) [filled red square with white cross], Schidmt et al. (1997) [filled blue square with white plus sign] and Puecker-Ehrenbrink and Jahn (2001) [filled grey square with black cross]. Data sources for peridotites (open circles), ocean island basalts (open squares), picrites (solid black triangles), komatiites (open diamonds), and MORB (open triangles) are from GEOROC and PetDB. PUM Pt/Os and

Re/Os estimate (filled black square with white cross) are from Chatterjee and Lassiter (2016) and Meisel et al. (2001).

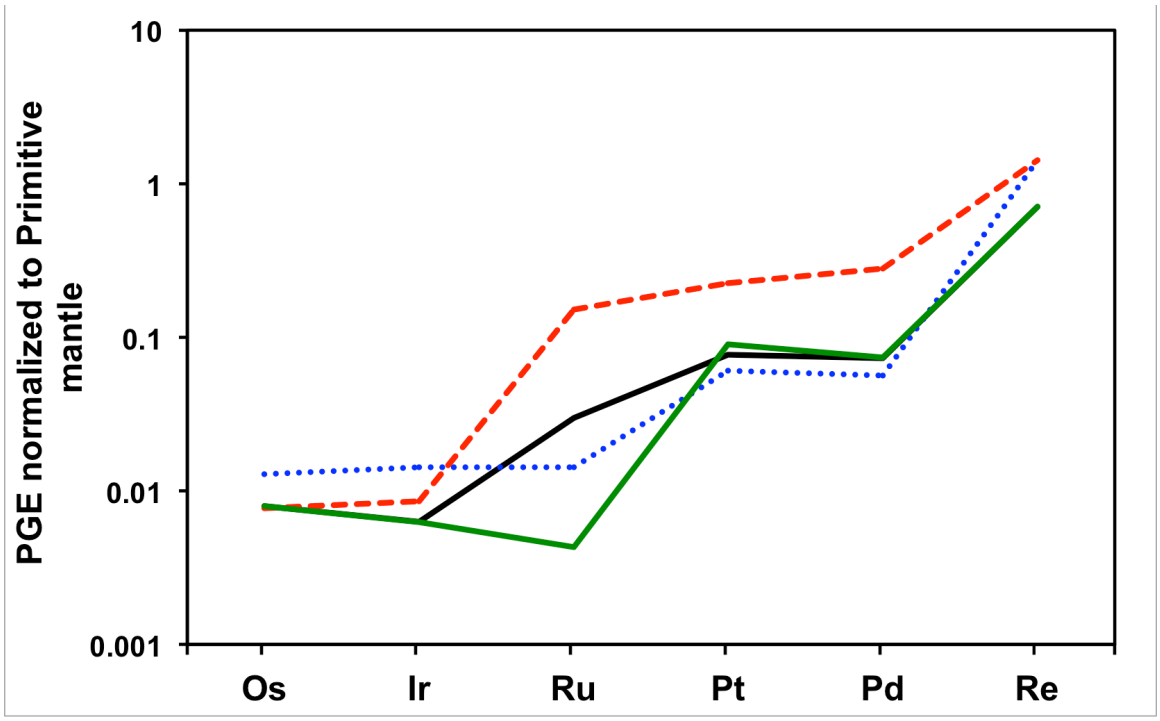

Figure 3.6 Estimate PGE concentrations in the upper continental crust.

Data is based on greywackes (blue dotted line; Wedepohl, 1995), loess [black solid line (Puecker-Ehrenbrink and Jahn, 2001) and green solid line (Park et al., 2012)], and impact melts (red dashed line; Schimdt et al., 1997). Primitive mantle values are from McDonough and Sun (1995).

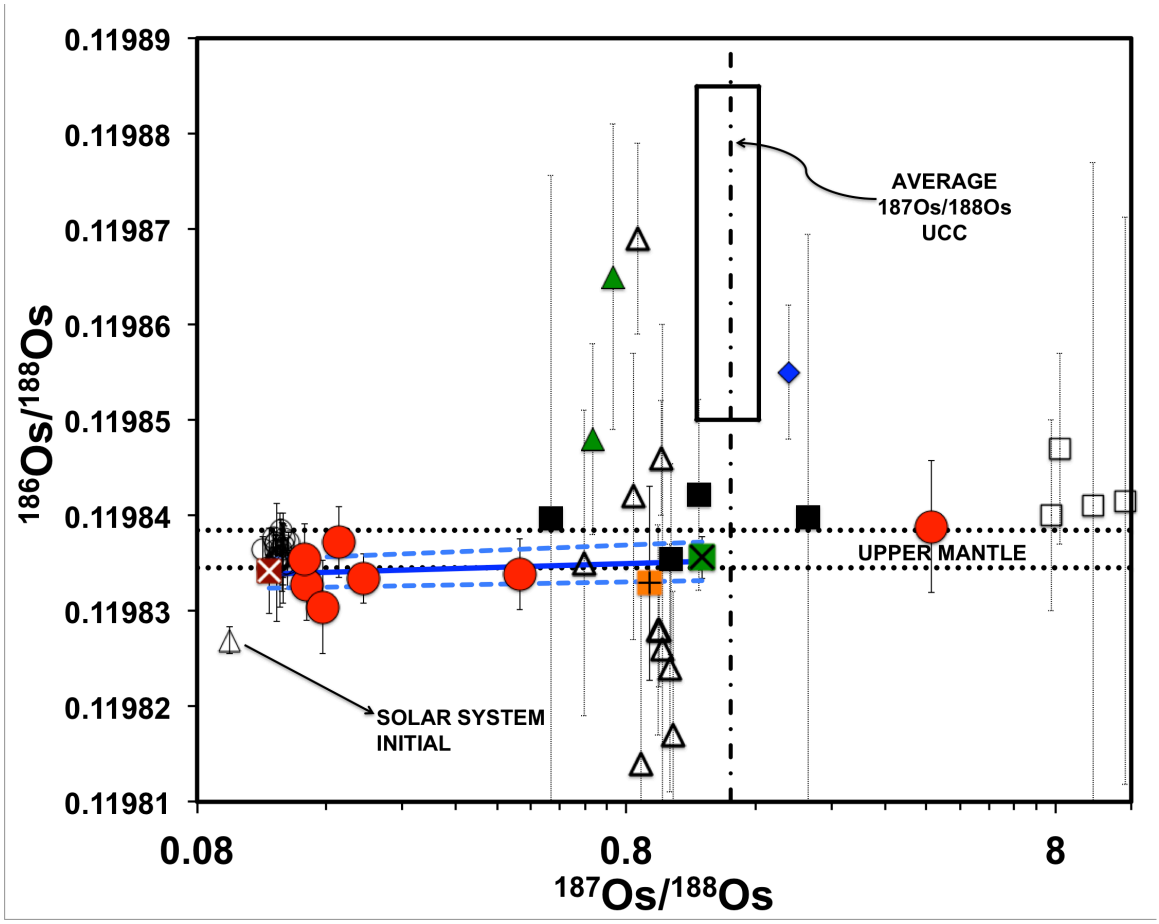

Figure 3.7 $^{187}Os/^{188}Os$-$^{186}Os/^{188}Os$ variations in steels.

Loess (filled green triangles), freshwater Mn nodules (filled blue diamonds), marine Mn nodules (open triangles; mean~ filled square with black plus sign) and black shales (present day-open squares; age corrected-filled black squares) are shown for comparison (McDaniel et al., 2004). $^{187}Os/^{188}Os$ and $^{186}Os/^{188}Os$ in steels are not statistically correlated. Regression of the $^{187}Os/^{188}Os$-$^{186}Os/^{188}Os$ trend with ± 2 SE uncertainties are shown by blue solid and dotted lines. Range of $^{186}Os/^{188}Os$ values reported for upper mantle peridotites (open circles) shown by black dashed lines (Chatterjee and Lassiter, 2016; Brandon et al., 2000). Estimated Os isotopic composition of the UCC (box) is based on McDaniel et al. (2004) and Puecker-Ehrenbrink and Jahn (2001). Inferred Os

isotopic composition of chromitites (filled red square with white cross) and BIF+coal (filled green square with black cross) are also shown. Solar system initial Os isotopic compositions are from Brandon et al. (2006) and Shirey and Walker (1998). Steel symbols same as figure 3.1.

5. CONCLUSIONS

Correlations between Os concentrations, $^{187}Os/^{188}Os$ and Cr content in steels are consistent with Os derivation from the primary components used in steel manufacture, namely iron ore (primarily BIFs), chromitite, and coke. Os in steels represents a mixture of unradiogenic, upper-mantle-like Os from chromitites and radiogenic, crustal-like Os from iron ores and coal. Pb isotopes in steel plot above the NHRL consistent, with Pb derivation from crustal components such as Banded Iron Formations and coals. Although steels span a wide range of $^{187}Os/^{188}Os$ (~0.1435-4.118), steels have mantle-like $^{186}Os/^{188}Os$ ratios, which are uncorrelated with $^{187}Os/^{188}Os$. Extrapolation of $^{187}Os/^{188}Os$-$^{186}Os/^{188}Os$ trends in steels to $^{187}Os/^{188}Os$ of chromitites yields a $^{186}Os/^{188}Os$ value of 0.1198339±15, which is similar to previous values reported for chromitites but slightly lower than present-day average upper mantle. Inferred and measured $^{186}Os/^{188}Os$ and measured $^{187}Os/^{188}Os$ for chromitites are consistent with derivation from mantle sources during the Archean to Proterozoic and subsequent evolution with sub-chondritic Pt/Os and Re/Os ratios. Extrapolation of $^{187}Os/^{188}Os$-$^{186}Os/^{188}Os$ trends in steels to the estimated $^{187}Os/^{188}Os$ of the crustal components used in steel manufacture (BIF+coals) yields a $^{186}Os/^{188}Os$ value of 0.1198352±20, which is indistinguishable from present-day upper mantle and similar to $^{186}Os/^{188}Os$ values reported for crustal weathering products (seawater derived marine Mn nodules and black shales). Inferred $^{186}Os/^{188}Os$ values for BIFs and coals are also indistinguishable from the PUM at the time of deposition and less radiogenic than bulk UCC at the time of deposition. Preferential weathering of crustal sulfides with low Pt/Os ratios and lower $^{186}Os/^{188}Os$ values than bulk UCC can explain

this discrepancy between crustal weathering products and the average upper continental crust.

Acknowledgements

This work was supported by NSF Grant EAR-1321937 and by the Jackson School of Geosciences, University of Texas at Austin.

Conclusions

The ^{190}Pt-^{186}Os isotope system is a powerful geochemical tool that can be utilized to answer a wide variety of geologic problems. However, this system faces a severe penalty due to the very low abundance of the parent isotope (^{190}Pt ~0.0129 % of Pt) and the incredibly long half-life (~460 Ga) that results in extremely limited natural variations in the course of Earth's history. Widespread utility of this isotope system has been largely limited due to the significant analytical challenge required for generating high precision $^{186}Os/^{188}Os$ system. This dissertation describes an analytical protocol that improves measurement precision of the ^{190}Pt-^{186}Os isotope system by identifying and reducing the primary sources of error. Next, the ^{190}Pt-^{186}Os system is utilized as a primary tool to examine different geochemical problems related to the chemical evolution of the upper mantle and the continental crust.

Examination of the various sources of analytical error affecting the $^{186}Os/^{188}Os$ isotope system indicates that Johnson noise during baseline integrations are the largest source of analytical error and can be improved by measuring baselines for longer durations. Use of within-run O isotope composition and the $^{192}Os/^{188}Os$ normalization is preferable although their effects on data correction are generally small. Extreme caution should be taken to monitor and exclude samples affected by interferences such as WO_3^- and/or organics that can result in anomalously high $^{186}Os/^{188}Os$ values.

Mantle peridotites from oceanic and continental settings reveal correlations between indices of melt depletion and $^{186}Os/^{188}Os$ consistent with long-term Pt/Os variations linked to melt depletion. Fertility-$^{186}Os/^{188}Os$ correlations allow extrapolations of PUM

$^{186}Os/^{188}Os$ and Pt/Os ratios. Our results are consistent with chondritic Pt/Os ratios in the Earth mantle, added by a late veneer of chondritic material. Although chondritic Re/Os and Pt/Os ratios in the Earth's mantle are consistent with late veneer addition, it is unclear why PUM Ru/Ir and Pd/Ir ratios are shifted towards supra- chondritic values. I propose that a small amount of metal and/or sulfide segregation to the Earth's core occurring simultaneously with late veneer addition can explain the observed departures in Ru/Ir and Pd/Ir ratios, without requiring appeal to additional exotic components. Variabilities in parent/daughter ratios (Pt/Os, Re/Os) and isotope ratios ($^{186}Os/^{188}Os$, $^{187}Os/^{188}Os$) allow us to infer timescales required for mantle heterogeneities to be destroyed by convective stirring in the Earth's mantle. Our results are consistent with convective stirring that involves the whole mantle.

Industrial steels allow a unique possibility to place constraints on the composition of the upper continental crust. Iron ores and coals used in steelmaking process are products of sediments derived from crustal weathering. Therefore, Os in steels inherited from iron ores and coals likely reflect the isotopic composition of weathered products of the continental crust. I demonstrate that the Os and Pb isotopic compositions in industrial steels in fact to first order reflect the composition of their primary components-namely iron ore, coals and chromititites. High Re/Os and Pt/Os ratios in a majority of crustal materials leads to radiogenic Os isotope compositions ($^{186}Os/^{188}Os$ and $^{187}Os/^{188}Os$) through ingrowth and is consistent with the observed Os isotope compositions measured in most direct crustal samples. Utilizing the Os isotopic trends in steels ($^{187}Os/^{188}Os$-$^{186}Os/^{188}Os$), I inferred that $^{186}Os/^{188}Os$ in both iron ores and/or coals are less radiogenic

than the bulk upper continental crust and similar to other weathering products of the continental crust despite having radiogenic present-day and initial $^{187}Os/^{188}Os$ values. I propose that the systematically lower $^{186}Os/^{188}Os$ values in weathered products of the continental crust might result from preferential removal of sulfides from bulk crustal rocks with low long-term Pt/Os ratios during oxidative weathering processes. Increase in the Earth's atmospheric oxygen levels following the Great Oxidation Event (GOE) may have destabilized crustal sulfides and therefore, resulted in their preferential removal during weathering.

Appendices

APPENDIX A: SUPPLEMENT TO CHAPTER 1

A.1 Data reduction steps

The raw Os data was corrected for instrumental mass fractionation using the exponential law. Except for evaluating the effects of mass fractionation using different normalizing ratios and different O isotopic compositions, correction was done relative to $^{192}OsO_3/^{188}OsO_3 = 3.092585$. This value is based on the normalizing value for $^{192}Os/^{188}Os = 3.083$ and assuming an O isotopic composition equal to the measured tank O isotopic composition. Although this value does not represent the actual O isotopic composition during a given analysis, subsequent stages of data correction use the within-run O isotopic composition and correct any residual mass fractionation. The exponential factors of mass fractionation correction for Pt (β_{Pt}) and Os (β_{Os}) are not correlated. Therefore, the ratios 228/236-233/236 measured in the interference routine were corrected for mass fractionation using a β_{Pt} obtained by correcting the measured $^{196}PtO_2/^{198}PtO_2$ to $^{196}PtO_2/^{198}PtO_2 = 3.495683$. This normalizing value is based on natural $^{196}Pt/^{198}Pt = 3.5239$ (Rosman et al., 1998) and assuming O isotopic composition to be equal to the value measured for our O tank. Later stages of data correction determine β_{Pt} using the measured, within-run O isotopic composition. Ratios 241/236 and 242/236 measured for determining the in-run O isotopic composition were not corrected for mass fractionation as it is the fractionated O isotopic composition that combines with Os to form OsO_3^- and should be used for oxide correction (Luguet et al., 2008b). All the ratios outside 2σ of the

mean were removed. The average value after removal of 2σ outliers was used in the next stages of data correction.

Although the effect of PtO_2^- interferences on the $^{186}OsO_3^-$ (234) peak is insignificant, PtO_2^- interferences could mask other interferences such as WO_3^- and organics, that have a large effect on the 234 peak. Therefore, monitoring and stripping of PtO_2^- interferences was considered important. PtO_2^- interferences on $^{184}OsO_3^-$ (232) and $^{186}OsO_3^-$ (234) peaks were calculated and stripped using measured IC (Ion counter) analyses of 228/$^{188}Os^{16}O_3$ measured before and after the Os isotope routine. A linear behavior for the Pt/Os signal during the course of a run was assumed to calculate the mean PtO_2^- signal during an analysis. Assuming the peak at 228 to be entirely PtO_2^-, the signal intensity at mass 228 corresponding to the $^{196}Pt^{16}O_2^-$ signal was determined by subtracting the rest of PtO_2^- peaks (using measured tank O isotopic composition) from the measured 228/236. Using relative abundances of the different Pt isotopes and measured $^{18}O/^{16}O$, $^{17}O/^{16}O$ from the oxygen tank, the proportion of different species of PtO_2^- (Table A.2) that would be present in the 229-234 mass range were calculated and subtracted from the measured peaks. β_{Pt} was calculated using raw 228/230 for normalization making residual counts on 230 after Pt subtraction ≡ 0. The residual peak at 231 was investigated for any potential WO_3^- interference, organics, or other unknown interferences. Median residual count at 231 was 42 cps but occasional runs have much higher residual counts. Runs that have shown high residual counts on 231 and corresponding higher $^{184}Os/^{188}Os$ and/or $^{186}Os/^{188}Os$ have not been included in the study as these are likely to have been compromised by WO_3^-, organics or some other unknown interference. Pt correction is

repeated using the determined within-run O isotopic composition for calculating the Pt-oxides in the subsequent stages of data correction.

Oxygen isotopic composition of the tank was determined at the beginning of this study by Dual Inlet isotope ratio measurement using Thermo Electron MA (253) Isotope Ratio Mass Spectrometer and was used in the first step of the oxide correction. The tank O isotopic composition is $^{18}O/^{16}O$ = 0.0020608 and $^{17}O/^{16}O$ =0.0003852. Subsequent steps use the O isotopic composition determined for a run. The within-run O isotopic composition was determined by measuring 241/236 and 242/236 ratios either using peak hopping during the main Os routine or by measurement in separate routines, run prior to and after the main Os routine. Masses 240, 241 and 242 represent various combinations of the O isotopes with ^{187}Os, ^{188}Os, ^{189}Os, ^{190}Os and ^{192}Os (Table A.2). $^{17}O/^{16}O$ & $^{18}O/^{16}O$ was determined by considering all oxide peaks from 241/240 and 242/240 ratios. Luguet et al., (2008b) only considered the predominant oxide peaks of $^{192}Os^{16}O_3^-$, $^{192}Os^{16}O_2{}^{17}O^-$ and $^{192}Os^{16}O_2{}^{18}O^-$ on 240, 241 and 242 respectively as the magnitudes of other oxide peaks are much smaller. There is only a 2.2 per mil difference between data corrected using our approach from the approach of Luguet et al., (2008b) and hence is not significant. Using the determined O isotopic composition, isobaric interferences from ^{17}O and ^{18}O on each of the masses from 233-238 and 240 were calculated and stripped. The dominant Os isotopic peak and the corresponding interferences for a given mass are listed in Table A.2. After stripping oxide interferences, the metal Os isotopic ratios were obtained by dividing the $Os^{16}O_3^-$ peak with the $^{188}Os^{16}O_3^-$ peak. Finally an instrumental mass fractionation correction was applied to all the ratios (232/236-238/236, 240/236)

with ^{192}Os /^{188}Os = 3.083 using the exponential law. $^{189}Os/^{188}Os$ = 1.21973 or 1.21978 was used for instrumental mass fractionation correction while evaluating the effect of using the $^{189}Os/^{188}Os$ normalization.

Table A1. Cup configuration for Os and O isotopic measurement						
Combined Os and O isotopic measurement routine						
CUP	L4	L3	L2	L1	Integration time	Idle time
Mass	232	233	234	235		
Sequence 1	$^{184}Os^{16}O_3^-$	$^{185}Re^{16}O_3^-$	$^{186}Os^{16}O_3^-$	$^{187}Os^{16}O_3^-$	16.777 s	3 s
Mass				239		
Sequence 2				$^{190}Os^{16}O_2{}^{17}O^-$	2.097 s	3 s
Separate O isotopic measurement routine (2nd half of campaign)						
Mass	232	233	234	235		
Sequence 1	$^{184}Os^{16}O_3^-$	$^{185}Re^{16}O_3^-$	$^{186}Os^{16}O_3^-$	$^{187}Os^{16}O_3^-$	2.097 s	5 s
Mass	239	240	241	242		
Sequence 2	$^{190}Os^{16}O_2{}^{17}O^-$	$^{192}Os^{16}O_3^-$	$^{192}Os^{16}O_2{}^{17}O^-$	$^{192}Os^{16}O_2{}^{18}O^-$	2.097 s	5 s
Mass	234	235	236	237		
Sequence 3	$^{186}Os^{16}O_3^-$	$^{187}Os^{16}O_3^-$	$^{188}Os^{16}O_3^-$	$^{189}Os^{16}O_3^-$	2.097 s	3 s
Combined Os and O isotopic measurement routine						
CUP	Axial	H1	H2	H3	Integration time	Idle time
Mass	236	237	238	240		
Sequence 1	$^{188}Os^{16}O_3^-$	$^{189}Os^{16}O_3^-$	$^{190}Os^{16}O_3^-$	$^{192}Os^{16}O_3^-$	16.777 s	3 s
Mass	240	241	242			
Sequence 2	$^{192}Os^{16}O_3^-$	$^{192}Os^{16}O_2{}^{17}O^-$	$^{192}Os^{16}O_2{}^{18}O^-$		2.097 s	3 s
Separate O isotopic measurement routine (2nd half of campaign)						
Mass	236	237	238	240		
Sequence 1	$^{188}Os^{16}O_3^-$	$^{189}Os^{16}O_3^-$	$^{190}Os^{16}O_3^-$	$^{192}Os^{16}O_3^-$	2.097 s	5 s
Mass						
Sequence 2					2.097 s	5 s
Mass	238	239	240	242		
Sequence 3	$^{190}Os^{16}O_3^-$	$^{190}Os^{16}O_2{}^{17}O^-$	$^{192}Os^{16}O_3^-$	$^{192}Os^{16}O_2{}^{18}O^-$	2.097 s	3 s

Table A.1 Cup configuration for Os and O isotopic measurement

Table A2. List of OsO_3^- , ReO3- , PtO_2^- interferences on mass 228-242

Mass Main OsO_3^- on the mass spectrum	228	229	230	231	232 $^{184}Os^{16}O_3^-$	233
Isobaric OsO_3^- / ReO_3^-/PtO_2^- interference	$^{196}Pt^{16}O_2^-$ $^{192}Pt^{18}O_2^-$ $^{194}Pt\ ^{16}O\ ^{18}O^-$ $^{194}Pt\ ^{17}O\ ^{17}O^-$ $^{195}Pt\ ^{16}O\ ^{17}O^-$	$^{194}Pt\ ^{17}O\ ^{18}O^-$ $^{195}Pt\ ^{16}O\ ^{18}O^-$ $^{195}Pt\ ^{17}O_2^-$ $^{196}Pt\ ^{16}O^{17}O^-$	$^{194}Pt\ ^{18}O\ ^{18}O^-$ $^{195}Pt\ ^{17}O\ ^{18}O^-$ $^{196}Pt\ ^{16}O^{18}O^-$ $^{196}Pt\ ^{17}O^{17}O^-$ $^{198}Pt\ ^{16}O_2^-$	$^{195}Pt\ ^{18}O\ ^{18}O^-$ $^{196}Pt\ ^{17}O^{18}O^-$ $^{198}Pt\ ^{16}O^{17}O^-$	$^{196}Pt\ ^{18}O^{18}O^-$ $^{198}Pt\ ^{16}O^{18}O^-$ $^{198}Pt\ ^{17}O^{17}O^-$	$^{185}Re^{16}O_3^-$ $^{184}Os^{16}O_2{}^{17}O^-$ $^{198}Pt\ ^{17}O^{18}O^-$
Mass Main OsO_3^- on the mass spectrum	234 $^{186}Os^{16}O_3^-$	235 $^{187}Os^{16}O_3^-$	236 $^{188}Os^{16}O_3^-$	237 $^{189}Os^{16}O_3^-$	238 $^{190}Os^{16}O_3^-$	239
Isobaric OsO_3^- / ReO_3^-/PtO_2^- interference	$^{184}Os^{16}O_2{}^{18}O^-$ $^{184}Os^{17}O_2{}^{16}O^-$ $^{185}Re^{16}O_2{}^{17}O^-$ $^{198}Pt\ ^{18}O^{18}O^-$	$^{186}Os^{16}O_2{}^{17}O^-$ $^{184}Os^{17}O_3^-$ $^{184}Os^{16}O^{17}O^{18}O^-$ $^{187}Re^{16}O_3^-$ $^{185}Re^{16}O_2{}^{18}O^-$ $^{185}Re^{17}O_2{}^{16}O^-$	$^{187}Os^{16}O_2{}^{17}O^-$ $^{186}Os^{16}O_2{}^{18}O^-$ $^{186}Os^{17}O_2{}^{16}O^-$ $^{184}Os^{17}O_2{}^{18}O^-$ $^{184}Os^{16}O^{18}O_2^-$ $^{185}Re^{17}O_3^-$ $^{185}Re^{16}O^{17}O^{18}O^-$ $^{187}Re^{16}O_2{}^{17}O^-$	$^{188}Os^{16}O_2{}^{17}O^-$ $^{187}Os^{16}O_2{}^{18}O^-$ $^{187}Os^{17}O_2{}^{16}O^-$ $^{186}Os^{17}O_3^-$ $^{186}Os^{16}O^{17}O^{18}O^-$ $^{184}Os^{17}O^{18}O_2^-$ $^{185}Re^{17}O_2{}^{18}O^-$ $^{185}Re^{16}O^{18}O_2^-$ $^{187}Re^{16}O_2{}^{18}O^-$ $^{187}Re^{17}O_2{}^{16}O^-$	$^{189}Os^{16}O_2{}^{17}O^-$ $^{188}Os^{16}O_2{}^{18}O^-$ $^{188}Os^{17}O_2{}^{16}O^-$ $^{187}Os^{17}O_3^-$ $^{187}Os^{16}O^{17}O^{18}O^-$ $^{186}Os^{17}O_2{}^{18}O^-$ $^{186}Os^{16}O^{18}O_2^-$ $^{184}Os^{18}O_3^-$ $^{185}Re^{17}O^{18}O_2^-$ $^{187}Re^{17}O_3^-$ $^{187}Re^{16}O^{17}O^{18}O^-$	$^{190}Os^{16}O_2{}^{17}O^-$ $^{189}Os^{16}O_2{}^{18}O^-$ $^{189}Os^{17}O_2{}^{16}O^-$ $^{188}Os^{17}O_3^-$ $^{188}Os^{16}O^{17}O^{18}O^-$ $^{187}Os^{17}O_2{}^{18}O^-$ $^{187}Os^{16}O^{18}O_2^-$ $^{186}Os^{17}O^{18}O_2^-$ $^{185}Re^{18}O_3^-$ $^{187}Re^{17}O_2{}^{18}O^-$ $^{187}Re^{16}O^{18}O_2^-$
Mass Main OsO_3^- on the mass spectrum	240 $^{192}Os^{16}O_3^-$	241	242			
Isobaric OsO_3^- / ReO_3^-/PtO_2^- interference	$^{190}Os^{16}O_2{}^{18}O^-$ $^{190}Os^{17}O_2{}^{16}O^-$ $^{189}Os^{17}O_3^-$ $^{189}Os^{16}O^{17}O^{18}O^-$ $^{188}Os^{17}O_2{}^{18}O^-$ $^{188}Os^{16}O^{18}O_2^-$ $^{187}Os^{17}O^{18}O_2^-$ $^{186}Os^{18}O_3^-$ $^{187}Re^{17}O^{18}O_2^-$	$^{192}Os^{16}O_2{}^{17}O^-$ $^{190}Os^{17}O_3^-$ $^{190}Os^{16}O^{17}O^{18}O^-$ $^{189}Os^{17}O_2{}^{18}O^-$ $^{189}Os^{16}O^{18}O_2^-$ $^{188}Os^{17}O^{18}O_2^-$ $^{187}Os^{18}O_3^-$ $^{187}Re^{18}O_3^-$	$^{192}Os^{16}O_2{}^{18}O^-$ $^{192}Os^{17}O_2{}^{16}O^-$ $^{190}Os^{17}O_2{}^{18}O^-$ $^{190}Os^{16}O^{18}O_2^-$ $^{189}Os^{17}O^{18}O_2^-$ $^{188}Os^{18}O_3^-$			

Table A.2 Os-trioxides and their potential isobaric interferences on the mass spectrum between 228 and 242

Table A3. Os isotopic compositions of repeat measurements of the UMD standard

UMD Standard		$^{184}Os/^{188}Os$	2 SE	$^{186}Os/^{188}Os$	2 SE	$^{187}Os/^{188}Os$	2 SE	$^{189}Os/^{188}Os$	2 SE	$^{190}Os/^{188}Os$	2 SE
UMD 1		0.0013002	0.0000023	0.1198485	0.0000031	0.1137968	0.0000026	1.2197274	0.0000081	1.9837974	0.0000107
UMD 2		0.0013082	0.0000019	0.1198476	0.0000030	0.1137936	0.0000026	1.2197307	0.0000079	1.9838058	0.0000101
UMD 3		0.0013028	0.0000018	0.1198433	0.0000023	0.1137937	0.0000024	1.2197327	0.0000069	1.9837970	0.0000089
UMD 4		0.0013003	0.0000019	0.1198449	0.0000025	0.1137997	0.0000029	1.2197317	0.0000067	1.9837956	0.0000090
UMD 5		0.0013062	0.0000021	0.1198487	0.0000027	0.1137947	0.0000031	1.2197167	0.0000080	1.9837879	0.0000092
UMD 6		0.0012993	0.0000019	0.1198507	0.0000034	0.1137925	0.0000028	1.2197266	0.0000078	1.9838058	0.0000098
UMD 7		0.0013051	0.0000019	0.1198436	0.0000029	0.1137946	0.0000026	1.2197250	0.0000075	1.9837958	0.0000094
UMD 8		0.0013057	0.0000021	0.1198477	0.0000025	0.1137913	0.0000026	1.2197228	0.0000072	1.9837967	0.0000088
UMD 9		0.0012990	0.0000016	0.1198427	0.0000025	0.1137923	0.0000025	1.2197156	0.0000070	1.9837949	0.0000078
UMD 10		0.0013015	0.0000014	0.1198483	0.0000021	0.1137951	0.0000023	1.2197208	0.0000061	1.9837881	0.0000079
UMD 11		0.0013130	0.0000024	0.1198409	0.0000034	0.1137947	0.0000028	1.2197404	0.0000075	1.9837886	0.0000104
UMD 12	30 sec	0.0013013	0.0000007	0.1198456	0.0000014	0.1137924	0.0000012	1.2197282	0.0000044	1.9837907	0.0000052
UMD 13	Baselines	0.0013026	0.0000012	0.1198426	0.0000018	0.1137933	0.0000016	1.2197239	0.0000050	1.9837881	0.0000065
UMD 14	n=34	0.0013025	0.0000013	0.1198451	0.0000019	0.1137923	0.0000017	1.2197210	0.0000050	1.9837936	0.0000072
UMD 15		0.0012996	0.0000020	0.1198427	0.0000029	0.1137837	0.0000026	1.2197311	0.0000076	1.9837984	0.0000093
UMD 16		0.0013024	0.0000012	0.1198485	0.0000019	0.1137928	0.0000018	1.2197412	0.0000055	1.9837913	0.0000065
UMD 17		0.0013004	0.0000009	0.1198448	0.0000017	0.1137893	0.0000014	1.2197272	0.0000046	1.9837927	0.0000059
UMD 18		0.0013091	0.0000015	0.1198463	0.0000025	0.1137890	0.0000022	1.2197353	0.0000064	1.9838050	0.0000075
UMD 19		0.0013053	0.0000014	0.1198472	0.0000023	0.1137933	0.0000021	1.2197272	0.0000061	1.9838036	0.0000078
UMD 20		0.0013028	0.0000031	0.1198412	0.0000035	0.1137900	0.0000033	1.2197285	0.0000111	1.9837746	0.0000137
UMD 21		0.0012990	0.0000019	0.1198471	0.0000025	0.1137971	0.0000028	1.2197312	0.0000064	1.9837750	0.0000091
UMD 22		0.0013099	0.0000023	0.1198452	0.0000034	0.1137957	0.0000026	1.2197120	0.0000074	1.9837852	0.0000096
UMD 23		0.0012994	0.0000021	0.1198522	0.0000032	0.1137849	0.0000033	1.2197195	0.0000104	1.9837788	0.0000105
UMD 24		0.0013041	0.0000016	0.1198464	0.0000021	0.1137915	0.0000020	1.2197414	0.0000064	1.9837933	0.0000081
UMD 25		0.0013051	0.0000008	0.1198475	0.0000013	0.1137943	0.0000012	1.2197372	0.0000041	1.9838062	0.0000057
UMD 26		0.0013066	0.0000018	0.1198525	0.0000024	0.1137946	0.0000026	1.2197403	0.0000062	1.9838102	0.0000085
UMD 27		0.0013020	0.0000014	0.1198494	0.0000021	0.1137912	0.0000021	1.2197424	0.0000055	1.9837979	0.0000076
UMD 28		0.0013036	0.0000013	0.1198474	0.0000019	0.1137960	0.0000014	1.2197348	0.0000057	1.9838071	0.0000068
UMD 29		0.0013031	0.0000010	0.1198461	0.0000017	0.1137944	0.0000016	1.2197325	0.0000048	1.9838024	0.0000063
UMD 30		0.0013112	0.0000013	0.1198505	0.0000016	0.1137927	0.0000016	1.2197367	0.0000056	1.9837817	0.0000075
UMD 31		0.0013040	0.0000023	0.1198482	0.0000030	0.1137876	0.0000026	1.2197360	0.0000080	1.9837927	0.0000097
UMD 32		0.0013018	0.0000013	0.1198478	0.0000024	0.1137903	0.0000020	1.2197262	0.0000065	1.9838049	0.0000074
UMD 33		0.0013054	0.0000014	0.1198467	0.0000022	0.1137885	0.0000022	1.2197200	0.0000062	1.9837875	0.0000076
UMD 34		0.0013053	0.0000014	0.1198468	0.0000021	0.1137931	0.0000019	1.2197211	0.0000064	1.9837702	0.0000081
UMD 35		0.0013028	0.0000014	0.1198490	0.0000020	0.1137896	0.0000019	1.2197278	0.0000062	1.9837873	0.0000079
UMD 36		0.0013013	0.0000012	0.1198465	0.0000018	0.1137920	0.0000020	1.2197282	0.0000062	1.9837824	0.0000078
UMD 37		0.0013028	0.0000013	0.1198465	0.0000023	0.1137938	0.0000021	1.2197232	0.0000060	1.9837888	0.0000085
UMD 38		0.0013028	0.0000011	0.1198450	0.0000019	0.1137935	0.0000019	1.2197269	0.0000060	1.9837742	0.0000074
UMD 39		0.0013068	0.0000011	0.1198470	0.0000018	0.1137933	0.0000018	1.2197225	0.0000060	1.9837767	0.0000070
UMD 40		0.0013065	0.0000006	0.1198494	0.0000013	0.1137920	0.0000011	1.2197167	0.0000044	1.9837854	0.0000057
UMD 41		0.0013055	0.0000012	0.1198480	0.0000020	0.1137942	0.0000020	1.2197268	0.0000063	1.9837933	0.0000089
UMD 42	5 min	0.0013038	0.0000013	0.1198500	0.0000020	0.1137920	0.0000019	1.2197274	0.0000065	1.9837935	0.0000096
UMD 43	Baselines	0.0012993	0.0000014	0.1198472	0.0000021	0.1137912	0.0000021	1.2197249	0.0000059	1.9837683	0.0000092
UMD 44	n=23	0.0013054	0.0000018	0.1198455	0.0000025	0.1137948	0.0000026	1.2197271	0.0000068	1.9837991	0.0000108
UMD 45		0.0013075	0.0000015	0.1198496	0.0000023	0.1137936	0.0000021	1.2197231	0.0000068	1.9837894	0.0000082
UMD 46		0.0013053	0.0000011	0.1198477	0.0000021	0.1137939	0.0000020	1.2197175	0.0000062	1.9837672	0.0000117
UMD 47		0.0013034	0.0000012	0.1198475	0.0000019	0.1137924	0.0000017	1.2197202	0.0000058	1.9837667	0.0000077
UMD 48		0.0013095	0.0000015	0.1198479	0.0000022	0.1137900	0.0000018	1.2197195	0.0000056	1.9837769	0.0000074
UMD 49		0.0013050	0.0000012	0.1198492	0.0000021	0.1137883	0.0000020	1.2197436	0.0000059	1.9837497	0.0000069
UMD 50		0.0013083	0.0000015	0.1198466	0.0000025	0.1137903	0.0000025	1.2197296	0.0000071	1.9837446	0.0000102
UMD 51		0.0013072	0.0000018	0.1198499	0.0000026	0.1137920	0.0000026	1.2197386	0.0000075	1.9837432	0.0000109
UMD 52		0.0013063	0.0000009	0.1198499	0.0000016	0.1137935	0.0000016	1.2197425	0.0000052	1.9837522	0.0000067
UMD 53		0.0013053	0.0000013	0.1198462	0.0000019	0.1137925	0.0000018	1.2197189	0.0000053	1.9837733	0.0000071
UMD 54		0.0013039	0.0000016	0.1198460	0.0000026	0.1137877	0.0000026	1.2197091	0.0000090	1.9837510	0.0000090
UMD 55		0.0013045	0.0000012	0.1198451	0.0000020	0.1137854	0.0000018	1.2197400	0.0000062	1.9837778	0.0000073
UMD 56		0.0013042	0.0000011	0.1198434	0.0000021	0.1137861	0.0000019	1.2197287	0.0000059	1.9837797	0.0000071
UMD 57		0.0013049	0.0000014	0.1198468	0.0000022	0.1137917	0.0000021	1.2197285	0.0000063	1.9838053	0.0000084

Table A.3 Os isotopic compositions of repeat measurements of the UMD standard

APPENDIX B: SUPPLEMENT TO CHAPTER 2

B.1 Analytical Methods

Most of the samples selected for this study have been previously analyzed for whole rock and mineral major and trace element compositions and detailed procedures are reported elsewhere (Bizimis et al., 2007; Byerly and Lassiter, 2012, 2014, 2015; Lassiter et al., 2014). For the remaining samples, I characterized whole rock and mineral major and trace element compositions using the following procedures. For bulk analyses, a portion of each sample was coarse crushed, washed in DI, dried and powdered in a ceramic mill. A diamond saw was used to remove any basaltic rind before crushing and care was taken to remove any saw marks using Si-C sand paper. Whole rock major and trace element compositions were analyzed via XRF and ICP-MS at the Geo-Analytical laboratory, Washington State University using procedures outlined in Jenner et al. (1990), Knack et al. (1994), and Johnson et al. (1999). Duplicates were run on two peridotite samples measured during the same analytical campaign as for the samples reported in this study. Duplicate measurements were reproducible to within 5% for most major elements, 10% for P, 10% for Al and Ca in CC-07-1-35 and 20% for Ti (Table B.5). Further, the potassium concentration in sample CC-07-1-35 was very low (0.01%) and was poorly reproducible. Most trace elements measured by XRF were reproducible within ~10% except Cu which was reproducible within ~25 % (Table B.5). In addition, sample 07EB 4-01 reported in this study was run in duplicate to assess the reproducibility of trace elements using the ICP-MS procedure. Duplicate measurements were reproducible to within 10% for most trace elements, 5 % for La, Eu, Ba and Ta, 15% for Dy, Ho, Er, Lu,

U and Rb, 30% for Yb, Nb, Hf and Zr and 40 % for Th (Table B.5). Accuracy of the XRF analyses were further constrained by analyzing peridotite standard JP-1. Measured values are accurate within ~2% for Si, Fe, Al, Mg and Ca and within ~10 % for K. Ti, Na and P showed poor reproducibility consistent with their very low concentrations in the standard (Table B.6). Trace elements are accurate within ~3% except for V, Ba, Rb, Zr and Zn, which are accurate within ~10-25 % (Table B.6).

Clinopyroxene, orthopyroxene, spinel and olivine were picked for mineral major and trace element analyses. Mineral major element compositions were analyzed using a JEOL JXA-8200 MPA at the University of Texas at Austin and a Cameca SX-50 at Texas A&M University, College Station. Analyses were performed with 15kV accelerating voltage and a 10nA beam current, using a focused beam. Reproducibility of mineral major element compositions was assessed using either the repeat analyses of the same grain or analyses of multiple grains from the same peridotite. Reported major element compositions are reproducible within 5% (2 SD). Clinopyroxene trace element compositions were measured by LA-ICP-MS at UT Austin using an Agilent 7500ce quadrupole with a New Wave UP-193FX laser system following methods outlined in Byerly and Lassiter (2012). The laser was operated at 10 Hz, 50% energy on 150 μm pre-ablated spots and dwell time was 60s with 40s washout time. NIST-612 was used as a primary standard and BCR-2g as a secondary standard. Average analyses of all elements for BCR-2g were accurate to better than 5% of the accepted values and Na, Y, Zr, Gd, Hf and Pb were accurate to better than 10% (Table B.7). Duplicate analyses of the BCR-2g

standard were reproducible to within 10% (2 SD) (Byerly and Lassiter, 2012; Lassiter et al., 2014).

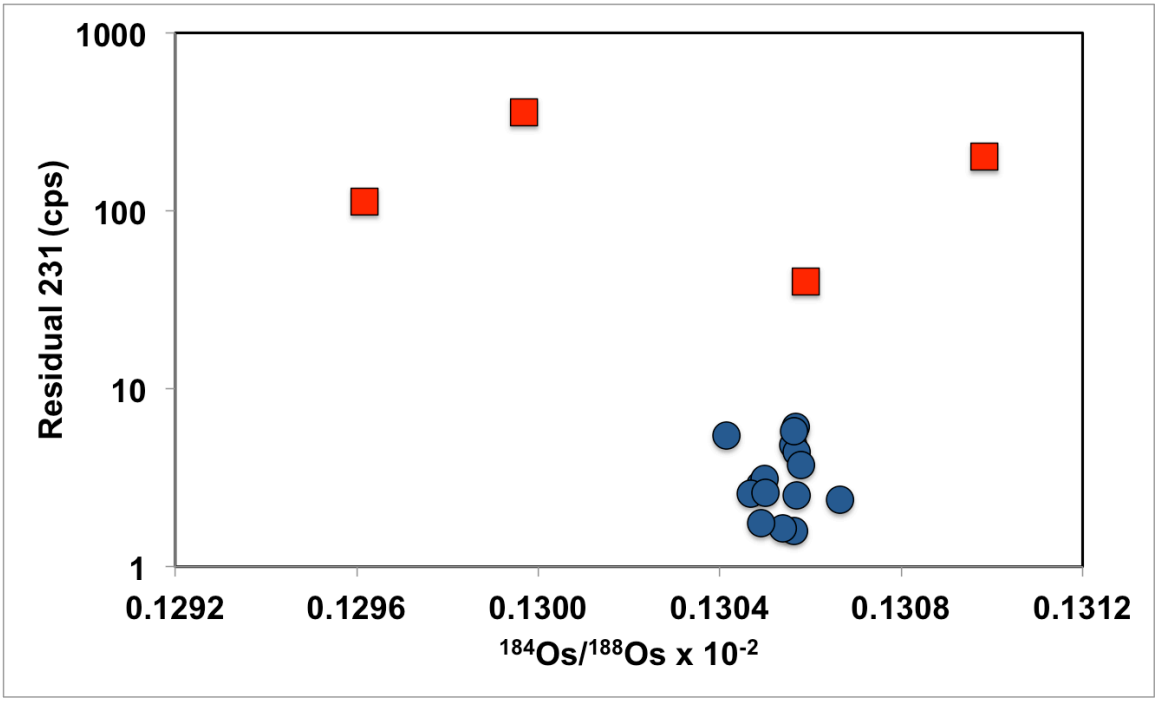

Figure B.1 Residual 231 vs $^{184}Os/^{188}Os$ x (10^{-2}) in peridotites

Blue circles are peridotites with normal $^{184}Os/^{188}Os$ (average: 0.001305±3) and residual 231 counts (<10 cps) after correcting for Pt interferences. Red squares (Sample #s: PS 66-253-6-6, PS 66-251-57, PS 66-255-7 and PS 66-253-36-1) are samples with 'anomalous' $^{184}Os/^{188}Os$ (except sample #- PS-66-255-7) and residual 231.

Table B.1 Bulk whole rock major and trace element concentrations

Sample #	PS66-253-6-6	PS66-251-57	PS66-255-7	PS66-251-47	PS66-253-36-1	PS66-262-106
Data Source	**1**	**2**	**2**	**2**	**1**	**2**
Major elements						
SiO2	36.74	39.63	41.64	38.05	36.08	37.60
TiO2	0.01	0.04	0.08	0.04	0.02	0.02
Al2O3	1.12	1.47	2.42	1.96	1.01	1.04
FeO*	7.43	6.87	7.14	7.57	6.44	7.26
MnO	0.11	0.09	0.16	0.11	0.08	0.11
MgO	34.80	37.83	33.87	34.31	36.08	36.46
CaO	4.10	0.88	0.42	3.27	2.40	5.52
Na2O	0.17	0.10	0.27	0.13	0.12	0.19
K2O	0.01	0.01	0.04	0.01	0.01	0.01
P2O5	0.04	0.02	0.01	0.03	0.00	0.03
Cr2O3					0.38	
Sum	84.52	86.93	86.05	85.48	82.62	88.24
LOI (%)	14.71	12.53	12.98	13.33	17.00	11.35
Total with LOI	99.24	99.46	99.04	98.81	98.31	99.59
Normalized Major Elements						
SiO2	43.46	45.59	48.39	44.52	43.67	42.61
TiO2	0.01	0.05	0.09	0.05	0.02	0.02
Al2O3	1.32	1.69	2.81	2.29	1.22	1.18
FeO*	8.79	7.91	8.30	8.86	7.80	8.23
MnO	0.13	0.10	0.19	0.13	0.10	0.12
MgO	41.17	43.52	39.35	40.14	43.67	41.32
CaO	4.85	1.01	0.49	3.82	2.90	6.26
Na2O	0.20	0.11	0.31	0.16	0.15	0.22
K2O	0.02	0.01	0.05	0.01	0.01	0.01
P2O5	0.04	0.02	0.01	0.03	0.00	0.03
Total	100.00	100.00	100.00	100.00	99.54	100.00
Mg #	89.30	90.75	89.42	88.98	90.89	89.95
Trace element (XRF)						
Ni	2097	2070	1870	1961		2202
Cr	2801	2423	3873	2126		2265
Sc	8.68	10.07	11.98	12.73		7.38
V	85.0	49.5	69.8	82.5		41.5
Ga	0.42	1.40	3.20	1.54		1.95
Cu	13.0	12.7	38.4	13.0		11.3
Zn	52.2	44.9	47.6	50.2		40.0
Trace element (ICP-MS)						
La	0.24		0.16			0.09
Ce	0.27		0.35			0.17
Pr	0.05		0.06			0.03
Nd	0.24		0.31			0.16
Sm	0.05		0.15			0.06
Eu	0.01		0.08			0.02
Gd	0.04		0.26			0.07
Tb	0.01		0.06			0.02
Dy	0.07		0.41			0.12
Ho	0.02		0.09			0.03
Er	0.05		0.27			0.07
Tm	0.01		0.04			0.01
Yb	0.07		0.25			0.08
Lu	0.01		0.04			0.01
Ba	1.15		0.67			1.67
Th	0.04		0.02			0.02
Nb	0.04		0.10			0.03
Y	0.51		2.16			0.71
Hf	0.02		0.08			0.07
Ta	0.00		0.01			0.00
U	0.89		0.81			0.77
Pb	0.12		2.71			0.08
Rb	0.07		0.55			0.20
Cs	0.01		0.05			0.01
Sr	639		11			870
Sc	9.71		14.56			7.47
Zr	0.93		2.20			1.82

Table B.1 Bulk rock major and trace element concentrations of peridotites

Table B.1 (continued)

Sample #	NMNH 115048-5a	NMNH 115048-26a	NMNH 115048-2a	NMNH 115048-4a	NMNH 115048-3a	NMNH 115048-25a
Data Source	**1**	**1**	**1**	**1**	**1**	**1**
Major elements						
SiO2	43.50	41.62	43.12	43.08	40.85	41.88
TiO2	0.05	0.10	0.04	0.06	0.12	0.07
Al2O3	3.28	2.16	2.38	2.36	1.81	3.15
FeO*	8.12	8.42	8.18	8.06	11.01	7.81
MnO	0.13	0.13	0.13	0.13	0.16	0.12
MgO	41.83	45.48	44.25	44.17	44.00	43.81
CaO	2.09	1.16	1.02	0.97	0.89	2.17
Na2O	0.19	0.16	0.12	0.11	0.12	0.17
K2O	0.02	0.03	0.01	0.01	0.05	0.01
P2O5	0.02	0.02	0.01	0.01	0.02	0.02
Cr2O3						
Sum	99.23	99.27	99.25	98.95	99.03	99.22
LOI (%)						
Total with LOI						
Normalized Major Elements						
SiO2	43.84	41.92	43.44	43.54	41.26	42.21
TiO2	0.05	0.10	0.04	0.06	0.12	0.07
Al2O3	3.30	2.18	2.40	2.39	1.83	3.17
FeO*	8.18	8.48	8.24	8.14	11.11	7.87
MnO	0.13	0.13	0.13	0.13	0.16	0.12
MgO	42.16	45.81	44.58	44.64	44.43	44.16
CaO	2.11	1.16	1.02	0.98	0.89	2.19
Na2O	0.19	0.16	0.12	0.11	0.12	0.17
K2O	0.02	0.03	0.01	0.01	0.06	0.01
P2O5	0.02	0.02	0.01	0.01	0.02	0.02
Total	100.00	100.00	100.00	100.00	100.00	100.00
Mg #	90.19	90.59	90.60	90.72	87.69	90.91
Trace element (XRF)						
Ni	2251	2481	2352	2324	3284	2467
Cr	3003	3239	2986	4132	1007	5175
Sc	12.18	6.72	9.76	8.82	3.32	11.05
V	51.8	39.3	43.1	45.9	25.2	52.8
Ga	4.76	3.78	2.15	4.06	8.08	5.74
Cu	17.2	12.5	9.0	11.6	11.0	16.5
Zn	53.3	58.0	56.7	61.7	109	61.1
Trace element (ICP-MS)						
La	1.01	1.16	0.40	0.56	0.46	0.97
Ce	1.76	2.28	1.09	1.27	1.37	1.99
Pr	0.24	0.29	0.17	0.20	0.22	0.23
Nd	0.97	1.29	0.83	0.92	1.16	0.99
Sm	0.23	0.31	0.24	0.27	0.35	0.22
Eu	0.07	0.10	0.08	0.09	0.13	0.08
Gd	0.23	0.31	0.22	0.24	0.36	0.20
Tb	0.04	0.04	0.03	0.04	0.05	0.04
Dy	0.25	0.27	0.16	0.20	0.27	0.20
Ho	0.05	0.05	0.03	0.04	0.05	0.04
Er	0.16	0.12	0.08	0.08	0.10	0.12
Tm	0.03	0.02	0.01	0.01	0.01	0.02
Yb	0.16	0.11	0.07	0.07	0.08	0.11
Lu	0.03	0.02	0.01	0.01	0.01	0.02
Ba	14.69	17.10	6.33	9.75	20.73	4.71
Th	0.15	0.15	0.05	0.08	0.06	0.18
Nb	0.85	0.80	0.56	0.47	1.54	0.79
Y	1.45	1.23	0.75	0.82	1.05	1.09
Hf	0.10	0.14	0.13	0.13	0.53	0.10
Ta	0.03	0.04	0.05	0.04	0.13	0.04
U	0.07	0.05	0.02	0.02	0.02	0.05
Pb	0.21	0.15	0.12	0.11	0.06	0.13
Rb	0.82	0.62	0.36	0.16	2.60	0.29
Cs	0.05	0.03	0.04	0.02	0.04	0.02
Sr	33	20	12	12	15	16
Sc	11.27	7.06	9.33	8.47	4.68	10.09
Zr	3.47	5.82	7.28	6.75	17.59	3.25

Table B.1 (continued)

Sample #	NMNH 115048-26	BELB 9-15	07EB 4.01	07EB 4.21	CC07-2-01
Data Source	**4**	**3**	**3**	**3**	**3**
Major elements					
SiO2	41.65	40.95	45.51	45.60	45.14
TiO2	0.03	0.00	0.17	0.08	0.18
Al2O3	0.82	0.65	4.42	3.62	2.73
FeO*	8.30	7.82	8.22	8.01	8.78
MnO	0.12	0.11	0.14	0.13	0.14
MgO	46.57	47.49	37.66	39.86	40.58
CaO	0.58	0.74	3.61	2.95	2.16
Na2O	0.08	0.00	0.27	0.16	0.22
K2O	0.01	0.00	0.01	0.00	0.05
P2O5	0.01	0.00	0.02	0.01	0.04
Cr2O3					
Sum	98.15	97.78	100.02	100.43	100.00
LOI (%)					
Total with LOI					
Normalized Major Elements					
SiO2	42.43	41.88	45.50	45.41	45.14
TiO2	0.03	0.00	0.17	0.08	0.18
Al2O3	0.84	0.67	4.42	3.60	2.73
FeO*	8.45	8.00	8.22	7.98	8.78
MnO	0.12	0.12	0.14	0.13	0.14
MgO	47.44	48.57	37.65	39.69	40.58
CaO	0.59	0.76	3.61	2.94	2.16
Na2O	0.08	0.00	0.27	0.16	0.22
K2O	0.01	0.00	0.01	0.00	0.05
P2O5	0.01	0.00	0.02	0.01	0.04
Total	100.00	100.00	100.00	100.00	100.00
Mg #	90.91	91.54	89.09	89.87	89.18
Trace element (XRF)					
Ni	2512				
Cr	2000				
Sc					
V	24.0				
Ga					
Cu					
Zn					
Trace element (ICP-MS)					
La		0.08	0.26	0.10	1.49
Ce		0.18	0.82	0.23	3.35
Pr		0.02	0.15		
Nd		0.06	0.84		
Sm		0.01	0.36	0.16	0.50
Eu		0.00	0.15		
Gd		0.01	0.54		
Tb		0.00	0.11		
Dy		0.01	0.74		
Ho		0.00	0.16		
Er		0.01	0.46		
Tm		0.00	0.07		
Yb		0.01	0.44	0.31	0.21
Lu		0.00	0.07		
Ba		0.14	6.51	1.96	19.57
Th		0.02	0.02		
Nb		0.66	0.16	0.10	1.81
Y		0.07	3.95		
Hf		0.04	0.24		
Ta		0.00	0.01		
U		0.16	0.01		
Pb		0.07	0.07		
Rb		0.59	0.18		
Cs		0.01	0.01		
Sr		15	18		
Sc		4.56	15.94		
Zr		3.79	6.80		

Data sources: 1) This study, 2) Lassiter et al. (2014), 3) Byerly and Lassiter (2012), and 4) Bizimis et al. (2007)

Table B.2 Major element compositions of spinels

Sample #	PS66-251-47	PS66-262-106	NMNH 115048-26a	NMNH 115048-3a	NMNH 115048-25a
Data source	**2**	**2**	**1**	**1**	**1**
SiO2					0.02
TiO2	0.10	0.06	1.162	0.152	0.09
Al2O3	45.54	44.15	25.698	35.717	37.44
FeO	15.13	11.63	17.59	15.86	14.82
Fe2O3		1.99			
MnO	0.12	0.31	0.109	0.16	0.16
MgO	16.71	17.61	15.909	17.335	17.41
CaO		0.03			0.00
Cr2O3	21.20	23.74	39.434	28.55	28.65
V2O3		0.09			
NiO	0.21	0.22	0.138	0.325	0.37
ZnO		0.19			
CoO					
Total	98.93	100.00	99.96	98.00	98.97
Cr#	23.8	26.5	50.7	34.9	33.9
Sample #	**NMNH 115048-26**	**BELB 9-15**	**07EB 4.01**	**07EB 4.21**	**CC07-2-01**
Data source	**4**	**3**	**3**	**3**	**3**
SiO2	0.09	0.08	0.08	0.06	0.09
TiO2	0.14	0.03	0.09	0.06	0.54
Al2O3	41.00	27.78	59.03	57.01	47.16
FeO	13.17	13.67	10.85	10.72	13.96
Fe2O3					
MnO	0.13	0.08	0.09	0.07	0.07
MgO	18.63	16.29	20.70	20.88	19.83
CaO	0.00	0.01	0.01	0.01	0.00
Cr2O3	26.75	41.36	7.90	10.60	18.48
V2O3	0.12				
NiO	0.25	0.17	0.40	0.38	0.35
ZnO	0.11				
CoO	0.04				
Total	100.44	99.28	99.16	99.79	100.49
Cr#	30.4	50.0	8.2	11.1	20.8

Data sources: 1) This study, 2) Lassiter et al. (2014), 3) Byerly and Lassiter (2012), and 4) Bizimis et al. (2007)

Table B.2 Major element compositions of spinels in peridotites

Table B.3 Major element compositions of clinopyroxenes

Sample #	PS66-251-57	PS66-251-47	PS66-251-47_DUP	PS66-262-106	NMNH 115048-5a	NMNH 115048-26a	NMNH 115048-2a
	2	2	2	2	1	1	1
SiO2	51.79	50.58	49.88	52.69	52.26	53.02	52.22
TiO2	0.20	0.24	0.18	0.29	0.18	0.50	0.19
Al2O3	5.36	6.04	5.87	5.09	5.51	4.05	5.21
FeO	2.53	2.68	3.19	2.30	3.52	3.36	3.51
MnO	0.10	0.12	0.10	0.00	0.13	0.12	0.11
MgO	17.65	16.25	15.88	14.87	15.66	15.90	15.13
CaO	20.95	22.58	22.39	21.51	20.44	19.23	19.52
Na2O	0.72	0.52	0.50	1.41	1.46	1.95	2.20
Cr2O3	1.41	1.20	1.15	1.59	1.12	2.04	1.54
NiO	0.05	0.03		0.04	0.17	0.16	0.18
K2O							
Total	100.78	100.24	99.14	99.78	100.46	100.31	99.82
Mg#	92.6	91.5	89.9	92.0	88.8	89.4	88.5
Cr#	15.0	11.8	11.6	17.3	12.0	25.3	16.6
Sample #	**NMNH 115048-3a**	**NMNH 115048-25a**	**NMNH 115048-26**	**BELB 9-15**	**07EB 4.01**	**07EB 4.21**	**CC07-2-01**
Data source	**1**	**1**	**4**	**3**	**3**	**3**	**3**
SiO2	53.52	53.45	53.48	53.63	50.99	51.17	51.76
TiO2	0.55	0.08	0.17	0.02	0.60	0.37	0.67
Al2O3	4.60	3.95	5.25	2.39	7.57	6.61	6.08
FeO	4.42	3.36	2.49	2.07	2.96	2.76	3.32
MnO	0.12	0.12	0.08	0.04	0.09	0.10	0.10
MgO	14.92	16.60	15.46	16.99	14.61	14.99	16.29
CaO	19.02	21.61	19.22	21.82	19.70	20.55	19.77
Na2O	2.14	0.73	2.41	0.84	1.77	1.53	1.07
Cr2O3	1.41	1.31	1.55	1.04	0.67	0.84	1.30
NiO	0.17	0.16		0.03	0.07	0.05	0.05
K2O			0.01				
Total	100.86	101.37	100.10	98.86	99.03	98.96	100.41
Mg#	85.8	89.8	91.7	93.6	89.8	90.6	89.7
Cr#	17.1	18.1	16.5	22.6	5.6	7.9	12.6

Data sources: 1) This study, 2) Lassiter et al. (2014), 3) Byerly and Lassiter (2012), and 4) Bizimis et al. (2007)

Table B.3 Major element compositions of clinopyroxenes in peridotites

Table B.4 Trace element concentrations of clinopyroxene

Sample #	PS66-251-47	PS66-262-106	NMNH 115048-5a	NMNH 115048-26a	NMNH 115048-2a	NMNH 115048-4a
Data source	**2**	**2**	**1**	**1**	**1**	**1**
Sr	1.49	11.5	75.0	239	191	260
Y	9.82	9.77	10.9	11.4	11.5	22.8
Zr	5.90	38.4	13.2	105	177	476
La	0.02	0.02	1.61	6.29	3.51	5.84
Ce	0.05	0.58	4.17	19.4	14.6	23.4
Nd	0.20	2.11	2.97	15.7	15.3	26.0
Sm	0.33	1.19	0.97	4.39	4.81	8.78
Eu	0.17	0.53	0.37	1.47	1.57	2.98
Gd	0.98	1.69	1.28	4.01	4.28	8.75
Dy	1.84	2.00	1.81	2.90	3.03	6.42
Er	1.51	1.12	1.26	1.11	1.15	2.19
Yb	1.38	1.04	1.28	0.82	0.88	1.43
Hf	0.23	1.31	0.38	1.62	2.93	14.2
Sample #	**NMNH 115048-25a**	**NMNH 115048-26**	**BELB 9-15**	**07EB 4.01**	**07EB 4.21**	**CC07-2-01**
Data source	**1**	**4**	**3**	**3**	**3**	**3**
Sr	45.6	200	67.9	67.2	8.9	181
Y	6.91	10.4	0.59	19.3	14.1	12.1
Zr	4.7	60.8	0.5	32.3	6.8	32.6
La	1.73	4.07	2.82	0.78	0.06	3.42
Ce	3.35	14.8	4.74	3.30	0.28	12.3
Nd	1.65	17.5	1.07	4.65	1.35	10.8
Sm	0.44	4.91	0.13	1.94	0.92	2.86
Eu	0.16	1.58	0.05	0.80	0.43	0.95
Gd	0.69	4.01	0.09	2.69	1.65	2.64
Dy	1.18	2.54	0.08	3.60	2.49	2.50
Er	0.85	1.00	0.08	2.20	1.60	1.27
Yb	0.82	0.87	0.14	2.10	1.61	1.07
Hf	0.14	0.46	0.02	1.05	0.38	0.97

Data sources: 1) This study, 2) Lassiter et al. (2014), 3) Byerly and Lassiter (2012), and 4) Bizimis et al. (2007)

Table B.4 Trace element concentrations of clinopyroxenes in peridotites

Table B.5 Reproducibility of whole rock peridotite duplicates using XRF and ICP-MS

Sample #	07 EB 1.11	07 EB 1.11 rep	% Difference	CC-07-1-35	CC-07-1-35 rep	% Difference	07EB 4-01	07EB 4-01rep	% Difference
Majors									
SiO2	43.09	42.87	*0.50*	44.08	44.36	*0.65*			
TiO2	0.013	0.011	*16.56*	0.028	0.024	*16.07*			
Al2O3	1.18	1.16	*1.82*	3.10	2.86	*8.29*			
FeO*	8.01	7.99	*0.35*	7.83	7.51	*4.28*			
MnO	0.130	0.131	*1.15*	0.124	0.122	*1.01*			
MgO	43.78	44.20	*0.96*	40.94	40.24	*1.75*			
CaO	0.93	0.93	*0.11*	2.56	2.82	*9.19*			
Na2O	0.00	0.00		0.09	0.09	*4.09*			
K2O	0.00	0.00	*9.21*	0.01	0.01	*83.29*			
P2O5	0.008	0.009	*8.18*	0.021	0.020	*7.58*			
Sum	97.14	97.30	*0.17*	98.78	98.05	*0.74*			
Traces by XRF (in ppm)									
Ni	2506	2546	*1.57*	2280	2191	*4.06*			
Cr	2239	2228	*0.49*	2851	2650	*7.58*			
V	31	29	*6.66*	47	51	*7.90*			
Ga				2	2	*6.25*			
Cu	3	4	*22.59*	12	16	*24.78*			
Zn	50	48	*4.10*	49	45	*8.67*			
Traces by ICP-MS (in ppm)									
La	0.15	0.16	*5*	1.21	1.28	*5*	0.26	0.26	*0*
Ce	0.33	0.35	*5*	2.76	3.01	*8*	0.82	0.81	*2*
Pr	0.04	0.04	*0*	0.33	0.36	*6*	0.15	0.15	*0*
Nd	0.14	0.13	*8*	1.26	1.34	*6*	0.84	0.87	*4*
Sm	0.03	0.03	*6*	0.22	0.25	*10*	0.36	0.36	*1*
Eu	0.01	0.01	*5*	0.08	0.08	*3*	0.15	0.14	*5*
Gd	0.04	0.03	*8*	0.20	0.21	*4*	0.54	0.54	*1*
Tb	0.01	0.01	*1*	0.04	0.04	*6*	0.11	0.11	*1*
Dy	0.04	0.04	*3*	0.23	0.26	*12*	0.74	0.71	*4*
Ho	0.01	0.01	*13*	0.05	0.06	*13*	0.16	0.16	*4*
Er	0.02	0.03	*16*	0.16	0.18	*10*	0.46	0.46	*1*
Tm	0.00	0.01	*21*	0.03	0.03	*5*	0.07	0.07	*0*
Yb	0.04	0.05	*20*	0.18	0.20	*9*	0.44	0.43	*3*
Lu	0.01	0.01	*3*	0.03	0.03	*12*	0.07	0.07	*2*
Ba	33	32	*4*				7	7	*2*
Th	0.03	0.05	*40*	0.08	0.10	*21*	0.02	0.03	*11*
Nb	0.29	0.29	*0*	0.45	0.35	*30*	0.16	0.16	*2*
Y	0.24	0.24	*1*	1.40	1.56	*10*	3.95	3.99	*1*
Hf	0.03	0.03	*16*	0.12	0.17	*28*	0.24	0.22	*8*
Ta	0.01	0.01	*1*	0.04	0.04	*1*	0.01	0.01	*1*
U	0.06	0.07	*11*	0.03	0.04	*10*	0.01	0.01	*12*
Pb							0.07	0.07	*8*
Rb	0.3	0.3	*1*				0.2	0.2	*12*
Cs	0.03	0.03	*20*				0.01	0.01	*13*
Sr	14	14	*0*	41	44	*8*	18	18	*1*
Sc	7.5	7.4	*1*	10.7	11.7	*9*	15.9	15.8	*1*
Zr	1	1	*22*	8	9	*15*	7	7	*1*

Table B.5 Reproducibility of whole-rock duplicates using XRF and ICP-MS

Table B.6 Accuracy of the whole rock standard JP-1 using XRF

Standard	SiO2	TiO2	Al2O3	FeO*	MnO	MgO	CaO	Na2O	K2O	P2O5	Total	LOI
JP-1 Measured	43.22	0.000	0.65	7.68	0.119	44.94	0.55	0.04	0.00	0.000	97.20	2.39
JP-1 Certified	42.38	0.006	0.66	7.77	0.121	44.60	0.55	0.02	0.00	0.002	96.11	2.39
% difference between measured and certified	1.97	100.00	0.83	1.15	1.50	0.76	0.64	74.97	9.03	81.29	1.13	0.00
Traces in (ppm)	Ni	Cr	Sc	V	Ba	Rb	Zr	Cu	Zn			
JP-1 Measured	2461	2874	7	25	16	1	5	7	48			
JP-1 Certified	2460	2807	7	28	20	1	6	7	42			
% difference between measured and certified	0.06	2.39	0.98	11.12	15.42	30.70	24.57	2.96	14.18			

Table B.6 Accuracy of whole-rock JP-1 standard using XRF

Table B.7 Accuracy and reproducibility of the LA-ICP-MS standard BCR-2g

Element (in ppm)	Na	Ca	Ti	V	Rb	Sr	Y	Zr	Nb	Cs	La	Ce	Pr
BCR 2-g measured (Average)	21650	51411	13964	436	46	342	32	175	12	1	25	53	6
SD	2660	572	219	5.6	0.8	3.4	0.5	2.3	0.1	0.0	0.4	1.0	0.1
BCR 2-g reported	23962	50457	14100	425	47	342	35	184	13	1	25	53	7
% difference between measured and certified	9.6	1.9	1.0	2.6	1.2	0.0	7.9	5.1	3.8	3.4	0.4	0.7	3.6
Element (in ppm)	Nd	Sm	Eu	Gd	Dy	Er	Yb	Lu	Hf	Ta	Pb	Th	U
BCR 2-g measured (Average)	28.12	6.53	1.91	6.32	6.21	3.54	3.31	0.49	4.56	0.76	10.23	5.82	1.68
2 SD	0.43	0.09	0.03	0.10	0.10	0.09	0.07	0.01	0.05	0.02	0.31	0.11	0.04
BCR 2-g reported	28.90	6.59	1.97	6.71	6.44	3.70	3.39	0.50	4.84	0.78	11.00	5.90	1.69
% difference between measured and certified	2.7	0.9	2.8	5.9	3.5	4.4	2.5	2.6	5.9	2.5	7.0	1.4	0.7

Table B.7 Accuracy and reproducibility of the BCR-2g standard

B.2 Global peridotite melt-depletion trends:

Whole rock and mineral major element, trace element and isotopic co-variations in spinel peridotites from continental and oceanic settings are shown in figures B.2-B.6. Peridotites selected for this study are shown for comparison. Data was compiled from GEOROC and PetDB and data sources will be made available upon request. Different indices of melt depletion (e.g., bulk rock Al_2O_3, spinel Cr#, clinopyroxene Yb) broadly correlate with each other. Peridotites selected for the study span much of the compositional range observed in the global peridotite compilation. Previous studies (cf. Dick and Bullen, 1984; Hellebrand et al., 2001) have interpreted these compositional trends to reflect variable melt extraction and/or refertilization. Correlations between bulk rock Al_2O_3 and $^{187}Os/^{188}Os$ in the samples selected for this study and peridotites globally reflect long-term Re/Os depletion due to ancient melt extraction (cf. Meisel et al., 2001).

Correlations between spinel Cr# and clinopyroxene Yb content (Figure B.6) reflect variable prior melt extraction (Hellebrand et al., 2001). The melting model shown is modified from Hellebrand et al. (2001) and Johnson et al. (1990). Spinel Cr# is calculated as a function of F using the formulation by Hellebrand et al. (2001) where F is the degree of fractional melting. Clinopyroxene Yb content is also calculated as a function of F using the formulation by Johnson et al. (1990). Peridotites selected for this study follow the modeled depletion trend and appear to have undergone between 0-20% melt extraction.

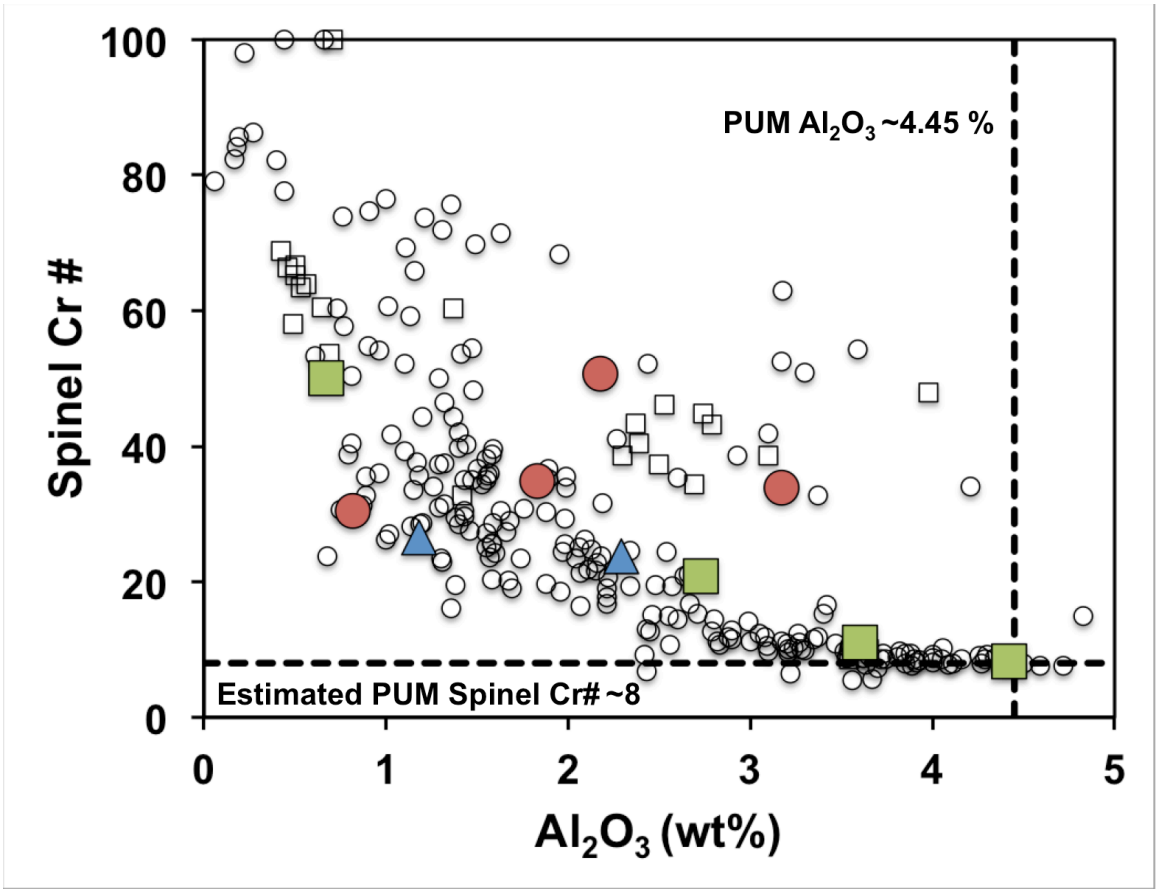

Figure B.2 Spinel Cr# vs bulk rock Al_2O_3 in peridotites.

Melt depletion lowers bulk rock Al_2O_3 and increases spinel Cr# in residual mantle. Horizontal dashed line represents the inferred spinel Cr# of mantle peridotite with a bulk composition similar to PUM, derived from the intersection of the spinel Cr#-Al_2O_3 melt depletion trend with PUM whole rock Al_2O_3 (~4.45 wt%; McDonough & Sun, 1995). Symbols: Continental peridotites- open circles, Oceanic peridotites- open squares Rest- same as in figure 1. Data is compiled from GEOROC and PetDB and data sources will be made available upon request.

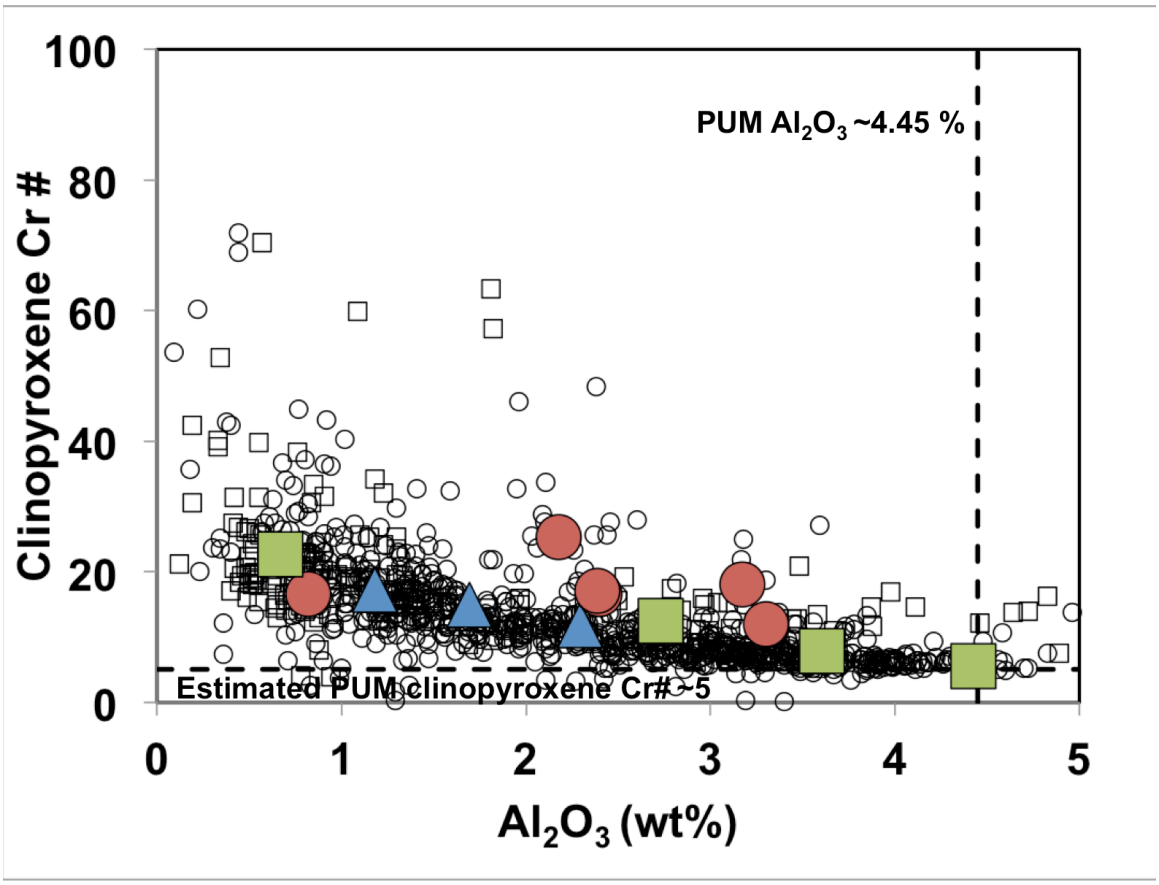

Figure B.3 Clinopyroxene Cr# vs bulk rock Al_2O_3 in peridotites.

Horizontal dashed line represents the inferred PUM clinopyroxene Cr# derived from the intersection of the clinopyroxene Cr#-Al_2O_3 melt depletion trend with PUM whole rock Al_2O_3 (~4.45 wt%; McDonough & Sun, 1995). Symbols and data sources are as in figure B.2.

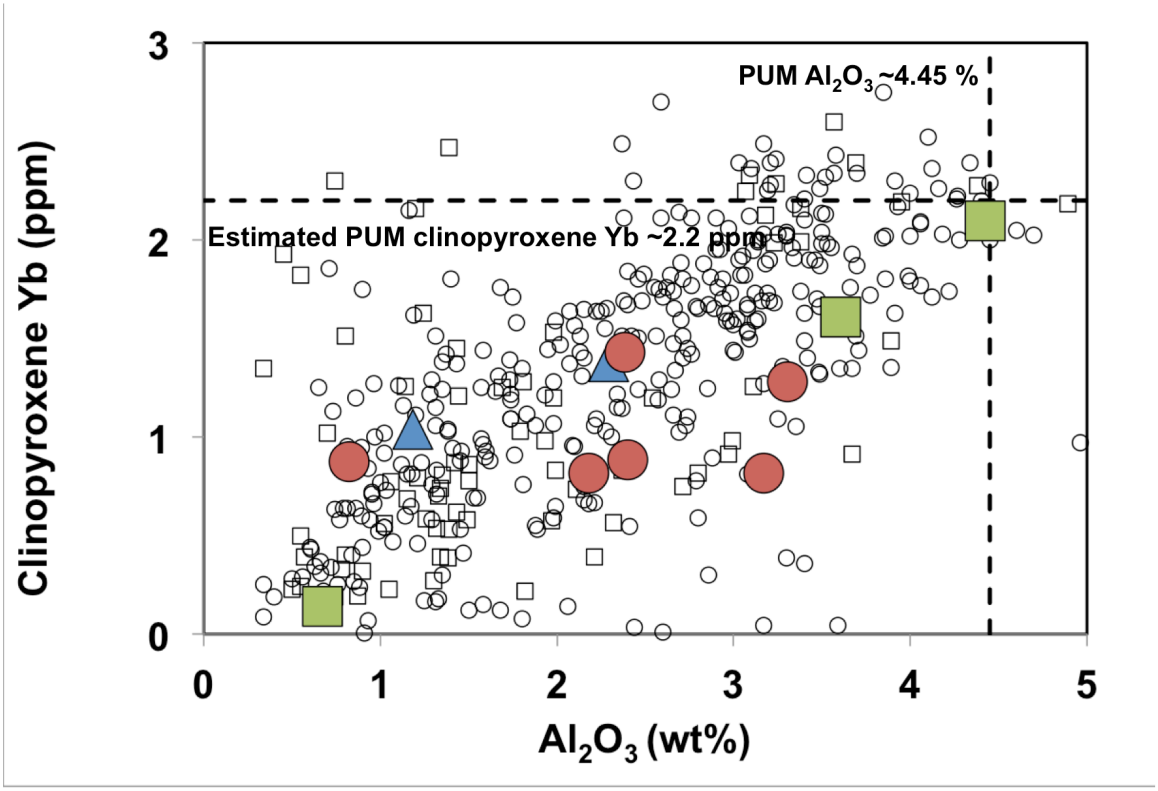

Figure B.4 Clinopyroxene Yb vs bulk rock Al_2O_3 in peridotites.

Horizontal dashed line represents the inferred PUM clinopyroxene Yb derived from the intersection of the clinopyroxene Yb-Al_2O_3 melt depletion trend with PUM whole rock Al_2O_3 composition (~4.45 wt%; McDonough & Sun, 1995). Symbols and data sources are as in figure B.2.

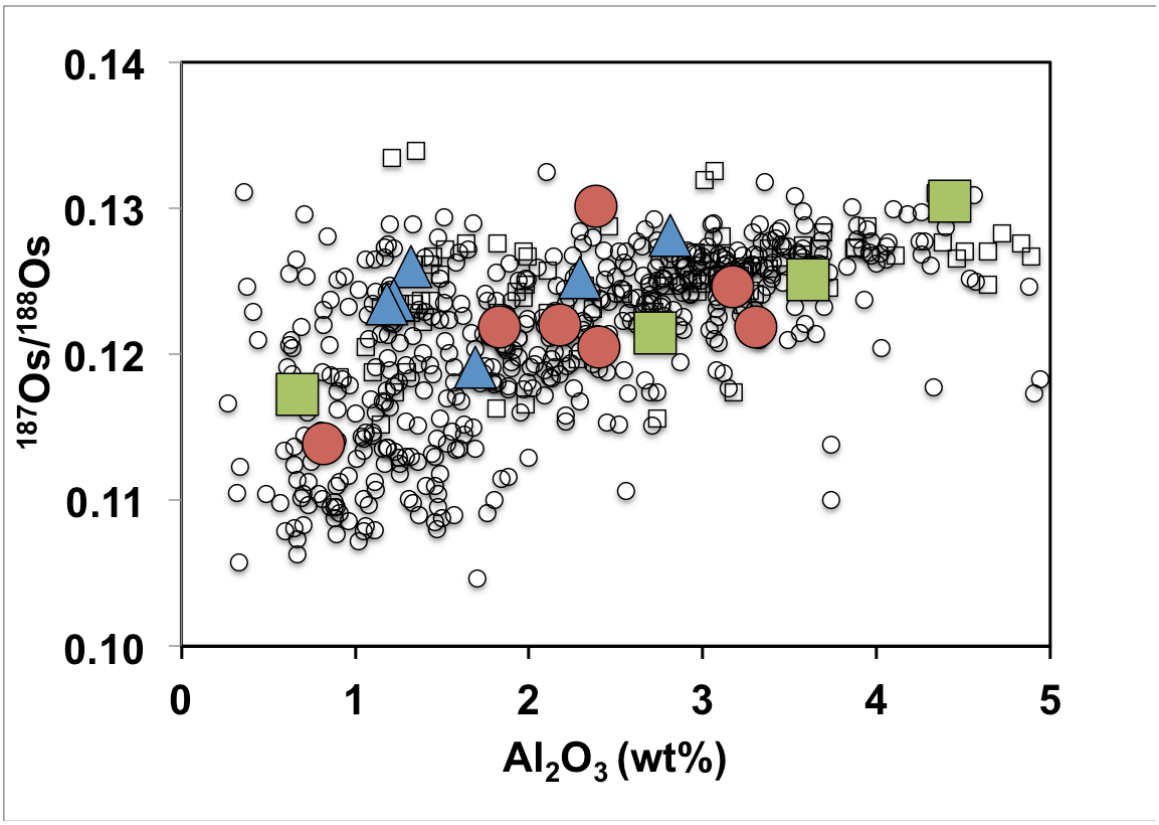

Figure B.5 $^{187}Os/^{188}Os$ vs bulk rock Al_2O_3 in mantle peridotites.

More refractory samples (low Al_2O_3) have lower average $^{187}Os/^{188}Os$ than fertile samples (high Al_2O_3), reflecting long-term Re-depletion in refractory (low- Al_2O_3) peridotites as a result of ancient melt depletion. Symbols and data sources are as in figure B.2.

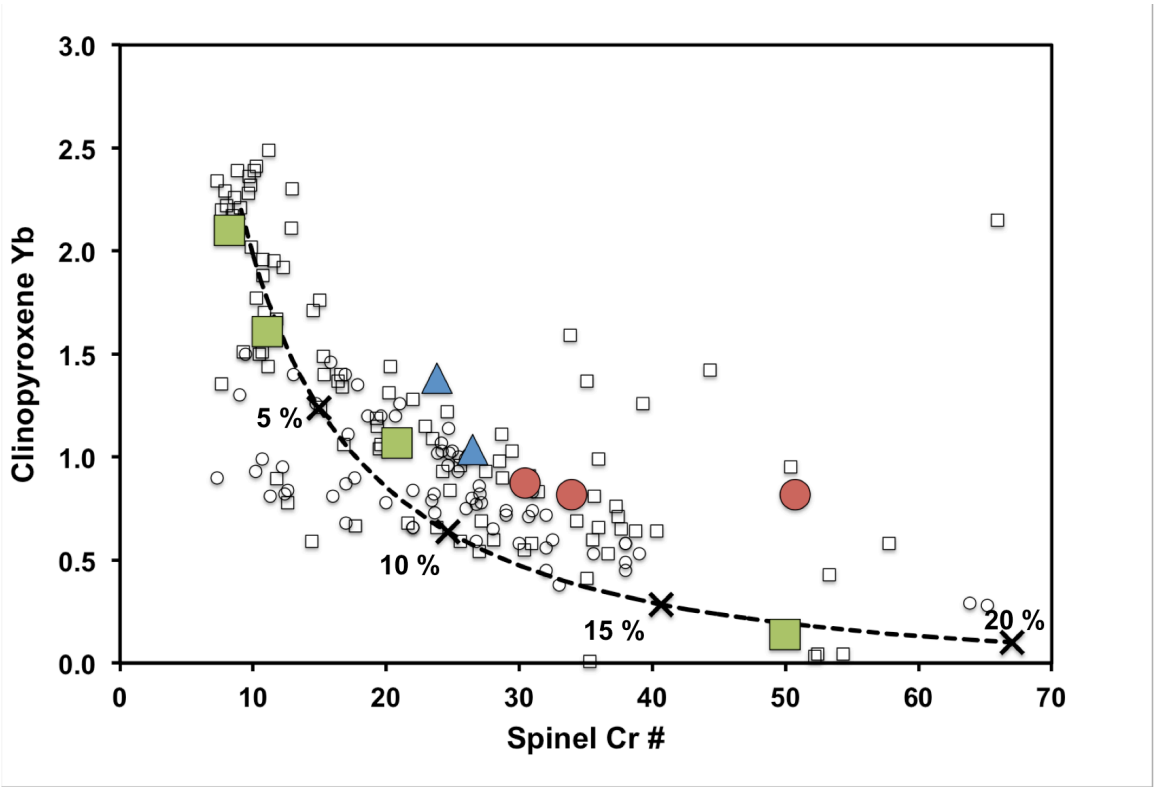

Figure B.6 Spinel Cr# vs clinopyroxene Yb in samples selected for the study and global peridotites.

Melting model is based on fractional melting inferred from spinel Cr# modeled after Hellebrand et al. (2001). Clinopyroxene Yb content is modeled as a function of fractional melting after Johnson et al. (1990). Black dashed line represents the melting model and tick marks represent increasing degree of fractional melting. Symbols and data sources are as in figure B.2.

B.3 Isotopic and parent/daughter heterogeneity in the convecting upper mantle

Pt/Os data for oceanic and continental peridotites are shown in Figure 2.2. Data was compiled from GEOROC and PetDB and were taken from the following sources: Wittig et al. (2010), Luguet et al. (2001, 2003), Brandon et al. (2000), Becker et al. (2006), Smith et al. (2009), Zhang et al. (2012, 2010, 2009), Maier et al. (2012), Xu et al. (2008) and Xiao et al. (2011). I restricted my dataset to samples with >1ppb Os as samples with unusually low Os concentrations are likely affected by high degrees of melt-rock reaction and/or weathering and alteration (cf. Handler et al., 1999). Further, only Pt/Os ratios determined using HPAS, Ni-S fire assay or high temperature Carius tube techniques have been included due to concerns about incomplete digestions in other techniques (cf. Meisel et al., 2003).

The degree of isotopic and parent-daughter heterogeneity in peridotites from the convecting upper mantle is related to mantle homogenization timescales (see section 5.3 of chapter 2). In order to estimate homogenization timescales, I compiled data for isotopic and parent/daughter ratios in mantle peridotites for the following isotopic systems: ^{187}Re-^{187}Os, ^{190}Pt-^{186}Os, ^{176}Lu-^{176}Hf and ^{147}Sm-^{143}Nd. I compiled Re/Os and ^{187}Os/^{188}Os data in oceanic peridotites (ocean island xenoliths and abyssal peridotites). Data were taken from Lassiter et al. (2014) and references therein. All samples that were 2σ outliers from the mean of the Re/Os and ^{187}Os/^{188}Os populations were removed from my analyses. Because the Pt/Os and ^{186}Os/^{188}Os dataset for oceanic peridotites is very limited, I included Pt/Os and ^{186}Os/^{188}Os data from both continental and oceanic settings. Data sources are as listed for figure 2.2. ^{143}Nd/^{144}Nd and ^{176}Hf/^{177} Hf, and Sm/Nd and

Lu/Hf data for oceanic peridotites were also compiled to calculate mantle-mixing timescales. Data were compiled from the following sources: Mallick et al. (2015), Stracke et al. (2011), Bizimis et al. (2007, 2004), Warren et al. (2009), Cipriani et al. (2004) and Salters et al. (2002). The standard deviation of both parent/daughter and isotopic ratios were calculated for each isotopic system. These estimates are utilized to estimate mantle homogenization timescales as described in section 5.3 of chapter 2.

APPENDIX C: SUPPLEMENT TO CHAPTER 3

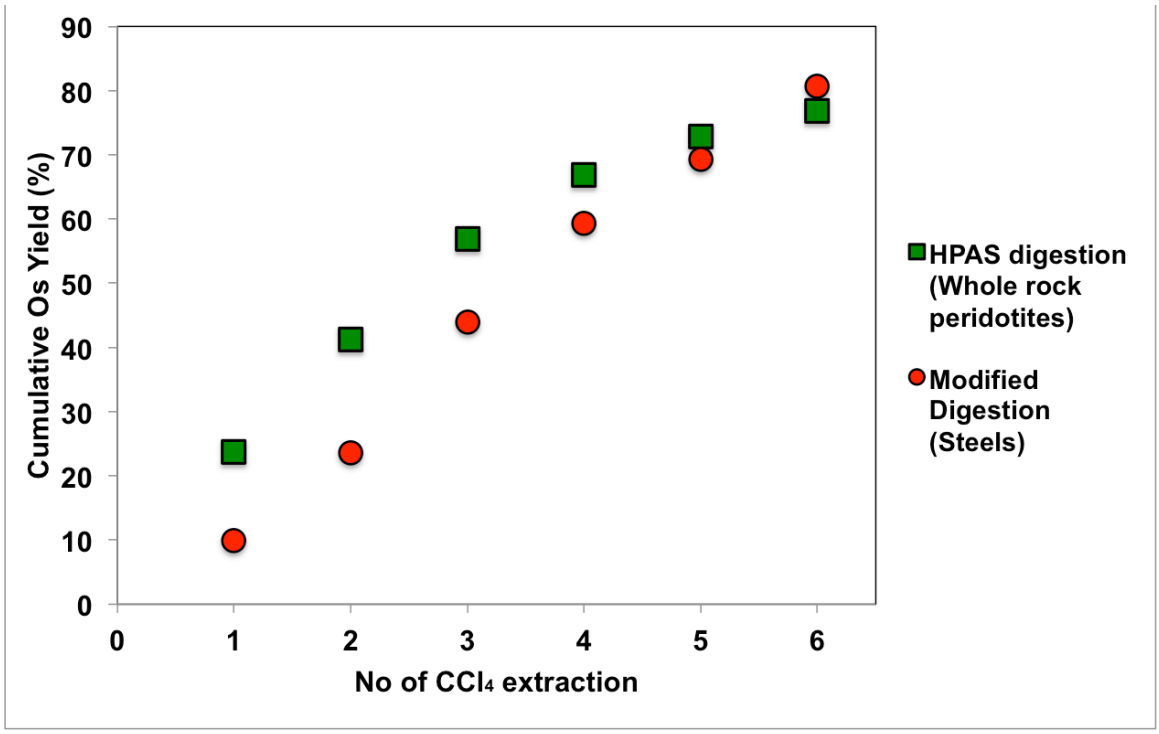

Figure C.1 Cumulative Os yields using HPAS digestion versus modified digestion technique for steels

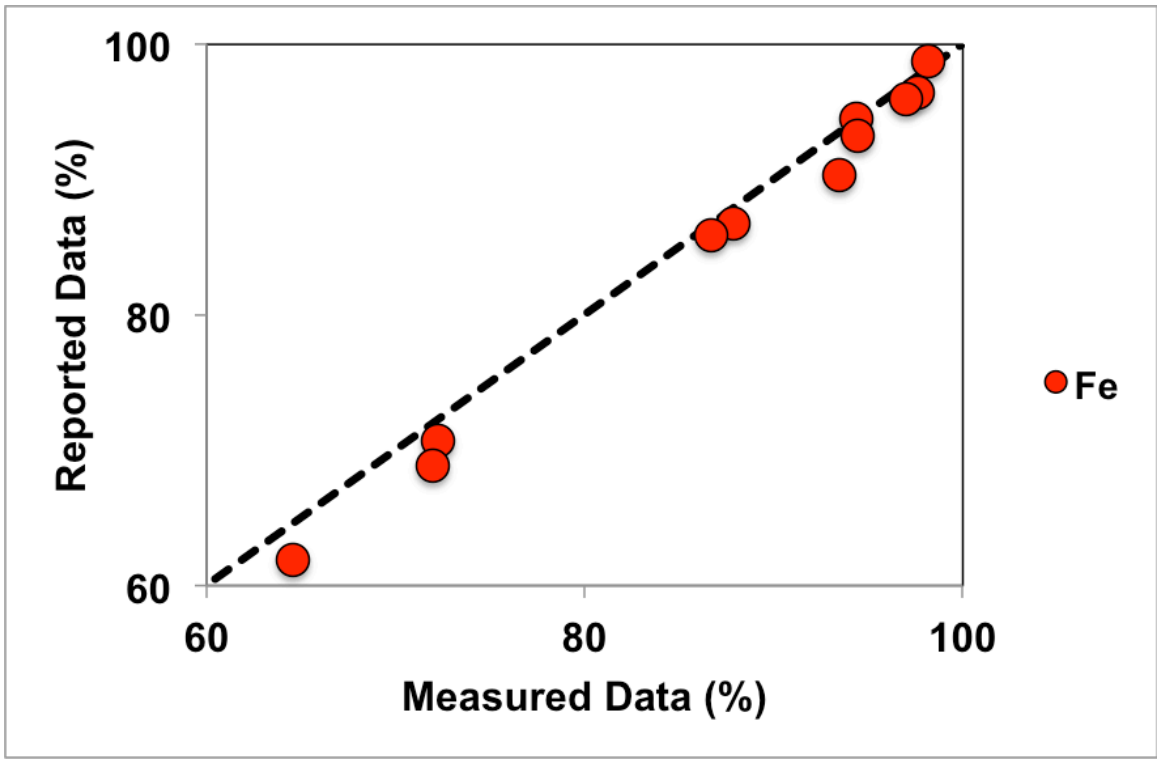

Figure C.2 Reported versus measured Fe concentrations in steels.

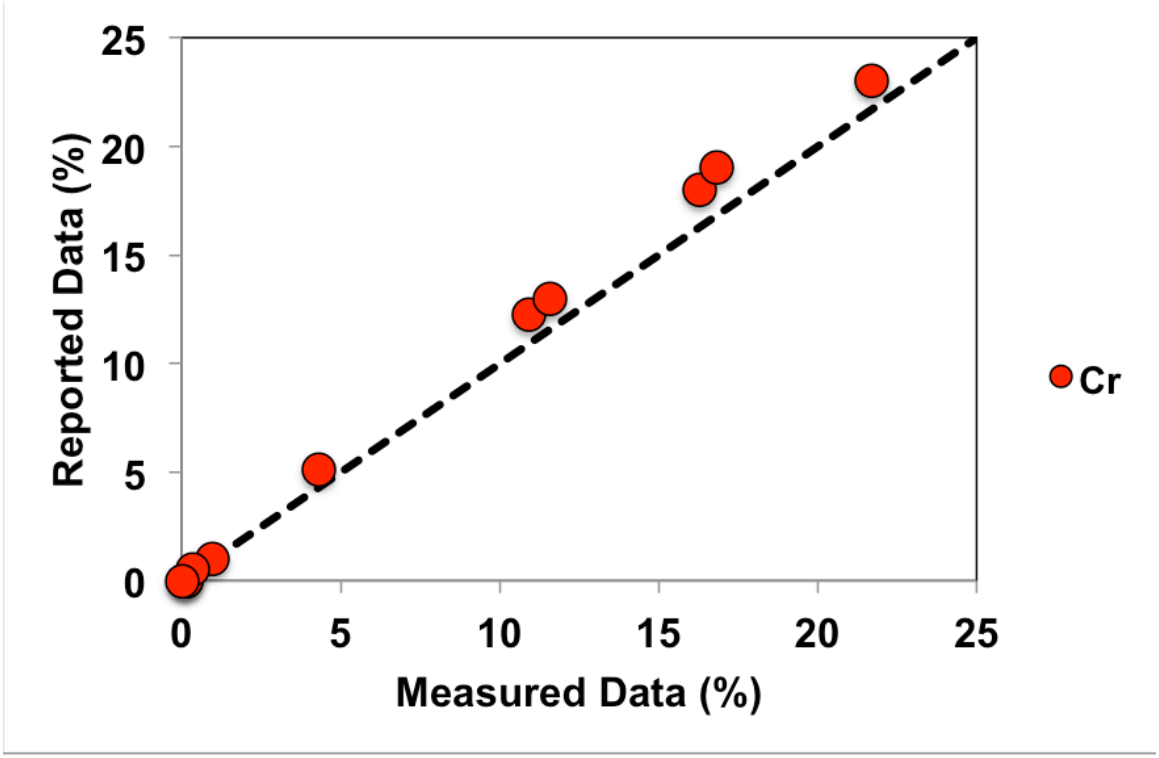

Figure C.3 Reported versus measured Cr concentrations in steels.

Conc (in ppb)	Fe	Cr	Mn	Ni	Mo
	10.32	2.11	3.99	6.31	11.61
	10.54	2.07	3.92	6.19	11.35
	10.30	2.05	3.91	6.16	11.44
	10.27	2.00	3.87	6.08	11.29
	10.43	2.00	3.87	6.13	11.30
	10.41	1.99	3.80	6.08	11.23
Average (measured)	10.38	2.04	3.89	6.16	11.37
% Standard deviation	1.0	2.3	1.6	1.4	1.2
Reported	9.81	2.04	3.90	6.24	12.14
% difference from reported	5.8	0.1	0.1	1.3	6.3

Table C.1 Accuracy and reproducibility of the secondary standard NIST-SRM 1643e

REFERENCES

Ackerman, L., Walker, R.J., Puchtel, I.S., Pitcher, L., Jelinek, E., Strnad, L., 2009. Effects of melt percolation on highly siderophile elements and Os isotopes in subcontinental lithospheric mantle: a study of the upper mantle profile beneath Central Europe. Geochimica et Cosmochimica Acta 73, 2400-2414.

Alard, O., Griffin, W.L., Lorand, J-P., Jackson, S.E., O'Reilly, S.Y., 2000. Non-chondritic distribution of the highly siderophile elements in mantle sulfides. Nature 407, 891-894.

Albarède, F., 1998. The growth of continental crust. Tectonophysics 296(1), 1-14.

Anbar, A. D., Duan, Y., Lyons, T. W., Arnold, G. L., Kendall, B., Creaser, R. A., Kaufman, A.J., Gordon, G.W., Scott, C., Garvin, J., Buick, R., 2007. A whiff of oxygen before the great oxidation event?. Science 317(5846), 1903-1906.

Baioumy, H.M., Eglinton, L.B., Peucker-Ehrenbrink, B., 2011. Rhenium–osmium isotope and platinum group element systematics of marine vs. non-marine organic-rich sediments and coals from Egypt. Chemical Geology 285, 70-81.

Ballhaus, C., 1998. Origin of podiform chromite deposits by magma mingling. Earth and Planetary Science Letters 156(3), 185-193.

Barry, J.J., Matos, G.R., Menzie, W.D., 2013. U.S. mineral dependence—Statistical compilation of U.S. and world mineral production, consumption, and trade, 1990–2010. U.S. Geological Survey Open-File Report 2013–1184, 1-6.

Becker, H., Horan, M.F., Walker, R.J., Gao, S., Lorand, J.P., Rudnick, R.L., 2006. Highly siderophile element composition of the Earth's primitive upper mantle: Constraints from new data on peridotite massifs and xenoliths. Geochimica et Cosmochimica Acta 70, 4528-4550.

Begemann, F., Ludwig, K.R., Lugmair, G.W., Min, K., Nyquist, L.E., Patchett, P.J., Renne, P.R., Shih, C.Y., Villa, I.M., Walker, R.J., 2001. Call for an improved set of decay constants for geochronological use. Geochimica et Cosmochimica Acta 65, 111–121.

Birck, J.L., Roy-Barman, M., Capmas, F., 1997. Re–Os isotopic measurements at the femtomole level in natural samples. Geostandards Newsletters 21, 19–27.

Bird, P., 1979. Continental delamination and the Colorado Plateau. Journal of Geophysical Research 84, 7561-7571.

Bizimis, M., Griselin, M., Lassiter, J.C., Salters, V.J.M., Sen, G., 2007. Ancient recycled mantle lithosphere in the Hawaiian plume: Osmium-hafnium isotopic evidence from peridotite mantle xenoliths. Earth and Planetary Science Letters 257, 259-273.

Bizimis, M., Sen, G., and Salters, V.J.M., 2004. Hf-Nd isotope decoupling in the oceanic lithosphere: Constraints from spinel peridotites from Oahu, Hawaii. Earth and Planetary Science Letters 217, 43–58.

Brandon, A.D., Graham, D.W., Waight, T., Gautason, B., 2007. ^{186}Os and ^{187}Os enrichments and high-3He/4He sources in the Earth's mantle: Evidence from Icelandic picrites. Geochimica et Cosmochimica Acta 71, 4570-4591.

Brandon, A.D., Humayun, M., Puchtel, I.S., Leya, I., Zolensky, M., 2005. Osmium Isotope Evidence for an s-process carrier in primitive chondrites. Science 309, 1233–1236.

Brandon, A.D., Norman, M.D., Walker, R.J., Morgan, J.W., 1999. ^{186}Os-^{187}Os systematics of Hawaiian picrites. Earth and Planetary Science Letters 174, 25–42.

Brandon, A.D., Snow, J.E., Walker, R.J., Morgan, J.W., Mock, T.D., 2000. ^{190}Pt–^{186}Os and ^{187}Re–^{187}Os systematics of abyssal peridotites. Earth and Planetary Science Letters 177(3), 319-335.

Brandon, A.D., Walker, R.J., Morgan, J.W., Norman, M.D., Prichard, H.M., 1998. Coupled ^{186}Os and ^{187}Os evidence for core-mantle interaction. Science 280, 1570–1573.

Brandon, A.D., Walker, R.J., Puchtel, I.S., 2006. Platinum–osmium isotope evolution of the Earth's mantle: Constraints from chondrites and Os-rich alloys. Geochimica et Cosmochimica Acta 70, 2093–2103.

Brandon, A.D., Walker, R.J., Puchtel, I.S., Becker, H., Humayun, M., Revillon, S., 2003. ^{186}Os–^{187}Os systematics of Gorgona Island komatiites: implications for early growth of the inner core. Earth and Planetary Science Letters 206, 411–426.

Brauns, M., Schwab, R., Gassmann, G., Wieland, G., Pernicka, E., (2013). Provenance of Iron Age iron in southern Germany: a new approach. Journal of Archaeological Science 40, 841-849.

Brenan, J.M., 2008. Re–Os fractionation by sulfide melt–silicate melt partitioning: a new spin. Chemical Geology 248, 140-165.

Brenan, J.M., Bennett, N.R., Zajacz, Z., 2016. Experimental results on fractionation of the highly siderophile elements (HSE) at variable pressures and temperatures during planetary and magmatic differentiation. Reviews in Mineralogy and Geochemistry 81(1), 1-87.

Burton, K.W., Schiano, P., Birck, J.L., Allègre, C.J., 1999. Osmium isotope disequilibrium between mantle minerals in a spinel-lherzolite. Earth and Planetary Science Letters 172(3), 311-322.

Butler, T.A., Yu, L.L., Turk, G.C., 2009. Standard reference material (SRM) 1643e: Trace elements in water. National Institute of Standards & Technology, 1-3.

Byerly, B.L., Lassiter, J.C., 2012. Evidence from mantle xenoliths for lithosphere removal beneath The Central Rio Grande Rift. Earth and Planetary Science Letters 355-356, 82-93.

Byerly, B.L., Lassiter, J.C., 2014. Isotopically ultra-depleted domains in the convecting upper mantle: Implications for MORB petrogenesis. Geology 42, 203-206.

Byerly, B.L., Lassiter, J.C., 2015. Trace element partitioning and Lu-Hf isotope systematics in spinel peridotites from the Rio Grande Rift and Colorado Plateau. Towards improved age assessment of clinopyroxene Lu/Hf-^{176}Hf/^{177}Hf in SCLM peridotite. Chemical Geology 413, 146-158.

Capobianco, C.J., Jones, J.H., Drake, M.J., 1993. Metal-silicate thermo-chemistry at high-temperature magma oceans and the excess siderophile element problem of the Earths upper mantle. Journal of Geophysical Research-Planets 98 (E3), 5433–5443.

Card, K.D., 1990. A review of the Superior Province of the Canadian Shield, a product of Archean accretion. Precambrian Research 48(1-2), 99-156.

Carlson, R.W., 2005. Application of the Pt-Re-Os isotopic systems to mantle geochemistry and geochronology. Lithos 82, 249-272.

Chatterjee, R., Lassiter, J.C., 2015. High precision Os isotopic measurement using N-TIMS: Quantification of various sources of error in $^{186}Os/^{188}Os$ measurements. Chemical Geology 396, 112-123.

Chatterjee, R., Lassiter, J.C., 2016. $^{186}Os/^{188}Os$ variations in upper mantle peridotites: Constraints on the Pt/Os ratio of primitive upper mantle, and implications for late veneer accretion and mantle mixing timescales. Chemical Geology (in review).

Chavagnac, V., 1998. Behavior of the Sm-Nd isotopic system during metamorphism: examples of the HT-LP metamorphic terranes of the Limpopo belt, South Africa and the UHP metamorphic terrane of Dabieshan, Central China. PhD Thesis, University of Rennes, France, 405 pp.

Chow, T.J., Earl, J.L., 1972. Lead isotopes in North American coals. Science 176, 510-511.

Cipriani, A., Brueckner, H.K., Bonatti, E., and Brunelli, D., 2004. Oceanic crust generated by elusive parents: Sr and Nd isotopes in basalt-peridotite pairs from the Mid-Atlantic Ridge: Geology 32, 657–660.

Coggon, J.A., Luguet, A., Nowell, G.M., Appel, P.W.U., 2013. Hadean mantle melting recorded by southwest Greenland chromitite 186Os signatures. Nature Geoscience 6, 871–874.

Coggon, J.A., Nowell, G.M., Pearson, D.G., Oberthür, T., Lorand, J.P., Melcher, F., Parman, S.W., 2012. The 190Pt-186Os decay system applied to dating platinum-group element mineralization of the Bushveld Complex, South Africa. Chemical Geology 302-303, 48–60.

Cohen, A.S., Coe, A.L., Bartlett, J.M., Hawkesworth, C. J., 1999. Precise Re–Os ages of organic-rich mudrocks and the Os isotope composition of Jurassic seawater. Earth and Planetary Science Letters 167, 159-173.

Cohen, A.S., Coe, A.L., Harding, S.M., Schwark, L., 2004. Osmium isotope evidence for the regulation of atmospheric CO2 by continental weathering. Geology 32, 157-160.

Davies, G.F., Richards, M.A., 1992. Mantle convection. Journal of Geology 100, 151-206.

Day, J.M. 2013. Hotspot volcanism and highly siderophile elements. Chemical Geology 341, 50-74.

De Wit, M.J., de Ronde, C.E., Tredoux, M., Roering, C., Hart, R.J., Armstrong, R.A., Green, R.W.E., Peberdy, E., Hart, R.A., 1992. Formation of an Archaean continent. Nature 357(6379), 553-562.

Degryse, P., Schneider, J., Kellens, N., Waelkens, M., Muchez, P., 2007. Tracing the resources of iron working at ancient Sagalassos (South-West Turkey): A Combined Lead And Strontium Isotope Study on Iron Artefacts and ores. Archaeometry 49(1), 75-86.

DePaolo, D.J., 1981. Trace element and isotopic effects of combined wall rock assimilation and fractional crystallization. Earth and Planetary Science Letters 53, 189-202.

Díaz Somoano, M., Kylander, M., Weiss, D.J., López Antón, M.A., Suárez Ruiz, I., Martínez Tarazona, M., 2007. Lead isotope variability in different world wide coal deposits. International Conference on Coal Science and Technology, Nottingham.

Dick, H.J.B., Bullen, T., 1984. Chromian spinel as a petrogenetic indicator in abyssal and alpine-type peridotites and spatially associated lavas. Contributions to Mineralogy and Petrology 86, 54-76.

Distler, V.V., Kryachko, V.V., Yudovskaya, M.A., 2008. Ore petrology of chromite-PGE mineralization in the Kempirsai ophiolite complex. Mineralogy and Petrology 92(1-2), 31-58.

Drummond, M.S., Defant, M.J., 1990. A model for trondhjemite-tonalite-dacite genesis and crustal growth via slab melting: Archean to modern comparisons. Journal of Geophysical Research: Solid Earth 95(B13), 21503-21521.

Elkins, L.J., Gaetani, G.A., Sims, K.W.W., 2008. Partitioning of U and Th during garnet pyroxenite partial melting: Constraints on the source of alkaline ocean island basalts. Earth and Planetary Science Letters 265(1), 270-286.

Esser, B.K., Turekian, K.K. 1993. The osmium isotopic composition of the continental crust. Geochimica et Cosmochimica Acta 57, 3093-3104.

Esser, B.K., Turekian, K.K., 1988. Accretion rate of extraterrestrial particles determined from osmium isotope systematics of Pacific pelagic clay and manganese nodules. Geochimica et Cosmochimica Acta 52(6), 1383-1388.

Fischer-Godde, M., Becker, H., Wombacher, F., 2011. Rhodium, gold and other highly siderophile elements in orogenic peridotites and peridotite xenoliths. Chemical Geology 280, 365-383.

Fleet, M.E., Crocket, J.H., Stone, W.E., 1996. Partitioning of platinum-group elements (Os, Ir, Ru, Pt, Pd) and gold between sulfide liquid and basalt melt. Geochimica et Cosmochimica Acta 60(13), 2397-2412.

Frei, R., Dahl, P.S., Duke, E. F., Frei, K.M., Hansen, T.R., Frandsson, M.M., Jensen, L. A., 2008. Trace element and isotopic characterization of Neoarchean and Paleoproterozoic iron formations in the Black Hills (South Dakota, USA): assessment of chemical change during 2.9–1.9 Ga deposition bracketing the 2.4–2.2 Ga first rise of atmospheric oxygen. Precambrian Research 162, 441-474.

Frei, R., Dahl, P.S., Frandsson, M.M., Jensen, L.A., Hansen, T.R., Terry, M.P., Frei, K. M., 2009. Lead-isotope and trace-element geochemistry of Paleoproterozoic metasedimentary rocks in the Lead and Rochford basins (Black Hills, South Dakota, USA): implications for genetic models, mineralization ages, and sources of leads in the Homestake gold deposit. Precambrian Research 172(1), 1-24.

Frei, R., Polat, A. 2007. Source heterogeneity for the major components of~ 3.7 Ga Banded Iron Formations (Isua Greenstone Belt, Western Greenland): tracing the nature of interacting water masses in BIF formation. Earth and Planetary Science Letters 253, 266-281.

Frey, F.A., Green, D.H., 1974. The mineralogy, geochemistry and origin of lherzolite inclusions in Victorian basanites. Geochimica et Cosmochimica Acta 38, 1023–1059.

Gallet, S., Jahn, B.M., Lanoë, B.V.V., Dia, A., Rossello, E., 1998. Loess geochemistry and its implications for particle origin and composition of the upper continental crust. Earth and Planetary Science Letters 156(3), 157-172.

Gao, S., Luo, T.C., Zhang, B.R., Zhang, H.F., Han, Y.W., Zhao, Z.D., Hu, Y.K., 1998. Chemical composition of the continental crust as revealed by studies in East China. Geochimica et Cosmochimica Acta 62, 1959-1975.

Geerdes, M., Chaigneau, R., Kurunov, I., 2015. Modern Blast Furnace Ironmaking: An Introduction (2015). IOS Press.

Griselin, M., van Belle, J.C., Pomies, C., Vroon, P.Z., van Soest, M.C., Davies, G.R., 2001. An improved chromatographic separation technique of Nd with application to NdO+ isotope analysis. Chemical Geology 172, 347-359.

Handler, M.R., Bennett, V.C., Dreibus, G., 1999. Evidence from correlated Ir/Os and Cu/S for late-stage Os mobility in peridotite xenoliths: implications for Re-Os systematics. Geology 27, 75–78.

Hart, S.R., 1984. A large-scale isotope anomaly in the Southern Hemisphere mantle. Nature 309, 753-757.

Harte, B., 1983. Mantle peridotite and processes – the kimberlite sample. Continental Basalts and Mantle Xenoliths (eds. C.J. Hawkesworth and M.J. Norry), Shiva Publishing, Nantwich, UK.

Harvey, J., Dale, C.W., Gannoun, A., Burton, K.W., 2011. Osmium mass balance in peridotite and the effects of mantle-derived sulphides on basalt petrogenesis. Geochimica et Cosmochimica Acta 75(19), 5574-5596.

Harvey, J., Gannoun, A., Burton, K.W., Rogers, N.W., Alard, O., Parkinson I.J., 2006. Ancient melt extraction from the oceanic upper mantle revealed by Re-Os isotopes in abyssal peridotites from the Mid-Atlantic ridge. Earth and Planetary Science Letters 244, 606-621.

Hattori, Y., Suzuki, K., Honda, M., Shimizu, H., 2003. Re-Os isotope systematics of the Taklimakan Desert sands, moraines and river sediments around the Taklimakan Desert, and of Tibetan soils. Geochimica et Cosmochimica Acta 67, 1203-1213.

Hellebrand, E., Snow, J.E., Dick, H.J.B., Hofmann, A.W., 2001. Coupled major and trace elements as indicators of the extent of melting in mid-ocean-ridge peridotites. Nature 410, 677–681.

Hofmann, A.W., 1997. Mantle geochemistry: the message from oceanic volcanism. Nature 385(6613), 219-229.

Hofmann, A.W., White, W.M., 1982. Mantle plumes from ancient oceanic crust. Earth and Planetary Science Letters 57, 421-436.

Horan, M.F., Walker, R.J., Morgan, J.M., Grossman, J.N., Rubin, A.E., 2003. Highly siderophile elements in chondrites. Chemical Geology 193, 5–20.

Hu, Z., Gao, S., 2008. Upper crustal abundances of trace elements: a revision and update. Chemical Geology 253(3), 205-221.

International Energy Agency, 2015. Key World Energy Statistics 2015. Report by Internal Energy Agency, 1-81.

Ireland, T.J., Walker, R.J., Brandon, A.D., 2011. ^{186}Os–^{187}Os systematics of Hawaiian picrites revisited: new insights into Os isotopic variations in ocean island basalts. Geochimica et Cosmochimica Acta 75, 4456–4475.

Jaffe, L.A., Peucker-Ehrenbrink, B., Petsch, S.T., 2002. Mobility of rhenium, platinum group elements and organic carbon during black shale weathering. Earth and Planetary Science Letters 198(3), 339-353.

Jagoutz, E., Palme, H., Baddenhausen, H., Blum, K., Cendales, M., Dreibus, G., Spettel, B., Wänke, H., Lorenz, V., 1979. The abundances of major, minor and trace elements in the earth's mantle as derived from primitive ultramafic nodules. Lunar and Planetary Science Conference Proceedings 10, 2031-2050.

Jamais, M., Lassiter, J.C., Brugmann, G., 2008. PGE and Os-isotopic variations in lavas from Kohala Volcano, Hawaii: Constraints on PGE behavior and melt/crust interaction. Chemical Geology 250, 16-28.

Jenner, G.A., Longerich, H.P., Jackson, S.E., Fryer, B.J., 1990, ICP-MS - A powerful tool for high-precision trace-element analysis in Earth sciences: Evidence from analysis of selected U.S.G.S. reference samples. Chemical Geology, 83, 133-148.

Johnson, D.M., Hooper, P.R., Conrey, R.M., 1999. XRF Analysis of Rocks and Minerals for Major and Trace Elements on a Single Low Dilution Li-tetraborate Fused Bead. Advances in X-ray Analysis 41, 843-867.

Johnson, K.T.M., Dick, H.J.B., Shimizu, N., 1990. Melting in the upper oceanic mantle- an ion microprobe study of diopsides in abyssal peridotites. Journal of Geophysical Research-Solid 95, 2661–2678.

Kelemen, P.B., 1995. Genesis of high Mg# andesites and the continental crust. Contributions to Mineralogy and Petrology 120(1), 1-19.

Kellogg, L.H., Turcotte, D.L., 1987. Homogenization of the mantle by convective mixing and diffusion. Earth and Planetary Science Letters 81, 371-378.

Kellogg, L.H., Turcotte, D.L., 1990. Mixing and distribution of heterogeneities in a chaotically convecting mantle. Journal of Geophysical Research 95 (B1), 421-432.

Kendall, B. (2014). An osmium-based method for assessing the source of dissolved rhenium and molybdenum to Archean seawater. Chemical Geology, 385, 92-103.

Klein, C. (2005). Some Precambrian banded iron-formations (BIFs) from around the world: Their age, geologic setting, mineralogy, metamorphism, geochemistry, and origins. American Mineralogist, 90(10), 1473-1499.

Knaack, C., Cornelius, S., Hooper, P.R., 1994. Trace element analyses of rocks and minerals by ICP-MS. Open File Report, Dept. Geol., Wash. State U., Pullman.

Kocks, H., Melcher, F., Meisel, T., Burgath, K.P., 2007. Diverse contributing sources to chromitite petrogenesis in the Shebenik Ophiolitic Complex, Albania: evidence from new PGE-and Os-isotope data. Mineralogy and Petrology 91(3-4), 139-170.

Lassiter, J.C., 2006. Constraints on the coupled thermal evolution of the Earth's core and mantle, the age of the inner core, and the origin of the $^{186}Os/^{188}Os$ "core signal" in plume-derived lavas. Earth and Planetary Science Letters 250, 306-317.

Lassiter, J.C., Blichert-Toft, J., E.H., Hauri, E.H., Barsczus, H.G., 2003. Isotope and trace element variations in lavas from Raivavae and Rapa, Cook-Austral islands: constraints on the nature of HIMU- and EM-mantle and the origin of mid-plate volcanism in French Polynesia. Chemical Geology 202, 115-138.

Lassiter, J.C., Byerly, B.L., Snow, J.E., Hellebrand, E., 2014. Constraints from Os-isotope variations on the origin of Lena Trough abyssal peridotites and implications for the composition and evolution of the depleted upper mantle. Earth and Planetary Science Letters 403, 178-187.

Lassiter, J.C., Hauri, E.H., 1998. Osmium-isotope variations in Hawaiian lavas: evidence for recycled oceanic lithosphere in the Hawaiian plume. Earth and Planetary Science Letters 164, 483-496.

Lassiter, J.C., Luhr, J.F., 2001. Osmium abundance and isotope variations in mafic Mexican volcanic rocks: evidence for crustal contamination and constraints on the geochemical behavior of osmium during partial melting and fractional crystallization. Geochemistry Geophysics Geosystems 2, (2000GC000116.2).

Le Roux, V., Bodinier, J.L., Tommasi, A., Alard, O., Dautria, J.M., Vauchez, A., Riches, A.J.V., 2007. The Lherz spinel lherzolite: refertilized rather than pristine mantle. Earth and Planetary Science Letters 259, 599-612.

Lee, C.T.A., Morton, D.M., Little, M.G., Kistler, R., Horodyskyj, U.N., Leeman, W.P., Agranier, A., 2008. Regulating continent growth and composition by chemical weathering. Proceedings of the National Academy of Sciences 105(13), 4981-4986.

Liu, Y., Huang, M., Masuda, A., Inoue, M., 1998. High-precision determination of osmium and rhenium isotope ratios by in situ oxygen isotope ratio correction using negative thermal ionization mass spectrometry. International Journal of Mass Spectrometry and Ion Processes 173, 163–175.

Lorand, J.P., Alard, O., Godar, M., 2009. Platinum-group element signature of the primitive mantle rejuvenated by melt-rock reactions: evidence from Sumail peridotites (Oman ophiolite). Terra Nova 21, 35-40

Lorand, J.P., Alard, O., Luguet, A., 2010. Platinum-group element micronuggets and refertilization process in Lherz orogenic peridotites (northeastern Pyrenees, France). Earth and Planetary Science Letters 289, 298-310.

Luck, J.M., Allegre., C.J., 1983. ^{187}Re-^{187}Os systematics in meteorites and cosmochemical consequences. Nature 302, 130-132.

Ludwig, K.R., 1997. Optimization of multicollector isotope-ratio measurement of strontium and neodymium. Chemical Geology 135, 325-334.

Ludwig, K.R., 2009. Isoplot 4.1. A geochronological tool kit for Microsoft Excel. Berkeley Geochronology Center Special Publication, Vol 4, 76.

Luguet, A., Alard, O., Lorand, J-,P., Pearson, N.J., Ryan, C., O'Reilly, S.Y., 2001. Laser-ablation microprobe (LAM)-ICPMS unravels the highly siderophile element geochemistry of the oceanic mantle. Earth and Planetary Science Letters 189, 285–294.

Luguet, A., Lorand, J.P., Seyler, M., 2003. A coupled study of sulfide petrology and highly siderophile element geochemistry in abyssal peridotites from the Kane Fracture Zone (MARK area, Mid-Atlantic ridge). Geochimica et Cosmochimica Acta 67, 1553–1570.

Luguet, A., Nowell, G.M., Pearson, D.G., 2008. $^{184}Os/^{188}Os$ and $^{186}Os/^{188}Os$ measurements by Negative Thermal Ionisation Mass Spectrometry (N-TIMS): Effects of interfering element and mass fractionation corrections on data accuracy and precision. Chemical Geology 248, 342–362.

Luguet, A., Pearson, D.G., Nowell, G.M., Dreher, S.T., Coggon, J.A., Spetsius, Z.V., Parman, S.W., 2008. Enriched Pt–Re–Os isotope systematics in plume lavas explained by metasomatic sulfides. Science 319, 453–456.

Luguet, A., Reisberg, L., 2016. Highly siderophile element and ^{187}Os signatures in non-cratonic basalt-hosted peridotite xenoliths: Unravelling the origin and evolution of the Post-Archean lithospheric mantle. Reviews in Mineralogy and Geochemistry 81, 305–367.

Maier, W.D., Peltonen, P., McDonald, I., Barnes, S.J., Barnes S-J., Hatton, C., Viljoen, F., 2012. The concentration of platinum-group elements and gold in Southern African and Karelian kimberlite-hosted mantle xenoliths: Implications for the noble metal content of the Earth's mantle. Chemical Geology 302-303, 119-135.

Mallick, S., Standish, S.J., Bizimis, M., 2015. Constraints on the mantle mineralogy of an ultra-slow ridge: Hafnium isotopes in abyssal peridotites and basalts from the 9–25◦E Southwest Indian Ridge. Earth and Planetary Science Letters 410, 42-53.

Mann, U., Frost, D.J., Rubie, D.C., Becker, H., Audetat, A., 2012. Partitioning of Ru, Rh, Pd, Re, Ir and Pt between liquid metal and silicate at high pressures and high temperatures-Implications for the origin of highly siderophile element concentrations in the Earth's mantle. Geochimica et Cosmochimica Acta 84, 592-613.

Marchesi, C., Garrido, C.J., Harvey, J., Gonzalez-Jimenez, J.M., Hidas, K., Lorand, J.P., Gervilla, F., 2013. Platinum-group elements, S, Se and Cu in highly depleted abyssal peridotites from the Mid-Atlantic Ocean Ridge (ODP Hole 1274): Influence of hydrothermal and magmatic processes. Contributions to Mineralogy and Petrology 166, 1521-1538.

Martin, H., 1994. The Archean grey gneisses and the genesis of continental crust. Developments in Precambrian geology 11, 205-259.

McDaniel, D.K., Walker, R.J., Hemming, S.R., Horan, M.F., Becker, H., Grauch, R.I., 2004. Sources of osmium to the modern oceans: new evidence from the ^{190}Pt-^{186}Os system. Geochimica et Cosmochimica Acta 68, 1243-1252.

McDonough, W.F., Sun, S-s., 1995. The composition of the Earth. Chemical Geology 120, 223-253.

McMaster-Carr, 2010a. More about steel alloys. Report by McMaster-Carr Supply Company, 1-7.

McMaster-Carr, 2010b. More about stainless steel alloys. Report by McMaster-Carr Supply Company, 1-2.

Meibom, A., Frei, R., Sleep, N.H., 2004. Osmium isotopic compositions of Os-rich platinum group element alloys from the Klamath and Siskiyou Mountains. Journal of Geophysical Research 109, pp14.

Meisel, T., Fellner, N., Moser, J., 2003. A simple procedure for the determination of platinum group elements and rhenium (Ru, Rh, Pd, Re, Os, Ir and Pt) using ID-ICP-MS with an inexpensive on-line matrix separation in geological and environmental materials. Journal of Analytical Atomic Spectrometry 18, 720-726.

Meisel, T., Walker, R.J., Irving, A.J., Lorand, J-P., 2001. Osmium isotopic compositions of mantle xenoliths: A global perspective. Geochimica et Cosmochimica Acta 65, 1311-1323.

Miller, R.G., O'Nions, R.K., Hamilton, P.J., Welin, E., 1986. Crustal residence ages of clastic sediments, orogeny and continental evolution. Chemical Geology 57, 87-99.

Morgan, J.W., 1986. Ultramafic xenoliths: clues to Earth's late accretionary history. Journal of Geophysical Research 91, 12375–12387.

Moyen, J.F., Stevens, G., Kisters, A. 2006. Record of mid-Archaean subduction from metamorphism in the Barberton terrain, South Africa. Nature 442(7102), 559-562.

Muehlenbachs, K., 1998. The oxygen isotopic composition of the oceans, sediments and the seafloor. Chemical Geology 145(3), 263-273.

Mungall, J.E., Su, S., 2005. Interfacial tension between magmatic sulfide and silicate liquids. Controls on kinetics of sulfide liquation and sulfide migration through silicate rocks. Earth and Planetary Science Letters 234, 135-149.

Nelsen, M.P., DiMichele, W.A., Peters, S.E., Boyce, C.K., 2016. Delayed fungal evolution did not cause the Paleozoic peak in coal production. Proceedings of the National Academy of Sciences 113(9), 2442-2447.

Newsom, H.E., 1990. Accretion and core formation in the Earth: Evidence from siderophile elements. In: Newsom, H.E., Jones, J. (Eds.), Origin of the Earth. Oxford University Press, Oxford, pp. 273–288.

Nier, A.O., 1950. A redetermination of the relative abundances of the isotopes of carbon, nitrogen, oxygen, argon and potassium. Physical Review 77, 789-793.

Nyquist, H., 1928. Thermal agitation of electric charge in conductors. Physical Review 32, 110-113.

Pacyna, J.M., (1984). Estimation of the atmospheric emissions of trace elements from anthropogenic sources in Europe. Atmospheric Environment 18, 41-50.

Papp, J.F., Lipin, B.R., 2001. Chromium. U.S. Geological Survey Open-File Report 2001–381, 1-130.

Park, J.W., Hu, Z., Gao, S., Campbell, I.H., Gong, H., 2012. Platinum group element abundances in the upper continental crust revisited–New constraints from analyses of Chinese loess. Geochimica et Cosmochimica Acta 93, 63-76.

Pearson, K., 1895. Notes on regression and inheritance in the case of two parents. Proceedings of the Royal Society of London 58, 240-242.

Percival, J.A., 2007. .4 Eo-to Mesoarchean Terranes of the Superior Province and Their Tectonic Context. Developments in Precambrian Geology 15, 1065-1085.

Peucker-Ehrenbrink, B., Hannigan, R.E., 2000. Effects of black shale weathering on the mobility of rhenium and platinum group elements. Geology 28, 475-478.

Peucker-Ehrenbrink, B., Jahn, B., 2001. Rhenium-osmium isotope systematics and platinum group element concentrations: Loess and the upper continental crust. Geochemistry, Geophysics, Geosystems Vol 2 (2001GC000172).

Peucker-Ehrenbrink, B., Ravizza, G., Hofmann, A.W., 1995. The marine $^{187}Os/^{186}Os$ record of the past 80 million years. Earth and Planetary Science Letters 130(1), 155-167.

Peucker-Ehrenbrink, B., Jahn, B.M., 2001. Rhenium-osmium isotope systematics and platinum group element concentrations: Loess and the upper continental crust. Geochemistry, Geophysics, Geosystems, 2(10).

Poulton, S. W., Fralick, P. W., & Canfield, D. E. (2010). Spatial variability in oceanic redox structure 1.8 billion years ago. Nature Geoscience 3(7), 486-490.

Poveromo, J.J., 1999. Iron ores. Making, Shaping and Treating of Steel-Ironmaking volume, 547-642.

Puchtel, I.S., Brandon, A.D., Humayun, M., 2004. Precise Pt-Re-Os isotope systematics of the mantle from 2.7-Ga komatiites. Earth and Planetary Science Letters 224, 157-174.

Puchtel, I.S., Brandon, A.D., Humayun, M., Walker, R.J., 2005. Evidence for the early differentiation of the core from Pt-Re-Os isotope systematics of 2.8-Ga komatiites. Earth and Planetary Science Letters 237, 118-134.

Qi, L., Gao, J., 2008. Revisiting platinum group elements of Late Permian coals from western Guizhou Province, SW China. International Journal of Coal Geology 75(3), 189-193.

Ravizza, G., 1993. Variations of the $^{187}Os/^{186}Os$ ratio of seawater over the past 28 million years as inferred from metalliferous carbonates. Earth and Planetary Science Letters 118(1), 335-348.

Ravizza, G., Pyle, D., 1997. PGE and Os isotopic analyses of single sample aliquots with NiS fire assay preconcentration. Chemical Geology 141(3), 251-268.

Rehkamper, M., Halliday, A.N., Alt, J., Fitton, J.G., Zipfel, J., Takazawa, E., 1999. Non-chondritic platinum-group element ratios in oceanic mantle lithosphere: petrogenic Re, Os, Ir, Pt and Pd signature of melt percolation. Earth and Planetary Science Letters 172, 65–81.

Reisberg, L., Lorand, J.-P., 1995. Longevity of sub-continental mantle lithosphere from osmium isotope systematics in orogenic peridotite massifs. Nature 376, 159-162.

Reisberg, L., Zindler, A., 1986. Extreme isotopic variation in the upper mantle: evidence from Ronda. Earth and Planetary Science Letters 81, 29-45.

Righter, K., 2011. Prediction of metal-silicate partition coefficients for siderophile elements: An update and assessment of PT conditions for metal-silicate equilibrium during accretion of the Earth. Earth and Planetary Science Letters 304, 158-167

Righter, K., Humayun, M., Danielson, L., 2008. Partitioning of palladium at high pressures and temperatures during core formation. Nature Geoscience 1, 321-323.

Ripley, E.M., Shafer, P., Li, C., Hauck, S.A., 2008. Re–Os and O isotopic variations in magnetite from the contact zone of the Duluth Complex and the Biwabik Iron Formation, northeastern Minnesota. Chemical Geology 249(1), 213-226.

Rosman, K.J.R., Taylor, P.D.P., 1998. Isotopic composition of the elements 1997. Pure and Applied Chemistry 70, 217-235.

Rubie, D.C., Frost, D.J., Mann, U., Asahara, Y., Nimmo, F., Tsuno, K., Kegler, P., Holzheid, A., Palme, H., 2011. Heterogeneous accretion, composition and core-mantle differentiation of the Earth. Earth and Planetary Science Letters 301, 31-42.

Rudnick, R.L., 1995. Making continental crust. Nature, 378(6557), 571-577.

Rudnick, R.L., Gao, S.X., 2003. Composition of the continental crust. Treatise on geochemistry 3, 1-64.

Rudnick, R.L., Walker, R.J., 2009. Interpreting ages from Re-Os isotopes in peridotites. Lithos 112S, 1083-1095

Salters, V.J.M., Dick, H.J.B., 2002. Mineralogy of the mid-ocean-ridge basalt source from neodymium isotopic composition of abyssal peridotites. Nature 418, 68-72.

Sattari, P., Brenan, J.M., Horn, I., McDonough, W.F., 2002. Experimental constraints on the sulfide and chromite-silicate melt partitioning behavior of rhenium and platinum-group elements. Economic Geology 97, 385-398.

Schiano, P., Bourdon, B., 1999. On the preservation of mantle information in ultramafic nodules: glass inclusions within minerals versus interstitial glasses. Earth and Planetary Science Letters 169, 173-188.

Schmidt, G., Palme, H., Kratz, K.L., 1997. Fractionation of highly siderophile elements in the Earth's upper continental crust, Yearbook Inst. Nuclear Chem, 15.

Schulte, R.F., Taylor, R.D., Piatak, N.M., Seal, R.R., II, 2010. Stratiform chromite deposit model. U.S. Geological Survey Open-File Report 2010–1232, 1-7.

Selby, D., Creaser, R.A., Stein, H.J., Markey, R.J., Hannah, J.L., 2007. Assessment of the 187Re decay constant by cross calibration of Re-Os molybdenite and U-Pb zircon chronometers in magmatic ore systems. Geochimica et Cosmochimica Acta 71, 1999-2013.

Sessions, A.L., Doughty, D.M., Welander, P.V., Summons, R.E., Newman, D.K., 2009. The continuing puzzle of the great oxidation event. Current Biology 19(14), R567-R574.

Sharma, M., Papanastassiou, D.A., Wasserburg, G.J., 1997. The concentration and isotopic composition of osmium in the oceans. Geochimica et Cosmochimica Acta 61(16), 3287-3299.

Sharma, M., Wasserburg, G. J., Hofmann, A. W., & Chakrapani, G. J. (1999). Himalayan uplift and osmium isotopes in oceans and rivers. Geochimica et Cosmochimica Acta 63, 4005-4012.

Siebert, C., Kramers, J.D., Meisel, T., Morel, P., Nägler, T.F., 2005. PGE, Re-Os, and Mo isotope systematics in Archean and early Proterozoic sedimentary systems as proxies for redox conditions of the early Earth. Geochimica et Cosmochimica Acta 69(7), 1787-1801.

Singh, S.K., Trivedi, J.R., Krishnaswami, S., 1999. Re-Os isotope systematics in black shales from the Lesser Himalaya: Their chronology and role in the $^{187}Os/^{188}Os$ evolution of seawater. Geochimica et Cosmochimica Acta 63(16), 2381-2392.

Smith, C.B., Pearson, D.G., Bulanova, G.P., Beard, A.D., Carlson, R.W., Wittig, N., Sims, K.W.W., Chimuka, L., Muchemwa, E., 2009. Extremely depleted lithospheric mantle and diamonds beneath the Southern Zimbabwe craton. Lithos 112S, 1120-1132.

Snow, J., Petrology Group ARK-XX-2., 2007. Petrology of Lena Trough and Gakkel Ridge, in "The Expeditions ARK-TIS-XX/1 and XX/2 of the Research Vessel "Polarstern" in 2004", Ber. Polar Meeresforsch 544, 153-208.

Snow, J.E., Hellebrand, E., von der Handt, A., Nauret, F., Gao, Y.J., Schenke, H.W., 2011. Oblique nonvolcanic seafloor spreading in Lena Trough, Arctic Ocean. Geochemistry. Geophysics. Geosystems 12, doi: 10.1029/2011GC003768.

Snow, J.E., Reisberg, L., 1995. Os isotopic systematics of the MORB mantle: results from altered abyssal peridotites. Earth and Planetary Science Letters 133, 411-421.

Stracke, A., Bizimis, M., Salters, V.J., 2003. Recycling oceanic crust: quantitative constraints. Geochemistry, Geophysics, Geosystems, 4(3).

Stracke, A., Snow, J.E., Hellebrand, E., von der Handt, A., Bourdon, B., Birbaum, K., Günther, D., 2011. Abyssal peridotite Hf isotopes identify extreme mantle depletion. Earth and Planetary Science Letters 308, 359-368.

Suzuki, K., Kato, Y., 2003. Re-Os isotope systematics of 3.8 Ga banded iron formation and cherts from Isua supracrustal belt, SW Greenland. Geochimica et Cosmochimica Acta Supplement 67, 459.

Taylor, S.R., McLennan, S.M., 1995. The geochemical evolution of the continental crust. Reviews of Geophysics 33, 241-265.

Thirlwall, M.F., 1991. High-precision multi collector isotopic analysis of low levels of Nd as oxide. Chemical Geology 94, 13-22.

Todt, W., Cliff, R. A., Hanser, A., & Hofmann, A. W. (1996). Evaluation of a ^{202}Pb–^{205}Pb double spike for high-precision lead isotope analysis. Earth processes: reading the isotopic code, 429-437.

Todt, W., Cliff, R.A., Hanser, A., Hofmann, A.W., 1993. Re-calibration of NBS lead standards using a ^{202}Pb+ ^{205}Pb double spike. Terra Abstracts 5(1), 396.

Uysal, I., Tarkian, M., Sadiklar, M.B., Zaccarini, F., Meisel, T., Garuti, G., Heidrich, S., 2009. Petrology of Al-and Cr-rich ophiolitic chromitites from the Muğla, SW Turkey: implications from composition of chromite, solid inclusions of platinum-group mineral, silicate, and base-metal mineral, and Os-isotope geochemistry. Contributions to Mineralogy and Petrology 158(5), 659-674.

Van Kranendonk, M.J., Hickman, A., Smithies, R.H., 2007. The East Pilbara Terrane of the Pilbara Craton, Western Australia: Formation of a continental nucleus through repeated mantle plume magmatism. Earth's Oldest Rocks. Developments in Precambrian Geology 15, 307-337.

van-Acken, D., Becker, H., Hammerschmidt, K., Walker, R.J., Wombacher, F., 2010. Highly siderophile elements and Sr-Nd isotopes in refertilized mantle peridotites- A case study from the Totalp ultramafic body, Swiss Alps. Chemical Geology 276, 257-268.

Veizer, J., 1989. Strontium isotopes in seawater through time. Annual Review of Earth and Planetary Sciences 17, 141.

Wade, J., Wood, B.J., 2005. Core formation and the oxidation state of the Earth. Earth and Planetary Science Letters 236, 78-95

Walker, R.J., Brandon, A.D., Bird, J.M., Piccoli, P.M., McDonough, W.F., Ash, R.D., 2005. ^{187}Os–^{186}Os systematics of Os–Ir–Ru alloy grains from southwestern Oregon. Earth and Planetary Science Letters 230, 211–226.

Walker, R.J., Carlson, R.W., Shirey, S.B., Boyd, F.R., 1989. Os, Sr, Nd, and Pb isotope systematics of southern African peridotite xenoliths: Implications for the chemical evolution of the subcontinental mantle. Geochimica et Cosmochimica Acta 53, 1583-1595.

Walker, R.J., Morgan, J.W., Beary, E.S., Smoliar, M.I., Czamanske, G.K., Horan, M.F., 1997. Applications of the ^{190}Pt-^{186}Os isotope system to geochemistry and cosmochemistry. Geochimica et Cosmochimica Acta 61, 4799-4807.

Walker, R.J., Prichard, H.M., Ishiwatari, A., Pimentel, M., 2002. The osmium isotopic composition of convecting upper mantle deduced from ophiolite chromites. Geochimica et Cosmochimica Acta 66, 329-345.

Warren, J.M., Shimizu, N., Sakaguchi, C., Dick, H.J.B., Nakamura, E., 2009. An assessment of upper mantle heterogeneity based on abyssal peridotite isotopic compositions. Journal of Geophysical Research, 114, B12203.

Wasserburg, G.J., Jacobsen, S.B., DePaolo, D.J., McCulloch, M.T., Wen, T., 1981. Precise determination of Sm/Nd ratios and Sm and Nd isotopic abundances in standard solutions. Geochimica et Cosmochimica Acta 45, 2311–2323.

Wedepohl, K.H., 1995. The composition of the continental crust. Geochimica et Cosmochimica Acta 59, 1217-1232.

Whitehouse, M.J., Neumann, E.R., 1995. Sr-Nd-Pb isotope data for ultramafic xenoliths from Hierro, Canary Islands: Melt infiltration processes in the upper mantle. Contributions to Mineralogy and Petrology 119(2-3), 239-246.

Wittig, N., Pearson, D.G., Baker, J.A., Duggen, S., Hoernle, K.A., 2010. A major element, PGE and Re-Os isotope study of Middle Atlas (Morocco) peridotite xenoliths: Evidence for coupled introduction of metasomatic sulphides and clinopyroxene. Lithos 115, 15-26.

Wood, B.J., Nielsen, S.G., Rehkamper, M., Halliday, A.N., 2008. The effects of core formation on the Pb- and Tl- isotopic composition of the silicate Earth. Earth and Planetary Science Letters 269, 326-336.

World Steel Association, 2014a. World Steel in figures 2014. Report by World Steel Association, 1-30.

World Steel Association, 2014b. Iron ore and Steel-Fact Sheet. Report by World Steel Association, 1-2.

Xiao, Yan., Zhang, Hong-Fu., 2011. Effects of melt percolation on platinum group elements and Re-Os systematics of peridotites from the Tan-Lu Fault zone, Eastern North China craton. Journal of Geological Society of London 168, 1201-1214.

Xu, G., Hannah, J.L., Stein, H.J., Bingen, B., Yang, G., Zimmerman, A., Weitschat, W., Mørk, A., Weiss, H.M., 2009. Re–Os geochronology of Arctic black shales to evaluate the Anisian–Ladinian boundary and global faunal correlations. Earth and Planetary Science Letters 288(3), 581-587.

Xu, Yi-Gang., Blusztajn, J., Ma, Jin-Long., Suzuki, K., Liu, Jiang-Feng., Hart, S.R., 2008. Late Archean to early Proterozoic lithospheric mantle beneath the Western North China

Craton: Sr-Nd-Os isotopes of peridotite xenoliths from Yangyuan And Fansi. Lithos 102, 25-42.

Yokoyama, T., Rai, V.K., Alexander, C.M.O'D., Lewis, R.S., Carlson, R.W., Shirey, S.B., Thiemens, R.H., Walker, R.J., 2007. Osmium isotope evidence for uniform distribution of s- and r-process components in the Early solar system. Earth and Planeary Science Letters 259, 567-580.

Zhang, Hong-Fu, Sun, Ya-Li., Tang, Yan-Jie., Xiao, Yan., Zhang, Wenhui., Zhao, Xin-Miao., Santosh M., Menzies, M.A., 2012. Melt-peridotite interaction in the Precambrian mantle beneath the Western North China craton: Petrology, geochemistry and Sr, Nd and Re isotopes. Lithos 149, 100-114.

Zhang, Hong-Fu., Goldstein, S.L., Zhou, Xin-Hua., Sun, Min., Cai, Yue., 2009. Comprehensive refertilization of lithospheric mantle beneath the North China Craton: Further Os-Sr-Nd isotopic constraints. Journal of Geological Society of London 166, 249-259.

Zhang, Hong-Fu., Goldstein, S.L., Zhou, Xin-Hua., Sun, Min., Zheng, Jian-Ping., Cai, Yue., 2010. Evolution of subcontinental lithospheric mantle beneath Eastern China: Re-Os isotopic evidence from mantle xenoliths in Paleozoic kimberlites and Mesozoic basalts. Contributions to Mineralogy and Petrology 155, 271-293.

Zhou, M.F., Sun, M., Keays, R.R., Kerrich, R.W., 1998. Controls on platinum-group elemental distributions of podiform chromitites: a case study of high-Cr and high-Al chromitites from Chinese orogenic belts. Geochimica et Cosmochimica Acta 62(4), 677-688.